UNIVERSIDAD DE GRANADA
PROGRAMA DE DOCTORADO EN FÍSICA Y MATEMÁTICAS (FISYMAT)

THE LONG/SHORT GRB HOST GALAXY DICHOTOMY:
MUTUAL INTERACTIONS BETWEEN ENVIRONMENT AND PROGENITOR

Memoria presentada por
José Feliciano Agüí Fernández

bajo la dirección de:
Dr. Christina C. Thöne y **Dr. Antonio de Ugarte Postigo**
para optar al grado de DOCTOR

April 30, 2025

Editor: Universidad de Granada. Tesis Doctorales
Autor: José Feliciano Agüí Fernández
ISBN: 978-84-1195-946-9
URI: https://hdl.handle.net/10481/108851

A mi Padre

Contents

Abstract

GRBs are among the most luminous explosions that we can observe in the Universe. They are known to happen during the collapse of massive stars (long GRBs) or during the merger of two neutron stars (short GRBs). This thesis aims to provide new insights into the dichotomy between short and long GRBs through the study of their observational properties as well as the study of the physical conditions of their environments.

GRBs are commonly divided into two types based on their observational properties and their assumed progenitors. In both cases, the product of this cataclismic events is a newborn massive neutron star or a black hole. An accretion disk is formed around the central engine and highly collimated ultrarelativistic jets are launched orthogonally to the accretion disk. These jets have two distinct observational phases. The first one, the so-called prompt emission is characterised by an extremely luminous and highly variable gamma-ray emission that is believed to be produced by internal shocks within the jets. The second electromagnetic emission is produced when the jet interacts with the circumburst medium and is decelerated, emitting synchrotron light produced by the accelerated particles within the collision. Traditionally, the distinction between short and long GRBs has been done through the duration of their prompt emission with a dividing line of $\sim 2s$ between long and short GRBs. However, some recent events challenge this division.

The distinction between short and long GRBs is not always clear, particularly in cases where long GRBs exhibit features resembling those of short GRBs with extended emission. In some of these events, kilonovae (KNe) have been detected, indicating a merger origin. Their different progenitors might be indicative of different environments. While collapsars typically occur in strongly star-forming, low metallicity regions of star-forming galaxies, mergers are detected in many different galaxy types, from star-forming to more massive and passive galaxies. And some of them are even located outside their host galaxies

In this thesis we study one example for each GRB type using different methods. GRB 160410A a short GRB for which we carried out the first (and only to date) study on the chemical abundances in its immediate environment, specifically, a short GRB with an extended emission during the prompt phase. We analysed its afterglow and, in particular, studied its spectrum observed by the X-shooter spectrograph on at the Very Large Telescope. This burst was located at redshift 1.7177, one of the furthest ever detected short GRBs and one of the very few short GRB with a redshift

determined from absorption lines in its afterglow spectrum. Our study revealed a very metal-poor environment, an unexpected result for this GRB type. Binary NSs require long delay times to merge as they lose gravitational energy through gravitational waves emission, which is a slow process in its early phases. However, a scenario in which a binary system evolves rapidly is a non-negligible possibility. In the case of GRB 160410A, the system would need a relatively rapid evolution to merge, considering its high redshift. This short GRB revealed that these explosions can also happen in an environment with low metal content. A more common short GRB was GRB 201221D, also included in this work. Although a chemical study was not possible for this burst, the spectrum revealed a low ionisation environment which could be indicative of the short burst happening in a young galaxy with a relatively low amount of massive stars.

The second GRB presented in this thesis, GRB 210610B, was a long GRB for which we obtained polarimetric, spectroscopic and photometric observations of its GRB afterglow, as well as late photometric observations of the host galaxy. The analysis of this burst revealed a dust-free long burst with a moderate polarisation degree at early stages associated with an ordered magnetic fields linked to a reverse shock. The polarisation level vanished achromatically towards the end of a plateau in its light curve evolution when the forward shock starts dominating the light curve and finally the polarisation increases to low levels in the final decay of the light curve, which could be indicative of small asymetries in the emitting region or due to turbulent magnetic fields.

Finally, we study the properties of collapsar-origin GRB host galaxies using the SHOALS sample with data covering from the UV to the MIR bands. SHOALS is the largest GRB host sample to date and based on several *Spitzer* large programs, complemented by data from GTC, HST, VLT and other facilities. We study a subsample of 61 galaxies from the SHOALS sample of 61 host galaxies with secure redshift masurements and with photometric detections in different bands, allowing for good spectral coverage. We perform Spectral Energy Distribution (SED) fit using the `CIGALE` code to obtain galaxy integrated properties such as stellar mass, star fomation rate (SFR), extinction, metallicity and the age of the main stellar population.

The SED analysis reveals that long GRB hosts are galaxies with a high SFR and overall low metallicities. The stellar mass distribution spans several orders of magnitude although it seems to show some trend towards lower masses but not to the lowest-end of the stellar mass distribution for field galaxies. The specific SFR is at the very upper range of the distribution for field galaxies which points to a high ongoing SFR at any host galaxy mass. Ongoing star formation episode is high comparatively to the total stellar mass. This is in agreement with the young age for the main stellar population and with the low metallicity we find.

Our results suggest that long GRBs occurring from the collapse of massive stars preferentially happen in galaxies with high SFR and low metallicity with overall relatively low stellar masses. This is consistent with previous studies (Krühler et al. 2015; Perley et al. 2016b; Palmerio et al. 2019) and this results also support the idea of collapsar GRBs happening in different environment than the one of merger GRBs.

Resumen

Las explosiones de rayos gamma (GRBs por sus siglas en inglés) se encuentran entre las explosiones más luminosas que podemos observar en el Universo. Se sabe que ocurren durante el colapso de estrellas masivas (GRBs largos) o durante la fusión de estrellas de neutrones (GRBs cortos). Esta tesis tiene como objetivo proporcionar nuevos conocimientos sobre la dicotomía entre los GRBs cortos y largos mediante el estudio de sus propiedades observacionales, así como las condiciones físicas de los entornos en los que ocurren.

Los GRBs suelen dividirse en dos tipos, según sus propiedades observacionales y sus supuestos progenitores. Pueden originarse en el colapso de una estrella masiva al final de su vida o en la fusión de dos objetos compactos. En ambos casos, el producto de estos eventos catastróficos es una estrella de neutrones masiva recién nacida o un agujero negro. Alrededor del motor central se forma un disco de acreción y se lanzan chorros ultrarrelativistas altamente colimados de forma ortogonal al disco. Estos chorros tienen dos fases observacionales distintas. La primera, conocida como emisión inicial (o prompt emission), se caracteriza por una emisión de rayos gamma extremadamente luminosa y altamente variable que se cree es producida por choques internos dentro de los chorros. La segunda emisión electromagnética ocurre cuando el chorro interactúa con el medio circundante (el circumburst medium) y se desacelera, emitiendo luz sincrotrón generada por las partículas aceleradas en la colisión. Tradicionalmente, la distinción entre GRBs cortos y largos se ha hecho según la duración de su emisión inicial, con una línea divisoria de aproximadamente 2 segundos entre ambos tipos. Sin embargo, algunos eventos recientes desafían esta división.

La distinción entre GRBs cortos y largos no siempre es clara, particularmente en casos donde los GRBs largos exhiben características similares a los GRBs cortos con emisión extendida. En algunos de estos eventos, se han detectado kilonovas (KNe), lo que apunta a un origen por fusión. Sus diferentes progenitores sugieren entornos distintos: mientras que los collapsars suelen ocurrir en regiones de formación estelar intensa y baja metalicidad en galaxias con formación estelar, las fusiones se detectan en muchos tipos de galaxias, desde galaxias con formación estelar hasta galaxias más masivas y pasivas. Algunas incluso están ubicadas fuera de sus galaxias anfitrionas.

En esta tesis estudiamos un ejemplo de cada tipo de GRB utilizando diferentes métodos. El GRB 160410A, un GRB corto, fue objeto del primer (y único hasta la fecha) estudio sobre las abundancias químicas en el entorno de un GRB corto, específicamente uno con emisión extendida

durante su fase inicial. Analizamos su postluminosidad (afterglow) y, en particular, el espectro de su postluminosidad observado por el espectrógrafo X-shooter en el Very Large Telescope (VLT). Este evento se detectó a un corrimiento al rojo de 1.7177, uno de los GRBs cortos más lejanos jamás detectados y uno de los pocos con un corrimiento al rojo determinado a partir de líneas de absorción en su espectro de postluminosidad. Nuestro estudio reveló un entorno con muy baja metalicidad, un resultado inesperado para este tipo de GRB. Los GRBs cortos requieren largos tiempos de retraso para fusionarse, ya que pierden energía gravitacional mediante la emisión de ondas gravitacionales, un proceso lento en sus fases iniciales. Sin embargo, un escenario en el que un sistema binario evoluciona rápidamente es una posibilidad no despreciable. En el caso de GRB 160410A, el sistema necesitaría una evolución relativamente rápida para fusionarse, considerando su alto corrimiento al rojo. Este GRB corto reveló que estas explosiones también pueden ocurrir en entornos con bajo contenido metálico. Otro GRB corto incluido en este trabajo fue GRB 201221D. Aunque no fue posible realizar un estudio químico para este evento, su espectro reveló un entorno de baja ionización, lo que podría ser indicativo de que el estallido ocurrió en una galaxia joven.

El segundo GRB presentado en esta tesis, GRB 210610B, fue un GRB largo para el cual obtuvimos observaciones polarimétricas, espectroscópicas y fotométricas de su postluminosidad, así como observaciones fotométricas tardías de su galaxia anfitriona. El análisis de este evento reveló un GRB largo sin polvo y con un grado moderado de polarización en sus etapas tempranas, asociado con campos magnéticos ordenados vinculados a un choque inverso (reverse shock). El nivel de polarización desapareció de manera acromatica hacia el final de una meseta en la evolución de su curva de luz, cuando el choque directo (forward shock) comenzó a dominar la emisión. Finalmente, la polarización aumentó a niveles bajos en la fase de decaimiento final, lo que podría ser indicativo de pequeñas asimetrías en la región emisora o debido a campos magnéticos turbulentos.

Finalmente, estudiamos las propiedades de las galaxias anfitrionas de GRBs de origen collapsar utilizando la muestra SHOALS, que incluye datos que abarcan desde bandas UV hasta MIR. SHOALS es la mayor muestra de galaxias anfitrionas de GRBs recopilada hasta la fecha y se basa en varios programas de gran escala de *Spitzer*, complementados con datos del GTC, HST, VLT y otras instalaciones. Estudiamos una submuestra de 61 galaxias de SHOALS con corrimientos al rojo bien determinados y detecciones fotométricas en diferentes bandas, lo que permite una buena cobertura espectral. Realizamos ajustes de Distribución de Energía Espectral (SED, por sus siglas en inglés) utilizando el código `CIGALE` para obtener propiedades integradas de las galaxias, como la masa estelar, la tasa de formación estelar (SFR, por sus siglas en inglés), la extinción, la metalicidad y la edad de la población estelar principal.

El análisis SED revela que las galaxias anfitrionas de GRBs largos tienen una alta SFR y, en general, bajas metalicidades. La distribución de masas estelares abarca varios órdenes de magnitud, aunque parece mostrar una tendencia hacia masas más bajas, pero no hacia el extremo inferior de la distribución de masas estelares de galaxias de campo. La SFR específica (sSFR, por sus siglas en inglés) se encuentra en el rango superior de la distribución para galaxias de campo, lo que apunta a una alta tasa de formación estelar continua en cualquier masa de galaxia anfitriona. Este episodio de formación estelar en curso es alto en comparación con la masa estelar total, lo que concuerda con la edad joven de la población estelar y con la baja metalicidad que encontramos.

Nuestros resultados sugieren que los GRBs largos, originados en el colapso de estrellas masivas, ocurren preferentemente en galaxias con alta SFR, alta sSFR y baja metalicidad, con masas estelares relativamente bajas en general. Esto es consistente con estudios previos (Krühler et al. 2015; Perley et al. 2016b; Palmerio et al. 2019) y también respalda la idea de que los GRBs por collapsar ocurren en entornos diferentes a los de los GRBs de fusión.

Chapter 1

Introduction

Contents

1.1 An introduction to Gamma-ray bursts history

Traditionally, astronomical objects have been considered stable, with evolutionary timescales far exceding a human lifetime or even human existence. The Universe was conceptualized unchanging over very long periods of time but new observing techniques revealed that this is not the case. In the last decades, the advances in astronomical instrumentations and telescope robotisation have given rise to the era of time-domain astrophysics. A wide range of unique and different transients are being discovered at an incredible speed. This novel area of astronomy experienced an extraordinary boost after the first Gamma-ray Burst, typically referred to as GRB, was discovered back in the late 1960s.

1.1.1 The discovery of GRBs

In the 1960s, the race for the development of nuclear weapons and the increasing number of them became an unacceptable threat to mankind. In an effort to slow down their production and avoid a fatal nuclear war, the United States, the Soviet Union and the United Kingdom signed the Partial Nuclear Test Ban Treaty in 1963. The aim was to forbid nuclear weapon testing, including tests on land, sea and the Space. To control the compliance of the treaty, the United States of America developed the so-called *Vela* program. The Vela program launched several satellites equiped with high-energies (HE) detectors with the aim of detecting the γ-ray emission produced by the blast wave of nuclear explosions.

It was in 1969 when Ray Klebesadel and Roy Olson, looking through the data collected by *Vela 4*, discovered a double peaked signal lasting for a few seconds. This detection was observed simultaneously by *Vela 4A* and *Vela 4B* on the 2$^{\text{nd}}$ of July, 1967. The signal duration and its energy was rather different from a nuclear bomb (Klebesadel et al. 1973). The signal they found was dubbed GRB 670702, the first ever detected Gamma-ray Burst, named after the year, month and day of its detection (see Fig. 1.1).

Following this first GRB, several other were detected by the *Vela 5* and *Vela 6* satellites, possibly around 16 bursts, with durations lasting from 0.1 to 30 seconds (Klebesadel et al. 1973). The improved instruments on-board this second generation of Vela satellites allowed for a higher accuracy on the detection time. This also made it possible to triangulate the burst detections on

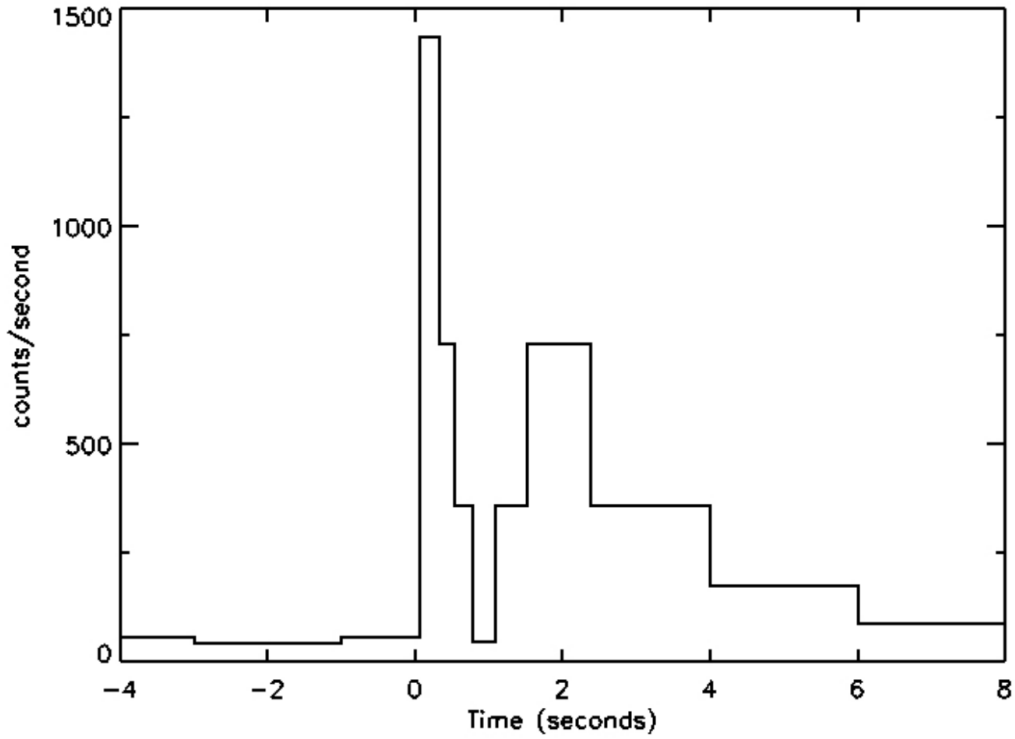

Figure 1.1: Light curve of GRB 670702, the first Gamma-ray Burst detected under the *Vela* program. (Strong & Klebesadel 1976)

the sky and, therefore, to rule out the Sun as a possible origin. However, it was still not possible to know whether the source were of Galactic or extragalactic origin.

1.1.2 The first GRB dedicated missions

The first effort to determine whether GRBs were located in the Milky Way or whether they were extragalactic was the Interplanetary Network (IPN). it was based on the use of γ-ray detectors installed on several space missions that detect GRBs and allow for precise triangulation (see Hurley et al. 2006 and references therein for a further description on the IPN). However, the large times needed to obtain the data and analyse them, the large error boxes and the lack of big telescopes in the 1970s when the IPN was created, made it impossible to detect GRB counterparts at optical wavelengths.

The origin of GRBs would remain unknown until the 1990s, when the Comptom Gamma-Ray Observatory (CGRO) with its on-board instrument Burst And Transient Source Experiment (BATSE) was launched. BATSE was built with eight detectors located on the corners of the satellite, which allowed to observe all the sky that was not obstructed by the Earth. It detected more than 2700 GRBs during its decade-long lifetime and its rough localisation capabilities permitted to determine accurately GRB location on the sky, thus demonstrating that their distribution covered the entire sky with no preference for the Galactic plane, which pointed towards to an extragalactic origin. (see Fig. 1.2 and Briggs et al. 1996). The BATSE mission presented a further and very important result. Kouveliotou et al. (1993) found that GRBs followed a bi-modal distribution based

in the time span within which GRBs emit 90% of the high-energy photons during the prompt emission, the T_{90}. They found there was a division at the value of 2 seconds with GRBs below this value presenting a harder spectra compared to longer GRBs.

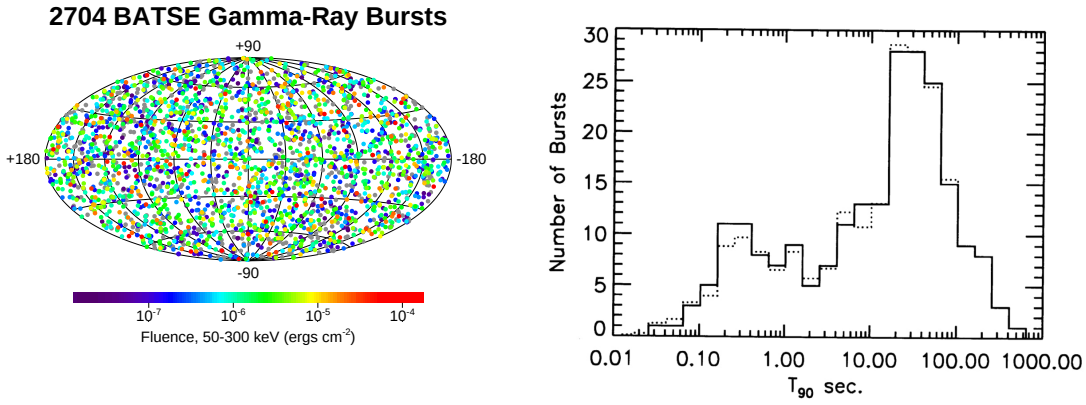

Figure 1.2: Left: Sky distribution of GRBs detected with BATSE. *Credit:* Michael S. Briggs. *Right:* GRB bi-modal distribution based on their T_{90} (Kouveliotou et al. 1993)

1.1.3 Unveiling the cosmological origin of GRBs

With the discovery of the isotropic distribution on sky of GRBs, a Galactic origin was very much disfavoured. However, it would not be definitively proven until the first secure distance measurement. In the 1990s, the NASA with the participation of Japan and France and Italy (with Dutch participation) developed two separate projects for a new high-energy satellite that would be capable of detecting and localising GRBs down to a few arcmin. The US mission, the High Energy Transient Explorer (HETE) could localise GRBs within several arcsec. It was launched in 1996, but the mission failed since HETE was uncapable to decouple from another payload it was attached to. A new copy of this satellite was launched in 2000, HETE-2, but it was already too late. The Italian mission BeppoSAX, launched in 1996, discovered GRB 970228 with a counterpart in X-rays (Costa et al. 1997). This was the first time an afterglow was detected in X-rays, and the first counterpart ever for a GRB. The rapid distribution of the GRB localisation allowed optical follow-up the same night the GRB was detected. Observations in *V*- and *I*-bands were obtained with the 4.2 m William Herschel Telescope (WHT) at La Palma, detecting a faint source in both bands (see Fig. 1.3). Further observations were obtained with the Nordic Optical Telescope (NOT) but no source was detected down to deep limits, since source was already too faint. A week later deep observations with the Isaac Newton Telescope (INT) discovered an even fainter and extended source at the same position, the GRB host galaxy (van Paradijs et al. 1997).

The first time a GRB had a measured redshift was on 11^{th} of May, 1997 through afterglow spectroscopy of GRB 970508 using the Low Resolution Imagin Spectrograph (LRIS) at the Keck telescope. This was the first time a GRB afterglow spectrum showed absorption lines, in this case, due to Mg II and Fe II all of them at a common redshift of 0.835 (Metzger et al. 1997). This discovery definitively ruled out the galactic origin hypothesis.

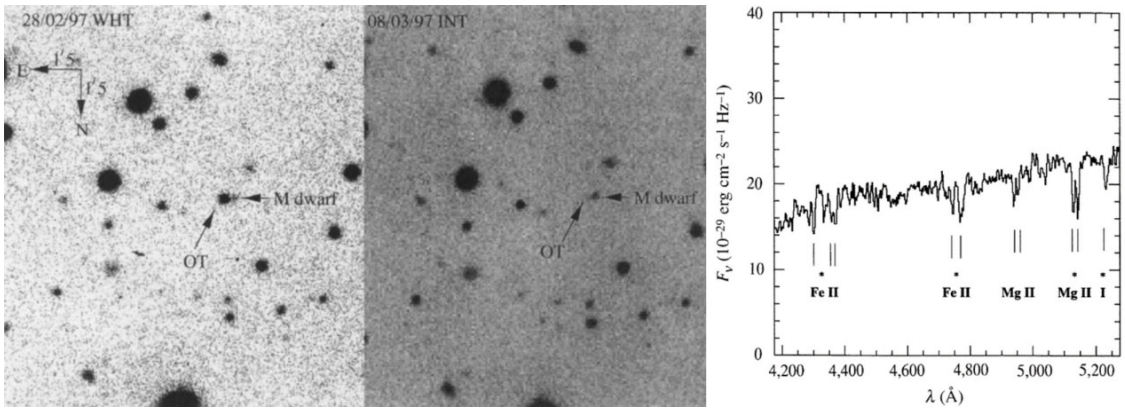

Figure 1.3: First detection of the optical counterpart of a GRB and first spectrum with absorption lines of a GRB afterglow. Left: WHT image with GRB 970228 afterglow detected in V-band. *Center:* Image obtained a week later with the INT in V-band where the afterglow had faded away. Image from van Paradijs et al. (1997). *Right:* Absorption lines in the afterglow spectrum of GRB 970508 (Metzger et al. 1997).

1.1.4 The first link between long GRBs and Broad-lined Type Ic Supernova

After settling the distance issue, the origin of these explosions became the main research topic. Several progenitors were proposed to explain the formation of long and short GRBs. The rapid variability was indicating a very small source, probably of stellar size. But it was very difficult to place the amount of energy needed into such a small volume. Ultrarelativistic effects and collimation were needed in order to produce such luminous sources. (see Sect. 1.3.1). This model suggested that, in addition to the GRB, a Broad-Lined Type Ic Supernova was expected. Again BeppoSAX, together with the BATSE mission, detected GRB 980425, a GRB in the spiral arm of a nearby galaxy. The fact that the area was very large allowed for some discussion about the link between SN 1998bw and GRB 980425 for which observations were obtained in different photometric bands (see Fig. 1.4). The peculiar low energy for this GRBs ($\sim 10^{47} erg$) as compared to 'normal' GRBs ($\sim 10^{53} erg$), made unclear if other GRBs show the same features or if GRB 980425 was a peculiar burst (Galama et al. 1998).

The conclusive link between long GRBs and SN-Ic BL had to wait until 2003. The HETE-2 mission brought, among others, the discovery of GRB030329. This cosmological GRB showed an energy release comparable with regular long GRBs and it had a redshift of 0.1685. It was the first GRB for which the spectroscopic evolution from a GRB afterglow to a Type Ic Broad-Line Supernova (see Fig. 1.4) was securely traced after afterglow component subtraction and it is still one of the best observed GRBs to date (Hjorth et al. 2003; Stanek et al. 2003).

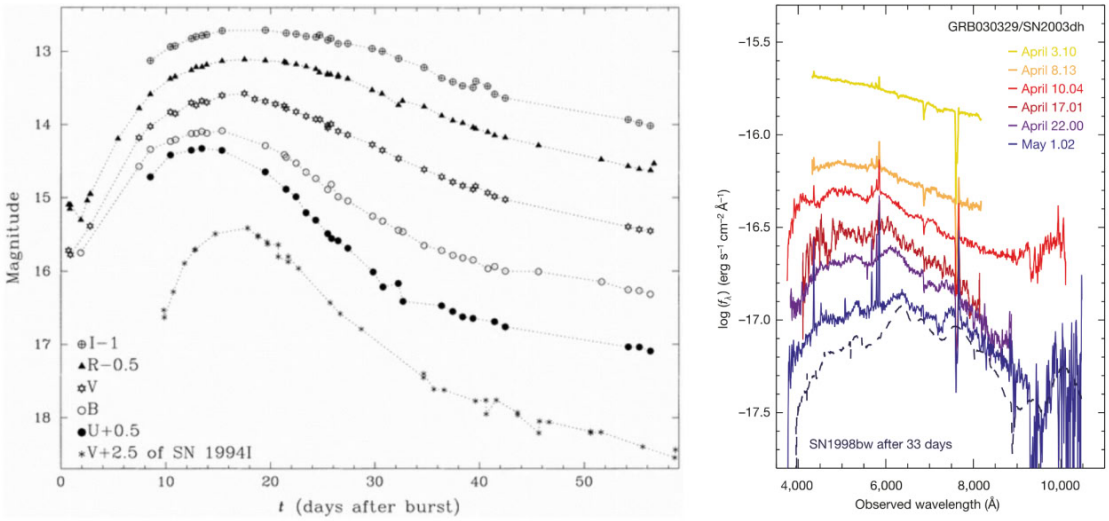

Figure 1.4: First detections of SN-Ic BL associated to long GRBs. Left: Light-curve of SN1998bw in different optical bands corrected for the undelying host galaxy and without afterglow contamination Galama et al. (1998). *Right:* Spectroscopic evolution of GRB 030329 (Hjorth et al. 2003).

1.1.5 The GRB revolution

The number of GRBs with an optical counterpart detected by the earlier 2000's was still small, especially those with early photometry. For this, GRB localisation on sky and prompt delivery of GRB alerts was critical. In 2004, the *Swift* satellite was launched (Gehrels et al. 2004). This satellite was designed to perform multiwavelength observations of GRBs and their afterglow upon discovery. *Swift* has three on-board instruments: The Burst Alert Telescope (BAT) with a sensitivity between 15 and 150 keV and a field of view (FoV) of 1.4 steradians (sr). This satellite scans the sky to search for GRBs and can locate them down to 4 arcmins. The X-ray Telescope (XRT) improves the bursts location down to few arcseconds. Finally, the Ultraviolet/Optical telescope (UVOT) with an aperture of 30 cm performs photometry in 6 filters, from 1700 Å to 6000 Å (see Fig. 1.5 for a sketch of the satellite). A very important characteristic of this satellite is the possibility to automatically slew to a newly detected burst within seconds, after BAT detection, and perform detailed observations with the XRT and UVOT instruments simultaneously. *Swift* has detected up to 100 bursts per year and gives accurate and fast localisations to allow follow-up from ground-based facilities. Its lower energy threshold allowed the detection of lower energy bursts and, therefore, to extend the distance to which GRBs have been detected.

The low-energy sensitivity of *Swift* prevented it from studying in detail the actual gamma-ray component of the GRBs, and limited its capability to detect short-hard GRBs. The *Fermi* mission was launched in 2008 to cover this HE energy range (see Fig. 1.5). Two on-board instruments performs gamma-ray observations of GRBs in both, discovery and follow-up mode. The Large Area Telescope (LAT) instrument covers from 20 MeV to 300 GeV with a FoV of 2.4 sr and delivers GRB alerts with an accuracy down to several arcminutes (Atwood et al. 2009). To study lower energies, *Fermi* is equipped with the Gamma-ray Burst Monitor (GBM) covering from 8 keV

to 40 MeV and gives burst localisations depending on the burst energetics and the number of detectors registering the event, with errors smaller than ~15 degrees (Meegan et al. 2009).

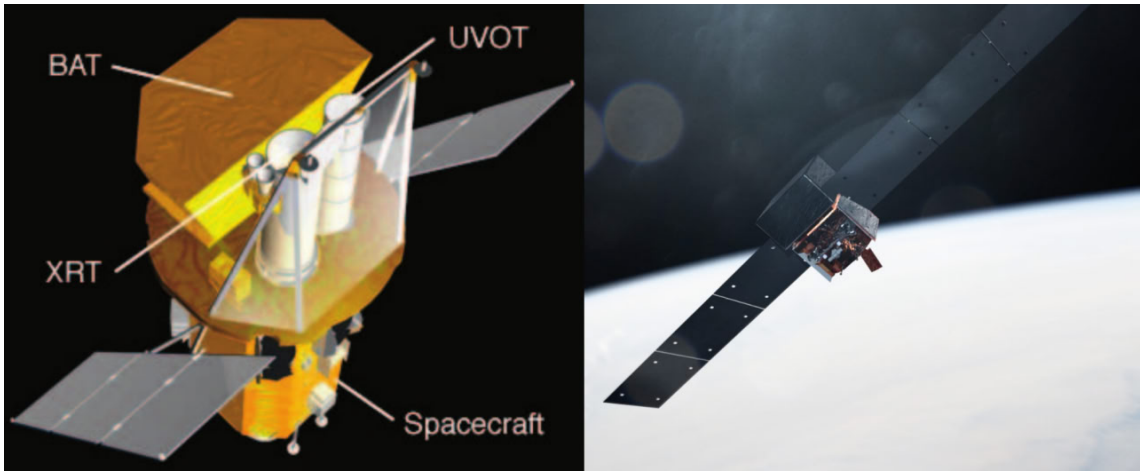

Figure 1.5: On the left, sketch of the *Swift* mission (Gehrels et al. 2004) and the *Fermi* mission on the right (Chris 2023).

These two missions have been and still are key to GRB research providing more than 2000 GRB detections that have revolutionised the GRB field and transient astronomy in general. The serendipitous discovery of GRBs showing very different properties has broadened the field resolving some questions and uncovering new ones. In 2009 the *Swift* mission detected GRB 090423, the farthest GRB observed to date with a measured spectroscopic redhift of 8.2 (Tanvir et al. 2009) and, few days later, GRB 090429B with a photometric redshift of 9.4, although this result was only published two years later (Cucchiara et al. 2011). Another special event was the detection of GRB 130603B, the first short GRB whose distance was determined through absorption line spectroscopy and the first for which a kilonova (KN) emission (see Sect. 1.3.2) was detected (Tanvir et al. 2013; de Ugarte Postigo et al. 2014b). A new milestone on GRB astronomy happened the 17^{th} of August, 2017 when the LIGO and Virgo Gravitational Waves (GW) detectors detected a signal associated to the merger of a binary system of two neutron stars, GW 170817 (Abbott et al. 2017a,b). This detection, delivered promptly to the transient comunity, allowed for a rapid follow-up with multiwavelength facilities. The *Fermi* satellite detected an electromagnetic counterpart just a few seconds after the GW alert, GRB 170817A located in the outskirts of the galaxy NGC 4993. It was the first and up to now the only time a GW signal had a simulteneous elecromagnetic counterpart linking definitively short GRBs with the merger of binary system of neutron stars (Goldstein et al. 2017; Savchenko et al. 2017; Tanvir et al. 2017; Levan et al. 2017).

Many other GRBs have brought a wealth of new insight into GRB physics, the GRB jet, the GRB afterglow, the environment in which these explosions happens. Discoveries such as GRB 190114C with the detection of photons up to the TeVs showed that inverse Compton emission might produce even higher energy photons than emitted by the GRB itself,, at least for some GRBs (MAGIC Collaboration et al. 2019). The Brightnest GRB of All Time (The BOAT), GRB 221009, outshone any other gamma-ray emitting source on sky and, actually, saturated the detectors of

GRB missions. With an energy release of $\sim 10^{55}$ erg and photons detected at 18 TeV (Burns et al. 2023; Sahu et al. 2023), GRB 221009 was the brightest GRB ever detected and has become in one of the most studies GRBs. The origin of the detected VHE photons for GRB 221009A is a matter of debate (see e.g. Sahu et al. 2023, 2024). No evident SN had been initially reported for this nearby (located at $z = 0.151$ (de Ugarte Postigo et al. 2022a; Malesani et al. 2023)) long GRB, suggesting it was hiden within the bright afterglow (Levan et al. 2023a). However, different and/or later observations reports does support the presence of a SN (de Ugarte Postigo et al. 2022b; Blanchard et al. 2024) and de Ugarte Postigo et al. in preparation.

1.1.6 GRBs in the coming years

Although the *Swift* and *Fermi* missions are still succesfully ongoing and providing new GRB detections, new efforts have to be made. Two new missions have been recently launched and are currently providing GRB alerts. The GRB-dedicated Sino-French mission *SVOM* (see Fig. 1.6) has four instruments on-board the satellite covering from 5 MeV down to optical wavelengths and provides subarcsec localisations on sky for those bursts detected with its optical telescope (Atteia et al. 2022; Wei et al. 2016). The Einstein Prove (EP) mission is surveying the sky focusing on the 0.5 keV to 4 keV bandpass. One of the main scientific goals is to increase the number of high-redshift GRBs and for this, it is equiped with a Wide-field X-ray Telescope (WXT) that covers 1.1 sr and the Follow-up X-ray Telescope (FXT) that slews to the transient events detected by the WXT (Yuan et al. 2015, 2022). This mission has already provided some surprises like the detection of EP 240315a, a long duration soft X-ray transient consistent with it being a GRB (Levan et al. 2024b). GRB science will enter in a golden decade with facilities in space detecting new HE transients while some other efforts will scan the sky from ground with an unprecedent cadence searching for transient in the visible spectral range.

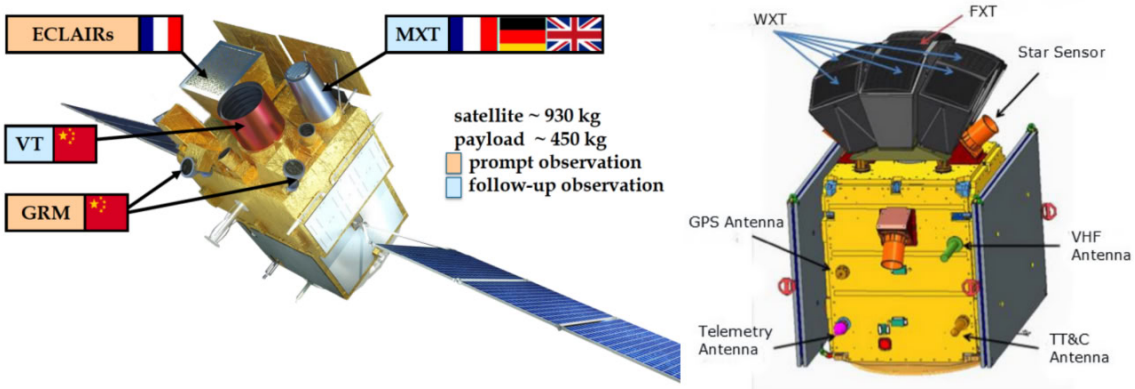

Figure 1.6: On the left, draw of the *SVOM* satellite and the four different on-board instruments, modified from (Atteia et al. 2022). On the right, the *EP* mission (Yuan et al. 2022).

1.2 The most poweful explosions in the Universe. The standard model

Gamma-ray bursts are the most energetic stellar explosions detected in the Universe. They are isotropically distributed in the sky and can last from milliseconds to hundreds of seconds and, for some cases, beyond a thousand seconds. They are typically divided into short and long GRBs based on the duration of the prompt emission phase. Short GRBs are associated with the merger of a binary system of two neutron stars, while long GRBs originate from the collapse of a massive star.

In both progenitor scenarios, a massive central compact object is formed with a fast evolving accretion disk. A highly collimated relativistic jet is launched in two oposite directions. This jet passes through the rest of the infalling material and once this jet reaches the edge of this material and is capable to escape, it leaves the collapsing system in opposite directions. When the optical depth within the jet is thin enough, γ-ray photons are able to escape and reach Earth if the jet cone is pointing towards us. As the jet moves away from the explosion site, different shells of material at different velocities are emitted, while generally slowing down as they move forward. Shells emitted later but at a higher velocity catch up with the slower ones, creating a shock front. In these internal shocks high energy photons are emitted generating the prompt emission. When the GRB jet reaches the circumburst medium (CSM), the shocks create the so-called afterglow emission.

These explosions have been discovered over a wide redshift. They are so bright that, for a brief moment, they outshine any other γ-ray source on sky. Their afterglow emission can last from hours to days and can be brighter than the host galaxy itself. For a schematic view of a GRB, see Fig. 1.7.

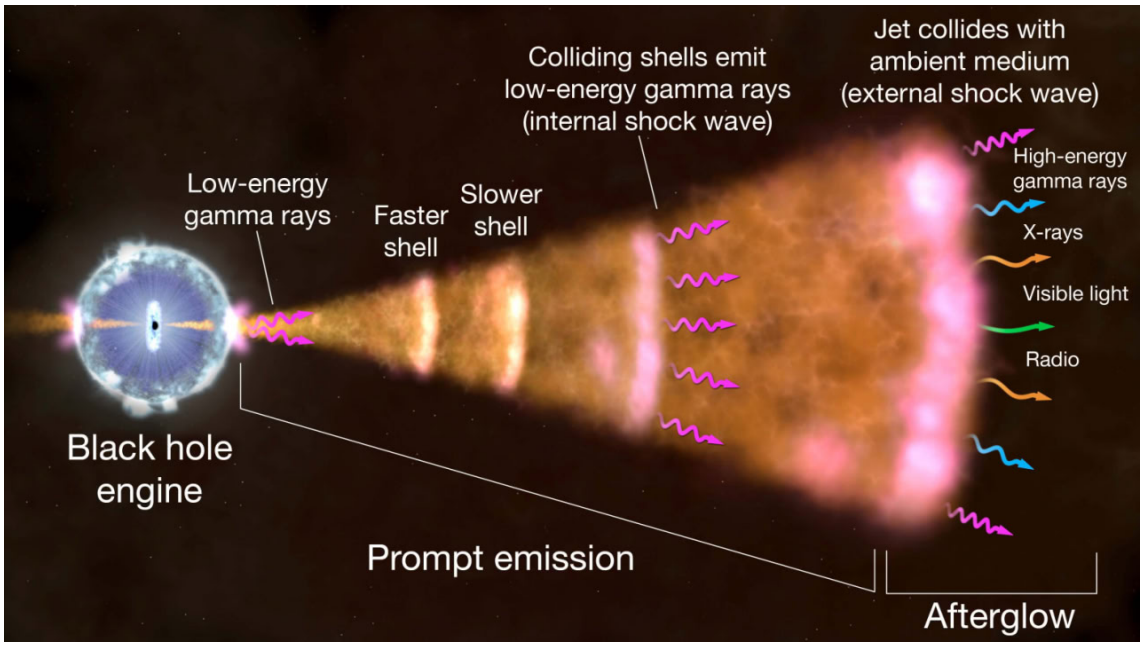

Figure 1.7: Schematic view of a GRB from the central engine to the afterglow emission. Credit: NASA Goddard Space Flight Center.

1.2.1 The prompt emission

The prompt emission is the first electromagnetic observable emission from a GRB. It delivers photons over a range from keV to GeV. The high energy emission is highly collimated and is well described by a power-law distribution. There are two main models to explain its emission mechanism: shocks in the outflow or Poynting-flux dissipation. In the Poynting-flux model, the GRB jet is magnetically dominated and the γ-ray emission is produced by magnetic dissipation. The energy released by the central engine creates strong magnetic fields. Magnetic energy dissipates as a consequence of magnetic reconnection of magnetic lines that breaks due to instabilities within the jet. During this process particles can be accelerated and produce the observed γ-ray emission. These instabilities are a consequence of early internal shocks that distort the ordered magnetic field (see e.g. Zhang & Yan 2011). These coherent large-scale magnetic fields produce synchrotron emission with a high degree of polarisation in the prompt emission, although measuring this polarization has remained an unsuccessful endeavor (Gill et al. 2020).

In the shocks model, energy dissipation happens through interaction between shells expanding at different velocities within the GRB jet. Large blobs of material, composed of baryions, $e^{\pm}$ and γ are launched by the central engine at different velocities. When a faster shell of plasma reaches a slower one, they collides losing kinetic energy and emitting through non–termal processes. In these collisions, a pair of shocks is produced, the forward shock (FS) propagating outwards and the reverse shock (RS) moving backwards. HE photons are accelerated mainly through synchrotron emission from electron acceleration at these internal shock regions, producing the γ–ray that causes the prompt emission. This model can naturally explain the different features we detect in GRB prompt emission light curves such as the spectral energy distribution, their frequency evolution or the pulse shapes (see e.g. Rahaman et al. (2024) and references there in).

The GRB prompt emission spectrum is typically described by a broken power law, the so-called Band function (see Eq. 1.1, (Band et al. 1993)), with the break energy indicating the transition between low-energy and high-energy emission.

$$N(E) = \begin{cases} A\left(\frac{E}{100\ \mathrm{keV}}\right)^{\alpha} \exp\left(-\frac{E}{E_0}\right), & E \leq (\alpha-\beta)E_0 \\ A\left[\frac{(\alpha-\beta)E_0}{100\ \mathrm{keV}}\right]^{\alpha-\beta} \exp(\beta-\alpha)\left(\frac{E}{100\ \mathrm{keV}}\right)^{\beta}, & E > (\alpha-\beta)E_0 \end{cases} \tag{1.1}$$

where $N(E)$ is the photon flux, A is the normalization factor, E is the photon energy, α and β are the low-energy and high-energy photon index, respectivelly and E_0 is the break energy in keV. Light curves can show different shapes and there are three main features: A single pulse light curve with a fast rise followed by an exponential decay (FRED), a multipeaked structure or a similar multipeaked structure followed by a softer exponential decay (see 1.8 for an example of each of the mentioned cases). In some GRBs, the prompt emission light curve can hide a substructure due to variability within the jet. This emission has two typical energies: the peak energy (E_{peak}) when the GRB reaches the maximum energy and the total energy released during the prompt emission assuming radially symmetric emission, the isotropic energy E_{iso}. E_{peak} typically ranges from 100 keV up to 1 MeV while E_{iso} have been found to vary from 10^{47} erg computed for GRB 170817

(Abbott et al. 2017a) up to 10^{55} erg emitted by the most powerful GRB ever detected (see e.g. Kann & Agui Fernandez 2022; Burns et al. 2023). This extremely high energy emission is highly collimated in a relativistic jet with an opening angle, $\theta_0 \propto 1/\Gamma$, where Γ is the Lorentz factor defined as $\Gamma = 1/\sqrt{1 - v^2/c^2}$, that produces a beaming effect which reduces E_{iso} to the real energy released, as $E_\gamma = E_{iso} \cdot f_b$, with the beaming factor $f_b = 1 - \cos\theta_0$.

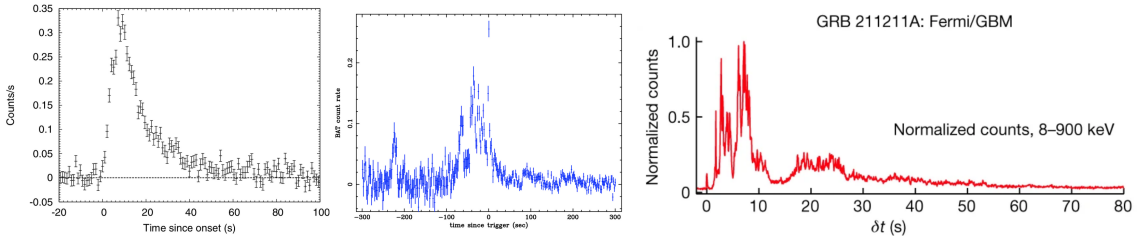

Figure 1.8: Prompt emission light curve examples. From left to right: GRB 051111 prompt emission light curve showing a FRED-like behaviour (Guidorzi et al. 2007). GRB 060210 with a multi-peak structure (Curran et al. 2007) and GRB 211211A with a multi-peaked structure right at the beginning of the burst followed by a soft exponential decay (Rastinejad et al. 2022).

1.2.2 Afterglow emission

As the prompt emission moves forward, the GRB jet decelerates and collides with the circumburst medium. This collision with the CSM or with clumps of material launched by the GRB progenitor in a previous mass-loss phase forms an external shock that produces a long-lasting emission due primarly to synchrotron radiation. This is the so-called GRB afterglow. This emission follows a power-law distribution

$$\frac{dN}{dE} \propto E^{-p} \tag{1.2}$$

where dN/dE is the number of particles per energy unit, E is the energy of particles and p the electron index, expected to vary as $2 < p < 3$. This shocked material is heated up and accelerates electrons through synchrotron mechanism with a Lorentz factor $\Gamma_e \geq \Gamma_m$, where, Γ_m is the Lorentz factor of the minimum energy for electrons in the distribution, also known as the minimum Lorentz factor:

$$\Gamma_m = \epsilon_e \Big(\frac{p-2}{p-1}\Big)\frac{m_p}{m_e}\Gamma \tag{1.3}$$

where ϵ_e is the energy fraction for the accelerated electrons and p is the spectral index and with expected values in the range $2 < p < 3$ (Sari et al. 1998).

The spectrum and light curve of a GRB afterglow is typically defined by three related frequencies, at which the emission properties undergo distinct changes. These define different segments in the afterglow spectrum, as can be seen in Fig. 1.9, ν_m is the frequency at which the GRB afterglow have it maximum emission. ν_c is the cooling frequency, i.e., the frequency above which electrons have had enough time to lose energy through radiative processes, while electrons below do not

cool significantly through radiative losses. The self-absorption frequency, ν_a, is the value below which the medium becomes optically thick to the synchrotron radiation emited.

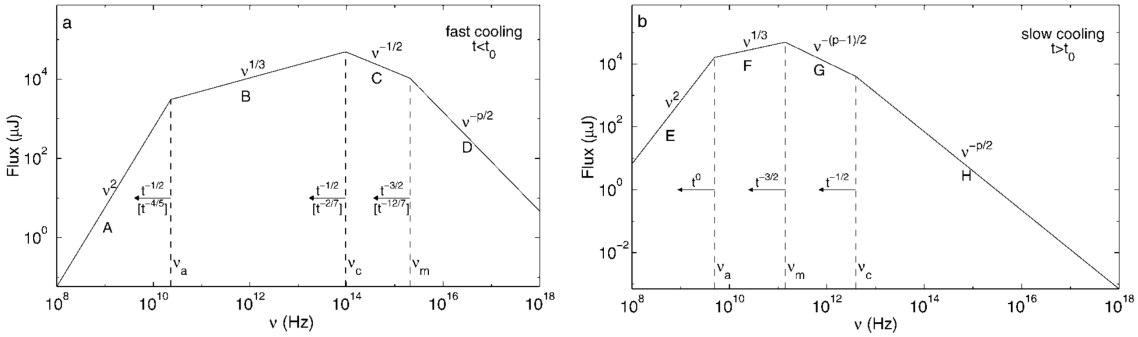

Figure 1.9: GRB afterglow synchrotron spectrum evolution in the fast (left) and slow (right) cooling regime. Modified from Sari et al. (1998).

The power-law distribution that describes the spectrum can be divided into two main cases:

1 The fast cooling regime is the one we usually find at early stages of the cooling of the shocked material. Here $\nu_m > \nu_c$ and electrons are affected by strong magnetic fields and radiate their energy more efficiently. The flux distribution for the fast cooling is as follows (taken from Sari et al. (1998)).

$$F_\nu = F_{\nu,max} \cdot \begin{cases} (\nu/\nu_c)^{1/3}, & \nu < \nu_c \\ (\nu/\nu_c)^{-1/2}), & \nu_c < \nu < \nu_m \\ (\nu_m/\nu_c)^{-1/2} \cdot (\nu/\nu_m)^{-p/2}, & \nu > \nu_m \end{cases} \tag{1.4}$$

2 The slow cooling regime is what we expect at later stages of the afterglow evolution. In this case, $\nu_m < \nu_c$ and electrons are not energetic enough to radiate energy fast enough and therefore, the flux decays. For the slow cooling regime, the flux distribution, is as follows (taken from Sari et al. (1998)):

$$F_\nu = F_{\nu,max} \cdot \begin{cases} (\nu/\nu_m)^{1/3}, & \nu < \nu_m \\ (\nu/\nu_c)^{-1/2}), & \nu_m < \nu < \nu_c \\ (\nu_c/\nu_m)^{-1/2} \cdot (\nu/\nu_c)^{-p/2}, & \nu > \nu_c \end{cases} \tag{1.5}$$

The blast wave, with an isotropical equivalent energy E_{iso}, propagates in a spherical shock evolving adiabatically with a Lorentz factor Γ into the CSM. Although the relativistic flow is highly collimated, the spherical approximation for the blast wave is still valid as long as we are in the jet cone direction and the edges of the cone are not visible. This is the case when the jet half opening angle is $\Gamma > 1/\theta_0$ and we observe all the flux concentrated in the GRB axis. As the jet interacts with the surrounding medium, its Lorentz factor decreases. At a certain point, the sideways expansion becomes important, and the entire jet cone becomes visible to the observer. This is known as the jet-break and it happens when Γ decreases to a value close to $1/\theta_0$. At

this stage, the beaming effect is too small and the jet starts to spread sideaway moving to a non-relativistic jet. The total flux is distributed over a wider region, which makes the effective observed flux lower and therefore, an important decrease of the afterglow flux is observed. This happens at an specific time in the dynamic evolution of the afterglow, the t_{break} (Nakar 2007):

$$t_{break} \approx 2(1+z) \cdot \left(\frac{E_{k,iso,50}}{n_{-2}}\right)^{1/3} \left(\frac{\theta_0}{0.2}\right)^{8/3} \; days \tag{1.6}$$

where n_2 is the ISM or IGM particle density in units of 10^{-2} cm^{-3} and $E_{k,iso,50}$ is the isotropic kinetic energy of the ejecta normalised to 10^{50} ergs. At this stage, the observed flux will no longer follow eqs. 1.4 and 1.5 but instead the following relation (Nakar 2007):

$$F_\nu \propto \begin{cases} \nu^2 t^0, & \nu < \nu_a \\ \nu^{1/3} t^{-1/3}, & \nu_a < \nu < \nu_m \\ \nu^{-(p-1)/2} t^{-p}, & \nu_m < \nu < \nu_c \\ \nu_c^{-p/2} t^{-p}, & \nu > \nu_c \end{cases} \tag{1.7}$$

This break can be observed with an achromatic change in the slope of the afterglow light curve followed by a significant drop in the flux (see e.g. Lamb et al. 2021).

1.2.3 Gamma-ray Bursts polarisation

Polarimetry observations are useful to constrain the physical processes happening during a GRB, from the jet emission mechanisms to the afterglow physics (Covino & Gotz 2016). During the prompt emission, polarisation can arise from different models which imply different predicted levels of polarisation. Usually, polarisation occurs in magnetic fields mainly generated by synchrotron emission althogh other mechanisms such as inverse Comptom scattering or thermal emission can induce some degree of polarisation (see e.g. Gill et al. 2021).

Observations of prompt emission polarisation can hold essential information about the jet geometry, its structure and the radiation mechanisms. If the synchrotron emission comes from shock-accelerated electrons within the jet and with an ordered magnetic field perpendicular to the jet axis, we expect locally high levels of polarisation, reaching up to 60%. The generated fields are locally ordered and the polarisation presents a high variability (see e.g. Granot & Königl 2003). In this model, the jet kinetic energy is converted to radiation at shocks, the jet is matter-dominated.

In a Poynting-flux dominated outflow, the synchrotron emission is generated by large-scale fields powered by the central engine, and the polarisation levels can reach up to ~50% (Lyutikov & Blandford 2003). In this model, the jet is magnetically dominated by large-scale and ordered magnetic fields and favours jet formation models such as the Blandford-Znajek models in which the energy that powers the jet is extracted from the newborn compact object spin (Blandford & Znajek 1977). The observed polarisation will present low variability during the prompt emission.

However, polarisation of the prompt emission is still very challenging and only very few measurements have been obtained so far by several missions. These polarisation degree (PD) measurements have been shown to be instrument-dependent and do not fully account for the systematic

errors. The POLAR mission reports overall low or no polarisation for the prompt emission while AstroSat CZTI finds predominantly high PD values. The GAP mission finds a wide range of values, from low to high PD while COSI excludes high PDs. The different results suggest that efforts should focus on the development of new dedicated missions and improving and standardizing the analysis methods ((see e.g. Gill et al. 2021) for an overview). The observations of GRB 221009A by the Imaging X-ray Polarimeter Explorer (IXPE) were only able to measure upper limits for the prompt emission mainly due to the high extinction on the line of sight towards the GRB (Negro et al. 2023)

Afterglow optical polarisation has been succesfully detected since the firsts GRB afterglow were observed in visible bands (Covino et al. 1999; Wijers et al. 1999) with low polarisation levels from around 1 to 5% and with some detections up to ∼10% (see e.g Bersier et al. 2003; Uehara et al. 2012). More importantly, polarisation of the afterglow emission has been observed during the entire lightcurve evolution. Detections at early times on GRB 190114C with evolution from higher to lower PDs are often associated to a reverse shock (RS) moving backwards in the jet. The polarisation was likely associated to entangled magnetic fields in the shock rather than to large-scale fields dominating the jet (Laskar et al. 2019). It is still unclear if these large-scale fields associated to the jet get distorted by the time the RS magnetic field ($\vec{B}$) becomes dominant or if the observed PD arises from a combination of the RS and the Forward Shock (Jordana-Mitjans et al. 2020).

The origin of the magnetic fields in the afterglow emission is still unclear. For the FS, since it is generated after the shock of the GRB jet against the CSM, a magnetic field would be expected to be formed in this shock and left behind the shockwave as it moves forward. The origin of this field is a consequence of an induced $\vec{B}$ field due to a two-streams outflow that contains charged particles at different velocities in the GRB plasma outflow and provokes instabilities such as the Weibel instability (Weibel 1959; Medvedev & Loeb 1999). Some other models points out that the afterglow $\vec{B}$ field can have its origin in large-scale fields such as compression of the ISM $\vec{B}$ field at the blast wave site (Laing 1980; Teboul & Shaviv 2021) or due to magnetic reconnection in a Pointing-flux dominated jet (Zhang & Yan 2011).

Different models have been proposed to explain the observed polarisation of GRB afterglow in optical bands, the polarisation level and changes in the position angle of the $\vec{B}$ field. In a scenario in which the magnetic field is generated in the blast wave, Gruzinov & Waxman (1999) finds that a polarisation of ∼10% would be expected and would vanish as PD $\sim 10^{3/2}$%, as long as the proper time after the shock of the blast wave τ is smaller than the coherence length $l \sim \epsilon c\tau$. This model assumes instabilities at the GRB afterglow like the Weibel instability (Weibel 1959), and consider that, as the blast wave shocks the circumstellar environment, different patches with randomly oriented magnetic field are created. Some of these patches will share the same direction with coherent magnetic fields generating a larger-scale $\vec{B}$ field. This will be detected as a linearly polarised afterglow that remains polarised as long as l is comparable to the thickness of the blast wave. This model implies that a compressed ISM $\vec{B}$ field cannot generate the observed PDs as it is much less intense than what is detected for GRB afterglows. Although the magnetic field of the ISM is not strong enough that its compression cannot explain the observed PD, it could

become stronger assuming a magnetized wind from the progenitor star (Granot & Königl 2003). The observed PD depends on the ratio between the ordered magentic field from the environment and the random component from the afterglow $\overrightarrow{B}$ generated at the blast wave.

In the two-streams model (Medvedev & Loeb 1999), instabilities create magnetic fields parallel to the shock front that fluctuate proportionally to the scale of the plasma shells. As the jet radiation is beamed towards the observer, the observable afterglow region is much smaller than the jet opening angle. Therefore, this emission region is detected as a fainter emission than the external parts since they are larger and less beamed. In appearence, these are observed as a narrow limb-brightened ring effect which brightness drops sharply with Γ towards the edge of the ring (Granot et al. 1999). Small-scale magnetic fields are created in this ring but they cancel out as the ring remains symmetric. In this case, polarisation happens as this symmetry breaks due to scintillations or due to gravitational lensing effects (Loeb & Perna 1998).

A different approach to explain polarisation of the GRB afterglow are geometrical models. In a similar way to the two-streams model (Medvedev & Loeb 1999). Ghisellini & Lazzati (1999) proposed a model in which the observer is slightly off-axis to the jet-axis direction. When observing the magnetic field generated at the front shock, some level of linear polarisation would be generated. The magnetic field is assumed to be highly tangled in an on-axis view (while not so tangled when observed off-axis), due to the interaction between the emitting region and the relativistic aberration. In this model, the polarisation degree varies as the Lorentz factor changes, which leads to some clearly observable features in the polarimetric evolution. At an early stage, when Γ is still very high, we observe a beamed, small and symmetric region with low to zero polarisation. As Γ decreases, the border of the emiting region starts to be observable and the symetry is broken. We observe that the PD changes as the jet border becomes more visible. The PD changes as the ratio between polarisation in the horizontal and the vertical plane changes, implying that there are two PD maxima with a change in the polarisation position angle of 90 degrees. Finally, when Γ is low to recover the light of the entire emitting region, it will be symmetric again and we then again detect zero polarisation.

The models described above assumes a homogeneous jet for which the emitted light along the jet axis and next to the jet external parts is the same. This might not be the case if the jet is structured jet. This implies that the emitted light along the jet axis would be highest while decreasing exponentially towards the borders and the jet brightness follows a Gaussian distribution. Polarisation in homogeneous jets depends on the symmetry of the region observed and emerges when we see the border. In structured jets, the required asymmetry is instrinsic to the jet as long as we observe it off-axis. The PD is weak during the first stages of the afterglow evolution and does not show a change in the magnetic field orientation i.e., there is no 90 degrees rotation of the position angle and, for gaussian jets, the polarisation maxima will be reached once the entire jet cone becomes visible at the jet break (Rossi et al. 2004).

1.3 The dichotomy of short and long GRBs. The progenitor problem

Two main different GRB types have been established since Kouveliotou et al. (1993) found a bi-modal distribution based on the GRB prompt emission T_{90} duration and their spectral hardness. GRBs with a $T_{90} < 2$ s and a hard X-ray spectrum are called short GRBs. Those with a duration above 2 seconds and with a softer spectrum were designated as long GRBs. This division drove the idea that two formation channels might exist. Long GRBs are commonly accepted to have their origin in the collapse of massive stars (see e.g. Cano et al. 2017) while short GRBs have been conclusively linked to the merger of a binary system of neutron stars (Abbott et al. 2017a,b).

1.3.1 Long GRBs

In the collapsar model (Woosley 1993; MacFadyen & Woosley 1999), a main sequence star with a mass above $\sim$25 $M_\odot$ that has exhausted its fuel and cannot continue holding the gravitational pressure, collapses. A neutron star is created at its iron core but the material from the rest of the star infalls freely and the neutron star grows in mass to collapse as a black hole. Later, also the outer layers of the dying star continue falling onto the newly formed compact object. The infalling material retains its angular momentum which will not allow it to fall into the black hole freely but instead, creating a disk of material around it.

The accretion disk lies in the equatorial plane and at a distance from the black hole at which it is fed efficiently while gravitational energy is radiated efficiently through a highly beamed outflow. As the material continues falling onto the accretion disk and angular momentum is conservated, a low density region is formed in the polar direction, along the rotational axis while an important amount of energy is deposited in this region. As energy continues increasing, a highly collimated and powerfull outflow is emitted at the poles, moving away from the central engine. The jet moves through the rest of the dying star that, if it is thin enough, will let the jet out from the surface. The GRB is then created inside the jet as described in Sect. 1.2.1. This expected to happen in some massive star collapse for which some level of angular momentum is required to funnel the material into the accretion disk. If these centrifugal forces are too high, they can dominate over the gravitational force and therefore, the material is not efficient enough spiraling onto the accretion disk, which prevents the collapsar from a GRB (MacFadyen & Woosley 1999). The metallicity of the progenitor could imply different properties such as luminosity, which could result from mass loss due to stellar winds during the pre-explosion progenitor phase. These mass losses could, in turn, cause variations in the progenitor's angular momentum. (Woosley & Heger 2006). It seems that stars with lower metallicities indeed require a higher initial mass to create a GRB than at higher metallicities (see e.g. MacFadyen & Woosley 1999; Yoon et al. 2006; Langer & Norman 2006).

Once the relativistic outflow is created and moves through the infalling material, there is an extra pressure from the jet towards the rest of the star as it moves through it, although not enough to produce the SN explosion (MacFadyen & Woosley 1999). The material continues to fall onto the central compact object, but as the material is compressed the degeneration pressure forming

a proto-NS and stop the collapse provoking a shock at the surface. However, this pressure is not enough to stop the collapse. In this proto-NS, neutrons are formed as protons capture electrons emitting electronic neutrinos. This neutrino flow re-energizes the shock and the star explodes (Woosley & Janka 2005).

As already mentioned in Sect. 1.1.4, the first detection of a SN associated to a long GRB was SN 1998bw although its prompt emission brightness was not within the common values for long GRB (Galama et al. 1998). The first undoubitable detection of a long GRB with a SN component was GRB 030329 (Hjorth et al. 2003; Stanek et al. 2003), demonstrating that long GRBs can be explained through the collapsar model. The SN explosion is typically detected days after the GRB, although it depends on the GRB redshift (the larger the redshift is, the later the SN component is detected). As the afterglow fades, the SN component starts to dominate the emission and becomes visible. It is detected as a chromatic bump in the light-curve and is further confirmed as its spectrum shows undulations that will move to redder wavelengths as the explosion cools down over time (see Fig. 1.4 in Sect. 1.1.4 for an example). The SN shows high velocity lines and lack hydrogen and hellium lines. These are common characteristics to stripped-envelope SN explosion and SN Ic Broad-Lined. For the GRB to be able to break the outter layers of the collapsing star, it has to have lost its external shells e.g., due to strong winds or the presence of a companion star, which further supports the collapsar model. This is a common characteristic of Wolf-Rayet stars, a progenitor candidate for long GRBs (MacFadyen & Woosley 1999).

1.3.2 Short GRBs

Short GRBs are associated to the merger of two compact objects. Several binary systems have been proposed as potential progenitor of short GRBs although only the merger of two neutron stars (NS) has so far been proven to produce short GRBs (Abbott et al. 2017a,b). In a NS-NS binary system, the only way to loose energy through the emission of gravitational waves. This process can take up to billions of years (Chruslinska et al. 2018). If the binary system suffers a kick during its formation, it can leave the environment where they were formed and actually be located outside the host galaxy (see e.g. Lee & Ramirez-Ruiz 2007; Bloom et al. 1999; Belczynski et al. 2002).

For short GRBs, the collimated jet is launched by the accretion disk around the central engine form a massive neutron star or a black hole with an accretion disk that feeds the compact object and the collimated outflow is launched producing the GRB. Contrarily to long GRBs, the accretion disk is less massive and it will not be fed by additional material from the disrupted system. This explain the shorter scales for this GRB type. For short GRBs lasting several seconds instead of fractions of seconds, a rapidly and highly magnetised neutron star can explain its larger prompt emission (see e.g. Lee & Ramirez-Ruiz 2007).

Short GRBs have an additional emission, a so-called “kilonova”. Short GRBs cannot produce a supernova as they do not have enough material to explode as such. They form a neutron-righ accretion disk with high densities where r-process elements are produced. The radioactive elements emit α and β particles from the accretion disk, which start heating the surrounding environment (see Fig. 1.10 for a sketch of the event). This late emission can be detected as an emission excess

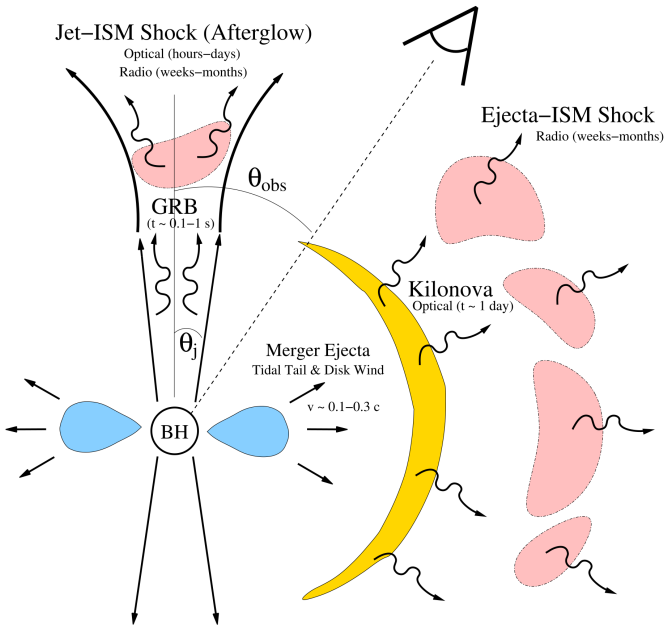

Figure 1.10: Short GRB and kilonova emission sketch from Metzger (2020). A Black Hole with an accretion disk feeding it creates a highly collimated outflow with an opening angle θ_j that will lead to a GRB. The *r*-process elements created in the accretion disk radiate in a quasi-spherical way heating the surrounding environment in the so-called kilonova emission, detectable from days to weeks and typically peaking at redder wavelengths.

in the near-infrarred (NIR) for a so-called "red kilonova" when the ejecta is lanthanide-rich as they have a high opacity at shorter wavelengths. If the outflow have a lower lanthanide-abundance, a so-called "blue kilonova" will be detected as the emission will peak at shorter wavelengths (see e.g. Metzger 2020).

Given the nature of the progenitor of short GRBs, they are strong candidates to emit gravitational waves (GWs). This massive compact systems emits detectable GWs as they spiral down and merge to form a massive NS or a BH. GWs were detected for the first time for GW/GRB 170817, where the GW detection triggered observations with *Fermi* and other high-energy satellites detecting electromagnetic counterpart for a GW detection (Abbott et al. 2017a,b). A KN emission was also detected for this GRB demonstrating that at least part of the detected short GRBs have their origin in NS-NS mergers (Tanvir et al. 2017; Goldstein et al. 2017; Savchenko et al. 2017). A KN component had already been detected in GRB 130603B (Tanvir et al. 2013) which was also the first short GRB for which absorption lines were detected, allowing to determine its distance was the first time absorption lines were detected in a short GRB afterglow, allowing for determining its distance (de Ugarte Postigo et al. (2014b), see Fig. 1.11).

1.3.3 The classification problem

To distinguish between long and short GRBs is not always straightforward. GRB 060614 was classified as a long GRB based on its duration. However, the absence of an associated supernova

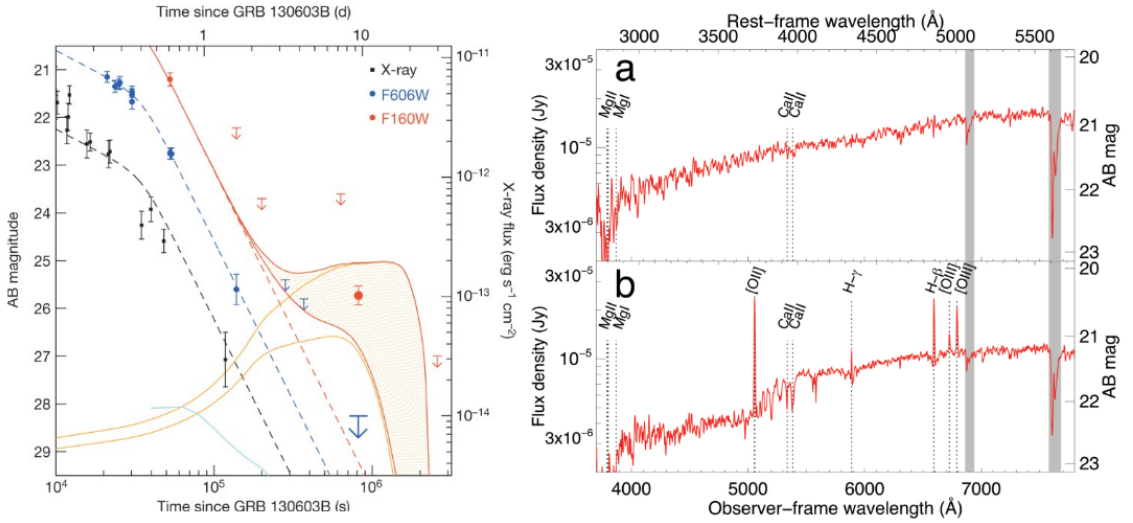

Figure 1.11: GRB 130603B light curve (*left*) from Tanvir et al. (2013) showing NIR excess at $\sim 10^6$ s after GRB and GRB 130603B afterglow spectrum (*right*) with Mg and Ca absorption lines at a common redshift of $z = 0.3565$ from de Ugarte Postigo et al. (2014b).

and its location in a region with low star formation raised doubts about its collapsar origin, as it had properties more similar to short GRBs. Despite deep observations, no SN component was found neither for GRB 060614 nor for GRB 060505 and indeed, their prompt emission properties ressembled those of other short GRBs with a T_{90} >100 seconds for GRB 060614 (Gehrels et al. 2006; Della Valle et al. 2006; Fynbo et al. 2006) and T_{90} >4 seconds for GRB 060505 (Ofek et al. 2007). Short GRBs can have an extended emission after the prompt emission spike, a soft X-ray tail decaying smoothly right after the first hard emission. The detection of the KN emission on GRB 211211A, a GRB that lasted for a minute on its prompt emission phase (Rastinejad et al. 2022), finally confirmed the merger origin for at least some of these presumably long GRBs.

The classification of a GRB as short or long has to rely on a broader parameter space than only the duration of the prompt emission. Short GRBs typically show a sharp hard spike during their prompt emission or a multi-peaked structure while long GRBs shows a smoother behaviour. Short GRBs are hard X-ray bursts, i.e., they emit more at higher X-ray energies compared to long GRBs, which are softer. In addition, short GRBs do not present a spectral lag, something that clearly differentiate them from long GRBs. Beyond the prompt emission properties, there are also important differences on the later evolution of both GRB types. The main diffference is the presence of a SN for long GRBs, which is absent for short GRBs. Another very important feature is the KN component in short GRBs, although some r-process element synthesis could also be expected to happen in long GRBs, however, the amount of material produced would still be low compared to NS-NS and this component would be fainter and harder to detect compared to short GRBs. Although it is still possible to classify a GRB as long or short when it show clear properties on its prompt emission, a more comprehensive study is needed for the more intrincate cases.

1.4 The host galaxy

The different progenitor for long and short GRBs might indicate that they needs different environments which then implies different host galaxies. It has been suggested that, as collapsar long GRBs occur in the collapse of massive stars, they should happen in star forming regions therefore, long GRBs would happen more frequently in star forming galaxies. They are detected at any redshift, making from them good tracers of star formation accross cosmic time.

For short GRBs, given the nature of the progenitor, we should expect a more evolved host galaxy. A NS-NS system would need a delay time to merge of the order of the Gyr. This means that we would expect they to happen in evolved galaxies. Surprisingly, less than 20% of sGRB hosts are early type galaxies and indeed, in some cases short GRBs can happen in star forming galaxies or even in dwarf galaxies (see e.g. Nugent et al. 2022, 2024).

1.4.1 Long GRB hosts

The most accepted progenitor for long GRB explosions are massive stars at their ends of their lifes (see 1.3.1). However, not all massive stars may produce a GRB at their collapse, the occurance of a GRB might be metallicity dependent. Studying the host galaxy might contribute to resolved this issue. Since the progenitor of a long GRB is expected to have a short evolution time we expect these explosions to happen at the site of ongoing star-formation and in highly SF regions with low metallicity and low mass where these massive stars are generated and host the GRB.

These expectations have been confirmed observationally in the first studies on the host galaxy of long GRB hosts. In 2006, Fruchter et al. (2006) found that the host galaxies of long GRBs are irregular, low luminosity galaxies that are actively forming stars. This supports the idea that not all massive stars that explode as BL-SN Ic produce a long GRB and therefore, GRBs might require a lower metallicity to be produced. This concept was further supported by Modjaz et al. (2008) who found that, in a limited sample, the metallicity of long GRB hosts is lower than for the corresponding one of BL-SN Ic explosions without detected GRB.

The first study of a large sample of GRB hosts analysed 46 targets over a wide redshift range and further confirmed that long GRB host galaxies are low-mass and star-forming galaxies with sub-solar metallicity (Savaglio et al. 2009). High-resolution observations have shown that long bursts are commonly found in blue galaxies with high specific SFR and at the brightest spots of their host galaxy (Svensson et al. 2010). This suggest that these explosions happens on violent star-forming events in low-metallicity regions.

Integrated properties of long GRB host galaxies with the optically unbiased Gamma-ray burst host (TOUGH) survey, demonstrated that long GRBs can also happen in galaxies with higher masses and metallicities with a diverse morphology and that long GRB hosts do not have a high extinction as compared to field star-forming galaxies (Hjorth et al. 2012; Michałowski et al. 2012). At higher redshift the host galaxies of long burst seems to be dustier, inferred from spectral energy distribution fits to a small sample of long GRB hosts (see Fig. 1.12, Perley et al. 2013).

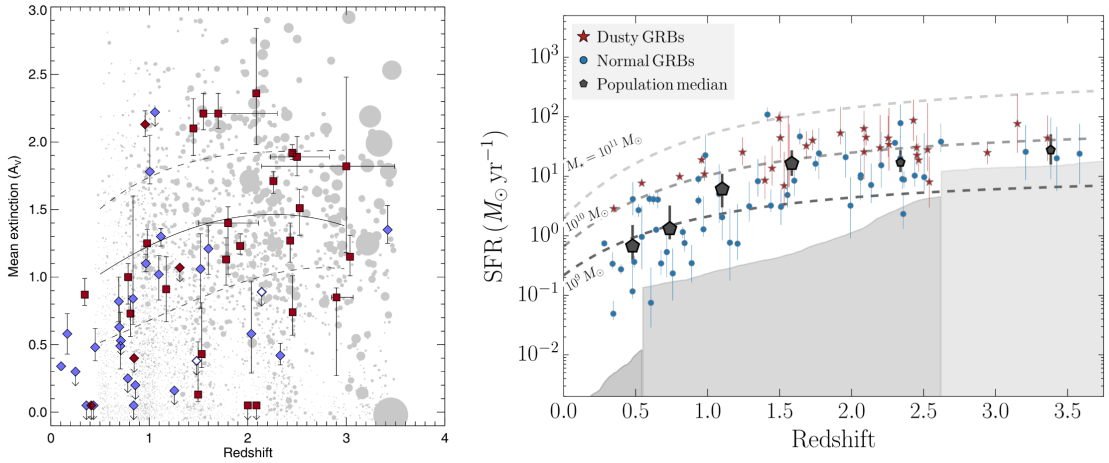

Figure 1.12: *Left:* Extinction in V-band evolution with redshift. In gray the values for field galaxies, dark-red for dusty GRBs while the oposite is in blue (Perley et al. 2013). *Right:* Star Formation Rate of dusty and normal GRBs accross cosmic time (Krühler et al. 2015)

SFR increases with redshift while only a weak correlation for the extinction increasing with redshift has been found (Krühler et al. 2015). This is consistent with the results for the SFR founds by Palmerio et al. 2019 that suggest that host galaxies stellar masses evolve with redshift while metallicity does not. They also argue that long GRBs have a preference for host galaxies with sub-solar metallicities while in Krühler et al. 2015 several host have metallicity values higher than solar metallicity. The Swift GRB host-galaxy legacy survey (SHOALS) further confirmed in an unbiased sample of 119 long GRB hosts that these galaxies are typically low-mass, low-metallicity and star-forming galaxies but that they happen in more massive galaxies at higher redshifts (see Chapter 5).

Long GRB hosts are morphologically heterogeneous and mostly found in star-forming, low-mass and low-metallicity hosts at low redshift however, about 20% of hosts at $z < 0.5$ occur in spiral galaxies (Thöne et al. 2024). Only very few, however, occur in massive galaxies, possibly because of their different environmental conditions. One of those exceptions was the host of GRB 171205A. The resolved study on the host galaxy of this GRB has shown that the explosion site was a low-metallicity and star-forming region with an underlying dominating young stellar population. This demonstrates that the GRB production depends on the physical conditions of the GRB explosion site which implies that massive galaxies with high specific SFR regions can still produce long GRBs (Thöne et al. 2024; de Ugarte Postigo et al. 2024).

Only a few GRB host have been observed using high spatial resolution. Christensen et al. 2008 found that GRB 980425 host galaxy shows similar properties to high redshift host galaxies with high specific star formation rate and low metallicity at the H II regions. This is consistent with the results for the GRB site in GRB 060505 host galaxy (Thöne et al. 2014) and with the analysis of GRB 100316D host, with the GRB located in the youngest, metal-poor and within the highest star forming region region in the host (Izzo et al. 2017). The SN-less GRB 111005A was found to happen in a star-forming galaxy while the GRB happened in a metal-rich region with an old stellar

population (Tanga et al. 2018). See Fig. 1.13 for a size comparison of these long GRB hosts.

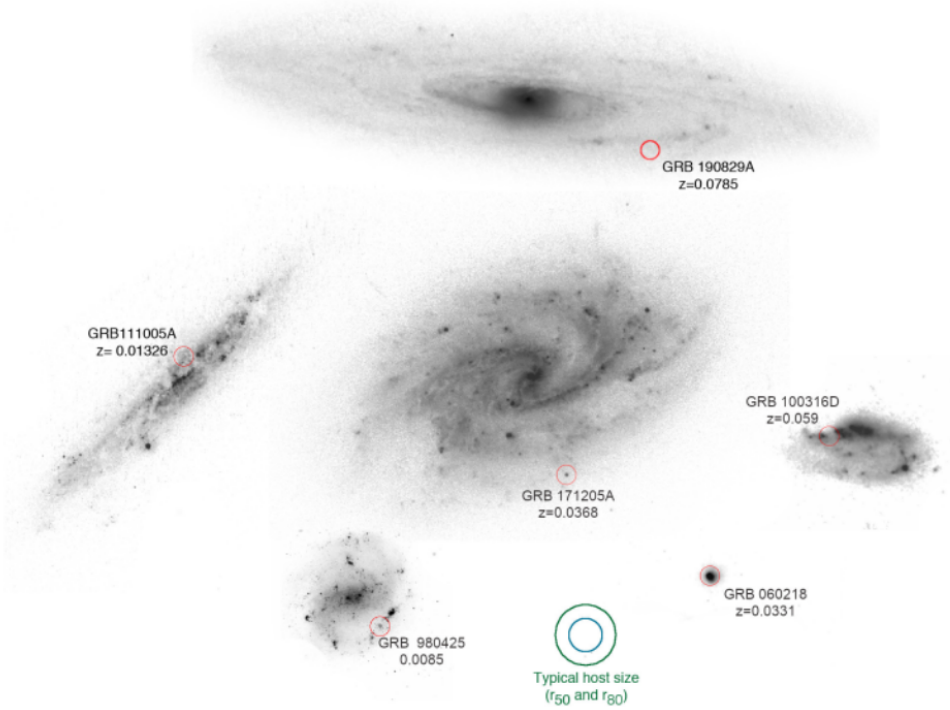

Figure 1.13: Size comparison of the different long GRB hosts with resolved spectroscopic studies. Taken from (Thöne et al. 2024).

1.4.2 Short GRB hosts

Since short GRBs originate from NS-NS mergers, their typical host galaxies were expected to be early type galaxies, an evolved and massive galaxy with low SFR. Although the progenitor stars of the two NS that form the binary system originate in SF regions, due to the large delay time, the SF region around them would have long disappeared. Moreover, the SN explosion can lead to a strong enough impulse to kick them out from the star-forming region and even from the host galaxy (see e.g. Berger 2010; Belczynski et al. 2002, 2006). In this later case, the NS-NS merger takes place in the intergalactic medium. The large distances of short GRBs from their host galaxies make secure host identification particularly challenging. Typically, the association between a GRB and its host galaxy is determined by statistically computing the probability of a chance alignment with field galaxies (Bloom et al. 2002). However, identifying the host is not always straightforward. The most reliable method to pinpoint the GRB host remains absorption-line spectroscopy of its afterglow, which not only provides the distance to the GRB and, therefore, its location but also makes short GRBs excellent probes of both the ISM and the IGM across cosmic time in an unbiased way.

The most secure host association is therefore an identical redshift from absorption line spectroscopy of the host and emission or absorption line spectroscopy of the host. Only for the short

GRBs 130603B and 201221D there exist spectra that shows absorption lines in their afterglow spectrum and an underlying galaxy. (see e.g. de Ugarte Postigo et al. 2014b; Agüí Fernández et al. 2023) For a third GRB, GRB 160410A absorption lines where detected in the afterglow but no host was detected at the GRB position and no field galaxy could be associated as the host galaxy (see Chapter 3).

More recent studies on integrated properties of short GRBs with a clear associated host galaxy indicates that they can be both early to late type galaxies and even low-luminosity galaxies (Fong et al. 2022). Short GRBs seems to happen frequently in sub-solar metallicity and star-forming galaxies with a SFR more consistent with values of field star-forming galaxies. However, at lower redshifts ($\lesssim 0.25$), over 10% of short GRB hosts are evolved galaxies that seems to be transitioning to quiescent galaxies (Nugent et al. 2022). Recent results from (O'Connor et al. 2022) point to a redshift evolution of short GRB-host offsets, in the sense that at lower redshifts, the offsets from the host are higher, and decrease with redshift. (see Fig. 1.14). However, the results of (Fong et al. 2022) suggest lower offsets overall and no redshift evolution. In general, short GRB host seems to be more consistent with field galaxies, 84% of them are star-forming galaxies with relatively low metallicity (Nugent et al. 2022) but with lower star formation rates when comparing to long GRBs. Despite what was previously thought, short GRB host galaxy characteristics are very heterogeneous including many types from evolved and quiescent to small and active galaxies.

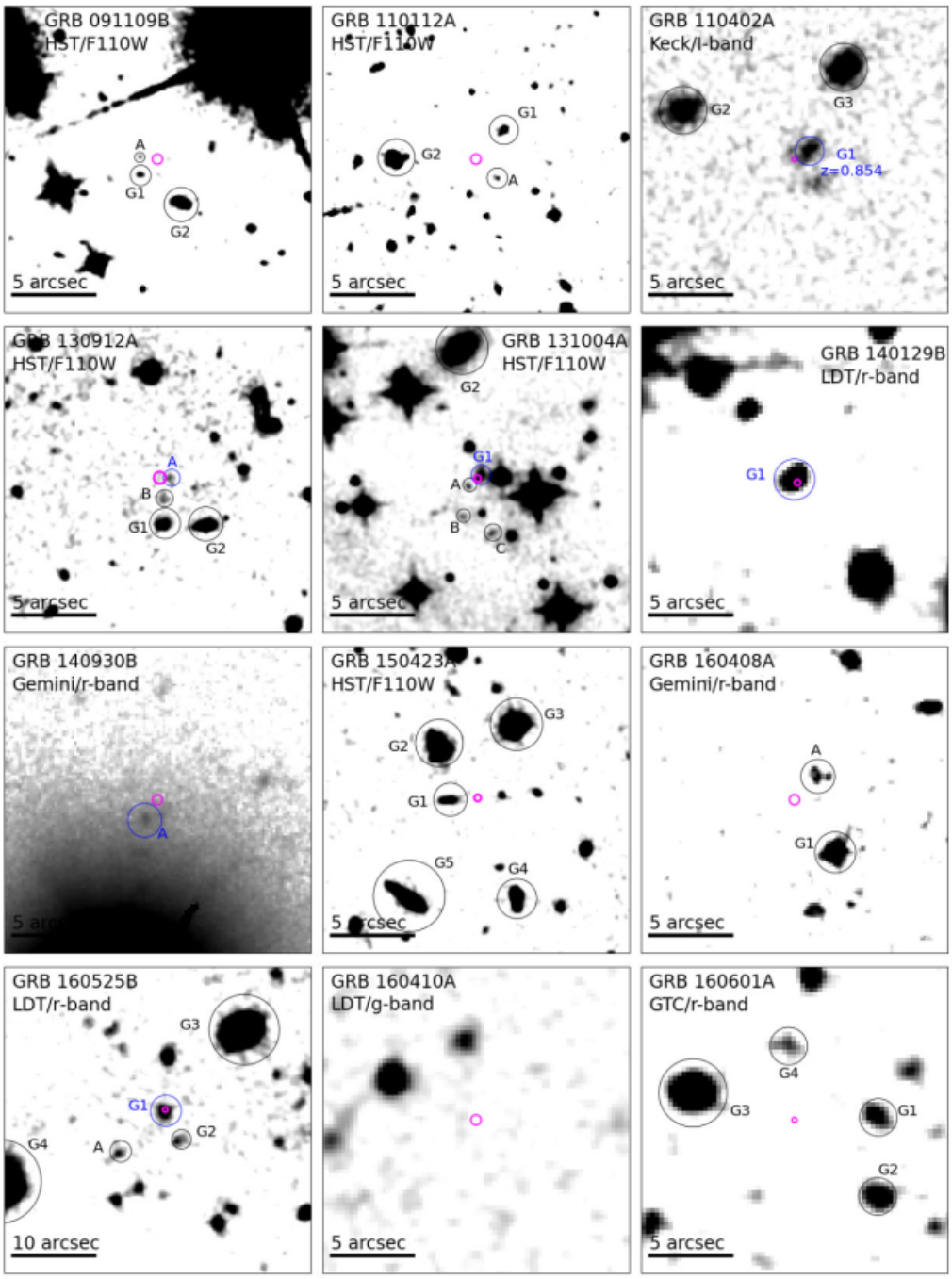

Figure 1.14: Finding chart for short GRBs with a detected optical counterpart. Marked as the galaxies candidates to be the GRB host galaxy. Taken from (O'Connor et al. 2022).

Chapter 2

Methodology

Contents

Introduction

Gamma-ray bursts (GRBs) are an excellent tool to trace the Universe properties across cosmic time. From the prompt emission, through the fading afterglow and to the host galaxy, the different phases of the observational follow up of GRBs offer us different kinds of information. From the prompt and afterglow emission, we can infer properties of the explosion progenitor and jet structure and also determine the density and structure of the circumburst medium (see e.g. Campana et al. 2010; Kann et al. 2010; Tanvir et al. 2019). The medium the GRB travels through on its way to Earth leaves a footprint on the observed afterglow. By measuring the shape of the afterglow spectrum, we can determine the amount and type of dust in the host galaxy along the line of sight. This is done by directly applying Spectral Energy Distribution (SED) techniques to the GRB afterglow light curve (see e.g. Kann et al. 2010; Zafar et al. 2011). The spectrum typically follows a power law and evolves with time. The intervening material allows us to determine the distance to the absorber system through absorption line spectroscopy. If fine-structure lines are detected, their evolution lets us determine the distance from the absorbing material to the explosion site. Beyond the distance determination, it is also possible to obtain chemical composition through the explosion line of sight. If Lyman alpha is covered by the spectrum (typically for bursts above redshift of ~2) we can determine the column density of hydrogen and by comparison of this value to the column densities of other elements calculate the metallicity of the host galaxy (Thöne et al. 2013; Bolmer et al. 2019; Heintz et al. 2023). A more precise measurement of dust traced by the GRB using spectroscopy allows us to study dust at many different redshifts and in many different galaxy types. But these are not the only methods. A interesting tool is polarimetry studies of the prompt and afterglow emission. These are important for understanding the central engine that powers GRBs, the way jets are formed and the afterglow and prompt emission geometry.

Many different techniques can be used, and there is a wealth of information we can derive from the explosive transient and the medium it goes through when observations are focused on the transient itself. Moreover, once the transient has faded completely, we can investigate the host galaxy properties using spectroscopic methods and/or resolved studies when possible. At higher redshifts, this becomes a more difficult task to pursue, as angular sizes of host galaxies are small and spectral coverage prevents us from observing them at great distances. But the main problem is the host galaxies faintness, this is where photometric techniques become an important tool.

Photometric observations can reveal morphological and physical properties. Modeling the SED of a GRB host enables us to infer key integrated properties of the galaxy such as the stellar mass or the star formation rate (SFR) and find out how both properties evolve with distance and whether they play a role in GRB production.

2.1 Insights from the prompt emission

The prompt emission is the first electromagnetic emission observable from a GRB. This emission is believed to come from shocks of different velocity shockwaves within the GRB jet (see Sect. 1.2.1). Imprints from the central engine in this emission that help us understand the nature of this motor as well as of the GRB jet.

Classically, GRBs have been divided into two classes: long soft and short hard GRBs. This has been long based on two main observable characteristics: The duration of this prompt phase i.e., the amount of time in which they emit between 5 % and 95 % of the total high-energy (HE) emission, the so-called T_{90} and the hardness ratio, defined as the ratio between the fluence in the 50-100 keV and the 25-50 keV bands (see Fig. 2.1). Long GRBs are observed to be softer bursts with a $T_{90} > 2$ s while the opposite is the case for short GRBs (Kouveliotou et al. 1993). However this clear association has been under debate since some observationally unmatching GRBs were detected, conducting the classification problem to be still under debate (see Sect. 1.3.3). The prompt emission seems to follow a linear relation between the rest-frame peak energy (E_{peak}) and the isotropic energy (E_{iso}, see Sect. 1.2.1 for an explanation of E_{peak} and E_{iso}), this is known as the Amati relation (Amati et al. 2002; Amati 2006) and implies that despite the heterogeneity among GRB prompt emission light curves, they should share similar physical conditions that produce a GRB. This relation also shares an offset between long and short burst (see Fig. 2.1).

However, these properties suffer from biases such as the detector sensitivity. This leads to different GRB missions detecting a different fraction of short and long GRBs, or a different redshift distribution based in different properties has been suggested (see Sec. 3.4 in Chapter 3 for further explanation on this).

2.1.1 The distance problem

Investigating the gas properties through cosmic time has always been a difficult task and mostly restricted to high-redshift quasars (QSO). This field has benefited from the discovery of GRB afterglows that act as background light sources which can be orders of magnitude brighter than QSO, albeit only for a short time. The spectra of these powerful sources follow a smooth power-law that decays with the spectrum flux density decreasing with time following a power-law trend. As the light travels to Earth, material within the line of sight absorbs light, leaving an imprint that carries a wealth of information. GRB spectroscopy is a powerful tool to investigate metal composition of the host galaxy where they happens as well as from different intervening clouds at different distances from the explosion site. GRBs can be detected over a very wide range of redshift, hence they are a perfect tool to investigate the metal enrichment at different distances and

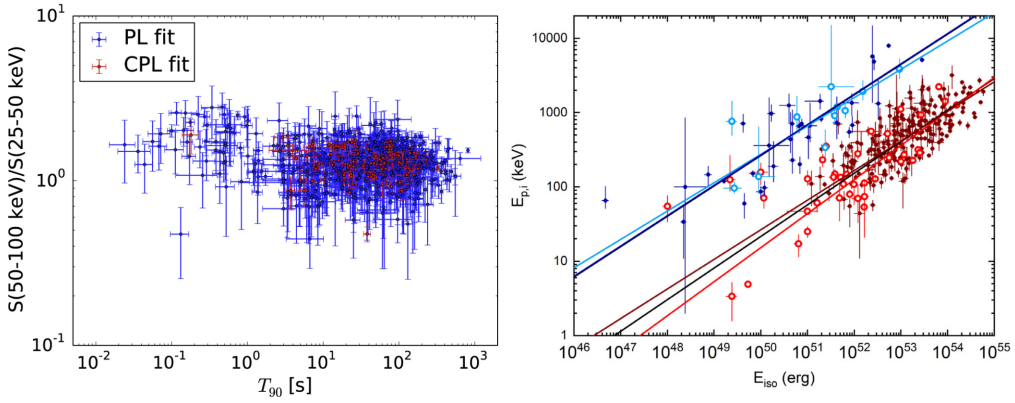

Figure 2.1: Main Prompt emission characteristics. *Left:* Hardness ratio - T_{90} distribution with two well differenciated hubs (Lien et al. 2016). *Right:* Amati relation for short (blue) and long GRBs (red) (Minaev & Pozanenko 2020, 2021).

in unbiased sightlines. GRBs might exist up to $z \approx 20$ (Kann et al. 2024) which implies that we could study the early Universe with them at distances difficult to reach by other means.

GRB afterglow spectra usually shows absorption fetures (see e.g. de Ugarte Postigo et al. 2018). These are associated to the presence of atomic and in rare occasions also molecular gas in the line of sight towards the GRB. The most commonly observed features are due to the presence of elements such as Fe, Mg, C or Si (Christensen et al. 2011). By measuring the wavelength at which these transitions are observed, and comparing them with their known rest wavelengths, we can determine the redshift at which they are produced. By assuming a model of cosmological expansion we can transform this redshift into a distance. However, this is not necessarily the distance to the GRB but to the intervening clouds, so strictly speaking this is a lower limit of the distance to the GRB. One would need to show that this clouds are within the host galaxy of the GRB to associate this distance to the event. The GRB itself emits synchrotron light across the entire electromagnetic spectrum characterised by several power-laws and characteristic frequencies. Within a single spectrum this emission is normally a simple power-law, without features and GRBs are so powerful that they can excite and even ionise atoms up to very large distances. This happens in the immediate environment of the burst, within the circumburst medium (CBM), or at larger distances such as the interstellar medium (ISM) or the intergalactic medium (IGM). It is common to detect absorption lines at different redshifts relative to the explosion site. Absorption lines from intervening systems allow us to determine the cosmological distance to the GRB site, giving us a lower limit on how far away the GRB is. Absorption lines from excited states, such as fine-structure lines caused by UV pumping from massive stars, allow us to model the surrounding material and help determine the distance from the absorbing system to the GRB.

To infer whether the afterglow is tracing the CBM, the ISM or the IGM there are different clues one can examine in their spectrum, spectral coverage permitting (see Fig. 2.2 for a sketch). By chance alignement, they may even be able to trace material across different galaxies. The different absorption lines detected in afterglow spectroscopy have different ionisation potentials (see e.g. de Ugarte Postigo et al. 2012) which means they might be generated in different environments. For

example, NV has a high ionisation potential and this implies a hot nearby source that emits in the UV ionising N to the higher states. These sources could be massive stars although ionisation can also occur in strongly shocked gas. This scenario is likely to happen in the CBM of a long GRB progenitor as they are formed in highly star-forming regions where massive blue stars could ionise the Nitrogen. However, we also find NV in isolated cold material in the CGM where densities are so low that the stripped electrons cannot be recovered. An indicator for ISM in afterglow spectroscopy are the high ionisation species such as SiIV or CIV. These transitions have a high ionisation potential but significantly lower compared to NV so they can be located farther away from the CBM. They are believed to be formed in a similar way to NV, due to UV emission from massive stars implying a nearby star-forming region but also by background powerful sources such as Active Galactic Nuclei (AGNs), shocked gas or gas outflows from AGNs or supernova explosions. Therefore, these transitions are found in the ISM or in the external parts of the host galaxy, in the surrounding gas, but they could also be in the CGM in a similar way to NV. A relevant feature that can be detected through afterglow spectroscopy is the cold neutral hydrogen HI. It is commonly expected in the IGM and is associated to cold and metal poor clouds in the external parts of galaxies acting as a galactic gas reservoir.

The most accurate method to determine the distance from the absorber to the GRB explosion site and, therefore, the precise distance to the GRB, is through the detection of fine-structure lines. These lines come from the spin-orbit coupling i.e., when the spin of atom's electrons interact with its total angular momentum allowing the presence of splitted energy levels for the same ground-state to different levels with slightly higher energies. This can happen through different processes although for GRBs it has been demonstrated that they arise from UV pumping, a phenomenon through which atoms absorb UV photons and jump to higher energy states (Vreeswijk et al. 2007). These fine structure lines are detected in afterglow spectroscopy at slightly different wavelengths from the one of the corresponding ground-state atom. The evolution of the column densities of these features, studied together with the light curve evolution of the afterglow, allow to derive properties of the absorber as well as the distance to the explosion site.

Furthemore, when fine-structure lines are not detected (and redshift allowing), one can still put stringent constraints to the GRB distance. Even when spectroscopy is not possible or it is shown as featureless, the non detection of the afterglow photometrically towards bluer wavelengths can put limits to their distances as the IGM absorbs all the photons below 912 Å, known as the Lyman limit, which will shift to redder wavelengths as the GRB light is redshifted. This is known as the drop-out technique that, if combined with spectroscopy with identified wavelengths, can lead to accurate measures of the distance to the GRB.

Typically the afterglow emission of a GRB is so bright that it outshines the underlying host galaxy. Emission lines from the host would have a very low S/N in the spectrum as the GRB continuum emission would be several orders above them and therefore, are hard to detect. As the afterglow fades, emission lines from the host galaxy become more prominent, so that one can determine accurately the distance to the GRB if the redshift is low enough and/or the spectral coverage is large to cover these emission lines.

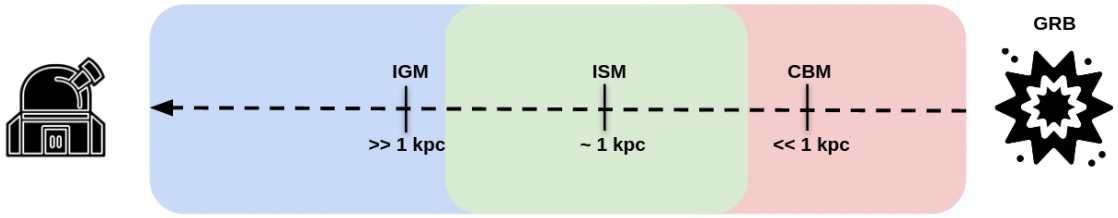

Figure 2.2: Schematic view of the different environments and rough distances to the GRB site. Not to scale

2.1.2 Determining column densities. Voigt profile

The absorption lines that the intervening material imprints in a GRB afterglow spectrum depend on the amount of material the light goes through. Each element X will absorb light at a specific wavelegth in a way that relates to the amount of atoms in the medium through the curve of growth.

This method allows to determine the column densities of specific ions through eq. 2.1 for multiple transitions of the same ion in the same ionization state.

$$N = \frac{EW}{\lambda} \cdot \frac{1.1 \times 10^{20} cm^{-2}}{f\lambda[\text{Å}]} \tag{2.1}$$

where EW is the equivalent width and N is the column density. When different transitions are not detected, the "multi-ion-single-component curve of growth" (MISC-CoG) is applied, using different ions with a shared broadening, b, which implies transitions with similar excitation energies. This approach assumes all ions originate from the same region in the interstellar medium (ISM). The method relates the column density to the equivalent width based on the saturation of the line, following different relations for unsaturated and saturated lines. At the non-linear regime, the transitions are saturated and b-parameter can significantly affect derived column densities.

Each element can present different transitions at different wavenlegths. However, these will not be observed as a sharp drop in the observed flux at the corresponding shifted wavelength. Absorption lines suffer from line broadening through different effects. The Doppler broadening comes from the movement of atoms within material cloud due to their thermal energy. Atoms absorb a specific wavelength, but due to their thermal movement the absoption will be blueshifted or redshifted as they move towards the background light source or away from it. This effect is observed in the line shape as a Gaussian profile that is temperature dependent. Another important source of broadening are the collisions and pressures within the cloud. Collisions between atoms or particles disturb the energy levels of the absorbing atoms, while high pressures increase the density of collisions, provoking broadening the absorption features. This is observed as a Lorentz profile in the absorption line i.e., a sharp absorption at the corresponding wavelength with wings that extend into the continuum. These two effects are described as a Voigt-Hjerting profile which is the combination of a Gaussian and a Lorentzian profile.

The total light observed is proportional to the optical depth of all the transition detected for each element:

$$I(\lambda) = \exp^{-\tau(\lambda)} = \exp^{-\tau_0 H(a,x)} \tag{2.2}$$

where τ is the optical depth and H(a, x) is the Voigt-Hjerting function:

$$H(a,x) = \frac{a}{\pi} \int_{-\infty}^{\infty} \frac{e^{-y^2}}{(x-y)^2 + a^2} dy \tag{2.3}$$

with

$$a = \frac{\lambda \Gamma}{4\pi b} \tag{2.4}$$

$$x = -\frac{c}{b}\left(1 - \frac{\lambda}{\lambda_0}\right) \tag{2.5}$$

with Γ the damping parameter, a value that is inverselly proportional to the mean lifetime of the transition, c is the speed of light and b is the Doppler parameter in km/s. This b parameter has typical values that range from few km/s to several tens of km/s (Christensen et al. 2011; de Ugarte Postigo et al. 2018) for individual components.

When measuring absorption line intensity for a specific atom, we are observing the light going through a system for which we do not know the shape. The material could be highly concentrated with a high density of atoms or the material is spread along a large region. We thus define the column density as:

$$N = \int ndl \tag{2.6}$$

where n is the atom density and l is the length of the absorbing material cloud the light goes through.

We define the equivalent width (EW) of an absorption line as the width between the two limiting wavelength values (λ_1 and λ_2) around an absorption line as:

$$W = \int_{\lambda_1}^{\lambda_2} \left(1 - \frac{I_\lambda}{I_{continuum}}\right) d\lambda \tag{2.7}$$

If we detect components at different velocities for the same transition, we are only able to differenciate them if the spectral resolution is high enough. When the spectral resolution is too low, it becomes difficult to discern the starting and ending points of absorption features. As a result, the absorption lines appear blended, making it is not possible to accurately measure the column density. In these cases, only relative values tied to a common component can be obtained. This problem arises when the GRB afterglow light passes through multiple absorbers that are either located too close to each other or contain nearly identical elements.

The column density of atomic species within the line of sight can be derived by fitting the Voigt profile to the line profile. For this the resolving power of the spectrograph has to be high enough to have a good sampling of the line, so significantly higher than (or at the very least comparable to) the Doppler parameter of the transition. Instrumental resolution permitting, column densities for different absorption lines can be obtained using modern codes such as VoigtFit (Krogager 2018) that can fit Voigt profiles with multiple components to different transitions of the same species

and even to different atoms at once in an interactive mode controlling physical parameters such as the line broadening, b. An example of the fit of a broad Lyman-α absorption in GRB 190106A afterglow spectum and accurate column density derivation using VoigtFit can be seen in Fig. 2.3.

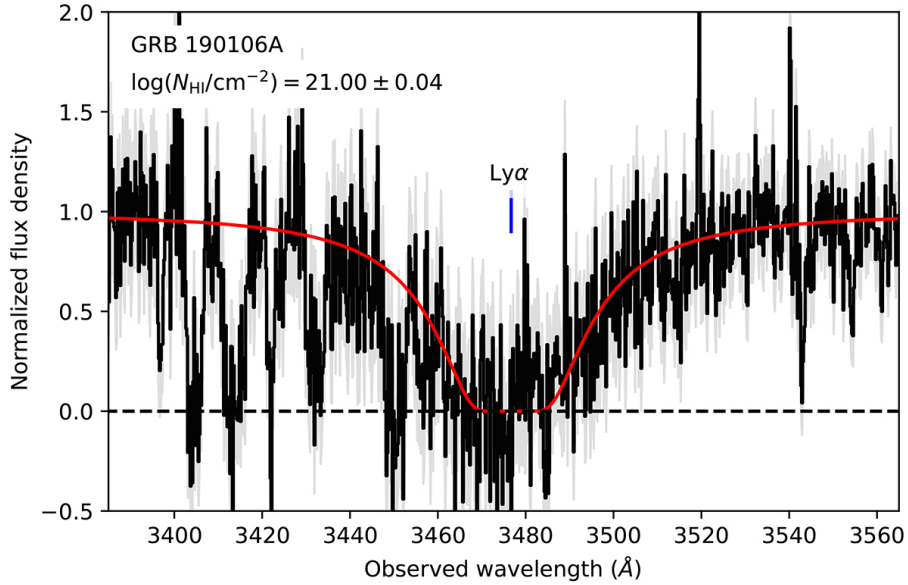

Figure 2.3: Voigt profile fit (red line) of the broad HI absorption line in the normalised and smoothed spectrum of GRB 190106A (in black) from (Heintz et al. 2023). We can see the non-smoothed spectrum in gray behind the smoothed one.

Metal lines in absorption

Ionised gas metallicity is measured using emission lines and applying different calibrators. Absorption line spectroscopy allows to directly derive abundances for different elements. To do so, we need to measure both the column density of metal lines and of HI, which is obtained by fitting the broad Ly-alpha feature at 1215.67 Å in rest-frame. This is possible when doing UV spectroscopy from space or for high-redshift sources, as the absorption shifts towards redder wavelenghts detectable from ground-based facilities beyond redshifts of $\sim 1.6 - 2$. Using the solar metallicity as reference (Asplund et al. 2009; Lodders et al. 2009) we determine the metallicity as:

$$[X/HI] = \log_{10}\left(\frac{N(X)}{N(HI)}\right) - \log_{10}\left(\frac{N(X)_{\odot}}{N(HI)_{\odot}}\right) \tag{2.8}$$

However, these values can be underestimated if part of the atoms are depleted onto dust. This happens when atoms attach onto dust grains and do not contribute to the absorption lines in the spectrum. Properties such as their binding energy condensation temperature can make atoms such as iron or silicon to bound and form dust grains, while these is more difficult for elements such as zinc or sulfur. This results in the undersetimation of the column density of a particular element, and consequently an underestimation of the metallicity. To minimise this effect, we can use the zinc metallicity as an indicator since this element is depleted less onto dust grains. As zinc is not always detected in afterglow spectroscopy, metallicity determination has often to rely

on different elements that suffer depletion. To correct for the dust depletion effect, we can use relative metallicities of different elements and correct the observed metallicity from depletion (δ_X) using the known relative degree of depletion for different species (see Sect. 3.3.2 for an extended explanation on the dust-depletion correction). The depletion parameter, δ_X, of element X presents different depletion patterns accordingly to the element for which we obtain a relative metallicity (see Fig. 2.4) since different elements are depleted by a different amount.

However, when deriving metallicities from a GRB afterglow we might be tracing the material from different parts from the host galaxy or the IGM (see Sect. 2.1.1). Most host galaxies show a large column densities of neutral hydrogen, with values of $\log_{10}(N(HI) > 20.3cm^{-2}$. These are known as Damped Lyman Alpha absorbers (DLAs) and are associated to the external parts of the ISM and to the halo of galaxies. For QSOs, lower values are detected which might indicate they are tracing less dense intervening galaxy parts than for GRBs. This could be an indication that GRBs trace gas from the inner parts of the host galaxy ISM. For short GRBs it is also possible that the GRB trace only the halo gas if they have suffered a kick-out.

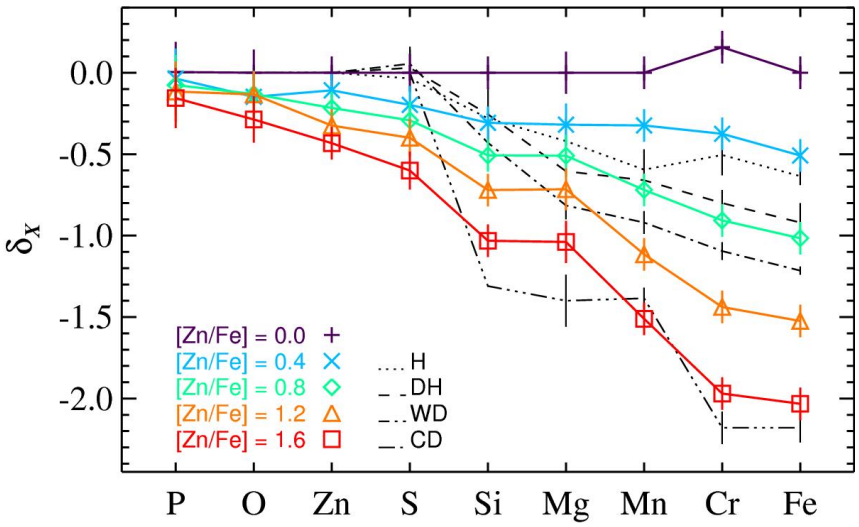

Figure 2.4: Dust depletion pattern for differen α-elements from (De Cia et al. 2016).

2.2 The physics behind imaging polarimety

The polarisation of the electromagnetic field is determined by the oscillation state of the electric field. In a simplistic way, if we consider a monochromatic light that is totally polarised, the vector that defines the electric field will travel drawing an ellipsoid in each perpendicular plane to the light propagation direction. The polarisation ellipse (see Fig. 2.5) is tilted with an angle ψ with respect to the x and y plane which corresponds to the observing plane. The decomposition of the semi-major and the semi-minor axis of the rotated ellipsoid will then give the projected E_{0x} and E_{0y}. It wild depend on the inclination of the ellipse that different polarisation states can be found. This is due to the "length" of each component leading to two very differentiated polarisation degenerated states, light that is linearly polarised or circularly polarised.

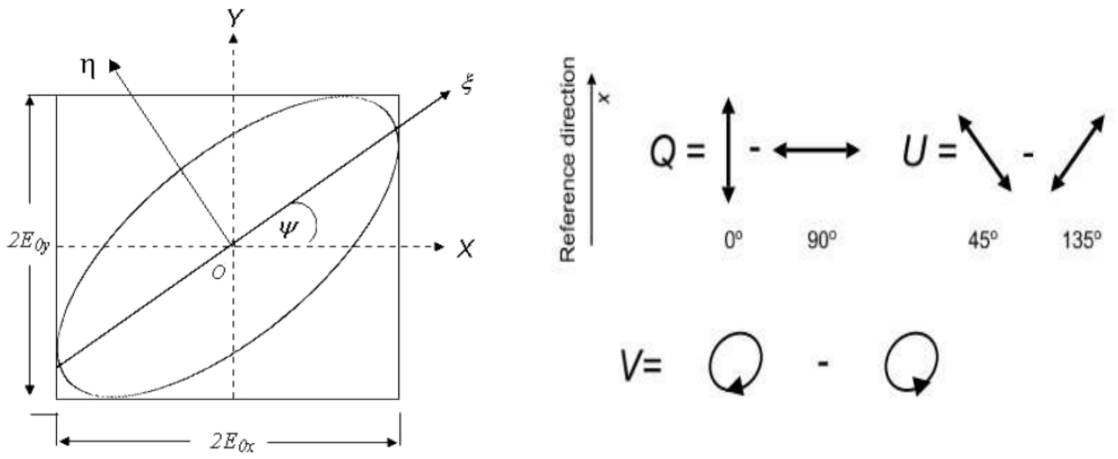

Figure 2.5: Polarisation ellipsoid sketch from (Collett & Schaefer 2008).

Linearly polarised light can happens in different scenarios. It can be vertically or horizontally polarised when E_{0x} or E_{0y} are zero, respectively. It is also be linearly polarised when $\psi = 0$ or $\psi = \pi/2$. When $\psi = \pi/4$ or $\psi = 3\pi/4$, both components are equal resulting in linearly polarised light (see Fig. 2.5). These different polarisation possibilities are commonly described by the Stokes parameters that can be defined as described in Eq. 2.9 for which the propagation plane is choosen to be the perpendicular one to the light direction to the observer (Landi Degl'Innocenti et al. 2007).

$$\begin{cases} I &= \langle E_{0x} x^2 \rangle + \langle E_{0y}^2 \rangle, \\ Q &= \langle E_{0x}^2 \rangle - \langle E_{0y}^2 \rangle, \\ U &= \langle 2E_{0x} E_{0y} \cos\psi \rangle, \\ V &= \langle 2E_{0x} E_{0y} \sin\psi \rangle, \end{cases} \tag{2.9}$$

The Stokes parameters are associated to the total light intensity, I, to the proportion of linear polarisation in the plane perpendicular to the propagation direction parallel plane Q, the polarisation in the $\pm 45°$ plane to the reference plane and the V-parameter that indicates if the circular polarisation is clockwise or counterclockwise (Landi Degl'Innocenti et al. 2007).

It is more common to use the the reduced Stokes parameters that are relative to the total intensity, I, (see Eq. 2.10)

$$\begin{cases} q &= \frac{Q}{I}, \\ u &= \frac{U}{I}, \\ v &= \frac{V}{I}, \end{cases} \tag{2.10}$$

This allow to define a relation to the angle between the semi-major axis and the x-axis that is commonly known as the position angle and follows:

$$\frac{u}{q} = \tan(2\psi) \tag{2.11}$$

These equations allows to measure the main properties of light in sources such as GRB afterglow for which we can obtain the polarisation degree calculated as described by 2.12. The position angle, ψ (Eq. 2.11), depends for an additive constant to take into account the correction of the system, that can have different values as indicated in Eq. 2.13 (Bagnulo et al. 2009).

$$p = \sqrt{q^2 + u^2} \tag{2.12}$$

$$\psi_0 = \begin{cases} 0, & \text{if } Q > 0 \text{ and } U \geq 0, \\ \frac{\pi}{2}, & \text{if } Q \leq 0, \\ \pi, & \text{if } Q > 0 \text{ and } U < 0. \end{cases} \tag{2.13}$$

This is further explained in Chapter 4 following the same formalism.

2.2.1 Measuring source polarisation using imaging polarimetry

Polarimetry measurements in optical astronomy are possible through a specific optical setup. The incoming light passes through a $\lambda/2$ retarder plate, placed in the optical path at a fixed position. A retarder plate introduces a phase difference between the orthogonal components of light, altering its polarization state. The $\lambda/2$ plate rotates the plane of polarization of linearly polarized light.Afterwards, light must go through a polariser, a Wollaston prism that will separate the light into the ordinary and the extraordinary rays. The $\lambda/2$ plate or half wave plate (HWP) functionality is to rotate in 22.5 degrees steps to change the angle (ψ) of the incoming light. In practice, this rotation alters the polarisation state of the light, allowing different polarisation angles to be observed without rotating the instrument. When the angle of the HWP is a multiple of $\alpha = k \cdot 45° = 0°, 45°$, or $\alpha = k \cdot 45° + 22.5° = 22.5°, 67.5°$, it modifies the polarisation of the incoming light allowing the measurement of the light flux at different position angles. The combination of the measurements in each HWP position allow to reconstruct the polarisation ellipsoid and compute the Stokes parameter, q and u following eq. 2.2.1. After the HWP the light needs to go through the Wollaston prism (see a picture in 2.6) which split the beam light into orthogonally polarised *ordinary* and *extraordinary* beams.

The reduced q, u Stokes parameters can be determined using imaging polarimetry methods i.e., imaging of a source after passing through the previously described optical elements. These are obtained as a rate between the background subtracted flux measured in the *ordinary* and *extraordinary* beams in each image obtained at different HWP positions as described in (Bagnulo et al. 2009):

$$q = \frac{1}{2}\left\{\left(\frac{f^o - f^e}{f^o + f^e}\right)_{\alpha=0°} - \left(\frac{f^o - f^e}{f^o + f^e}\right)_{\alpha=45°}\right\} \tag{2.14}$$

$$u = \frac{1}{2}\left\{\left(\frac{f^o - f^e}{f^o + f^e}\right)_{\alpha=22.5°} - \left(\frac{f^o - f^e}{f^o + f^e}\right)_{\alpha=67.5°}\right\}$$

and with the corresponding errors as indicated in Eq. 2.15 where x corresponds to the q, u parameters with $\psi_0 = 0.0$ for $x = q$ and $\psi_0 = 22.5$ for $x = u$:

$$\sigma_x'^2 = \left(\left(\frac{f^o}{(f^o + f^e)^2} \right)^2 \sigma_{f^o}^2 + \left(\frac{f^e}{(f^o + f^e)^2} \right)^2 \sigma_{f^e}^2 \right)_{\alpha=\psi_0} + \left(\left(\frac{f^o}{(f^o + f^e)^2} \right)^2 \sigma_{f^o}^2 + \left(\frac{f^e}{(f^o + f^e)^2} \right)^2 \sigma_{f^e}^2 \right)_{\alpha=45°+\psi_0} . \tag{2.15}$$

However, polarimetry measurements can be contaminated in many different ways changing the original polarisation of the light emitted by an astronomical source. The interstellar medium that the light goes through, either in the environment of the source (host galaxy of extragalactic objects such as GRBs), or within the Milky Way can alter the signal. Light from the Moon can also contribute to polarising the background of our target. Finally, we also have to take into account the effects of the optical elements in the polarimeter. Some of them are due to chromaticity of the optical elements as they may be different from their theoretical values or the different filter transmitance (González-Gaitán et al. see 2020 for an extended explanation in this). However, most of these effects can be corrected by properly calibrating the instrument (f.ex. with flat fields) and through the study of the polarisation with different HWP angles.

Further explanations on how we can masure q and u parameters and correct them from contamination polarisation sources can be found in Sect. 4.4.1. In this section is also explained how the polarisation can be corrected from the bias introduced by its definition as an intrinsically positive quantity.

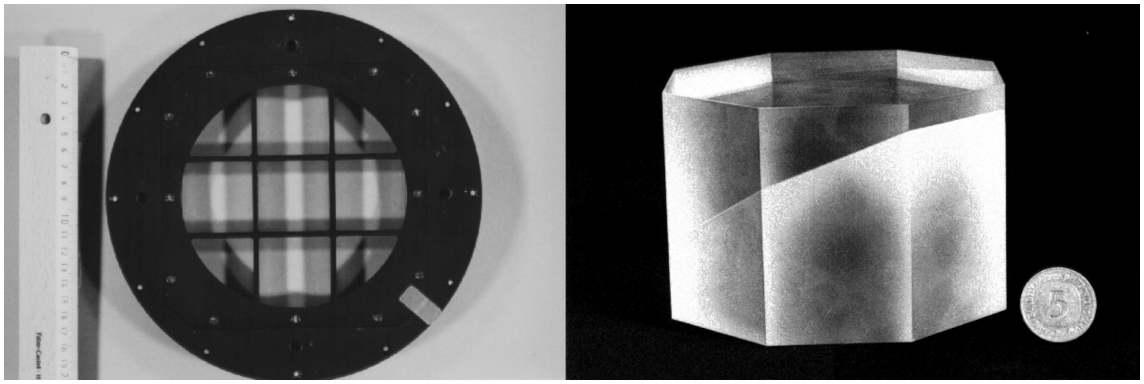

Figure 2.6: Optical elements in the light path for imaging polarimetry (Images from https://www.eso.org/sci/facilities/paranal/instruments/fors/inst/pola.html). *Left:* Retarder $\lambda/2$ plate that acts as direction of the light beam selector. *Right:* Wollaston prism. Light passing through is splitted into two well separated beams with the electrical vectors in orthognal directions.

2.3 Integrated properties of GRB host galaxies. Spectral Energy Distribution fitting

At low redshift, resolved studies of bright galaxies allow to unveil the properties of smaller galaxy regions. However, when the redshift is large and the targets are small and faint this type of observation is not possible. From non-spatially-resolved observations we can derive the integrated properties of a galaxy through methods like Spectral Energy Distribution (SED) fits. By collecting the integrated photometry of the host in different bands we can build an SED of the galaxy. The galaxy emission from the highest energies down to the radio emission has contributions from the different components that co-exist in galaxies, including gas emission due to star-formation, stellar continuum, UV light absorption due to dust and its re-emission in IR. The total flux of unresolved galaxies is a complex sum of all emitting components and makes it challeging to identify the contribution of each component to the galaxy SED. SED fitting codes attempt to determine the contribution of those components in the overall light of the galaxy using different approaches depending on galaxy properties (e.g. galaxy type dust characteristics as compared to SF galaxies). With these codes we can obtain integrated properties for the modeled galaxy such as the total stellar mass, the star formation rate or the metallicity, among others.

There are many different SED fitting codes. Each of them is based in a number of assumptions and uses specific approaches to compute values like the total stellar mass or the Star Formation Rate (SFR) of a galaxy. A comparison of different SED fitting codes shows consistent results in certain physical properties such the stellar mass but tend to be more discrepant in some other properties, such as the SFR (Pacifici et al. 2023) which could be an effect due to differences in how the star formation history is implemented. Figure 2.7 shows that different codes can yield slightly different results when computing the same properties. The ability to incorporate infrared (IR) observations, along with the option to include additional emission components—such as emission from active galactic nuclei (AGN)—can be crucial when selecting among the various available SED fitting codes. These codes are based on the selection of galaxy templates that consider different galaxy types, their evolutionary state and other physiscal characteristics. They typically implement the different theoretical aproaches and let the user choose those that better matches the objects.

There are two main branches of SED fitting codes, one in which SED templates are built on the fly as the user select models and model parameters. This is the case of `Prospector`, a python-based SED fitting code that relies in Monte Carlo methods to compute the physical properties of the fitted galaxy SEDs (Johnson et al. 2021). A different approach is to use a grid of already modelled SEDs and compute the physical parameters accordingly to the available photometry. A good example for this method is the Code Investigating GALaxy Emission `CIGALE` (Boquien et al. 2019), a python-based code that assumes that all absorbed UV photons are re-emitted in the IR by dust. This physical condition makes the availability of mid- and far-ingrared (MIR and FIR) very desirable to obtain solid results. The grid-based fitting approach in `CIGALE` is computationally more efficient when analyzing large samples, especially in cases where computing resources are limited. In contrast, `Prospector` can become computationally expensive when the parameter

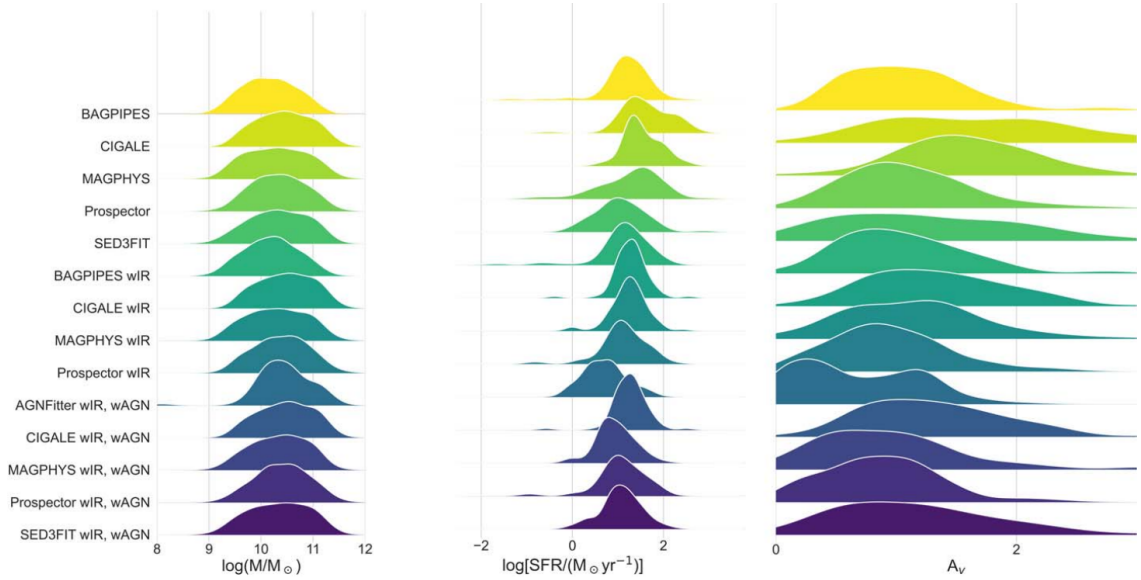

Figure 2.7: Results distribution obtainend after using the same datasample and fitting the corresponding SED following the same fashion. Comparison is done after using different configurations i.e., not including IR observations, with IR photometry (wIR) and including an AGN component (wAGN). Taken from Pacifici et al. 2023.

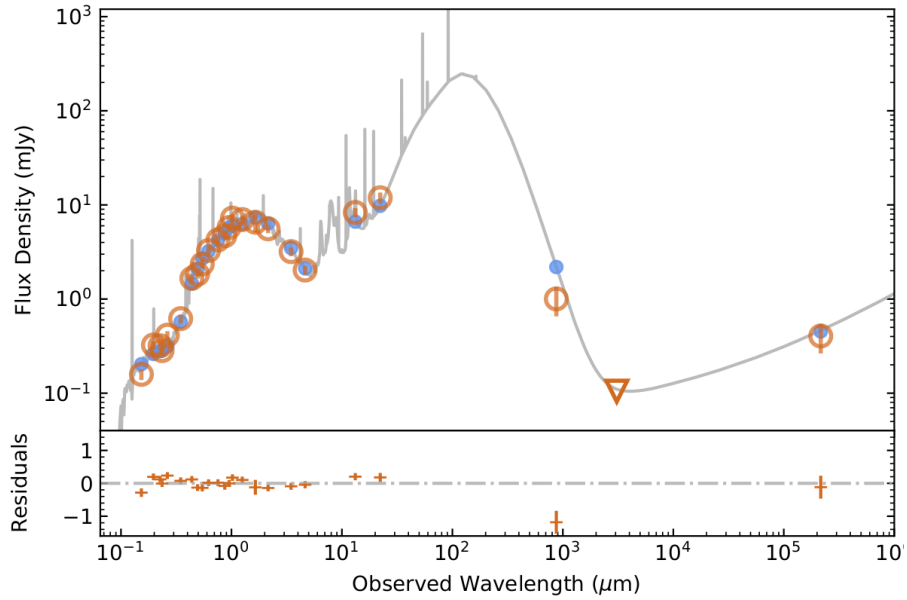

Figure 2.8: Best fit SED model to the host of GRB 171205A using `CIGALE` (Boquien et al. 2019). In the upper panel the flux density distribution is shown in gray. Orange circles are the photometric data while blue dots are the expected fluxes from the best model. The lower panel shows the residuals of the model - the photometry. Taken from de Ugarte Postigo et al. 2024.

space is sufficiently large (Csizi et al. 2024).

Another key difference lies in its modularity and flexibility. For example, `CIGALE` allows fit-

ting the star formation history (SFH) using both parametric and nonparametric functions, while Prospector relies solely on nonparametric SFH modeling. Although this can lead to better constraints on the SFH, it also requires broad wavelength coverage, ideally from the UV to the near-infrared (NIR).

Overall, `Prospector` tends to be slower when applied to large datasets, though it can offer more detailed SED modeling for individual galaxies. For studies involving large samples, `CIGALE` may be the more practical choice, as the differences between codes become less significant. Indeed, in Fig. 2.7, we see that the results for stellar mass and SFR are not significantly different when using different SED fitting codes, while A_V appears to be less well constrained, although still consistent across codes (see (Pacifici et al. 2023) for an extended comparison of SED fitting methods). Figure 2.8 shows an example of a SED fit to a long GRB host galaxy with observations covering from the far-ultraviolet (FUV) to radio wavelenghts using `CIGALE`.

The selection of the models that we use to fit our data requires that we take into account several variables. The main one is the spectral range that the available data covers, this helps to understand what modules should be taken into account for the SED computation. The next step is to know the galaxy type and its typical properties. As for the host of long GRBs, they are expected to be immersed in galaxies that have an ongoing star-forming burst. This does not imply that these host are strictly young galaxies but instead they could have an older underlying stellar population with a recent burst of star-formation. Among the different possibilities described in Boquien et al. (2019) for the star formation history (SFH) modellisation, the best choice is a model with a delayed star formation rate as described in Eq. 2.3. The input parameters allows to model the SFH with a free age for the stellar population and to take into account the most recent burst that would give birth to a previously detected GRB:

$$\mathrm{SFR}(t) \propto \begin{cases} \frac{t}{\tau_0^2} \cdot e^{-t/\tau_0} & \text{if } t < t_0 - t_1, \\ \frac{t}{\tau_0^2} \cdot e^{-t/\tau_0} + k \cdot e^{-(t-t_0+t_1)/\tau_1} & \text{if } t \geq t_0 - t_1. \end{cases}$$

t_0 and t_1 are the age of the main stellar population and the beginning of the star formation burst and, respectivelly, τ_0 and τ_1 are the peak of the star formation episode for the main stellar population and the star formation burst. This SFH choice allows to model the mass fraction of the stellar mass that correspond to the star-formation burst as a variable of the burst amplitude, k:

$$k = \frac{f_{\mathrm{burst}}}{1 - f_{\mathrm{burst}}} \cdot \frac{\sum_{t=0}^{t_0} \frac{t}{\tau_0^2} \cdot e^{-t/\tau_0}}{\sum_{t=t_0-t_1}^{t_0} e^{-(t-t_0+t_1)/\tau_1}}$$

It is also important when choosing the models to select the most appropriate Initial Mass Function (IMF). The first step is to select a library of single stellar population (SSP). One of the most common and flexible SSP library is the one from Bruzual & Charlot (2003) that allows to

fit either a Salpeter (1955) IMF or a Chabrier (2003), from which the later IMF is more suited for Bruzual & Charlot (2003) which allows for a wider metallicity range than other SSP models like Maraston (2005). This metallicity refers to the metallicity per mass fraction (Z), which is defined as the ratio between the mass of metals and the total stellar mass. It quantifies how much of a galaxy's stellar mass is composed of metals. According to this definition, the solar metallicity is $Z_{\odot} = 0.02$ meaning that only 2% of the Sun total mass is made of elements heavier than helium.

`CIGALE` includes various models for dust absorption based on the updated Calzetti et al. (2000) law (explained in Boquien et al. 2019), allowing separate modeling of attenuation for the stellar continuum and for the emission lines. In star forming region dust is typically denser than for the stellar component which would result in lower SFR values. The nebular emission lines attenuation can be fitted using the attenuation laws of Cardelli et al. (1989) for a Milky Way like model or (Pei 1992) for the Small and Large Magellanic Clouds attenuation models. Both the stellar component and the nebular component are linked through the ratio between the color excess of the stellar component and the color excess for the emission lines

As dust absorbs light, it heats up and re-emits the energy in the infrared. To model this, a good choice are the Dale et al. (2014) templates for dust emission which depend only on the index α_{IR} of the distribution of the heating intensity per mass. These templates are an update of Dale & Helou (2002) models specific for star-forming galaxies (Dale et al. 2014).

The aforementioned codes are just examples of the many options that can be used to fit galaxy SEDs to derive physical properties.

Chapter 3

GRB 160410A: the first Chemical Study of the Interstellar Medium of a Short GRB

Contents

Abstract

Short gamma-ray bursts (SGRBs) are produced by the coalescence of compact binary systems which are remnants of massive stars. GRB 160410A is classified as a short-duration GRB with extended emission and is currently the farthest SGRB with a redshift determined from an afterglow spectrum and also one of the brightest SGRBs to date. The fast reaction to the *Neil Gehrels Swift Observatory* alert allowed us to obtain a spectrum of the afterglow using the X-shooter spectrograph at the Very Large Telescope (VLT). The spectrum shows several absorption features at a redshift of $z = 1.7177$, in addition, we detect two intervening systems at $z = 1.581$ and $z = 1.444$. The spectrum shows Lyα in absorption with a column density of $\log(N(\mathrm{HI})/\mathrm{cm}^2) = 21.2 \pm 0.2$ which, together with FeII, CII, SiII, AlII and OI, allow us to perform the first study of chemical abundances in a SGRB host galaxy. We determine a metallicity of $[\mathrm{X/H}] = -2.3 \pm 0.2$ for FeII and -2.5 ± 0.2 for SiII and no dust depletion. We also find no evidence for extinction in the afterglow Spectral Energy Distribution (SED) modeling. The environment has a low degree of ionisation and the CIV and SiIV lines are completely absent. We do not detect an underlying host galaxy down to deep limits. Additionally, we compare GRB 160410A to GRB 201221D, another high-z short GRB that shows absorption lines at $z = 1.045$ and an underlying massive host galaxy.

3.1 Introduction

For a brief moment, gamma-ray bursts (GRBs) are capable of outshining any other source in the Universe. Their γ-ray flashes can last from significantly less than a second to hundreds or even thousands of seconds (Kouveliotou et al. 1993). According to their duration and spectral characteristics, GRBs can be divided into two classes, long/soft GRBs (LGRBs) and short/hard GRBs (SGRBs). LGRBs are associated with the collapse of very massive stars and their prompt γ-ray emission in most cases lasts for more than 2 s. They have been shown to be linked to broad-lined Type Ic core-collapse supernovae (e.g. Galama et al. 1998; Hjorth et al. 2003; Woosley & Bloom 2006; Hjorth & Bloom 2012; Cano et al. 2017).

SGRBs, in contrast, are associated with the merger of a binary system of compact objects, usually two neutron stars (NSs, Berger 2014; Abbott et al. 2017a). They show a harder γ-ray spectrum than LGRBs and have a T_{90}[1] of less than 2 s (Kouveliotou et al. 1993), although some events show extended emission (EE), albeit with a softer spectrum, and recently, an event, GRB 211211A, which was almost indistinguishable from a long GRB, has been associated with a compact object merger (Rastinejad et al. 2022; Gompertz et al. 2022; Yang et al. 2022; Troja et al. 2022). SGRB afterglows are typically less luminous than those of LGRBs (Kann et al. 2011) which makes them much more difficult to detect at higher redshifts. A recent study by Dichiara et al. (2021) suggests that at high redshifts, there is a bias towards SGRBs with extended emission as they are typically brighter than regular short GRBs.

In a SGRB, during coalescence of the binary system, a relativistic jet forms producing the prompt emission and later the afterglow emission by interaction with the circumburst environment, the same way the afterglow is produced for LGRBs. SGRBs also show a so-called *kilonova* emission (KN), powered by the radioactive decay of heavy elements produced via the *r*-process in a neutron-rich environment (Metzger et al. 2010). The KN emission is normally much fainter than the afterglow and hence is only detected a few days after the GRB when the afterglow has faded (e.g. Metzger 2019).

Until recently, GRBs have only been detected by high-energy instruments on-board satellites such as the *Neil Gehrels Swift Observatory* (*Swift* hereafter)/Burst Alert Telescope (BAT, Gehrels et al. 2004; Barthelmy et al. 2005), *Fermi*/Gamma-Ray Burst Monitor (GBM, Meegan et al. 2009), or Konus-*Wind* (Aptekar et al. 1995). In 2017 a gravitational wave (GW) was detected by LIGO/Virgo together with a corresponding electromagnetic counterpart at various wavelengths and the SGRB 170817A detected by *Fermi*/GBM and the SPI-ACS (SPectrometer on INTEGRAL - Anti-Coincidence Shield) on *INTEGRAL* just ~ 1.7 s after the GW detection, firmly linking NS mergers to SGRBs (Goldstein et al. 2017; Savchenko et al. 2017; Abbott et al. 2017a,b; Tanvir et al. 2017). However, to date this has been the only event where an electromagnetic counterpart has been detected in association with a GW signal from a NS-NS merger (e.g. Antier et al. 2020). Optical surveys of the sky such as the Zwicky Transient Facility (ZTF) are expected to significantly increase the KN detection rate, even in the absence of a γ-ray or GW signal (Bellm et al. 2019; Graham et al. 2019; Andreoni et al. 2021).

[1] T_{90} is defined as the time span during which from 5% to 95% of the total counts emitted by a GRB are detected.

The presence of KN emission has been claimed for a small number of SGRBs, however, the first conclusive detection was obtained for GRB 130603B (Tanvir et al. 2013; Berger et al. 2013). This SGRB was also the first showing absorption lines in the afterglow spectrum (de Ugarte Postigo et al. 2014b). Since then, only a few SGRBs had a redshift spectroscopically determined via the afterglow. This makes the study of the redshift distribution and properties of the interstellar medium (ISM) challenging for the class of SGRBs and often only an indirect redshift via association with a likely host galaxy is available (e.g. Berger 2010).

Short bursts are associated with host galaxies featuring a wide distribution of stellar population ages and galaxy types. SGRBs do not seem to have a preferred location in their host galaxies. Some have even been detected at large distances from their putative hosts (e.g. Leibler & Berger 2010; Berger 2010; Fong & Berger 2013). The offset distribution can be explained by the time needed for the compact objects to form from their massive star binary progenitors and the subsequent delay time for the system to merge due to GW energy loss (Beniamini & Piran 2019; Belczynski et al. 2006; Paterson et al. 2020).

Several studies suggest compact object mergers (NS-NS, or Neutron Star - Black Hole, NS-BH) as a major source for *r*-process element enhancement (Watson et al. 2019; Roederer et al. 2016) in dwarf galaxies (Beniamini et al. 2015) as well as in ultra-faint dwarf (UFD) galaxies (Beniamini et al. 2016a). This is the case for Reticulum II, a UFD containing very metal-poor stars with a higher abundance of *r*-process elements than expected from chemical evolution driven by typical core-collapse supernovae (CC-SNe). It has been suggested that a single NS-NS merger could generate the *r*-process element abundances observed in these galaxies, however, rare CC-SNe cannot be ruled out (Ji et al. 2016a; Beniamini et al. 2016b).

In contrast, long GRBs are commonly found in bright, metal-poor regions within their host galaxies (e.g. Fruchter et al. 2006; Jakobsson et al. 2006; Thöne et al. 2008; Lyman et al. 2017) and typically with large neutral hydrogen column densities. Most LGRB hosts have $\log(N(\mathrm{HI})/\mathrm{cm}^2) > 20.3$ (e.g. Tanvir et al. 2019), which is the definition for a Damped Lyα (DLA) system. LGRBs have proven to be ideal beacons in the study of neutral and ionised gas evolution in absorption in the ISM, the Circumgalactic Medium (CGM) and the Intergalactic Medium (IGM) (e.g. Wolfe et al. 2005; Starling et al. 2013; Selsing et al. 2019; Bolmer et al. 2019; Gatkine et al. 2019).

In this paper we present a study of the optical counterpart of GRB 160410A and its afterglow spectrum. GRB 160410A is the first SGRB for which the spectral observations span a large enough spectral range, together with the SGRB redshift, to cover the Lyα absorption line and has sufficient quality to make a chemical study of the gas in its host galaxy. We also include GRB 201221D in our analysis, a SGRB with absorption lines in the spectrum, which had a lower redshift of $z = 1.045$ and a less broad spectral coverage (see Sect. 3.2.6). The paper is structured as follows: In Sect. 4.3 we present the observations of the afterglow and host galaxy of both GRBs, Sect. 4.4 presents the results on the analysis of the spectrum of the burst afterglow and its light curve as well as observations of the field to detect the host galaxy. For GRB 201221D we also present the analysis and properties of its associated host galaxy. In Sect. 4.5 we put the results in context of similar studies for long GRBs and in Sect. 4.6 we present our final conclusions.

Throughout this study, we adopt a cosmological model with $H_0 = 67.3\,\mathrm{km\,s^{-1}Mpc^{-1}}$, $\Omega_M =$

0.315, $\Omega_\Lambda = 0.685$ (Planck Collaboration et al. 2014a).

3.2 Observations

3.2.1 High-energy detection of GRB 160410A

Swift/BAT triggered on a source at RA = $10^h\ 02^m\ 43^s$, Dec. = $+03°\ 26'\ 37''$ with an uncertainty of $3'$ on the 10^{th} of April, 2016 at 05:09:48 UT (Gibson et al. 2016). The event localisation was refined by the UVOT instrument on-board *Swift* that took a finding chart with the *white* filter with a total exposure time of 150 s only 91 s after the BAT trigger, locating the burst to RA = $10^h\ 02^m\ 44.37^s$, Dec. = $+03°\ 28'\ 427$ with an uncertainty of 049 (Marshall & Gibson 2016). In the refined analysis of Sakamoto et al. (2016) the burst shows a duration of $T_{90} = 8.2 \pm 1.6$ s in the $15 - 350$ keV band and a spectral lag of 8 ± 14 ms between the $50 - 100$ keV and $15 - 25$ keV bands and -3 ± 7 ms between the $100 - 350$ keV and $25 - 50$ keV bands, which is consistent with zero, as expected for SGRBs (Norris & Bonnell 2006). The BAT light-curve analysis of Sakamoto et al. (2016) shows signs of faint extended emission, ~0.038 counts $\mathrm{det}^{-1}\ \mathrm{s}^{-1}$ at T+10 s.

The *Swift* X-Ray Telescope (XRT, Burrows et al. 2005a) observed the GRB at five epochs starting from 83 s after the GRB. Data were initially acquired in Windowed Timing (WT) mode due to the brightness of the source, and later in Photon Counting (PC) mode. The XRT light curve shows an initial steep decay with a power law decay index of 2.0 ± 0.1, and possibly two small flares superimposed. The light curve continued with a flattening, starting from ~ 750 s followed by another decay. However, the XRT data collected in PC mode are too sparse to provide a deeper analysis of the lightcurve.

Observations from Konus-*Wind*, sensitive to higher energies in the 20 keV-10 MeV range, show a peak energy of $E_{\mathrm{peak,\ observed}} = 1416^{+528}_{-356}$ keV, a $T_{90} = 2$ s, and an isotropic energy release of $E_{\mathrm{iso,\ rest}} = 4.0 \times 10^{52}$ erg (Frederiks et al. 2016). However, Frederiks et al. (2016) used a different cosmology than the one adopted in this work so we re-calculated it (see Sect. 3.5.1 and Sect. 3.4). Given the energy released as observed by Konus-*Wind*, the initial pulse complex (Frederiks et al. 2016), the extended softer emission (Dichiara et al. 2021), and the negligible spectral lag (Sakamoto et al. 2016), this burst has been classified as a short GRB with extended emission (see Sect. 3.5.1 and Sect. 3.4 for further discussion on this issue).

3.2.2 X-shooter observations of GRB 160410A

The X-shooter spectrograph (Vernet et al. 2011) was automatically triggered after the *Swift* alert using the Rapid-Response Mode (RRM). Observations of the afterglow of GRB 160410A started at 05:18:08.00 UT, 8.4 minutes after the *Swift* trigger. The acquisition image showed the afterglow at $r' = 20.249 \pm 0.037$ mag (AB photometric system). The initial results of the analysis of the spectrum were reported by Selsing et al. (2016)[2]. The observations consisted of a total of 3 exposures of 600 s each in a dithering pattern ABB taken just before the twilight and before the telescope limit at 20° elevation was reached. The seeing was ~ 0.9" and transparency conditions were clear.

[2]We note that this spectrum was also presented as part of the X-shooter sample by Selsing et al. (2019).

Due to the high airmass (∼ 2.4) at which the observation was performed, the spectral trace changes its position on the slit as a function of wavelength, which we modelled in the spectral extraction. The spectra were reduced using the ESO/X-shooter pipeline v.2.6.8 (Modigliani et al. 2010) and Reflex (Freudling et al. 2013). The final spectrum has a spectral resolution in the UVB arm of 54 km s^{-1} and of 28 km s^{-1} in the VIS arm. No features were detected in the NIR arm. An initial sky-subtraction was performed on the unrectified image. The spectral response function was generated using observations of a spectrophotometric standard-star (Vernet et al. 2010; Hamuy et al. 1994) with an optimal extraction, as was also done for the science spectrum. We show the complete normalised spectrum in Fig. 3.1. The signal-to-noise (SNR) per resolution element varies between ∼5–15 in the UVB arm and between ∼7–10 for the VIS arm for the continuum in the regions where we detect absorption lines. In the NIR we find an average SNR of ∼1.2.

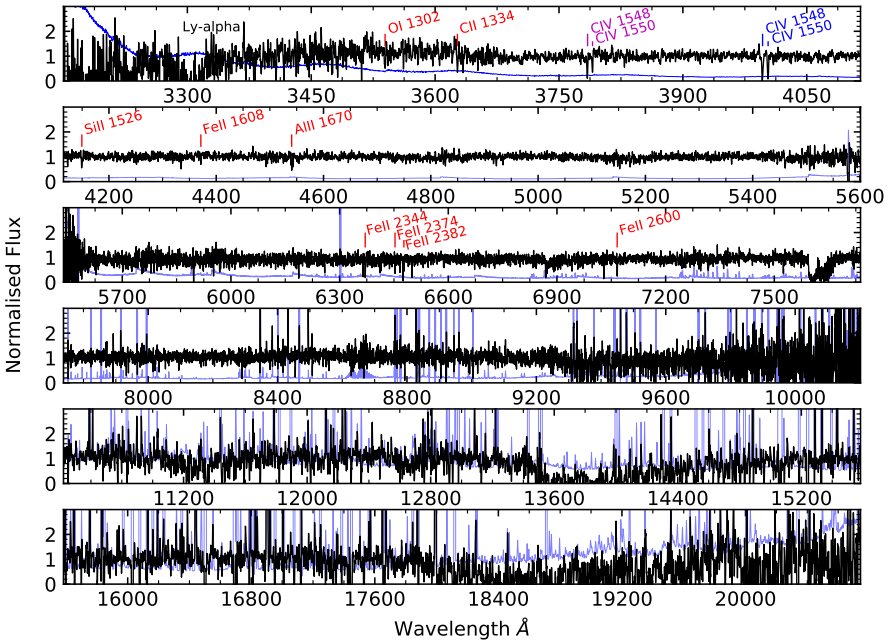

Figure 3.1: X-shooter spectrum (black) of the optical afterglow of GRB 160410A smoothed using a Gaussian kernel with 1σ for the first four panels and 2σ for the last two panels showing the NIR spectrum. The error spectrum is plotted in blue for the unbinned spectrum. Vertical lines denote the absorption lines: Red corresponds to absorption lines at the GRB redshift, blue is the intervening system at $z = 1.581$, and magenta the intervening system detected at $z = 1.444$. The error spectrum in the blue end is higher than the actual spectrum due to the absence of binning for the error spectrum.

3.2.3 Photometric Observations of GRB 160410A

For our analysis of the GRB we also obtained imaging of the optical and near-IR afterglow of GRB 160410A. In addition to the observations listed below, we used the acquisition image of the X-shooter observations (see Sect. 3.2.2) as well as literature data from Skynet PROMPT (Trotter et al.

2016) and a late detection by the 2.4 m GMG telescope (Wang et al. 2016). For our analysis, we do not use the afterglow limits reported by Muraki et al. (2016); Juvan et al. (2016); Cobb (2016); Rastinejad et al. (2021). Finally, we obtained late observations of the field in the optical with the 10.4 m Gran Telescopio de Canarias (GTC) and in infrared with the *Spitzer* space observatory to search for an underlying host galaxy (see Sects. 3.2.4, 3.2.4 and Fig. 3.2).

TAROT observations

The 0.25 m Télescope à Action Rapide pour les Objets Transitoires (TAROT) La Silla telescope observed the location of GRB 160410A very rapidly, beginning 28 s after trigger (16.8 s after notice). Observations (originally published in Klotz et al. 2016) were obtained in trailing mode (Klotz et al. 2006). The afterglow is detected as a very faint trail. The photometry method was based on the division of the afterglow flux by the flux of a reference star. To verify the validity of the method we chose another known star as a check. The magnitudes of the two stars ($r' = 13.517$ mag, $r' = 16.720$ mag, respectively) were taken from the Sloan Digital Sky Survey (SDSS) Data Release 12 (Alam et al. 2015). To evaluate the flux density uncertainties we computed the standard deviation of the background. The check star allowed us to validate the photometric method since the SDSS magnitude lies fully within the computed limits for each measurement. The TAROT best mean magnitude is 0.08 mag fainter than the SDSS value, however, the TAROT image is unfiltered, explaining this small colour effect.

The afterglow evolution shows a decay with a possible superposed flaring behaviour (see Sect. 3.3.4). We note that the columns on which the afterglow trail was located from 55 − 60 s are less sensitive than the surrounding ones and we can only claim an upper limit here. Furthermore, the afterglow magnitude fell below the detection limit by the end of the trailed observation.

UVOT observations

The *Swift*/UltraViolet Optical Telescope (UVOT, Roming et al. 2005) began observing the field of GRB 160410A 91 s after the *Swift*/BAT trigger. Observations were taken in both event and image modes. The afterglow is detected in all UVOT filters except for *uvw*2 and *uvm*2, as these lie blueward of Lyα at the redshift of GRB 160410A. Before extracting count rates from the event lists, the astrometry was refined following the methodology of Oates et al. (2009). The source counts were extracted initially using a source region of 5″ radius. When the count rate dropped to below 0.5 counts/s, we used a source region of 3″ radius. In order to be consistent with the UVOT calibration, these count rates were then corrected to 5″ using the curve of growth contained in the calibration files. Background counts were extracted using three circular regions of radius 10″ located in source-free regions. The count rates were obtained from the event and image lists using the *Swift* tools `uvotevtlc` and `uvotsource`, respectively. They were converted to magnitudes using the UVOT photometric zero points (Poole et al. 2008; Breeveld et al. 2011). To improve the signal-to-noise ratio, the count rates in each filter were binned using $\Delta t/t = 0.2$, leading to longer but deeper exposures at later times. The early event-mode *white* and *u* finding charts were bright enough to be split into multiple exposures.

GROND observations

We obtained multi-band photometric observations with the Gamma-Ray burst Optical and Near-infrared Detector (GROND) (Greiner et al. 2008; Greiner 2019) mounted on the 2.2 m MPG telescope at ESO La Silla observatory (originally published in Yates et al. 2016) in the $g'r'i'z'JHK$ bands. GROND observations began about half an hour after the GRB, at very high airmass (2.7). Only a single 4M4TD[3] observation Block (OB) could be obtained before the telescope hit a pointing limit. The effective integration time was somewhat reduced by the low quality of one of the dithering positions. However, the afterglow is still detected in $g'r'i'z'$. The following night, observations started at lower airmass but under adverse conditions. A total of 28 8M4TD OBs were obtained, but only OBs $1-21$ were usable. The afterglow had faded considerably, and was only detected in $g'r'i'$.

Afterglow magnitudes in the optical were calibrated against standard stars in the same field from the SDSS catalogue (Alam et al. 2015). Near-infrared magnitudes (all upper limits) were measured against comparison stars in the field taken from the 2MASS catalogue (Skrutskie et al. 2006). Reduction and analysis were performed within a custom pipeline calling upon IRAF tasks (Tody 1993), following the methods of Krühler et al. (2008); Yoldaș et al. (2008).

NOT observations

Observations were taken in the r' band with the Alhambra Faint Object Spectrograph and Camera (AlFOSC) at the 2.5 m Nordic Optical Telescope (NOT) at the Roque de la Muchachos Observatory on La Palma, Canary Islands, Spain (originally published by Malesani & Kirkpatrick 2016; Malesani et al. 2016, see Fig. 3.2). The afterglow was directly calibrated against four SDSS stars in the field. In the second epoch, forced aperture photometry on the afterglow position yields a tentative 3σ detection, which, however, is in agreement with the decay extrapolated from earlier times. We therefore include it as a detection.

3.2.4 Host observations of GRB 160410A

We performed deep photometric observations with a ground-based facility in search of an underlying galaxy hosting GRB 160410A. We also observed with the IRAC instrument on-board the *Spitzer* satellite.

GTC observations

We searched for a possible underlying host galaxy at the GRB position at late times in the r' band using OSIRIS at GTC. Data were taken on the night of the 24th of May 2016, comprising a total of ten images with an exposure time of 180 s each[4]. The observations were obtained at an airmass of ~ 1.4 and calibrations were performed using four SDSS field stars. We do not detect

[3]Denoting the integration time in the NIR is 4 min in total, and there are four optical images at four different dithering positions, therefore a 4M(inute)4T(elescope)D(ithers).

[4]Observations obtained under GTC programme GTC22-16A (PI: C.C. Thöne).

any source at the position of the afterglow down to a 3σ limit of 27.17 mag (AB, corrected for Galactic extinction) (see Fig. 3.2).

Spitzer observations

We obtained observations of the field of GRB 160410A with the Infrared Array Camera (IRAC) on-board the *Spitzer* Space Telescope on 2017 August 22 as part of the extended *Swift*/*Spitzer* GRB Host Galaxy Legacy Survey (SHOALS; Perley et al. 2016a). One hour of integration (36×100 s dithered images) was obtained in IRAC channel 1 ($3.6\,\mu$m). We downloaded the *Spitzer* Post-Basic Calibrated Data (PBCD) co-added images from the *Spitzer* Heritage Archive and used the methods of Perley et al. (2016b) to model and subtract nearby contaminating sources within a $20''$ box around the location of the GRB. There is no source visible consistent with the location of the optical afterglow in this image. We derive a 3σ limit on the magnitude within a $2''$ aperture centred on the GRB afterglow location of $m_{ch1} > 24.74$ mag (AB).

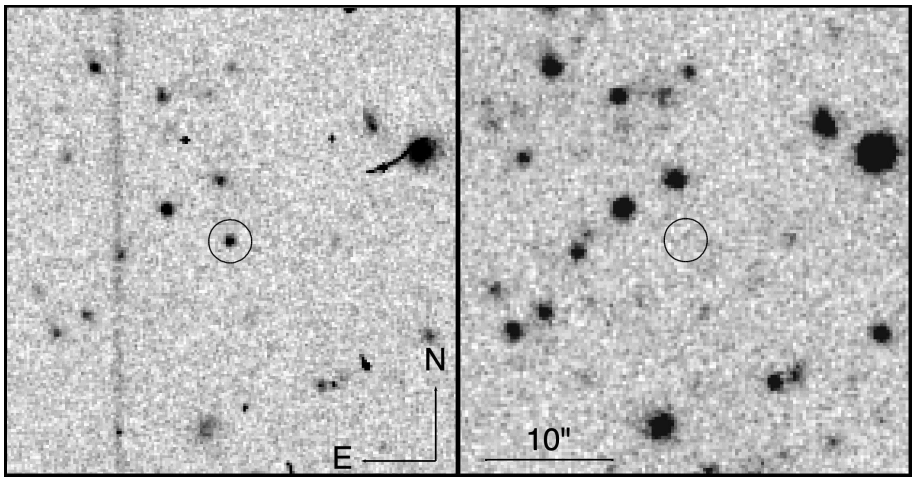

Figure 3.2: Optical observations of the field of GRB 160410A. *Left:* r'-band image obtained by NOT 0.7 days after the burst where the afterglow is clearly detected. *Right:* Deep late observation at 44.7 days in the same band by the 10.4 m GTC, where no source is detected down to a limit of $r' > 27.17$ mag (AB, corrected for Galactic extinction).

3.2.5 High-Energy detection of GRB 201221D

Swift/BAT detected the short GRB 201221D at 23:06:34 UT on 21 December 2020 (Page et al. 2020). The burst is located at RA = $11^{\rm h}\ 24^{\rm m}\ 14.09^{\rm s}$, Dec. = $+42^\circ\ 08'\ 40.0''$ (J2000) with an uncertainty of ~ 11. It had a duration of $T_{90} = 0.16 \pm 0.04$ s in the 15-350 keV band (Krimm et al. 2020) and a peak energy in observer frame of 98 ± 8 keV as seen in *Fermi*/GBM observations (Hamburg et al. 2020). GRB 201221D was observed by the Konus-*Wind* observatory showing a peak energy of $E_{\rm peak,\,observed} = 148^{+86}_{-37}$ keV (Frederiks et al. 2020), which implies that it was a clear short GRB.

3.2.6 GTC Spectroscopic observations of GRB 201221D

We observed the GRB afterglow using GTC/OSIRIS starting 2.76 hours after the trigger. The observations consisted of an acquisition image in r' band followed by long slit spectroscopy[5]. Four exposures of 1200 s were obtained covering the 3700 Å to 7800 Å spectral range, at an airmass ranging from 1.45 to 1.83.

The data were reduced using a self-developed pipeline based on IRAF routines. Data reduction included bias and response correction, and wavelength calibrations using HgAr and Ne lamps, which were also used to do a 2D distortion correction. Cosmic rays were removed using the `lacos_spec` routine (van Dokkum 2001). The flux calibration was performed using as reference the spectrophotometric standard star G191B2B (Oke 1990). The 1D spectrum was obtained through optimal extraction (Horne 1986).

This is the first afterglow spectrum of a short GRB showing evidence for absorption lines obtained since GRB 160410A and only the third spectrum of a short GRB afterglow to have them, which is why we include it in this paper for comparison. The spectrum shows emission and absorption features while the continuum is dominated by the host galaxy (see Sect. 3.4.1). Unfortunately the low signal-to-noise ratio of the spectrum of GRB 201221D limits the amount of information that can be extracted from these data.

3.2.7 Host observations of GRB 201221D

The Large Binocular Telescope (LBT) observed the underlying host galaxy of GRB 201221D at two epochs. A first observation was obtained on the 24$^{\text{th}}$ of December, 2020 when we observed in the near-infrarred J and K_s filters with the LBT Utility Camera in the Infrared (LUCI, Seifert et al. 2003) imager and spectrograph under good seeing with 10 on average, (first reported in Rossi & CIBO Collaboration 2021). The second observation was obtained the 10$^{\text{th}}$ of January, 2021 in the $g'r'i'z'$ bands with the Large Binocular Camera (LBC, Giallongo et al. 2008) under moderate seeing conditions (16 on average).

LBT data were reduced using the data reduction pipeline developed at INAF-Osservatorio Astronomico di Roma (Fontana et al. 2014) that includes bias subtraction and flat-fielding, bad pixel and cosmic ray masking, astrometric calibration and coaddition. For LUCI, it includes also dark subtraction and sky subtraction. The astrometry was calibrated against field stars in the GAIA DR2 catalogue (Gaia Collaboration et al. 2018) and has an astrometric precision of 015.

All data were analysed by performing aperture photometry using `DAOPHOT` and `APPHOT` under `PyRAF/IRAF`. We have carefully selected the size of the apertures to avoid faint sources close to the host, in particular a faint source 35 NW from the host. The photometric calibration was performed in the optical against the SDSS DR12 catalogue (Alam et al. 2015) and in the NIR against 2MASS stars.

[5]Observations obtained under GTC programme GTCMULTIPLE2G-20B (PI: de Ugarte Postigo).

3.3 Analysis and results

Our comprehensive analysis of the GRB 160410A afterglow comprises data from high energies to optical wavelengths. Unfortunately, no near-infrared data of sufficient quality are available. For GRB 201221D, the data coverage is significantly sparser than for GRB 160410A.

3.3.1 X-Ray analysis of GRB 160410A

We extracted the spectrum in WT mode, avoiding the small flares (i.e., in the 89−150 s time-frame) collecting ∼700 source counts. This is to avoid possible contamination from the flare emission on the spectral parameters. We fitted the X-ray data with a power-law model, with the Galactic absorption fixed to $N_{\rm H,\,Gal} = 1.8 \times 10^{20}$ cm^{-2} and a free intrinsic absorption at $z = 1.72$ of the host galaxy. We adopted C-statistics and data were binned to 1 count per energy bin in the 0.3 − 10 keV energy range. The best-fit power-law photon index is $\Gamma = 1.6 \pm 0.1$ ($1\,\sigma$ confidence level). The intrinsic absorption column density is $N_H(z) = 3.0^{+2.3}_{-1.9} \times 10^{21}$ cm^{-2}. The spectrum evolves to a softer value as the flux decreases ($\Gamma \sim 2$), but the lower number of counts prevented us to better constrain the photon index.

3.3.2 Spectral analysis

In the spectrum of GRB 160410A we detect several absorption features typically found in long GRB sight-lines (Christensen et al. 2011). The wavelength coverage of X-shooter allows the detection of Lyα absorption from a host galaxy DLA system at the blue end of the spectrum which, together with other metallic lines, is used to derive the metallicity of the host galaxy gas. We do not detect any fine-structure lines commonly associated with gas in the close GRB environment (Vreeswijk et al. 2007, 2011; D'Elia et al. 2009b,a). For FeII* λ 2612 we derive a rest frame limit of < 0.15Å a value 30% lower than what has been measured for this line in a GRB composite spectrum (Christensen et al. 2011). However, the absorption lines observed are very weak so the non-detection of fine-structure lines is consistent with their relative strength in the aforementioned composite spectrum.

The lines observed are only in the UVB and VIS arms, neither emission nor absorption features are observed in the NIR arm. Selsing et al. (2016) reported a first determination of the redshift of GRB 160410A, based on the detection of FeII and AlII absorption lines, resulting in a value of $z = 1.717$. In our analysis, we find additional features, not mentioned in the original GCN, of OI, CII and SiII at the same redshift. Contrary to the claim in Cao et al. (2016), we detect neither the CIV λ 1548, 1550 doublet in our spectrum, nor MgII λ 2976, 2803 doublet. The non-detection of high-ionisation lines, commonly seen in other GRB sight-lines (Christensen et al. 2011), point to a low ionisation environment. The MgII lines fall inside the telluric A-band and can therefore not be recovered in our spectrum. Emission lines would fall as well in the NIR and are not detected, which is not surprising given the high redshift, the non-detection of a host galaxy (see Sect. 3.3.3) and the fact that the emission lines fall in regions with strong telluric features or high noise levels.

In Tab. 3.1 we list the detected features and their corresponding equivalent widths (EW). Line

identifications and measurements were obtained using the tools in the GRBspec database (de Ugarte Postigo et al. 2014a; Blažek et al. 2020). The different absorption lines are centred at slightly different redshifts due to different velocity components (see Sect. 3.3.2) and we obtain a non-weighted mean value of $z = 1.7177 \pm 0.0001$, which matches the redshift of the strongest FeII component.

Absorption line fitting

Table 3.1: Observed absorption-line list for the spectrum of GRB 160410A. Top: lines at the redshift of the GRB. We include the 3σ limits derived for SiIV and CIV (see Sect. 3.3.2). Middle and bottom parts: CIV absorbers detected at $z = 1.581$ and $z = 1.444$ respectively. The first column shows the absorption line ID and its rest-frame wavelength. The second column lists the corresponding centroid for the redshifted absorption line. The third column is the measured EW in the rest frame, the fourth column is the total column density we derive using the `VoigtFit` fitting code (Krogager 2018) for each transition.

Feature	Observed wavelength (Å)	EW (Å)	log(N) (cm^{-2})
Lyα 1215.670	3304	–	21.20 ± 0.20
OI 1302.170	3539.4000	0.32 ± 0.08	> 15.04
CII 1334.530	3626.9869	0.26 ± 0.08	> 14.77
SiII 1526.710	4149.5107	0.33 ± 0.06	14.25 ± 0.11
AlII 1670.790	4540.6191	0.29 ± 0.07	13.13 ± 0.21
FeII 1608.450	4371.3224	0.17 ± 0.04	14.32 ± 0.09
FeII 2344.210	6370.6764	0.35 ± 0.08	...
FeII 2382.770	6475.4289	0.36 ± 0.06	...
FeII 2374.460	6452.9438	0.19 ± 0.06	> 14.22
FeII 2586.650	7029.2700	0.35 ± 0.04	...
FeII 2600.170	7066.1812	0.30 ± 0.05	...
SiIV 1393.760	–	< 0.36	> 13.60
SiIV 1402.770	–	< 0.39	> 13.93
CIV 1548.200	–	< 0.24	> 13.76
CIV 1550.770	–	< 0.24	> 14.06
CIV 1548.200	3996.2713	0.57 ± 0.06	> 14.82
CIV 1550.770	4002.9657	0.52 ± 0.06	...
CIV 1548.200	3784.1820	0.38 ± 0.07	> 14.91
CIV 1550.770	3790.4285	0.27 ± 0.07	...

We fitted Voigt profiles to the observed lines at the GRB redshift to obtain column densities, including the broad Lyα absorption. The spectrum was normalised and as systemic redshift we adopted the strongest velocity component of the FeII λ 2600 line as $v = 0\,\mathrm{km\,s^{-1}}$. For the line fitting we used the `VoigtFit` fitting code (Krogager 2018) that allows to define and tie parameters for each component such as the b-parameter, the column density or the redshift. We find that, for most of the detected transitions, the absorption can be fitted to two components while for AlII and up to three FeII lines we find only one component. For FeII λ 1608, 2344, 2382 and SiII the line profile is fitted well using two components and tying them for SiII to the ones of FeII. However, for OI and CII, the first component is fitted to a broader b-parameter. For FeII λ 2374, 2586, 2600 and AlII, only first component is well fitted. The non-detection of the second component for this FeII transitions might imply that we are underestimating the amount of FeII in this lines. This could be due to the low resolution of the spectrum or the low amount of FeII at this second component. We therefore adopt the measured column density for FeII λ 2374, 2586, 2600 lines as limits and choose the measures for FeII λ 1608, 2344, 2382 as values.

In Tab. 3.1 we present the total measured column density for each line. The OI and CII lines are likely saturated hence we consider them as lower limits, something which could also explain the different metallicity value obtained from these two lines. The fitting results are shown in Tab. 3.2. We plot the lines in velocity space in the normalised spectrum in Fig. 3.4, centered at the main component. The absorption lines show a small offset towards higher velocities in the absorption lines detected in the VIS arm compared to the UVB arm (see Fig. 3.4). A similar shift in wavelength has been reported in the past between the VIS and NIR arms of X-shooter and also suggested for the UVB arm as a problem related to the wavelength calibration (see e.g. Selsing et al. 2019; Gonneau et al. 2020).

In the spectrum of GRB 160410A, the broad Lyα absorption lies at the very blue end of the X-shooter wavelength coverage, where the continuum is rather noisy (see Fig. 3.3). However, we were able to determine the column density using `VoigtFit` and masking the blue wing from -1000 km s^{-1}. We obtain a total column density of $\log(N(\mathrm{HI})/\mathrm{cm}^2) = 21.2 \pm 0.2$, which is consistent with Selsing et al. (2019) and puts the system in the category of DLAs. The column density is also close to the median value that is found in long GRB spectra, i.e. $\log(N(\mathrm{HI})/\mathrm{cm}^2) = 21.59$ (Tanvir et al. 2019).

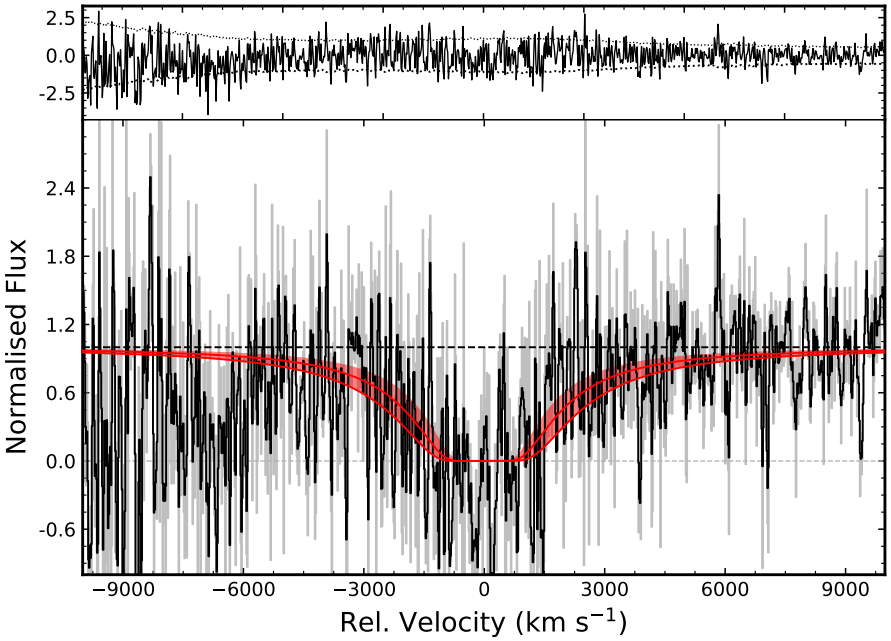

Figure 3.3: Voigt profile fitting of the Lyα absorption line. The top panel shows the residuals and the 1σ error spectrum (dotted line). In the bottom panel we plot the spectrum smoothed with a Gaussian kernel of 2σ in black and the original, non-smoothed, spectrum in grey. The red solid line represents the best-fit Voigt profile. For clarity, we show in shaded red the corresponding errors.

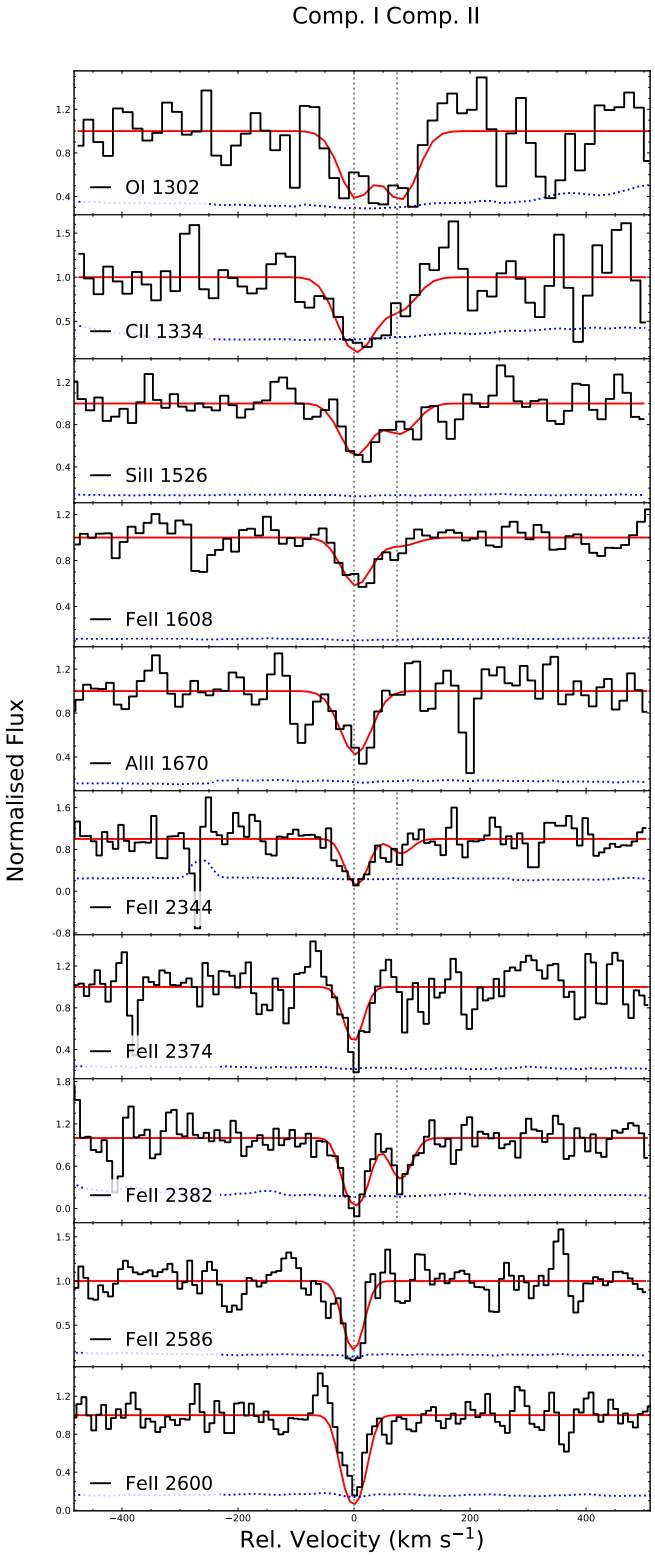

Figure 3.4: Absorption features detected in the GRB 160410A afterglow emission as observed in the X-shooter afterglow spectrum. Black lines correspond to the normalised spectrum in velocity space, centered at the redshift of the GRB. We also plot the error spectrum for each line (blue dotted line) and in vertical grey we mark the components listed in Tab. 3.2. The red solid line shows the Voigt best-fit profile for each absorption feature.

Table 3.2: Column densities derived fitting a Voigt profile to the different velocity components in the absorption system at the GRB redshift. We also show the corresponding derived metallicities. $v = 0$ km s^{-1} corresponds to the FeII line at 2600 Å as the line with the highest S/N. Solar metallicities are photospheric, meteoric, or the average value between the two, following Lodders et al. (2009).

Ions	Transitions (Å)	Component I			Component II			[X/H]
		v (km s^{-1})	b (km s^{-1})	log (N) (cm^{-2})	v (km s^{-1})	b (km s^{-1})	log (N) (cm^{-2})	
FeII	2374, 2586, 2600	0	15	> 14.21	–	–	–	> -2.44
AlII	1670	...	...	13.13 ± 0.21	–	–	–	-2.50 ± 0.30
FeII	1608, 2344, 2382	0	15	14.27 ± 0.10	74	18	13.31 ± 0.10	-2.34 ± 0.22
SiII	1526	...	...	14.10 ± 0.15	74	18	13.69 ± 0.16	-2.46 ± 0.23
OI	1302	0	22	> 14.53	74	18	> 14.84	> -2.85
CII	1334	...	...	> 14.65	...	...	> 14.03	> -2.86

Metallicity

GRB 160410A is currently the only SGRB event where we are able to study the metallicity along the sight-line in its host galaxy. The different ions of C, O, Si, Al and Fe give slightly different metallicities. The values for C and O can only be considered as lower limits since the absorption lines are likely saturated. The metallicity values derived from Si, Al and Fe are very similar and consistent within errors (see Tab. 3.2). All the metallicity values are very low, even compared to the uncorrected metallicities for dust-depletion for LGRB environments (see Fig. 3.6).

Dust depletion can affect the observed abundances when large fractions of refractory elements are locked into dust grains. We performed a dust depletion correction on our observed metallicities following the method developed by De Cia et al. (2013, 2016, 2018). In these studies, the correction was based on the [Zn/Fe] ratio but, since we did not detect Zn we used the observed SiII line to derive $[\mathrm{Zn/Fe}]_{\mathrm{exp}}$ using the following relation from De Cia et al. (2018) with their corresponding fitting parameters $A_{1,\mathrm{Si}}$ and $B_{1,\mathrm{Si}}$ as derived in De Cia et al. (2016).

$$[Zn/Fe]_{\mathrm{exp}} = \frac{[Si/Fe] - A_{1,\mathrm{Si}}}{B_{1,\mathrm{Si}} + 1}$$

We found a ratio of $[Si/Fe] = -0.08 \pm 0.15$ and, with $A_{1,\mathrm{Si}} = 0.26$ and $B_{1,\mathrm{Si}} = -0.51$, we got that $[Zn/Fe]_{\mathrm{exp}} = -0.69 \pm 0.32$ implying no depletion. However, De Cia et al. (2018, see their Appendix A) state that $A_{1,\mathrm{Si}}$ and $B_{1,\mathrm{Si}}$ might not be very well constrained.

We performed the same analysis including only the component at $v = 0\,\mathrm{km\,s^{-1}}$. Using values for this first component (see Tab. 3.2) we got $[Si/Fe] = -0.18 \pm 0.18$, resulting in $[Zn/Fe]_{\mathrm{exp}} = -0.90 \pm 0.40$. Furthermore, we derived δ_X, a parameter that indicates how much an observed element is depleted by dust (De Cia et al. 2016), for both, the total absorption and only for the component defined at $v = 0\,\mathrm{km\,s^{-1}}$. In Fig. 3.5 we plot the dust depletion pattern compared to the sequence expected for different amounts of depletion derived in De Cia et al. (2016). In both cases, the values that we obtain would formally result in negative depletion and hence nonphysical values. This indicates that there is no depletion in the system and, therefore, we adopt zero values for the depletion, as shown in Fig. 3.5.

Our analysis results in a very low value of $[Fe/\mathrm{H}] = -2.3 \pm 0.2$ for the metallicity along the sight-line. To put the value into the context of cosmic chemical evolution, we compared our results with those shown by De Cia et al. (2018), which are corrected for dust depletion following the single-reference method (see Fig. 3.6). The metallicities in the QSO-DLA sample have been determined using the FeII absorption and are dust-corrected (De Cia et al. 2018). We note that De Cia et al. (2018) relax the DLA condition to a slightly lower column density ($\log(N(\mathrm{HI})/\mathrm{cm}^2) \geq 20.0$, De Cia et al. 2016, 2018) than the common definition of a DLA system ($\log(N(\mathrm{HI})/\mathrm{cm}^2) \geq 20.3$, Wolfe et al. 2005), however, the number of QSOs outside the strict DLA definition is small. In addition, we include DLAs in long GRB hosts from the literature, not corrected for dust-depletion as QSO-DLA and GRB 160410A are and, therefore, not formally comparable. We clearly see the existence of an observational bias on redshift that results from the realistic spectral coverage when obtaining GRB spectroscopy[6]. We note a small tendency of long GRB-DLAs towards

[6] As GRB afterglows fade within hours or days, spectroscopy is generally obtained with ground-based facilities, and

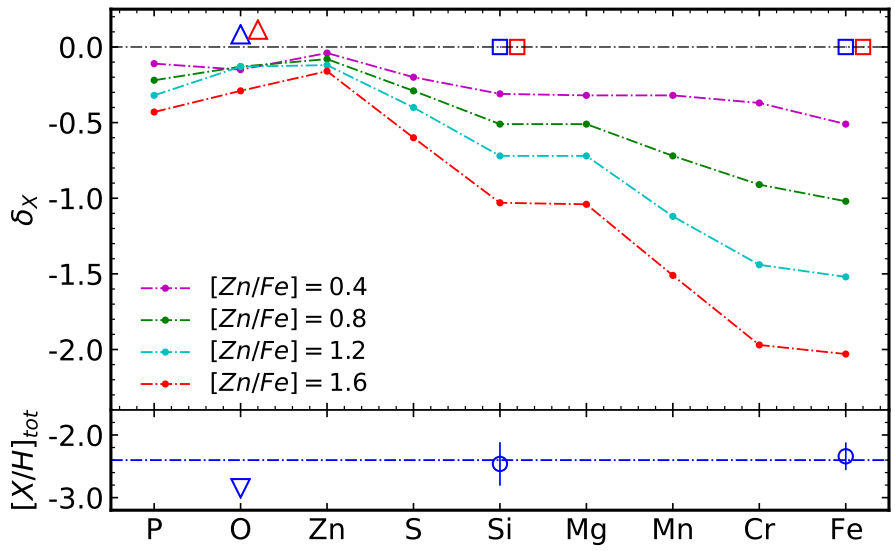

Figure 3.5: Dust depletion pattern and metallicity for the measured column densities of the features found in absorption in the afterglow of GRB 160410A. *Top panel:* Dust depletion sequence for GRB 160410A. Squares (top panel) and circles (bottom panel) denote the Si and Fe lines meanwhile triangles refer to the limits we derive for the saturated O line. With an small offset for visualization purposes. Red squares denote the depletion δ_X values obtained for the common velocity component to all the elements observed, blue squares are the depletion considering the total column density measured. For comparison, we plot with a dash-dotted line in different colours the dust depletion sequence obtained from the fitting of QSO-DLA absorption systems in De Cia et al. (2016). *Bottom panel:* Corresponding metallicity for the observed ions considering all the velocity components. The mean metallicity is shown with a dashed-dotted line.

higher metallicities (see e.g. Fynbo et al. 2008; Prochaska et al. 2007), which is consistent with LGRBs tracing more enriched gas than QSO-DLAs as an effect of tracing gas in star-forming regions. However, since LGRB-DLA metallicities are not dust-depletion corrected, the differences between both samples might be somewhat larger. From the QSO-DLA sample, we clearly see that GRB 160410A shows one of the lowest metallicity values for a DLA, together with a few QSO-DLAs.

Line strength and host ionisation

de Ugarte Postigo et al. (2012) established a new parameter to compare the ISM of different GRBs by determining the relative ratio between the EWs of different lines with the average EW of (long) GRBs. We apply this method to the spectrum of GRB 160410A using the EW measurements listed

the atmospheric ultraviolet cutoff implies that Lyα is only measurable at $z \gtrsim 1.5$ (Updike et al. 2008). Detection of Lyα enabling lower redshift metallicity determinations would need an UV-capable space-based spectrograph such as HST/COS or *Swift*/UVOT grism spectroscopy, with the latter needing an extremely bright afterglow such as in the case of GRB 191221B (Kuin & Swift/UVOT Team 2019).

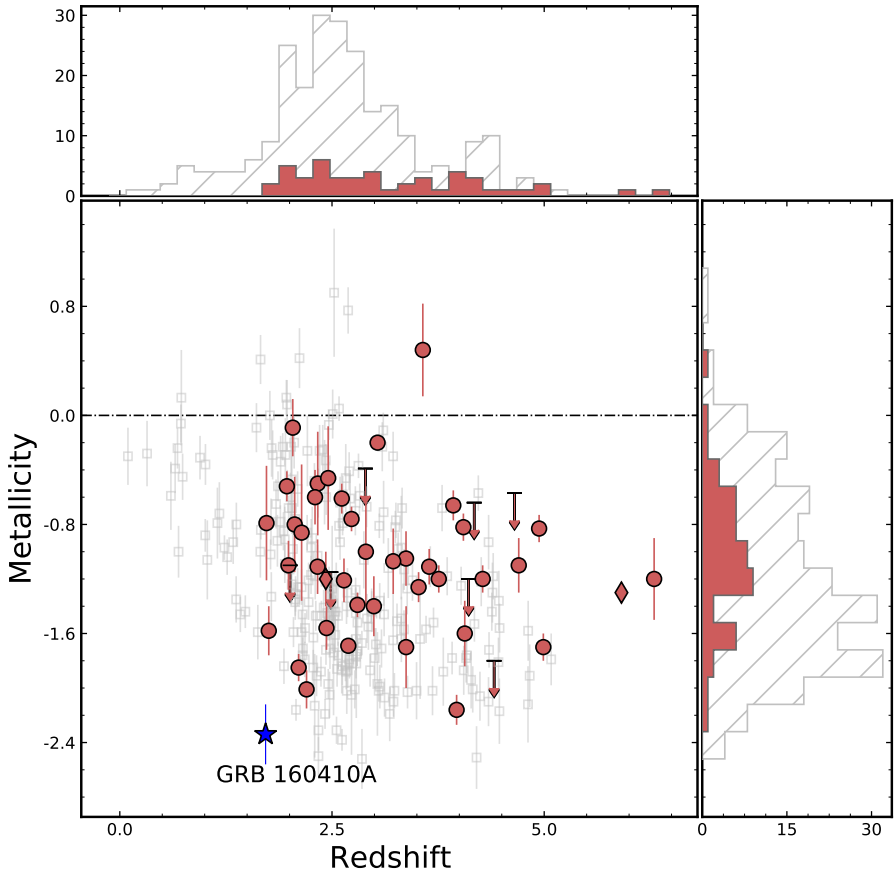

Figure 3.6: Metallicity of GRB host galaxies and QSO-DLAs vs. redshift. *Middle panel:* Clear grey empty squares mark QSO-DLAs from the sample published in De Cia et al. (2018). Red filled circles show the metallicities for long GRB-DLAs and a red filled diamond marks sub-DLA systems. Most of the data are from Thöne et al. (2013). We note that these values are not dust-corrected. We add some more recent metallicity values from the literature (de Ugarte Postigo et al. 2018; Krühler et al. 2013; Friis et al. 2015; Heintz et al. 2018b, and J. Greiner, priv. comm.). The values from de Ugarte Postigo et al. (2018) and Heintz et al. (2018b) are dust-corrected following De Cia et al. (2016). The value from Friis et al. (2015) is dust-corrected following De Cia et al. (2013). We also show the distribution of metallicities on the right and the distribution in redshift on the top. Hatched histograms show QSO-DLAs, red filled values show the long GRB-DLA sample. While QSO-DLA metallicities are based only on Fe and dust-corrected, the GRB-DLA metallicities are based on several elements such as Sulfur, Silicon, Zinc, Iron and Oxygen and are, generally, not dust-corrected. As GRB 160410A is a completely new class in itself, we do not show it in the histograms.

in Tab. 3.1. We see that all EWs measured for GRB 160410A are lower than these of the long GRB sample by more than 1σ. This, together with the large column density measured for the neutral hydrogen, are indicative of low metallicity, which is consistent with the values we derive in sec. 3.3.2. We obtain a value for the Line Strength Parameter of LSP $= -1.92 \pm 1.07$, implying that

the features detected in GRB 160410A are only 0.7% as strong (or 99.3% weaker) as the average strength of long GRB absorption lines.

Fig. 3.7 shows how all the spectral features that we measured are well below the lower 1-σ region for the EW of the sample. This difference is even stronger in the case of high-ionisation features. The CIV and SiIV limits that we derive are further away from the lower 1-σ EWs of the sample than the CII and SiII lines. This is indicative of a low ionisation.

The low ionisation is clearly seen in Fig. 3.8, where we plot the line ratios CIV/CII and SiIV/SiII of our sight-line, as compared to the sample of de Ugarte Postigo et al. (2012). In the case of GRB 160410A, we use the 3-σ limits to the detection of CIV and SiIV. GRB 160410A is located in the lower left area of the diagram, just outside the 1-σ region of the sample, amongst the lowest ionisation sight-lines of the sample. The moderate S/N of our spectrum prevents us from showing stronger limits to the high-ionisation lines.

Intervening systems

In the afterglow spectrum we detect two further systems in the line-of-sight as already mentioned by Selsing et al. (2019), at redshifts $z = 1.581$ and $z = 1.444$. Both show the CIV $\lambda\lambda$ 1548, 1550 doublet, but no other features were detected due to the low S/N of the spectrum. We perform a Voigt fitting to both CIV absorbers by defining a broad component at $v = 0\,\mathrm{km\,s^{-1}}$ with a b-parameter of $b = 40\,\mathrm{km\,s^{-1}}$ for the doublet. The fitting results are plotted in Fig. 3.9, resulting in a total column density of $\log(N/\mathrm{cm}^2) > 14.82$ for the system at $z = 1.581$ and $\log(N/\mathrm{cm}^2) > 14.91$ for the one at $z = 1.444$. Both values can only be considered as an upper limit since the feature is clearly saturated in both cases. We tentatively detect two possible absorption features at the corresponding wavelength for CIV at $z = 1.663$, however, we cannot securely confirm these lines.

3.3.3 A hostless burst?

We do not find any source at the GRB 160410A position in our late GTC/OSIRIS image (right panel of Fig. 3.2, Fong et al. 2022 also do not detect the host in other filters to shallower limits). We obtain a limiting magnitude of $r' > 27.17$ mag (AB, corrected for Galactic extinction), which corresponds to an absolute magnitude limit of $M_{r'} > -18.44$ mag. None of the nearby sources in the field are likely to be the possible host of GRB 160410A. The closest object is at a projected distance of $r \sim 4.9$" from the GRB position which translates to a distance[7] of ~ 42 kiloparsecs. The host galaxy is also not detected at 3.6 μm in our deep *Spitzer*/IRAC observations. Following the methods of Perley et al. (2016a,b), combined with the significantly deeper optical upper limit, this yields an upper limit on the stellar mass of $M_* \lesssim 1.14 \times 10^9\ \mathrm{M}_\odot$.

Given our upper limit on the host stellar mass we compare our results to the mass-metallicity relation (MZR) following the equations presented in Ma et al. (2016). The low Fe-based (see Sect. 3.3.2) metallicity value would imply a stellar mass of $\log(M_*/M_\odot) = 6.18 \pm 0.52$. This value indicates a low stellar mass for the host galaxy of GRB 160401A. This together with the deep

[7]We made use of the `astropy` packages `SkyCoord` and `Cosmology`.

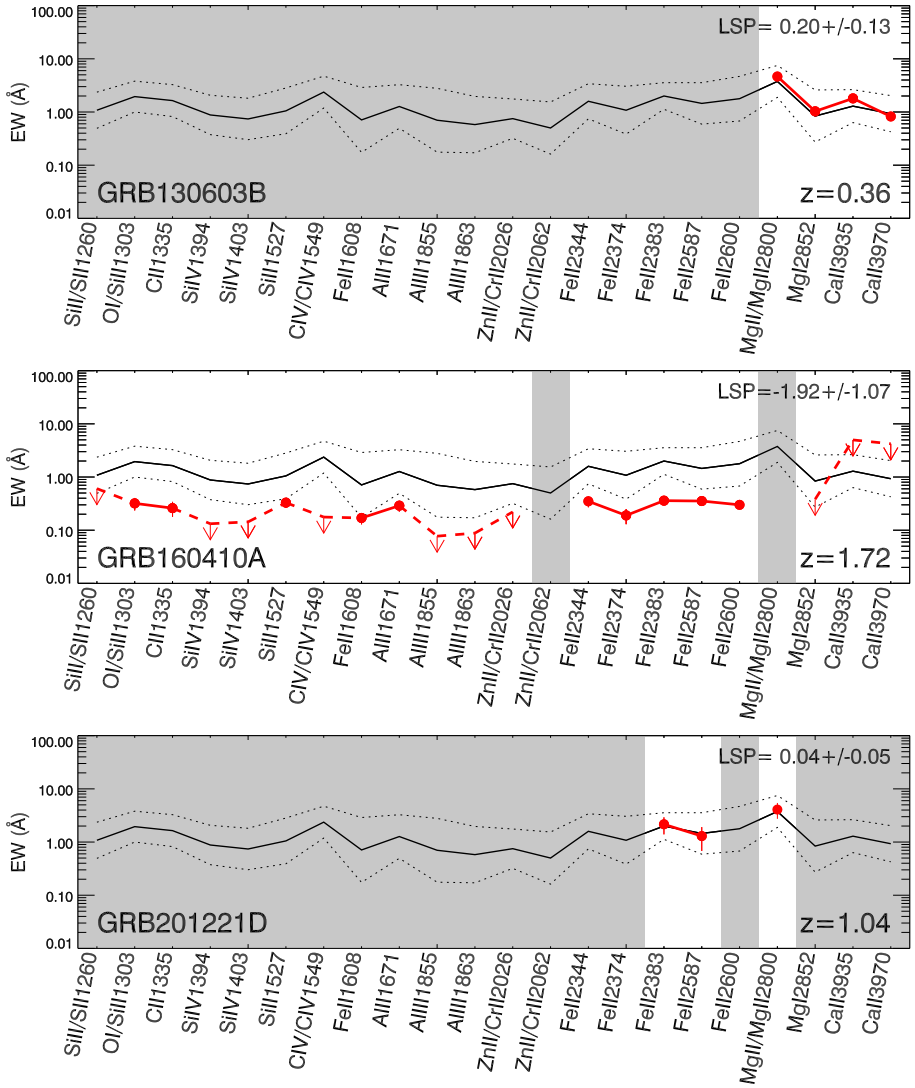

Figure 3.7: Equivalent width diagrams for the GRB 130603B (de Ugarte Postigo et al. 2014b), GRB 160410A and GRB 201221D afterglow spectra and GRB 201221D spectrum following the process described in de Ugarte Postigo et al. (2012). Red dots denote the corresponding EW for the absorption lines detected, whereas the red triangles show an inferred upper limit. The black solid line marks the average of the sample used in de Ugarte Postigo et al. (2012) and the upper and lower dotted lines show the standard deviation. Grey areas represent no detection of the corresponding spectral features is possible.

limits in r-band and 3.6 μm (see Sect. 3.2.4) is telling us that the host galaxy for GRB 160410A must be very faint

We compare our host galaxy limit to other, securely associated, long and short GRB hosts from the literature. For short GRBs, we use the sample from Leibler & Berger (2010) and O'Connor et al. (2022), for long GRB hosts we use the SHOALS sample (Perley et al. 2016a, D. A. Perley, S. Schulze, priv. comm.). We selected only those GRB hosts with detections or upper limits in the

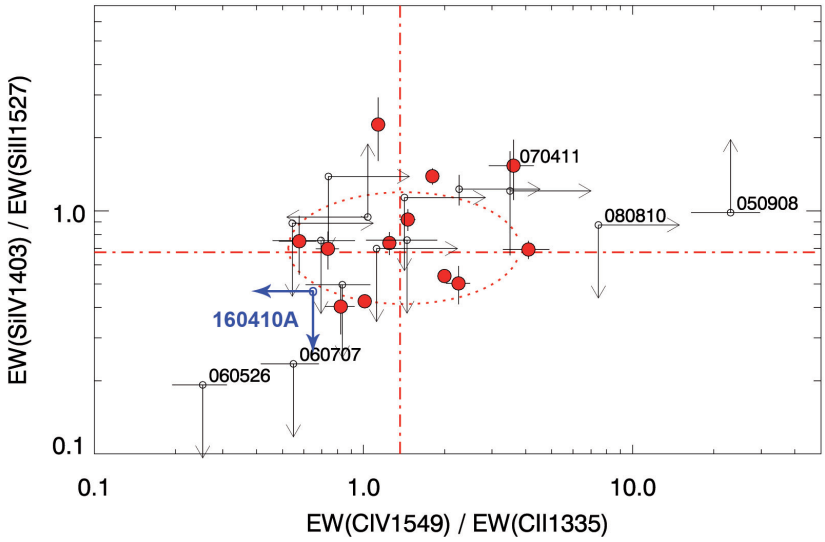

Figure 3.8: High-/low-ionisation C and Si line EW ratio comparison for GRB 160410A (*in blue*) compared with the sample of and using the method presented in de Ugarte Postigo et al. (2012). The red filled dots mark the ratio for detections in the afterglow spectroscopy of long GRBs, empty dots with arrows show upper limits in one or both ratios. The red dash-dotted lines represent the average values of the sample, the ellipse marks the 1σ region.

r' and R_C bands. In Fig. 3.10 we see that, for short GRBs, the associated hosts have a broad distribution in brightness. Note, however, that only three SGRBs have a spectroscopically confirmed redshift from absorption lines in their GRB afterglow, whereas the rest get their redshifts from the associated host galaxies. At the same time, SGRBs at redshifts beyond $z \sim 1$ are very sparse, hence we have to be aware of possible biases here, as had been found for LGRB hosts before the presentation of unbiased samples (see e.g. Perley et al. 2016a,b). However, we can conclude that any host of GRB 160410A would be at the faint end of the distribution, even compared to long GRB hosts.

The photometric observations alone, without spectroscopic confirmation of the redshift, could have led us to think that GRB 160410A belonged to the class of hostless SGRBs. However, the presence of a DLA as well as the metallic absorption features are indicative of the burst being hosted by a galaxy.

3.3.4 GRB 160410A afterglow light curve and its spectral energy distribution.

The light curve of the optical afterglow is described by a smoothly double-broken power-law, which yields a steep/shallow/steep decay with decay indices $\alpha_{\rm steep}$, $\alpha_{\rm plateau}$, and $\alpha_{\rm late}$, respectively, as well as two break times $t_{b,1}$, $t_{b,2}$. We find $\alpha_{\rm steep} = 1.11 \pm 0.17$, $\alpha_{\rm plateau} = 0.19 \pm 0.04$, $t_{\rm b,1} = 0.0052 \pm 0.0030$ d (446 ± 256 s); and $\alpha_{\rm late} = 1.86 \pm 0.18$, $t_{\rm b,2} = 0.162 \pm 0.030$ d. The break sharpness was fixed to sharp values ($n = -10, 10$ respectively), and the host galaxy was neglected,

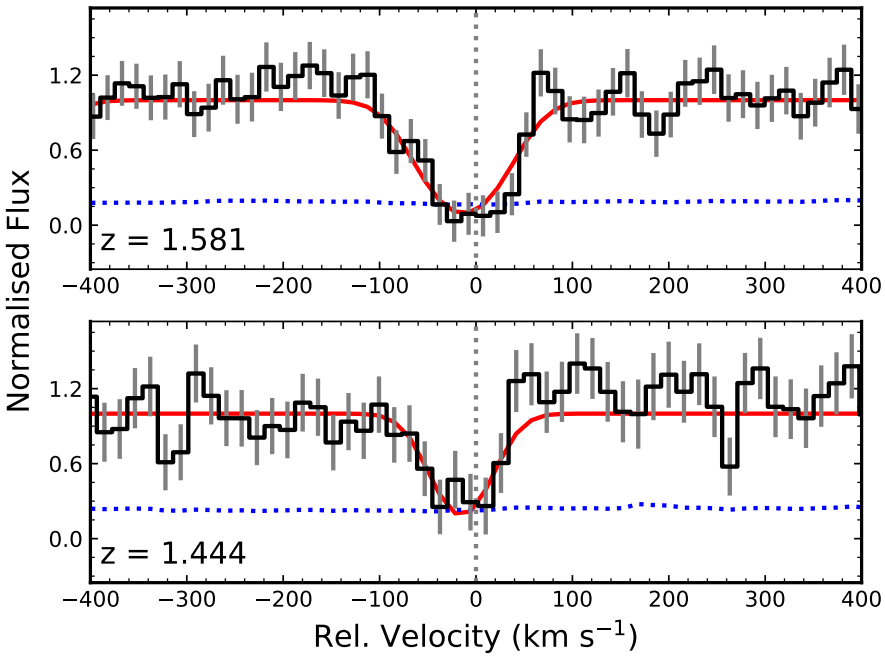

Figure 3.9: Absorption features detected along the line-of-sight towards GRB 160410A for the two intervening systems. *Top:* CIV ($\lambda\lambda$ 1550Å) line at $z = 1.581$. *Bottom:* Absorption line corresponding to CIV ($\lambda\lambda$ 1550Å) at $z = 1.444$. See the caption of Fig. 3.4 concerning the colour coding. The vertical dotted grey line is the fitted broad component at $v = 0\,\mathrm{km\,s^{-1}}$. We see that the minimum of the Voigt best-fit profile, in both cases, is clearly shifted to the left due to the lines being saturated.

as we find no evidence for any host down to very deep limits (Sect. 3.3.3). We show the optical afterglow of GRB 160410A in Fig. 3.11, including the best-fit triple power-law.

We use the fit to construct the Spectral Energy Distribution (SED), which stretches from *uvw*1 to z'. We fit the SED with both a simple power-law (no dust) and dust models for Milky Way (MW), Large (LMC), and Small Magellanic Cloud (SMC) dust (Pei 1992). Therefore, we exclude the *uvw*1 and *u* bands as these lie blueward and within Lyα respectively. The SED and the fits are shown in Fig. 3.12.

For no extinction, we find $\beta = 0.46 \pm 0.25$, and a fit with χ^2/d.o.f. $= 0.19$. For the three dust models, we find: MW dust: $\beta = 0.30 \pm 0.35$, $A_V = 0.14 \pm 0.22$ mag; LMC dust: $\beta = -0.18 \pm 1.21$, $A_V = 0.34 \pm 0.63$ mag; and SMC dust: $\beta = 2.55 \pm 2.81$, $A_V = -0.74 \pm 0.99$ mag. All these fits are show over-fitting (χ^2/d.o.f. from 0.06 to 0.16). However, the SMC fit is clearly unphysical (yielding negative extinction, i.e. emissive dust), and the negative intrinsic spectral slope for LMC dust is also not expected for GRB afterglows. Only the MW fit yields a sensible result, however, dust extinction is 0 within errors, so we find no evidence for dust and hence continue to work with the no-extinction fit. The no-extinction model is also the one showing the least overfitting.

To compare this high-redshift SGRB afterglow with other SGRBs, we take SGRBs with redshifts and well-detected afterglows (as well as the deep upper limits of GRB 050509B) from the

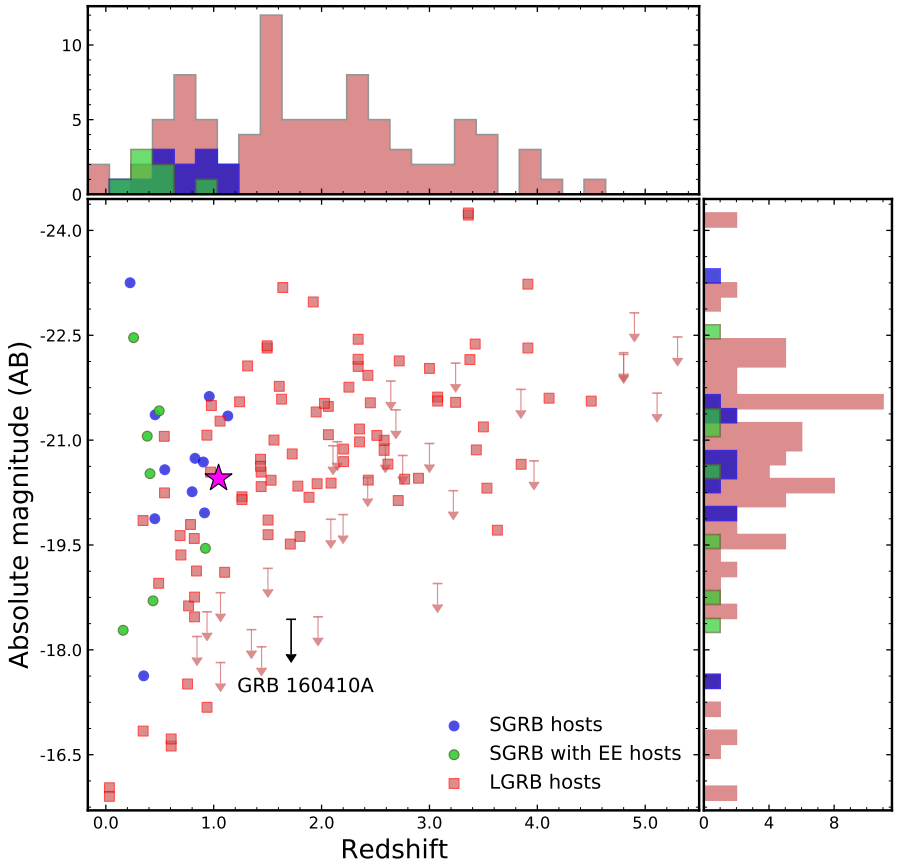

Figure 3.10: Long GRB host magnitudes in the r' and R_C bands from the SHOALS sample (D. A. Perley, S. Schulze, priv. comm.). For SGRB hosts, we take r' and R magnitudes from Leibler & Berger (2010) and O'Connor et al. (2022) when available. The sample is the same one utilized in the "Amati" relation (see Sect. 3.5.1). Note that we are using a fixed (observer-frame) band-pass filter despite a wide redshift distribution, hence the actual rest-frame band would be blue-shifted by $(1 + z)$. For clarity, we plot r' and R_C with the same colour. On top and left-most we show the distribution in redshift and absolute magnitude, respectively, for each sample. In blue, we show the SGRB hosts, in clear green the SGRB with EE hosts and in clear red, the distribution for long GRB hosts. The GRB 160410A upper limit is plotted with a black arrow and GRB 201221D, with a magenta star. All the absolute magnitudes are corrected for Galactic extinction (Schlafly & Finkbeiner 2011).

sample of Kann et al. (2011) (there called "Type I GRBs"), and provide additional analysis for four further SGRBs (one with an unsure classification) in section A.1. We show the observed (corrected for Galactic foreground extinction and, if needed, host-galaxy contribution) light curves in the section, in Fig. A.1.

GRB 160410A lies at a higher redshift than any of these events except for GRB 181123B, which lies at a slightly higher redshift. Knowing the redshift and SED, we use the method of Kann et al. (2006) to shift all afterglows to a common redshift of $z = 1$, corrected for dust extinction (see

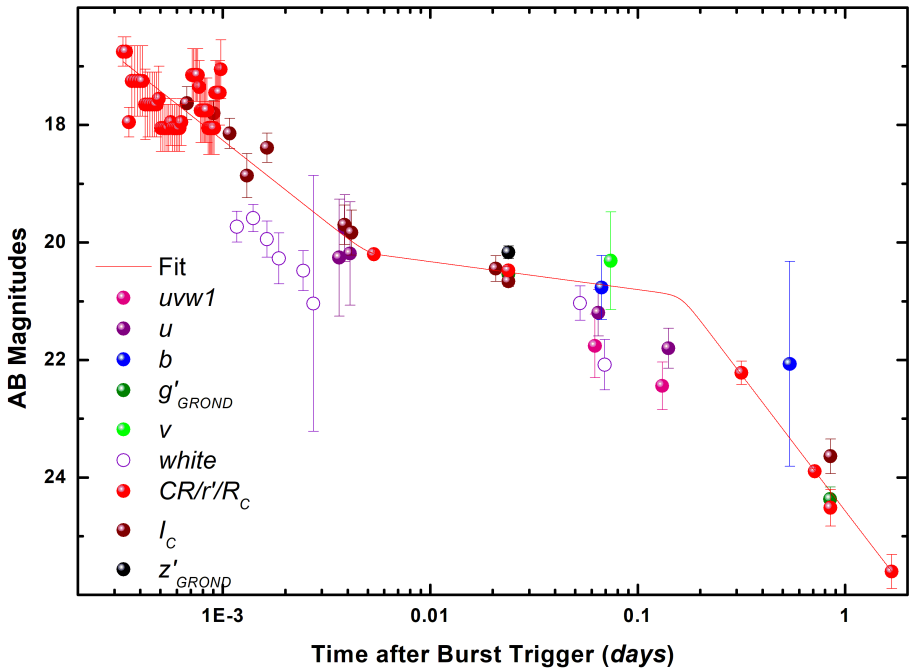

Figure 3.11: Light curve of the GRB 160410A afterglow. For reasons of clarity, upper limits are omitted. Early I_C data are from Trotter et al. (2016), the R_C data point at 0.31 d is from Wang et al. (2016), the rest from this work. Data are in the AB magnitude system and corrected for Galactic foreground extinction. The red line show the modelled light curve for the $CR/r'/R_C$-band. A clear steep-shallow-steep transition is visible.

Fig. 3.13). The afterglow of GRB 180418A is the brightest SGRB afterglow at very early times, but not far above that of GRB 160410A. During the plateau phase, the afterglow of GRB 160410A has a similar luminosity as that of the extremely intense GRB 090510. At later times, the very extended plateau of the GRB 150424A afterglow makes it brighter than GRB 160410A at the same time. Due to their (relatively) high redshifts and brightness at early times the nature of GRBs 160410A and 180418A have been heavily discussed (see also Sect. 4.5). However, at 12 h post burst, both afterglows still lie among the faintest LGRB afterglows, which is further evidence that these are likely true SGRBs.

3.4 Further analysis of the short/long nature of GRB 160410A

Further to the analysis of the Amati relation and the hardness ratio presented below in Sect. 3.5.1, we here detail an extended study of the short/long GRB nature of GRB 160410A.

Zhang et al. (2009) introduced the "Type I" and "Type II" classification scheme, independent of the classic T_{90} division, which was originally motivated by the temporally long, peculiar GRB 060614 (Gehrels et al. 2006; Zhang 2006). Type II GRBs are those associated with the core-collapse of massive stars (so usually long and soft), whereas Type I GRBs are those that are not - usually short and hard GRBs, which are at least in part associated with the merger of compact

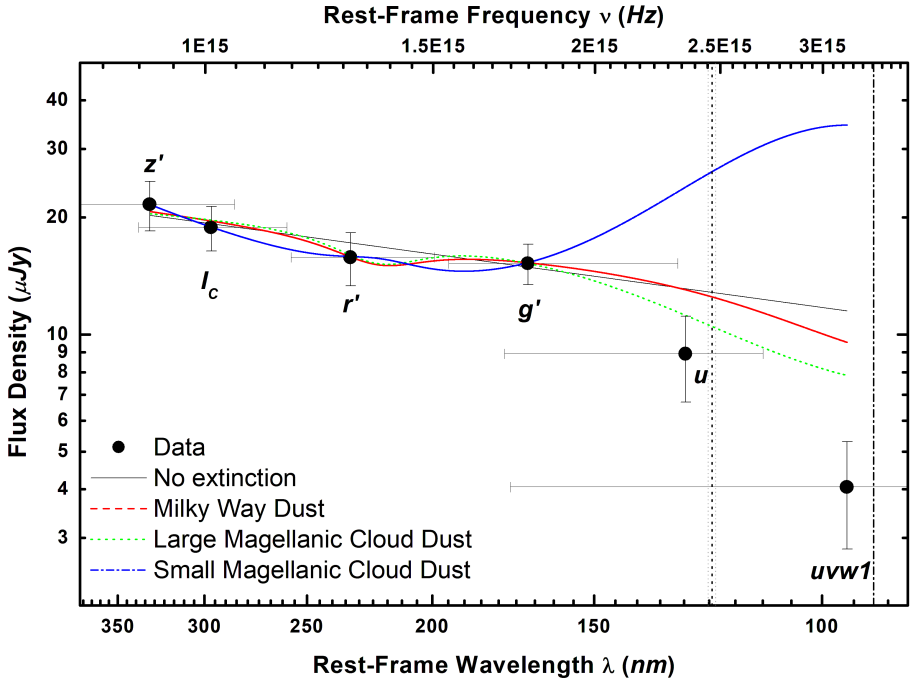

Figure 3.12: Spectral Energy Distribution of the afterglow of GRB 160410A. Flux densities are determined at break time, 0.162 d. Horizontal error bars represent filter widths, these errors were not included in the fits. We show fits with no extinction (straight black line), Milky-Way dust (red dashed line), Large-Magellanic-Cloud dust (green dotted line), and Small-Magellanic-Cloud dust (blue dash-dotted line). The SMC fit is clearly unphysical, and the results of the LMC fit also show it is not realistic, see Sect. 3.3.4. The MW is possible, but a fit with no extinction is the preferred model. The *u* and *uvw*1 data points were excluded from the fit as they are affected by Lyα and Lyman forest/limit absorption. The Lyα wavelength at the redshift of the GRB is marked by a vertical dotted line, with the adjacent dotted gray lines marking the FWHM of the Lyα line. A dash-dotted vertical line marks the Lyman cutoff.

objects, specifically inspiralling binary neutron stars (e.g. Abbott et al. 2017a,b).

We follow figure 8 of Zhang et al. (2009) to derive a classification for GRB 160410A in the Type I/II scheme . The GRB has (as measured by *Swift*) a $T_{90} > 2$ s, and also a $T_{90}/(1+z) > 2$s. However, it shows a short "Initial Pulse Complex" followed by an "Extended Emission" bump, which is an often-seen feature of Type I GRBs (Norris & Bonnell 2006). In Fig. 3.14 we show the *Swift*/BAT light curve obtained by the analysis of the *Swift*/BAT Gamma-Ray Burst Catalogue[8].

There is no information on any supernova (SN) contribution as the redshift is too high, nor are we aware of any late-time follow-up. Similarly, there is little information on the host galaxy as it is not detected even in our very deep late-time follow-up. Further decisions in the decision tree also cannot be answered with certainty, until the last step.

The bolometric isotropic energy release for this GRB is $\log E_\gamma/\mathrm{erg} = 53.1$, certainly not a low value, strictly leading to an "unknown" classification. However, we note the extremely energetic

[8]http://swift.gsfc.nasa.gov/results/batgrbcat

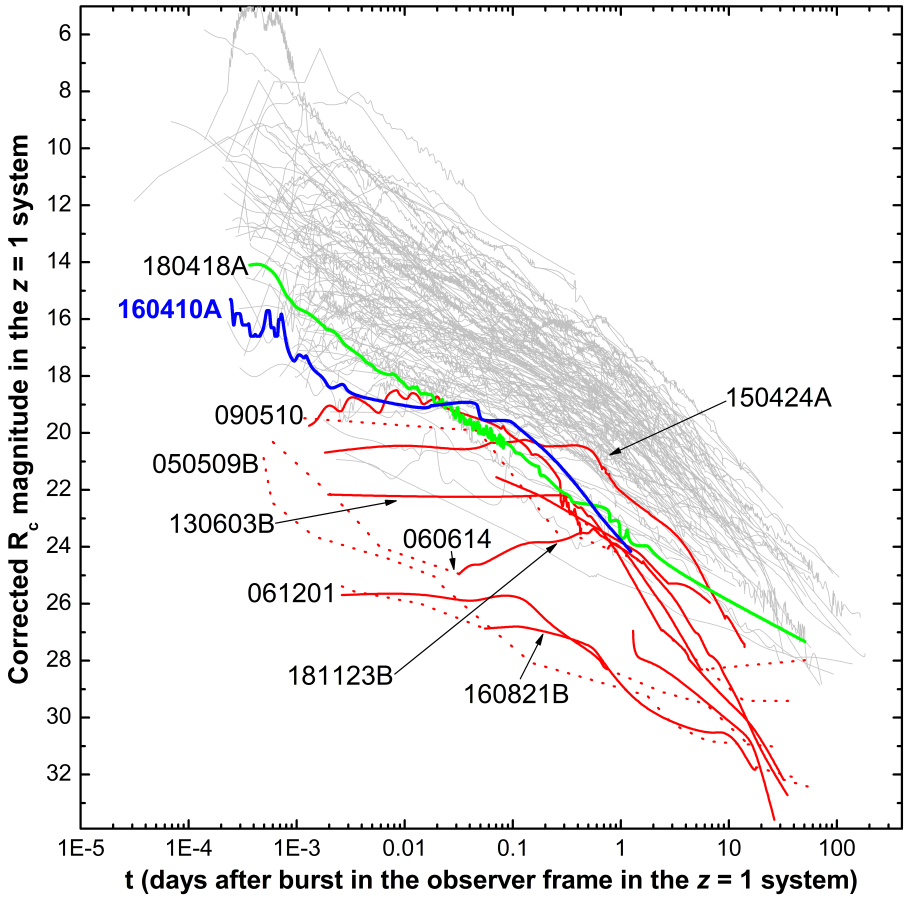

Figure 3.13: Afterglow of GRB 160410A (thick blue line) in the context of a large sample of GRB afterglows. Thin grey lines are afterglows of long GRBs. Thicker red lines are a selection of afterglows of other SGRBs. GRB 180418A (green line) has an insecure classification. The afterglows are given in the $z = 1$ system, see text for more details.

GRB 090510 which has a similar isotropic energy release[9] is also categorised as a short GRB (Ackermann et al. 2010; Kann et al. 2011). Therefore, using this scheme, we classify GRB 160410A as a Type I candidate.

Lü et al. (2010) devise a new parameter $\epsilon(\kappa) \equiv E_{\gamma,\mathrm{iso},52}/E^{\kappa}_{p,z,2}$ with $E_{\gamma,\mathrm{iso},52}$ being the bolometric isotropic energy release in units of 10^{52} erg, and $E^{\kappa}_{p,z,2}$ being the intrinsic peak energy in units of 10^2 keV. They find $\kappa = 5/3$ in their study. A study of GRBs with known parameters reveals four regions separated by low/high $T_{90,z}$ and low/high κ, the delineations being $\epsilon = 0.03$ ($\log \epsilon = -1.52$) and $T_{90,z} = 5$s ($\log T_{90,z} = 0.26$). For the parameters given by Konus-*Wind* (Tsvetkova et al. 2017) we derive $E_{p,z} = 3853^{+1429}_{-973}$ keV and $E_{\gamma,\mathrm{iso},52} = 13.21^{+0.50}_{-0.68}$. It is $T_{90,z} = 3.02 \pm 0.59$ s for *Swift* (with extended emission) and $T_{90,z} = 0.58 \pm 0.045$ s for Konus-*Wind* (only the initial pulse complex is detected). Using these values, we derive $\log \epsilon = -1.71$, which places it into the sector of Type

[9] Tsutsui et al. (2013) argue the bolometric energy release for GRB 090510 should be measured in the 1 keV − 100 MeV energy frame, resulting from the extremely high peak energy. In this frame, $E_{\mathrm{iso,bol}}$ is five times higher than in the usual frame and exceeds that of GRB 160410A.

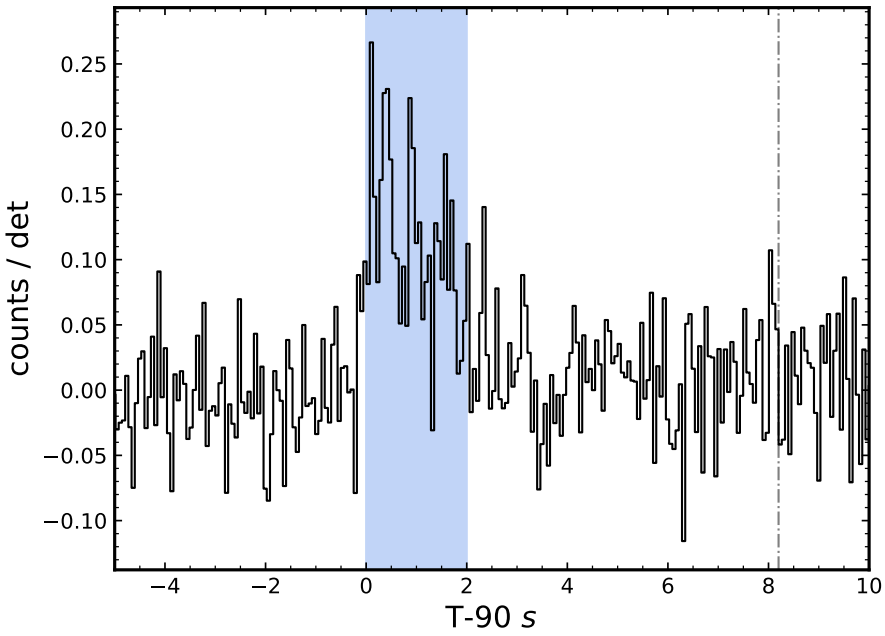

Figure 3.14: BAT mask-weighted lightcurve in the 15 to 350 keV range of GRB 160410A with 64 ms binning. The blue area marks a multi-peaked structure during the first two seconds. The dash-dotted line marks the end of the T_{90} duration from Sakamoto et al. (2016) in the same energy band.

I GRBs, though in the bottom left quadrant of Fig. 1 in Lü et al. (2010) and, within that sector, in the top right corner, close to the bulk of the Type I GRBs with EE. Only for the combination of lowest peak energy and highest isotropic energy release would it fall slightly into the sector of intrinsically short Type II GRBs.

Lü et al. (2014) discuss the "amplitude parameter" f which they define as the ratio between the 1 s peak count rate and the background count rate over the same time span. They simulate what f value will be derived for long GRBs when adding noise to the point that the $T_{90} < 2$ s, a value they designate as $f_{\rm eff}$. They find $f_{\rm eff}$ values for such noised long GRBs have a mean value $\overline{f}_{\rm eff} = 1.24$, whereas $f \gtrsim 2$ for Type I GRBs. For GRB 160410A, $f = 2.13$ is derived, with $f_{\rm eff}$ being essentially the same value as the extended emission is very faint (H.-J. Lü, priv. comm.). This indicates GRB 160410A is a true Type I GRB, but the evidence is marginal.

Li et al. (2020) create a method to use multiwavelength data to determine the probability whether a GRB is of Type I or Type II. This uses both prompt emission data as well as environment/host galaxy data (metallicity, offset, stellar mass). Their data collection is based on Li et al. (2016) which does not include GRB 160410A. We used their webpage[10] to input all known parameters of GRB 160410A (the mean values as determined by Li et al. 2020 are used where we do not have information, such as on the host offset). Using all prompt-emission parameters and the upper limit on the host mass (see Sect. 3.3.3), we derive a 97% probability that this is a Type I GRB. However, if the extremely low metallicity is added, the probability switches completely, being

[10] http://www.physics.unlv.edu/~liye/GRB/grb_cls.html

vanishingly small for a Type I GRB. Considering all the other results in this section, this mainly points to the host environment of GRB 160410A being extreme within the known parameter range of Type I GRB host galaxies (likely coupled to the high redshift), in a way that is unaccounted for in the classifier.

From an analysis of large samples of long and short GRBs, Shahmoradi & Nemiroff (2015) deduce the statistically most significant indicator of classification is E_p/T_{90}[keV,s^{-1}] (observer-frame values), with 99% of long GRBs having values $\lesssim 50$ and 95% of short GRBs having values $\gtrsim 50$. For GRB 160410A, we find $E_p/T_{90} = 173$ for the *Swift*-BAT T_{90} value, and $E_p/T_{90} = 893$ for the Konus-*Wind* duration, favoring that this is a short GRB.

Jespersen et al. (2020) present a method to classify GRBs based on prompt emission characteristics alone. They find that GRB 160410A is a long GRB. In their result table, they list the T_{90} duration to be 96 s, significantly in excess of the value of 8.2 s (Sakamoto et al. 2016). (We note that the *Swift* automatic BAT analysis page for this GRB[11] even gives a value of $\sim$ 320 s.) *Swift* entered the South Atlantic anomaly after several hundred seconds, which may influence the analysis and the significance of the Extended Emission. This, then, may also influence the classification of Jespersen et al. (2020) (C. K. Jespersen, priv. comm.).

3.4.1 The GRB 201221D spectra

This is the only SGRB since GRB 160410A for which we were able to detect absorption lines in the spectrum, albeit with a low S/N. The GRB afterglow is detected in the acquisition image with a magnitude of $r' = 23.95 \pm 0.20$ mag, calibrated using five Pan-STARRS field stars and not corrected for Galactic extinction (Schlafly & Finkbeiner 2011). In the GRB 201221D spectrum, we find up to four absorption lines that we interpret as due to the MgII doublet and to FeII lines. In addition, we also observe [OII]λ3727 in emission from the host. The emission falls within a telluric band and its detection tells us that the emission must therefore be rather strong (see de Ugarte Postigo et al. 2020). All the features are at a redshift of $z = 1.0450 \pm 0.0008$, making GRB 201221D another high-redshift SGRB and, in this case, with a clearly star-forming host galaxy. The spectrum is shown in Fig. 3.15.

We measure EWs in the spectrum using the GRBspec database and compare it to the sample of long GRBs (de Ugarte Postigo et al. 2012) in Fig. 3.7. In this case, the strength of the absorption features is consistent with the average for long GRBs (LSP = 0.04 ± 0.05) in contrast to GRB 160410A where the lines were much weaker. Due to the wavelength coverage, we cannot detect the high ionisation absorption lines of SiIV and CIV and hence cannot come to a conclusion on the ionisation of the ISM. In any case, the *r'*-band value measured for the GRB afterglow is consistent within errors with the one for the host galaxy (see Tab.3.3) and therefore, continuum contamination from the host galaxy is present in our spectrum. Thus, the EW/LSP measures might be contaminated and are not fully comparable to GRB 160410A and GRB 130603B.

[11] https://gcn.gsfc.nasa.gov/notices_s/682269/BA/

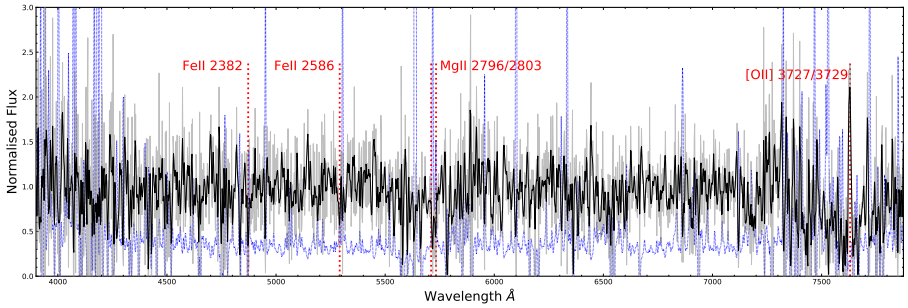

Figure 3.15: GTC/OSIRIS spectrum of the afterglow emission of GRB 201221D. For plotting reasons, we smooth the spectrum by applying a Gaussian kernel of 1σ to the data. The colour coding is the same one as used in Fig. 3.1. We add the non-smoothed spectrum (grey) in the background.

Table 3.3: Photometry of the GRB 201221D host galaxy. Data are given in AB magnitudes and are corrected for Galactic foreground extinction (Schlafly & Finkbeiner 2011).

Time after burst (days)	Magnitude (AB)	Exposure Time (s)	Band	Instrument
19.349	23.80 ± 0.12	120	g'	LBC
19.349	23.83 ± 0.15	120	r'	LBC
19.349	23.44 ± 0.18	120	i'	LBC
19.349	23.11 ± 0.25	120	z'	LBC
13.879	22.40 ± 0.17	60	J	LUCIFER
13.895	22.15 ± 0.20	60	K_S	LUCIFER

3.4.2 The host of GRB 201221D

In contrast to GRB 160410A we do find a faint host candidate for GRB 201221D at the same position as the GRB. The photometry of the host candidate is shown in Tab. 3.3 for all the bands observed with the LBT telescope.

We analyse the Spectral Energy Distribution (SED) of the host galaxy with the available photometry using `CIGALE`[12] (Burgarella et al. 2005; Noll et al. 2009; Boquien et al. 2019) in its most recent version. We apply a delayed star-formation history with an age for the main stellar population varying freely from 1.0 Gyr to 13 Gyr and a more recent burst whose age varies from 20 Myr to 1 Gyr. The Initial Mass Function (IMF) we use is described in Chabrier (2003) with a Bruzual & Charlot (2003) stellar population model, assuming a metallicity (Z) of 0.008, 0.02 or 0.05 (where $Z = 0.02$ is Solar metallicity Bruzual & Charlot 2003).

The dust attenuation is modeled with the modified attenuation law described in Calzetti et al. (2000) as implemented in `CIGALE` (see Sect. 3.4.2 in Boquien et al. 2019). We consider a Milky

[12] https://cigale.lam.fr/

Way (MW) (Cardelli et al. 1989) extinction model with a $R_V = 3.1$ and a colour excess in the nebular lines starting in 0.1 and then, varying in steps of 0.05 between 0.05 and 1.0. We also considered a Small Magellanic Cloud (SMC) and a Large Magellanic Cloud (LMC) (Pei 1992) extinction model but in both cases, the model was unsatisfactory compared to the one performed considering a MW model. We also allow the attenuation curve slope to vary from −0.4 to 0.4, changing it in steps of 0.2 (see Eq. 8 in Boquien et al. 2019). For the re-emitted energy from dust heated by stellar photons, we use the models from Dale et al. (2014) and let $\alpha_{\rm IR}$, the exponent of the radiation field intensity distribution (Dale & Helou 2002), vary between 1.0, 2.0 or 3.0.

We find a best fit to the SED using a model galaxy spectrum with an intermediate mass and a moderate star-formation rate (SFR), as well as a low specific star-formation rate (sSFR). However, our modelling shows some degree of over-fitting, which might be due to the low number of data points. The results for the SED modeling are listed in Tab. 3.4 and a figure of the best model can be seen in Appendix A.3.

Table 3.4: Properties of the putative host galaxy of GRB 201221D.

Property	Value
A_V (mag)	0.56 ± 0.34
Z	0.02
$\log_{10}(M)(M_\odot)$	$9.79^{+0.13}_{-0.19}$
$\log_{10}(SFR)\ (M_\odot/yr)$	$0.81^{+0.19}_{-0.33}$
$sSFR\ (Gyr^{-1})$	1.06 ± 0.67
Reduced χ^2	0.45

3.5 Discussion

3.5.1 On the short/long nature of GRB 160410A

Ever since the discovery of a bimodal distribution of GRB prompt emission light curves both in the temporal range (Mazets et al. 1981) as well as the spectral hardness (Kouveliotou et al. 1993), methods to discern between "long/soft" and "short/hard" GRBs have been extensively discussed in the literature (see e.g. Lü et al. 2010, 2014; Tsutsui et al. 2013; Shahmoradi & Nemiroff 2015; Zhang et al. 2016, 2018; Li et al. 2016, 2020; Jespersen et al. 2020, for some works on this topic). Here we will study GRB 160410A with several classification methods to derive clues on its nature.

Tsutsui et al. (2013) first found significant statistical evidence for an "Amati" relation between the isotropic energy release $E_{\rm iso}$ and the rest-frame peak energy of the prompt emission spectrum $E_{\rm peak,\,rest}$, long known for long GRBs (Amati et al. 2002; Amati 2006), for SGRBs parallel to that of long GRBs but offset by a factor of $\sim$ 100. Using a significantly increased sample, Minaev & Pozanenko (2020, 2021, henceforth MP20) confirm this result, and GRB 160410A fits

with the Amati relation for SGRBs (Fig. 3.17)[13]. Furthermore, MP20 introduce two classifiers, *EH* and *EHD* (Energy-Hardness and Energy-Hardness-Duration, respectively). They find that GRB 160410A is in full agreement with the high values found for other short GRBs.

To confirm the results of MP20, we gathered GRB energetics, mostly from Tsvetkova et al. (2017, 2021) and compute the isotropic energy[14]. The final sample is shown in Fig. 3.17 and we perform a simple fitting to the two GRB classes following Eq. 3.1 as presented in MP20.

$$\log\left(\frac{E_{\rm peak}}{100\ {\rm keV}}\right) = a \cdot \log\left(\frac{E_{\rm iso}}{10^{51}\ {\rm erg}}\right) + b \tag{3.1}$$

For SGRBs we found a slope of $a_{\rm short} = 0.30$ and $b_{\rm short} = 0.78$ with a standard deviation of $\sigma_{\rm short} = 0.05$ and $R^2 = 0.50$, for long GRBs the slope is $a_{\rm long} = 0.33$, $b_{\rm long} = -0.01$ with a $\sigma_{\rm long} = 0.02$ and $R^2 = 0.52$. We do not perform a more extended fitting as it is done in MP20 since it is not the aim of the present paper.

Another classification distinction is the *hardness ratio* (HR), which is the ratio of the fluence in the 50–100 keV band over the 25–50 keV band. Dichiara et al. (2021) obtained a HR = 2.3±0.5 for the main spike and claim GRB 160410A is a short GRB with extended emission. GRB 160410A can be classified as a long GRB (see Fig. 3.16), if we only consider the T_{90} as the classification criterion. However, if we consider the initial peak complex and GRB 160410A as a short GRB with EE, as in Dichiara et al. (2021), we see that it matches with the short GRB scheme.

Kann et al. (2011) compare the afterglows of SGRBs to a large sample of those of long GRBs. They find $\overline{M_B} = -23.14 \pm 0.17$ mag (FWHM 1.61 mag) for long GRB afterglows at one day in the $z = 1$ frame, and $\overline{M_B} = -17.34 \pm 0.50$ mag (FWHM 1.65 mag) for the short GRB afterglows at the same time. For GRB 160410A, we derive $M_B = -19.04$ mag from our fit to the late-time light curve. This places the absolute magnitude of the afterglow at the upper edge of the FWHM of the SGRB afterglow absolute magnitude distribution, but 2.5 mag below that of long GRB afterglows, making it more likely that GRB 160410A is a short GRB.

Further classifiers in the context of GRB 160410A can be found in Sect. 3.4. With a few exceptions, these find that GRB 160410A is a genuine SGRB, or at least more likely to be one than a long GRB. We therefore conclude that GRB 160410A has evidence showing it to be a member of the SGRB population.

The other SGRB studied here, GRB 201221D, actually matches very well the location for long GRBs in the Amati relation (see Fig. 3.17). However, it shortness and hardness (see Sect. 3.2.5 and Fig. 3.16) put this GRB clearly within the SGRB category.

3.5.2 The GRB 160410A environment in the context of long GRBs and short GRBs

The sample of short GRBs with detected absorption lines in its spectrum is still very small: GRB 130603B (de Ugarte Postigo et al. 2014b), GRB 160410A, and GRB 201221D (both in this

[13]Note the Amati relation is also a powerful tool for the opposite case, such as the recently reported GRB 200826A (Rossi et al. 2022; Ahumada et al. 2021; Zhang et al. 2021), which was temporally short but fully in agreement with the long-GRB Amati relation and was shown to be accompanied by a supernova.

[14]https://github.com/steveschulze/GRB_Eiso.git

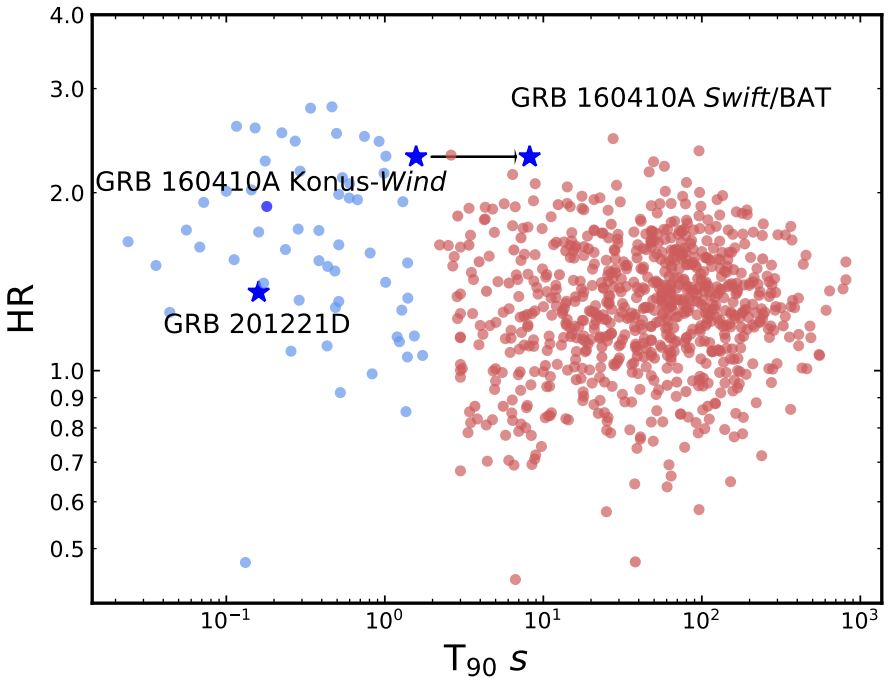

Figure 3.16: Hardness Ratio (HR) vs. duration T_{90} using data from Lien et al. (2016). Based on the work from Kouveliotou et al. (1993), we show SGRBs in blue and long GRBs in red. The hardness ratio of GRB 201221D is marked with a blue stars as derived from the *Swift*/BAT data products (https://gcn.gsfc.nasa.gov/notices_s/682269/BA/). For GRB 160410A we plot the HR derived in Dichiara et al. (2021) with the T_{90} from *Swift*/BAT on top right and T_{90} derived for the initial peak complex from Konus-*Wind* data (Minaev & Pozanenko 2020) on top left.

study). GRB 160410A is the only one that allows a chemical study of the gas in the host to be performed, as it has been commonly done for long GRBs (see e.g. de Ugarte Postigo et al. 2018; Krühler et al. 2013; Heintz et al. 2018b). The spectrum shows features common to long GRBs such as FeII, AlII or SiII; however, it does not show any high ionisation lines of SiIV nor CIV, which are usually detected in long GRB environments (see e.g. Vreeswijk et al. 2004; Christensen et al. 2011; de Ugarte Postigo et al. 2012; Heintz et al. 2018b). Cao et al. (2016) report the detection of CIV lines in their afterglow spectrum together with the MgII $\lambda\lambda$2796,2803 doublet, which, however, happens to fall within the telluric A-band.

Despite the scarcity of currently available SGRB afterglow spectra, it seems that SGRB sightlines show a large diversity, as it is the case for their host galaxies. The spectra of all three SGRBs with absorption line spectra cover the MgII and the FeII lines as common features. GRB 201221D and GRB 130603B show the MgII λ2796, 2803 doublet, while the FeII lines are only present in GRB 201221D. In GRB 160410A we do not observe CaII or NaI detected in GRB 130603B. However, we detect a large number of additional absorption lines that were out of the observable range in the other two SGRBs due to their lower redshift. There is also a tentative detection of

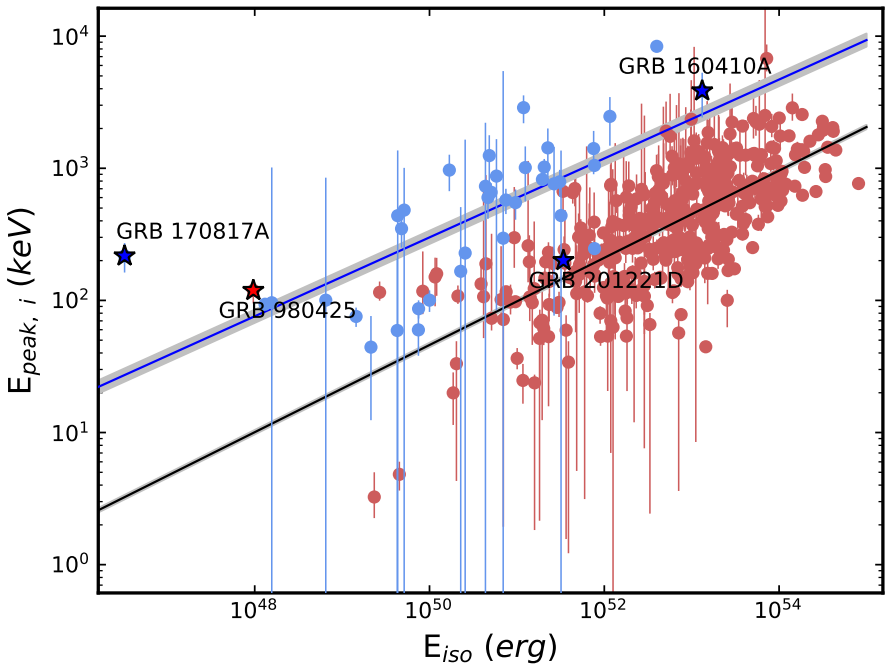

Figure 3.17: Modified version of the Amati relation. We highlight the positions of GRB 160410A and GRB 201221D with blue stars, as derived from the Konus-*Wind* published data, see Sect. 3.5.1. SGRBs are plotted in blue, long GRBs in red. In the corresponding colours, the best linear fits are plotted together with a shaded area around them marking the 1σ region for each fit. Here we do not distinguish between SGRBs and SGRBs with extended emission.

NiII but the significance is very low.

GRB 130603B happened in a spiral galaxy in what appears to be a tidally disrupted arm (de Ugarte Postigo et al. 2014b). In the spectrum of GRB 201221D we detect [OII]λ3727 emission lines, implying the presence of an underlying star-forming host galaxy. Furthermore, both we and multiple other observing teams (Dichiara et al. 2020; Kilpatrick et al. 2020; Rastinejad et al. 2020; Dimple et al. 2020) report the detection of a faint extended source at the afterglow position. The host of GRB 201221D (see Sect. 3.4.2) is a massive galaxy consistent with the common value found in prior works on SGRB hosts (see e.g. Leibler & Berger 2010). The star-formation rate is also in agreement with the values found for SGRB hosts (Berger 2009).

For GRB 160410A, however, we found no host galaxy down to very deep limits (see Sect. 3.3.3) and we find no hint of emission lines in the NIR. In contrast, the detection of the broad Lyα absorption line and the large column density tell us that the GRB happened within or behind a DLA, which are usually associated with a galaxy (see e.g. Wolfe et al. 2005; Christensen et al. 2014). This implies that there must be an underlying galaxy for GRB 160410A but it might be very faint. It is also possible that the progenitor system of GRB 160410A has been kicked out from its host and merged outside the host or in the halo. The fact that we detect a DLA in the sight-line implies that the GRB still has to be well within the Hi halo of the galaxy. Given the high redshift of the system and typical kick velocities, a binary NS-NS system could move tens of kiloparsecs

away from the host galaxy beyond the extension of hydrogen of the galaxy (Mandhai et al. 2022). The distance in projection to the closest observable galaxy in the GRB 160410A field is ~ 42 kpc (under the assumption this galaxy is at the redshift of GRB 160410A), making it very unlikely to be the host of the GRB while observing such a large neutral hydrogen column density and many other absorption lines.

In prior works, the detection of the highly ionized CIV and SiIV absorption lines has been assumed to originate in the hot gas of the galactic halo of DLAs (see e.g. Ledoux et al. 1998; Wolfe & Prochaska 2000; Maller et al. 2003; Fox et al. 2008; Heintz et al. 2018b). The detection of a DLA system and the non-detection of these lines in the GRB 160410A afterglow spectrum would hence not favour this GRB to be in the halo or it would imply that the host has no hot gas halo.

Our analysis shows that the environment of GRB 160410A is very different from the ones measured in the case of long GRB hosts. The probed material has a very low ionisation and very weak lines in general (see Sect. 3.3.2). In contrast, GRB 201221D (see Sect. 3.4.1) and GRB 130603B show LSPs of 0.04 ± 0.05 and 0.20 ± 0.13, respectively, very close to the average value for long GRB sight-lines (de Ugarte Postigo et al. 2012). A high LSP value typically points toward an environment highly ionised due to star-formation and, conversely, a low value pinpoints the opposite. For long GRBs, the LSPs are usually high since these are commonly associated with star-forming environments. The SGRBs 130603B and 201221D occurred within their hosts galaxies; however, for GRB 160410A, no underlying galaxy was detected. We see in Fig. 3.7 that, whereas for GRBs 130603B and 201221D the EW profiles follow the average one of long GRBs. However, we note that for GRB 201221D, EW values might be contaminated by the host continuum (see Sect. 3.4.1) and, therefore, the LSP. GRB 160410A is completely different compared to either long GRBs or to the other two SGRBs with detected features in their afterglows. With a significantly lower value for the LSP and the non-detection of an underlying galaxy, GRB 160410A seems to have happened in a environment that is not actively forming stars.

Furthermore, the measured [Si/Fe] ratio between an α-element such Si, that is produced in core-collapse SNe, and the detection of Fe, mostly produced in Type Ia SNe, might be indicating that there is no α-enhancement and therefore the absence of recent star formation in the host galaxy, which is consistent with the non detection of the galaxy, the low ionisation and the low metallicity of the traced gas (see e.g. Wiersma et al. (2009); Vargas et al. (2013)).

In line with those observations, the metallicity of the material observed along the sight-line is very low (Sect. 3.3.2), comparable to the lowest values for QSO absorbers (see e.g. De Cia et al. (2018) and Fig. 3.6). Compared to galaxies in the local Universe, the metallicity is higher but inline with values obtained for e.g. Tucana II, an UFD galaxy with a metallicity of [Fe/H]~ -3.0 (Ji et al. 2016b). Note, however, that this metallicity was determined from four stars, neither the ISM nor the CGM. This would further support the idea of an underlying very faint host galaxy for GRB 160410A, however, the average metallicity of galaxies at $z \sim 1.7$ is also lower than in the local Universe.

The fact that we have a low metallicity environment and possibly a very faint host galaxy contradicts general expectations for the environment of short GRBs. If the absorption lines are weak

because we have an evolved galaxy with an old population that has exhausted most of the gas, we would expect a high metallicity. However, if the progenitor BNS had been kicked out from its host we should expect a low metallicity. Also Zhang et al. (2009) assume in their classification scheme of short vs. long GRBs that SGRB hosts have a high metallicity (see also Li et al. 2020). The only two other GRBs with absorption line spectroscopy and hence secure host galaxy associations do seem to be different from GRB 160410A, showing much stronger lines and luminous hosts.

The question is whether SGRBs with EE might have somewhat different progenitors and in consequence different hosts or environments. The list of SGRBs with EE is rather short (see e.g. Lien et al. 2016) and only a few of them have an associated host galaxy. Minaev & Pozanenko (2020) list eleven events as SGRBs with EE (GRBs 050709, 050724, 060614, 061006, 061210, 070714B, 071227, 080123, 110402A, 150424A and 160410A). We compare the derived host properties from the GRB afterglow spectrum of GRB 160410A as well as from the field observation with *Spitzer*/IRAC with SGRBs with EE and an associated host galaxy (see Fig.3.10). There is no difference in the distribution of absolute magnitudes between the hosts of normal SGRBs and those with EE, the slight shift towards lower redshifts might be an observational issue since higher redshifts make the detection of the lower luminosity EE more challenging. Taking the stellar masses obtained by SED modeling from Nugent et al. (2020) for those seven SGRB showing EE (GRBs 050709, 050724, 061006, 061210, 070714B, 071227 and 080123, Minaev & Pozanenko 2020), we see that their masses are typically larger than the upper limit we obtain from the *Spitzer* observations (see Sect. 3.3.3), although a few have stellar masses lower than our limit for the host of GRB 160410A. A more recent and complete study on one SGRB with EE, GRB 050709, shows a low-luminosity host, a subsolar metallicity and a low SFR (Nicuesa Guelbenzu et al. 2021), which would be all in line with what we see for GRB 160410A. A more recent case is GRB 181123B, a SGRB with EE and an associated star-forming and massive host at $z = 1.754$ (see Paterson et al. 2020; Dichiara et al. 2021). Its association with the galaxy is still under debate (Rowlinson et al. 2021). However, in Rastinejad et al. (2022), the properties of the associated host galaxy of GRB 211211A are in line with the limits for the host of GRB 160410A. Despite its prompt emission shape and duration, GRB 211211A is claimed to be a SGRB with EE and the associated host galaxy seems to be a galaxy with a low stellar mass and a low SFR.

It would be important to settle the issue of the host galaxy association by deep imaging with e.g. the Hubble Space Telescope (HST) or the James Webb Space Telescope (JWST), to determine the nature of the host and the location of the GRB within it to understand why we observe this peculiar environment in this burst.

SGRBs have also been proposed to happen within galaxy clusters (see e.g. Berger 2010), so that could be a possible explanation for the absence of detection of a host for GRB 160410A. However, again, the large column density of neutral hydrogen goes against this hypothesis as DLAs are commonly associated with galaxies, as mentioned before. We also do not see a very crowded field in Fig. 3.2.

DLA systems found in QSO absorbers have been associated with the halo of galaxies (Wolfe et al. 2005). The non-detection of an underlying galaxy and the fact that the closest possible galaxy is at 42 kpc from the GRB location could also mean that the GRB itself happened at a large distance

from its host and that the lines we see in the afterglow spectrum are actually an intervening system. However, the non-detection of the GRB afterglow in the *uvw2* and *uvm2* bands and the detection in the *uvw1* band (see Sect. 4.3 and Appendix A.2) establish a redshift upper limit for the GRB afterglow using the Lyman "drop-out" technique of $z = 1.8$. This points to an association of the afterglow with the ISM detected at the absorption line redshift, making it unlikely that the DLA belongs to a foreground galaxy.

3.6 Conclusions

In this paper, we present the first study of the ISM of a SGRB host galaxy. The burst itself was one of the hardest and brightest events ever detected and at the highest redshift ever measured directly from its afterglow spectrum (and not from the association with a potential host galaxy). The X-shooter spectrum shows a broad HI absorption with a large column density consistent with being a DLA. We derive a very low metallicity of [Fe/H] = −2.5, one of the lowest (dust-depletion corrected) value ever measured. GRB 160410A shows a very low ionisation compared to what is commonly found for the environments of LGRBs. SED fitting to the light curve of the afterglow and dust depletion analysis from absorption lines finds no indication for dust extinction along the sight-line. We do not find any host galaxy down to a very deep limit; however, the presence of the DLA system in the burst afterglow spectrum indicates that there has to be an underlying host.

The GRB 160410A afterglow seems to be rather different compared to the other two SGRB afterglows with detected absorption lines, being significantly brighter than any other SGRB afterglow at very early times except for the controversial case of GRB 180418A (note both early detections were obtained with TAROT). GRB 201221D is located within a more massive, star-forming ionised host galaxy, consistent with previous findings for SGRB hosts. However, our spectral coverage does not allow us to determine its metallicity. The spectrum of GRB 160410A was obtained less than ten minutes after the GRB alert and has the largest sample of lines observed in a short GRB afterglow spectrum. This demonstrates the importance of the rapid response mode for observing these events. More data sets of this quality are needed to obtain more robust statistical conclusions on the ISM and environments of SGRBs.

Chapter 4

Varying linear polarisation in the dust-free gamma-ray burst 210610B

Contents

4.1 Abstract

Long gamma-ray bursts (GRBs) are produced by the collapse of some very massive stars, that emit ultra-relativistic jets. When the jets collide with the interstellar medium they decelerate and generate the so-called afterglow emission, which has been observed to be polarised. We study the polarimetric evolution of the GRB 210610B afterglow, at $z = 1.1341$. This allows us to evaluate the role of geometric and/or magnetic mechanisms in the GRB afterglow polarisation. We observed GRB 210610B using imaging polarimetry with CAFOS on the 2.2 m Calar Alto Telescope and FORS2 on the 4×8.1 m Very Large Telescope. Complementary optical spectroscopy was obtained with OSIRIS on the 10.4 m Gran Telescopio Canarias. We studied the GRB light-curve from X-rays to the optical bands and the Spectral Energy Distribution (SED). This allowed us to strongly constrain the line-of-sight extinction. Finally, we studied the GRB host galaxy using optical to NIR data to fit the SED and derive its integrated properties. GRB 210610B had a bright afterglow with a negligible line-of-sight extinction. Polarimetry was obtained at three epochs: during an early plateau phase, at the time when the light curve breaks, and after the light curve steepened. We observe an initial polarisation of $\sim 4\%$ that goes to zero at the time of the break, and it then again increases to $\sim 2\%$, with a change in the position angle of 54 ± 9 deg. The spectrum shows features with very low equivalent widths. This indicate a small amount of material in the line of sight within the host. The lack of dust and the low amount of material in the line of sight to GRB 210610B allowed us to study the intrinsic polarisation of the GRB optical afterglow. The GRB polarisation signals are consistent with ordered magnetic fields in refreshed shock or/and hydrodynamics-scale turbulent fields in the forward shock.

4.2 Introduction

Gamma-ray bursts (GRBs) are among the most energetic electromagnetic explosions that have been observed in the Universe. These events have two main emission episodes: the prompt-emission and the afterglow-emission phases. The prompt emission represents the first observable electromagnetic emission and is dominated by gamma-ray photons lasting seconds to minutes after the onset of the burst. The afterglow has a synchrotron spectrum ranging from radio to gamma-rays and evolves in time during much longer time spans.

GRBs are typically classified as short or long according to their measured T_{90}[1] duration in gamma-rays (Kouveliotou et al. 1993). Short GRBs (sGRB) are associated with the coalescence of two compact objects, their T_{90} duration is typically shorter than 2 seconds, and their X-ray spectrum is hard. The discovery of a sGRB associated with the gravitational wave (GW) detection GW 170817 definitively linked a sGRB with the merger of two neutron stars (Abbott et al. 2017a). On the other hand, long GRBs (lGRB) that show T_{90} longer than 2 seconds and have a softer spectra in the prompt emission phase. These are cataclysmic events associated with the collapse of massive stars. They are also associated with the detection of broad-line (BL) type Ic supernovae (SNe) (see e.g. Galama et al. 1998; Hjorth et al. 2003). Lately, several events detecting a kilonova (KN) emission in a burst with a duration of dozen seconds have cast doubts on the 2-seconds division as the unique criterion to distinguish between sGRBs and lGRBs (Rastinejad et al. 2022; Troja et al. 2022; Yang et al. 2022; Gompertz et al. 2022; Levan et al. 2023b, 2024a).

The prompt emission in a GRB is powered by a newly formed compact object that is fed by the surrounding material. Accretion onto this compact object launches ultra-relativistic jets, in which the prompt emission is generated through internal dissipation processes including internal shocks (see e.g. Rees & Meszaros 1994; Sari & Piran 1997; Kobayashi et al. 1997). This prompt high-energy emission releases isotropic-equivalent energies that can reach up to 10^{55}erg (see e.g. Burns et al. 2023), although the real released energy can be several orders of magnitude lower due to the jet collimation.

Polarimetry is an essential tool for explaining GRB physics. Using this technique, we can test models that include magnetic fields and the geometrical characteristics that are at play, and we can determine how they evolve throughout the different phases of the GRB. The study of the prompt emission polarisation and its temporal evolution can help us to understand how the jet is powered by the central engine. The long and extremely bright GRB 221009A was observed during the prompt- and afterglow-emission phase by the Imaging X-ray Polarimetry Explorer (IXPE) and only upper limits were obtained (Negro et al. 2023). Studies of the prompt-emission polarisation with instrument calibrated to perform polarimetry are rare so far. The Astrosat mission with the on-board Cadmium-Zinc-Telluride Imager (CZTI) instrument shows the prompt emission as highly polarised, while for POLAR, GRBs are lowly polarised or not polarised at all (see e.g. Gill et al. 2021).

The material ejected through the jets eventually collides with the circumburst material, decel-

[1]The T_{90} is the time span within which a GRB releases between 5% and 95% of the total energy during the prompt phase.

erating as interacts with it. These forward shocks generate a broadband synchrotron emission that is known as the afterglow. This bright shock can be observed during days or even months in the case of radio frequencies. In certain cases, a reverse shock that propagates backwards within the relativistic jet can be observed at early times (see e.g. Mészáros & Rees 1997; Piran 1999). Different models predict this emission to be polarised. Gruzinov & Waxman (1999) proposed a model in which the afterglow would show patches with locally ordered magnetic fields randomly oriented but with many of them sharing a common direction leading to a global low level of polarisation in the GRB afterglow.

The number of studies using optical linear imaging polarimetry and spectropolarimetry techniques is still very small (see e.g. Covino & Gotz 2016). The first GRB with a polarisation detection in the afterglow was GRB 990510. Its polarisation degree (PD) was 1.7 %, 0.7 days after detection (Covino et al. 1999; Wijers et al. 1999). Many efforts have been made to increase the sample of polarimetric measurements, but the faintness of these objects, their fast evolution, and the long observing times required for a good signal-to-noise ratio (S/N) leave us with less than 20 GRBs with a measurement above 3σ. Fast reaction is crucial for observing the first GRB phases in which a higher PD might be expected. The highest measured value was for GRB 120308A with a PD of 28 % 5 minutes after the burst, which rapidly decreased to 16 % as the afterglow evolved (Mundell et al. 2013). A high PD of ∼10 % was also measured for GRB 020405, GRB 090102 and GRB 091208B (Bersier et al. 2003; Steele et al. 2009; Uehara et al. 2012). All of them were observed earlier than 0.01 days after the GRB detection. Observations at later stages shows this sources as lowly-polarised with some degree of variability throughout their light-curve evolution. The most detailed example is GRB 030329 (Greiner et al. 2003) whose PD evolves somewhat randomly from 0.91 % at 0.5 days to 1.4 % 37.5 days after the burst. Afterglow polarisation must be understood together with the surrounding environment. Dust in the line of sight can change the observed PD and prevent the measurement of the intrinsic polarisation (Lazzati et al. 2003). This measurement by itself is also incomplete when it is not followed by the study of the light-curve evolution. It is crucial for distinguishing between the models that have been proposed to explain the GRB jet physics to understand whether there is a break in the light curve and how the polarisation behaves before, during and after this break (see e.g. Covino & Gotz 2016).

We present a comprehensive study of GRB 210610B, its afterglow emission and its environment using different techniques. Polarimetric, spectral and photometric observations were secured for this bright long GRB. We also observed the putative host galaxy in order to characterise it and place the GRB into context. This work is structured as follows: In section 4.3 we present the observations of both, the afterglow and the underlying galaxy. In section 4.4 we present the results of the analysis of the linear polarimetry of the afterglow, the light curve and its spectrum, as well as the analysis of the galaxy. In section 4.5 we discuss the results by setting the framework into which GRB 210610B is embedded. We also place the results of the GRB afterglow polarimetry measurements into context. Finally, in section 4.6 we present the conclusions.

Throughout this study, we describe the spectral and temporal evolution of the data using the convention by which $F_\nu \propto t^{-\alpha}\nu^{-\beta}$. We adopt a cosmological model with $H_0 = 67.3\,\mathrm{km\,s^{-1}Mpc^{-1}}$, $\Omega_M = 0.315$ and $\Omega_\Lambda = 0.685$ (Planck Collaboration et al. 2014b).

4.3 Observations

4.3.1 High-Energy data

GRB 210610B was first detected by the Gamma-ray Burst Monitor (GBM) on board the *Fermi* observatory at 19:51:05.05 UT of 10 June 2021 with a T_{90} = 55.04±0.72 s and a fluence of $(1104.2 \pm 0.5) \times 10^{-5}$ erg cm^{-2} in the 10 keV to 10 MeV band (Malacaria et al. 2021; von Kienlin et al. 2020). At the redshift of the GRB (see sect. 4.4.3), the computed isotropic energy is $E_{\rm iso,\,rest} = 4.17^{+0.02}_{-0.02} \times 10^{53}$ erg in the 0.1 keV to 10 MeV band. This value is fully consistent with the so-called Amati relation (Amati et al. 2002; Amati 2006) for long GRBs. The burst was detected ∼22 s later by the Burst Alert Telescope (BAT; Barthelmy et al. 2005) on board the *Neil Gehrels Swift Observatory* with coordinates RA = 16$^{\rm h}$ 15$^{\rm m}$ 45$^{\rm s}$, Dec. = +14° 23 29 and an uncertainty of 3. The X-Ray Telescope (XRT; Burrows et al. 2005b) started observing the source 89.9 s after BAT and quasi-simultaneously, the Ultraviolet/Optical Telescope (UVOT; Roming et al. 2005) observed the field in the *White* band. The image showed a new bright source within the XRT position with a magnitude in the *Swift*/UVOT native system of 13.70±0.14, uncorrected for galactic extinction (Page et al. 2021). The later analysis, presented in Siegel et al. (2021), updated this value to 13.63±1.10 and the source location to RA = 16$^{\rm h}$ 15$^{\rm m}$ 40.40$^{\rm s}$, Dec. = +14° 23 56.9 with an uncertainty of 0.42".

In the refined analysis from the BAT data, the burst had a T_{90} duration of T_{90} = 69.38±2.53 s in the 15 to 350 keV band with an $E_{\rm peak}$ = 339.3±218.6 keV(Krimm et al. 2021). The burst showed a hardness ratio (HR)[2] of 1.78±0.04. This falls in the upper part of the bulk of the HR distribution for long GRBs (see e.g. Lien et al. 2016). The burst was also detected by Konus-*Wind* observatory with a duration ∼ 100 s (Frederiks et al. 2021). The HR of the burst, its T_{90}, and its isotropic energy release classify GRB 210610B as a long GRB.

4.3.2 Linear polarimetry imaging

We observed the GRB 210610B following the *Swift*/BAT alert with two different instruments in linear polarimetry mode. We first observed it with the Calar Alto Faint Object Spectrograph (CAFOS) mounted on the 2.2 meter telescope at Calar Alto Observatory[3]. The observations started 0.08 days after the *Swift*/BAT detection with an exposure per half-wave plate (HWP) position angle (see below) of 900 s in *R* band. A second observation was obtained with the FOcal Reducer and low dispersion Spectrograph (FORS2) mounted on the Unit Telescope 1 of the Very Large Telescope (VLT) of the European Southern Observatory (ESO)[4]. The VLT/FORS2 observations started 0.24 days after the GRB alert in $R_{Special}$, b_{High}, and $z_{Special}$ bands with 180 s exposure time per image and with two cycles with the same configuration.

For both instruments, observations were obtained using the HWP in four different rotation angles of 0.0°, 22.5°, 45.0°, and 67.5° and with a Wollaston prism to split the light into the ordinary

[2]The hardness ratio or spectral hardness (Kouveliotou et al. 1993) for a GRB is the ratio between the fluence emitted during the prompt emission in the 50–100 keV band over the 25–50 keV band.

[3]Observations were obtained with programme F21-2.2-021 (PI: Agüí Fernández, J. F.).

[4]Observations were obtained with programme 106.21T6.003 (PI: Tanvir, N.).

(o) and extraordinary (e) beams. A mask was set to avoid overlapping of the light from the two beams.

To calibrate the CAHA/CAFOS observations, one high- and one zero-polarised standard star were observed following the same procedure as for the GRB. The flat-fields in the corresponding band were obtained with the full optical setup in the light path. For the VLT/FORS2 data, calibration and standard observations were performed as specified in the FORS2 User Manual (Anderson 2015).

We obtained a second epoch with VLT/FORS2 in $R_{Special}$ ~1 day. We increased the exposure time per image up to 300 s to account for the fading of the source by performing two cycle for this observations.

4.3.3 Photometry

Photometric observations were performed using several instruments at different observatories and in multiple bands. In this section, we describe the details of each of the observations. The measured photometry is compiled in Table B.1.

Small Binocular Telescope

The Small Binocular Telescope (SBT), located at the Ondřejov Observatory, observed GRB 210610B at dusk with the two 20 cm Newtonian astrographs mounted on a common mount. The main detectors have 4096×4096 pixel CCDs that provide a field of view of 3.5°×3.5° with a 3.14" sampling. Operations are designed such that the readout time of one camera equals the exposure time of the other camera to avoid any blind time during the observation.

The SBT observations started ~ 860 s after the burst. During the early follow-up phase, 12 s exposures were taken without a filter. Afterwards, the observations consisted of up to 34 exposures of 120 s each in SDSS-r' band (see Table B.1 for further details). Observations were interrupted at 23:47 UT, almost 4 h after the GRB detection.

The afterglow was not detected in single exposures, and we therefore stacked the images to obtain an acceptable (S/N). We used `montage` to obtain a weighted image co-addition similarly to Morgan et al. (2008), which optimises for the variable background caused by dusk and thick cirrus.

As for the images in r' band, photometric calibration was performed against the Atlas catalogue, which uses the Pan-STARRS catalogue for faint targets. Images in the clear band were calibrated against the r' band and a polynomial correction involving photometric colours $g' - r'$, $r' - i'$, and $i' - z'$ was performed. Photometric measurements obtained this way are shifted compared to the original standard r' band by a correction that depends on the object colour. This correction can be computed from the fitted relation when the photometric colours of the afterglow are known. By fitting the complete photometric set with an empirical broken power law we, determined this correction to be $k_{\mathrm{c-r}} = -0.0045$ mag. Therefore, under the assumption that the afterglow shows no colour evolution, we are able to convert the unfiltered values from SBT into r' by simply subtracting $k_{\mathrm{c-r}}$.

FRAM-ORM telescope

The 25 cm telescope FRAM-ORM, is operated as part of CTA-N at Roque de los Muchachos at La Palma, Spain. The telescope is equipped with a 1024 × 1024 pixel CCD detector and a Bessel filter set, which provides a field of view of 26′×26′ with a pixel scale of 1.5”.

FRAM-ORM observed the GRB starting at 20:49 UT (1h after trigger) and obtained a total of 83×60 s images in *R* band using a total of 1.5 h of observing time. Images were reduced using standard procedures and combined into groups in order to provide a good (S/N). Photometry was performed in a similar way as for the SBT unfiltered images, using *r’* band and *r’-i’* band catalogue values. The derived correction factor is $k_{\mathrm{R-r}} = -0.036$ mag.

Telescope D50

The D50 Telescope is a 0.5 m Newtonian robotic telescope located at Ondřejov Observatory. It has a 1024x1024 EMCCD camera with a field of view 20′×20′, scaled at 1.18” per pixel. The telescope is equipped with an SDSS filter set.

D50 started observing 0.06 days after the burst detection, starting with SDSS-*r’* band and followed by a set of observations in SDSS-*g’*, *r’*, *i’*, and *z’* bands using different exposure times (see Tab.B.1 for further details). During the first night, the telescope spent 3.2 h on target and stopped at 01:05 UT. There were additional observations in night 2, 4, 5, and 7, collecting 16.75 h of further follow-up data.

All images were processed in a standard manner performing dark subtraction, flat-field correction, and fringe removal for i' and z', and the images were co-added when necessary. Photometry was performed using the SDSS catalogue in the corresponding band. The GRB afterglow emission is detected even at the latest epoch.

CAHA/CAFOS

In addition to the polarimetric observation, we performed further imaging of the afterglow in the second night with CAFOS on the 2.2 m telescope of the Calar Alto Observatory. The images were corrected using bias and flat fields using standard procedures in IRAF. The observations were performed with the R_C filter and calibrated with respect to PanSTARRS field stars, for which a filter correction was used to derive AB magnitudes in the R_C band. These magnitudes were then transformed into the r' band using the colour information that we have from the afterglow. The final values are shown in Table B.1.

GTC/HiPERCAM

The field of GRB 210610B was observed in four epochs using the HiPERCAM multi-band imager (Dhillon et al. 2021) mounted on the 10.4 m Gran Telescopio de Canarias (GTC) at Roque de los Muchachos Observatory (La Palma, Spain) using programme GTCMULTIPLE2C-21A (P.I.: de Ugarte Postigo). HiPERCAM simultaneously obtains observations in the five SDSS filters (*u’*, *g’*, *r’*, *i’*, *z’*) using efficient dichroic beam-splitters and multiple cameras. The last of our observations

was obtained almost two months after the burst when the emission was dominated by the host galaxy (see Fig. 4.1).

The data reduction was performed using an automatic shell script that finds and organises the files, calls commands from the HiPERCAM pipeline to perform bias and flat corrections and converts the HiPERCAM one-dimension fits files into classical two-dimension fits images. Further IRAF procedures allow us to obtain an even background from the different quadrants of each detector. Finally, the images are registered and combined using SWARP (Bertin 2010). Photometry was performed with aperture photometry using reference field stars from the PanSTARRS catalogue. For the last epoch, we used the same aperture to compare the results to the rest of the data. Additionally, we performed photometry of the complete host galaxy adapting the aperture to its light, and in a similar way, we obtained photometry of a nearby object north-west of the host, which we identified as a companion galaxy at the same redshift (see Sect. 4.4.4).

Perek 2 m telescope

The Perek 2.0 m telescope at the Ondřejov Observatory observed GRB 210610B afterglow 6 days after the burst in SDSS-*g'* band. The photometric camera of this telescope has a 1092×736 pixel CCD with a field of view of $5' \times 7'$ scaled at 0.4″/pixel. After standard imaging data reduction and after imaging co-addition, photometry was performed as for the D50 telescope. The GRB afterglow is well detected.

GTC/EMIR

Late-time near-infrared (NIR) observations were performed on 19 February 2022 in search for the host galaxy of GRB 210610B with the EMIR instrument (Garzón et al. 2022) mounted on the 10.4m GTC telescope with programme GTCMULTIPLE2H-21B (PI: de Ugarte Postigo). The observation consisted of a total exposure of 349×3 s in H band. The data reduction was performed using a self-made pipeline that corrects flat fields, does background subtraction, bad-pixel masking, alignment and combination of the frames. The host galaxy was not detected in the final frame down to a 3-σ limiting magnitude of 22.9 mag.

4.3.4 Spectroscopy

We observed GRB 210610B using the long-slit mode of the Optical System for Imaging and low Resolution Integrated Spectroscopy (OSIRIS) (Cepa et al. 2000) mounted on the 10.4 m GTC. The observation consisted of 3×900 s exposures with grism R1000B and a slit width of 1″ oriented at the parallactic angle[5]. The mean epoch of the observation was 11 June 2021 at 01:59:14 UT (6.12972 hr after the *Swift* trigger) at a mean airmass of 1.13.

Flux calibration was performed relative to an observation of the Ross 640 (Oke 1974) spectrophotometric standard, observed at the beginning of the same night and using the same grism. The afterglow spectrum shows a very strong continuum, with a median (S/N) of ∼ 100 per dispersion element and weak absorption features.

[5]The observations were obtained under the program GTCMULTIPLE2C-21A (PI: de Ugarte Postigo).

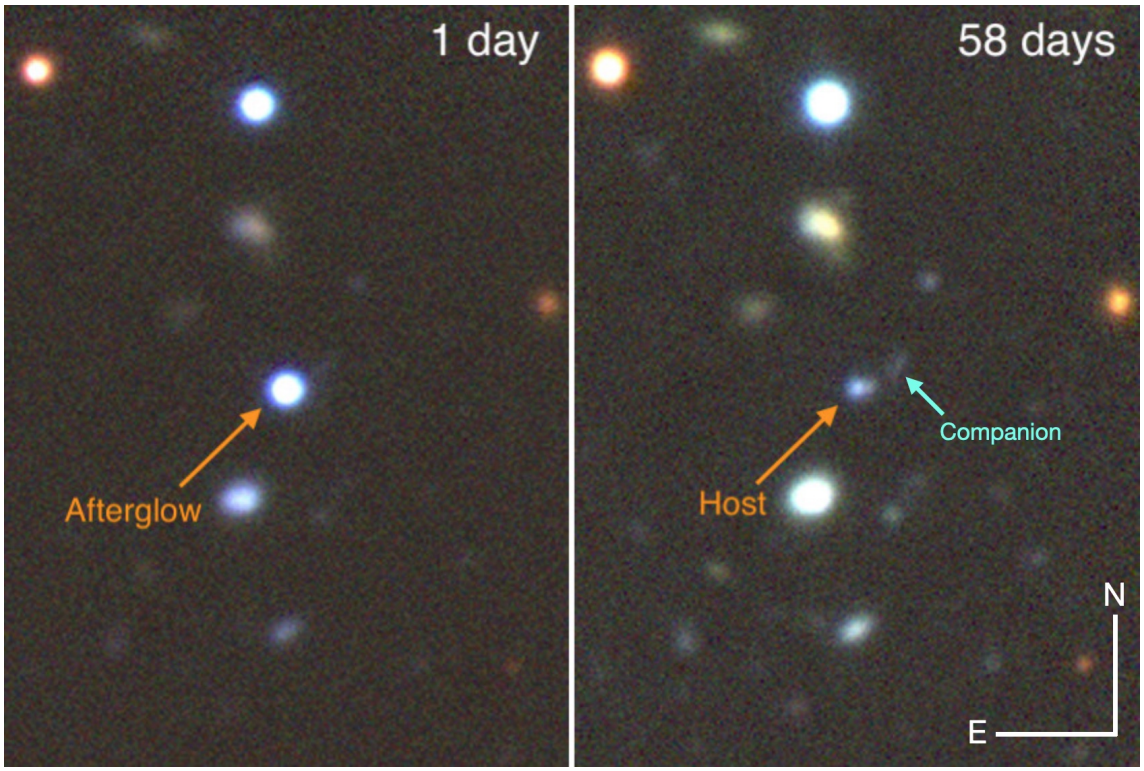

Figure 4.1: Colour images of the field using the *g'*, *r'* and *i'* bands of HiPERCAM at 1 day and 58 days after the burst, respectively. In the first image the afterglow is strongly detected, in the second image, it has faded and the host galaxy dominates the emission. 2.7 arcsec north-west of the host galaxy lies a companion galaxy at the same photometric redshift of the host (see Sect.4.4.4).

4.4 Results

4.4.1 Linear polarimetric analysis

For all linear polarimetry data, we performed regular imaging-reduction processes. Images were bias subtracted and flat-field corrected using `PyRAF` tasks (Science Software Branch at STScI 2012). The flat field correction for VLT/FORS2 was performed as specified in González-Gaitán et al. (2020). For CAHA/CAFOS, we combined the flat fields using `PyRAF`, and we used a customized `Python` script to separate the *o* and *e* beams into two separate images. We normalised each beam to the corresponding median value and created the *o* and *e* beam combined flat. We followed the same procedure for each image. We performed this correction since flat fields were obtained with the full optics on the light pathway. This led to a rather different count rate in each beam what would have led to an inaccurate normalisation. Finally, we split all the reduced images into an *o* and *e* image and applied the `L.A. Cosmic` algorithm (van Dokkum 2001) to remove cosmic rays.

We used `PyRAF` to measure the on-frame full width at half maximum (FWHM) in each image including the high- and zero-polarised standard stars. The FWHM was measured independently for the *o* and *e* beam since the shape of the point spread function (PSF) can vary, especially for

sources with a high degree of polarisation.

To obtain reference field stars we used a source detection algorithm based on `DAOStarFinder` in `Photutils` and applied it to the background-subtracted o and e images separately. The selected sources were those with a threshold above the median plus three times the standard deviation of the background. The statistics were calculated per beam and per angle position of the HWP using a sigma clipping of the masked image. From these sources, we discarded those that were clearly extended and those that lay too close or partially within the instrumental mask edges. We also checked whether the source was saturated in any of the beams. We ended up with five sources, including GRB 210610B, in the FORS2 images and five sources in the CAFOS images. The sources from FORS2 and CAFOS images are different due to saturation or because sources fall at the mask edges.

We performed aperture photometry using circular apertures with a radius equal to the FWHM and applied infinite-aperture corrections using a custom `Python` script to the FORS2 data. In order to avoid contamination by a nearby spurious source, we measured the flux for the CAHA/CAFOS data using a fixed aperture of three times the FWHM per image and per beam and subtracted the sky of an annulus around the source with an inner and outer radius of four and five times the FWHM, respectively. In the FORS2 images, this spurious source was outside the measured region. The errors for the aperture photometry were obtained considering each beam as an unique image, that is, we separated the ordinary stripes from the extraordinary stripes.

With the measured flux values per source and per beam, f_o and f_e, we obtained the Stokes parameters Q and U describing the linear polarisation (see e.g. Patat & Romaniello 2006; Bagnulo et al. 2009) for each of our images. We used the normalised Stokes parameter for the linear polarisation.

$$\frac{Q}{I} = q = \frac{2}{N}\sum_{i=0}^{N-1} F_i \cos\frac{i\pi}{2} \tag{4.1}$$

$$\frac{U}{I} = u = \frac{2}{N}\sum_{i=0}^{N-1} F_i \sin\frac{i\pi}{2} \tag{4.2}$$

where N is the number of positions of the half-wave plate, I is the intensity, and F_i is the normalised flux difference per HWP position angle,

$$F_i = \frac{f_{o,i} - f_{e,i}}{f_{o,i} + f_{e,i}} \tag{4.3}$$

Following the equations above, we can obtain the polarisation degree P_{lin},

$$P_{lin} = \sqrt{q^2 + u^2} \tag{4.4}$$

$$\tag{4.5}$$

For the position angle, we followed the formalism as used in Bagnulo et al. (2009).

We then corrected for the effects of optics and detector in the polarisation images. To do this, zero-polarised standard stars were observed in the corresponding bands with VLT/FORS2 following the procedures detailed in Anderson (2015). For CAHA/CAFOS, observations of standard stars were carried out in the same night. In the case of VLT/FORS2, *b*- and *z*-band standards were completely saturated, and no subsequent standards were found in the ESO archive around the time of the observation. For the *R* band, the standards were also saturated. We then used WD1620-391 for the zero-polarised standard star, observed 18 days after the GRB, for VLT/-FORS2, and BD+33 2642 (Turnshek et al. 1990) for CAHA/CAFOS observed in the same night as GRB 210610B.

We finally removed the effect on the polarisation induced by the dust in the Milky Way (MW). To do this, we measured the *q* and *u* parameters for the field stars in our images. However, FORS2 is known to have a radial profile in which the polarisation varies across the field from the optical axis towards the edges of the detectors (see e.g. González-Gaitán et al. 2020). To account for this effect, we applied the corresponding correction by using the *q, u* background correction and the instrumental polarisation maps presented in González-Gaitán et al. (2020). We then measured the Galactic interstellar polarisation (Galactic ISP, or GISP) using three methods, following Wiersema et al. (2012): First, we measured the mean values for the *q, u* parameters from the field stars. Then we performed a one-dimensional Gaussian fit to the *q, u* values of the field stars by generating a normal distribution of values for the *q, u* within their corresponding errors, and we then fitted a Gaussian to each Stokes parameter. Finally, we performed a two-dimensional Gaussian fit to the *q, u*, adapting the procedure from the one-dimensional Gaussian fit (see Fig. 4.2 for an example of the two-dimensional Gaussian fit). All the *q, u* fitted parameters are consistent within the errors, and we therefore vectorially subtracted the mean value from the *q, u* values for the GRB. The mean sky values are listed in Tab. 4.1, which are all consistent with or close to zero. Both *q* and *u* show some variation from one epoch to the next, which we assumed is due to different sky background light between the epochs[6].

For the CAFOS images, the same analysis was performed, although we were unable to correct for background polarisation and instrumental polarisation across the images because we lack a characterisation as we have for FORS2. However, lunar illumination was close to 0%, and we do not expect a high instrumental polarisation (Patat & Taubenberger 2011) for CAFOS. Indeed, the two-dimensional Gaussian fit to the field stars (see Fig. 4.2) shows it to be consistent with no polarisation from the ISM and implicitly, no polarisation from the CAFOS instrument.

After the polarisation induced by the MW dust was removed we calculated the final polarisation from both instruments in all the filters. Next, we needed to consider the contribution to the polarisation from the dust in the host galaxy itself. Since the information is more limited than for the dust in the MW we assumed a Serkowski law (Serkowski et al. 1975) for the host galaxy. From the spectral energy distribution (SED) fit of the GRB light curve, we obtained the colour excess on the line of sight (see Sect. 4.4.2). Assuming this value as the extinction of the afterglow at the host galaxy, using $P_{ISP}(\%) \leq 9.0 \times E(B-V)$, we find that the contribution from the host galaxy could be as high as $P_{\text{Host ISP}} \leq 0.09\%$. We note that in extragalactic sight lines, this may not be applicable

[6] ESO weather log.

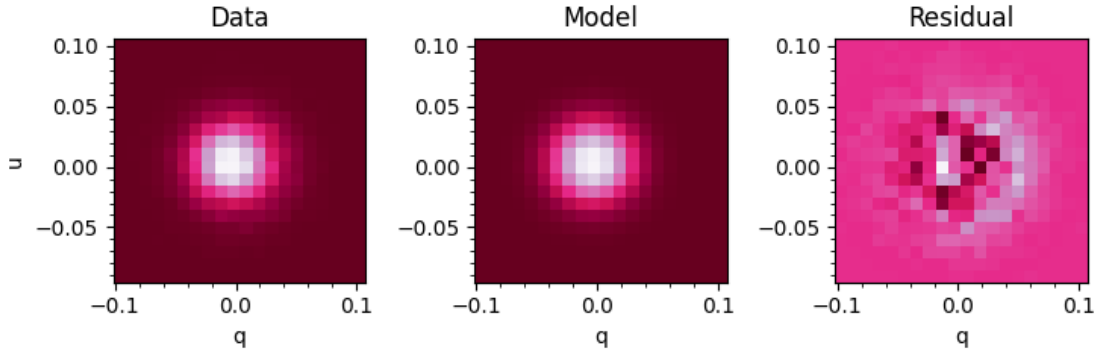

Figure 4.2: Two-dimenssional gaussian fit to the field stars q, u parameters. *Left*: Normal distribution of randomly generated data around the q, u values. The amplitude to generate the data is the Stokes parameter errors. *Central panel:* two-dimensional gaussian model fitted to the data points. *Right:* Residuals.

because the dust properties may differ from those of the MW (Nagao et al. 2022). This value is well below the PD measured for the afterglow, and we therefore considered the host contribution to be negligible. Finally, we corrected for the polarisation definition bias with the modified asymptotic estimator (MAS) Plaszczynski et al. (2014). The corrected values for the polarisation degree are shown in Tab. 4.1 before and after the bias correction.

We also determined the polarisation position angle (PA) for the GRB afterglow. The FORS2-measured raw PA was corrected for chromaticity using the tabulated values per bandpass presented in Anderson (2015). We then corrected for it using the standard star Hiltner 652, observed on the 19, July 2021, although the PA correction is very small with $\Delta\theta = 0.5 \pm 0.9$. The high polarisation standard in $R_{Special}$ band closest in time to the GRB was also saturated in at least one beam. We corrected the derived PA value of the standard to the value presented in Cikota et al. (2017). As the measured b-band value for the PA in Hiltner 652 is very close to the B band value in Cikota et al. (2017) we use B band to correct for the b-band value. For the z band, no observations were found so far for this standard, and we therefore used the PA for the I band in (Cikota et al. 2017). The high polarisation standard observed for CAFOS, Hiltner 960, was corrected to the "theoretical" value following Schmidt et al. (1992).

We detect polarisation at $\gtrsim 3\sigma$ significance for the first and last epochs, while the second epoch is consistent with zero polarisation. We detect 1σ polarisation in the R band on the second epoch. We consider this measurement, together with the R band observation at ~0.26 days for the b and z band as limit, however. Since the MAS correction is not completely applicable when $\mathrm{PD}/\sigma_P < 3.0$, we did not apply this correction to the mentioned limits. In this PD regime, the PA would behave erratically and, we therefore cannot treat it as a limit.

Table 4.1: Measured values for the linear polarisation and PA of GRB 210610B. When the standard corrected PA is negative, it was corrected to positive values by subtracting it from 360°. We measured the (S/N) in each beam and at each HWP angle image. The value we present here is the lowest we measured in one beam in one image at a certain HWP angle.

Epoch $t-t_0$ (day)	Bandpass	Instrument/Telescope	q_{sky} (%)	u_{sky} (%)	P_{Lin} (°)	$P_{Lin,Debiased}$	θ	S/N
0.1205	R_C	CAHA/CAFOS	0.2±2.4	-0.01±0.31	4.50 ± 1.45	4.27 ± 1.45	183 ± 9	> 500
0.2418	$R_{Special}$	VLT/FORS2	-0.30±0.32	-0.29±0.20	0.28 ± 0.20	–	267 ± 19	> 710
0.2593	$R_{Special}$	VLT/FORS2	-0.79±0.28	0.81±0.22	0.60 ± 0.24	–	17 ± 11	> 690
0.2698	b_{High}	VLT/FORS2	–	–	0.18 ± 0.16	–	187 ± 24	> 395
0.2803	$z_{Special}$	VLT/FORS2	–	–	0.23 ± 0.28	–	199 ± 35	> 180
1.2674	$R_{Special}$	VLT/FORS2	-0.13±0.22	0.06±0.07	2.28 ± 0.22	2.27 ± 0.22	237 ± 3	> 330
1.2766	$R_{Special}$	VLT/FORS2	-0.36±0.39	0.06±0.07	1.72 ± 0.27	1.69 ± 0.27	238 ± 5	> 300

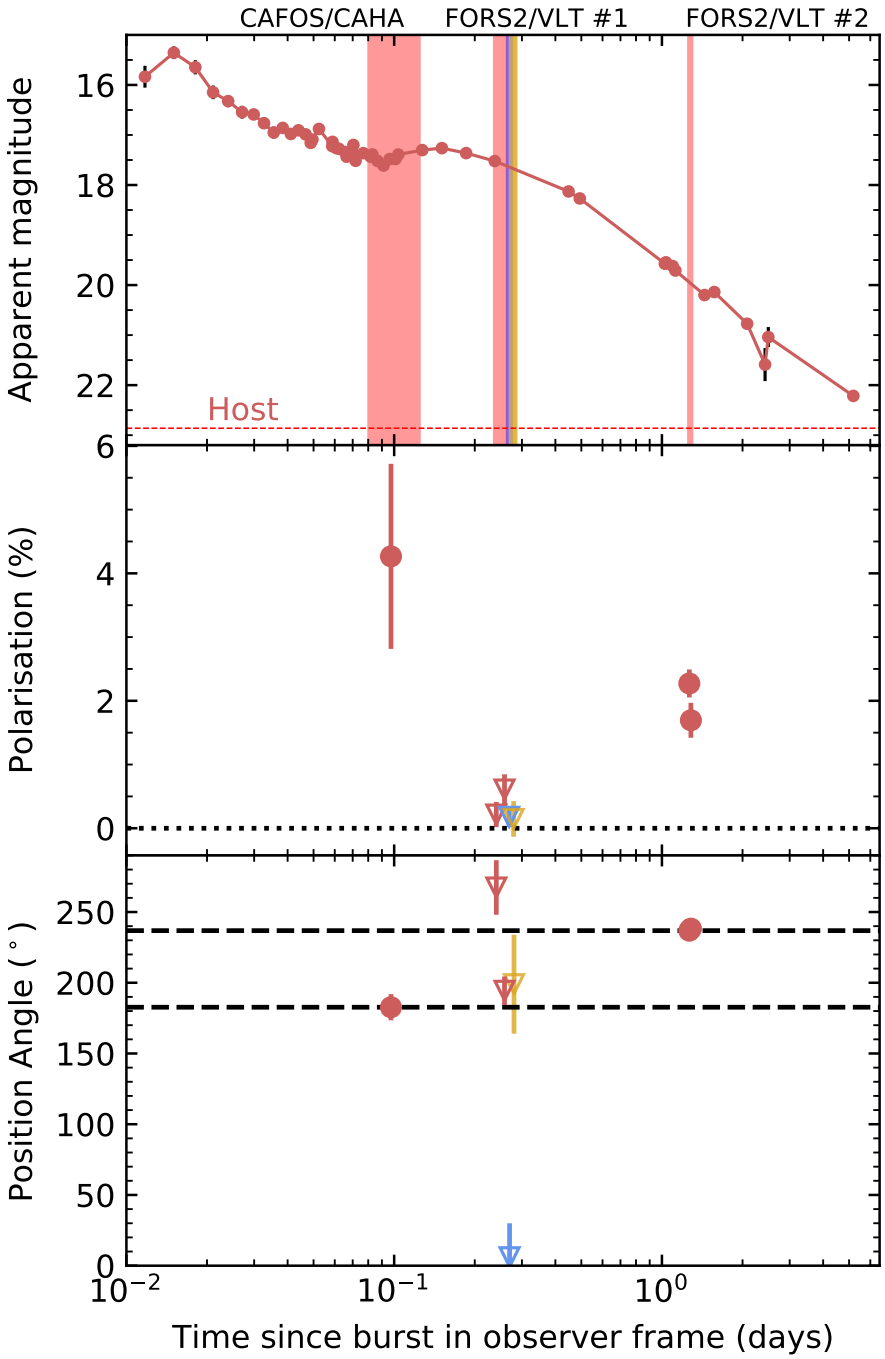

Figure 4.3: Afterglow, PD and PA evolution of GRB 210610B. *Top panel:* GRB 210610B light curve for the *r* band (see Tab. B.1). We converted the SBT *Clear* band and *R* band into *r* band as indicated in 4.3.3 and 4.3.3. The vertical stripes from left to right denote the first polarimetry epoch (CAHA/CAFOS) and the second and third epochs (both with VLT/FORS2). The host observations in *r* band are marked with a dashed red line. *Middle panel:* Evolution of the linear polarisation of GRB 210610B. The red dots shows the measured polarisation for *R* band, and blue and orange triangles denote the lower limits in the *b* and *z* bands. *Bottom panel:* Linear polarisation measured PA for GRB 210610B. The detections are marked with filled circles, and the corresponding PAs for the PD limits are marked with empty squares as these values are neither lower nor upper limits. The dashed black lines denote the PA for the first (bottom) and the third (top) epoch.

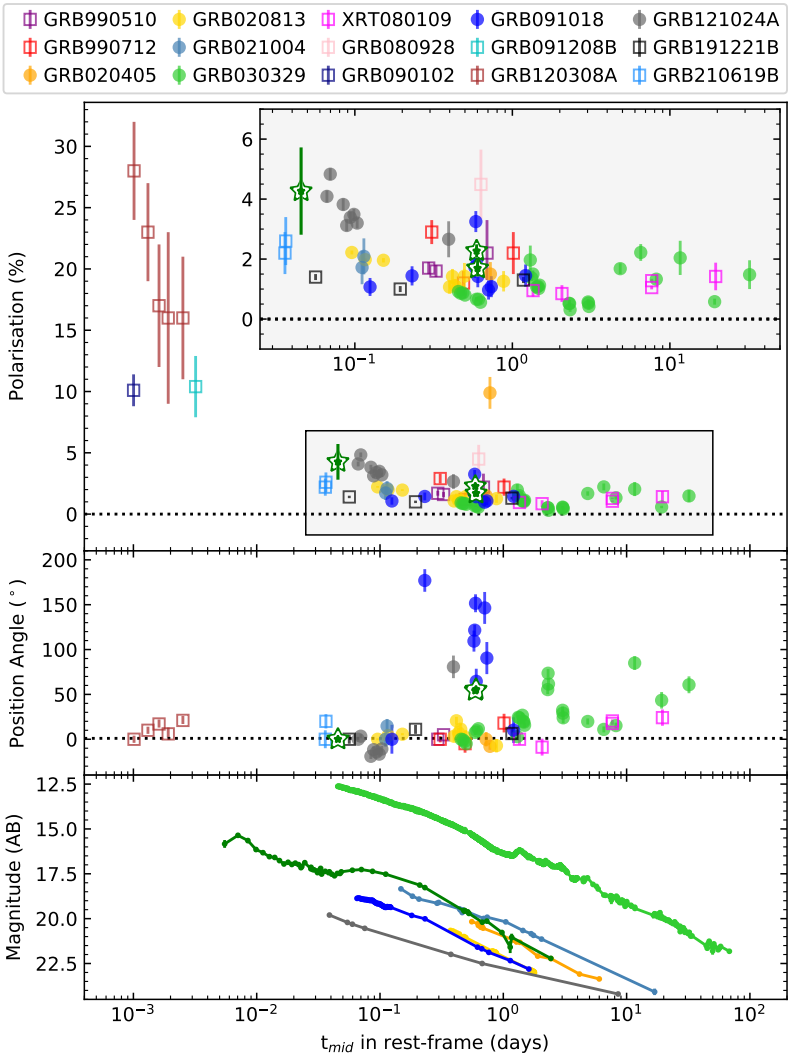

Figure 4.4: Comparison of GRB 210610B polarisation evolution to previous detections of GRB afterglow positive polarisation. *Top:* Measured GRB linear polarisation degree on the optical afterglow emission. The white and green stars mark the polarisation degree measured for GRB 210610B in all bands. As for all the data points, we did not make a distinction on the photometric band in which the polarisation was measured. We only selected the measured values that show a $P/\sigma_P > 3$ for all bursts, including GRB 210610B. The filled circles indicate the bursts for which a light curve is shown in bottom panel, and empty squares represent the bursts that are not represented in this last panel. The data and references can be found in Tab. C.1. *Middle pannel:* PA measured for each corresponding burst and epoch in the same fashion as in the top panel. Note that as for GRB 021004 there is no measured PA. To better distinguish the PA changes, we subtracted the first PA value to all values and calculated the absolute value for those with a mean value below zero. We do not find significant PA changes except for GRB 121024A, GRB 091018, GRB 030329, and GRB 210610B. We note that the measures were carried out with different instruments, and the data reduction and analysis can be different from the one we followed in this work. *Bottom panel:* Light curve for some exemplary burst with data available in the literature (GRB 020405 (Masetti et al. 2003), GRB 020813 (Gorosabel et al. 2004), GRB 021004 (de Ugarte Postigo et al. 2005), GRB 030329 (Lipkin et al. 2004), GRB 091018 (Wiersema et al. 2012), GRB 121024A (Wiersema et al. 2014) and GRB 210610B.

4.4.2 Light-Curve analysis

We first modelled the optical and X-ray light curves simultaneously with a smoothly broken power law (Beuermann et al. 1999), $F = (F_1^\kappa + F_2^\kappa)^{-1/\kappa}$, where $F_x = f_{break}(t/t_{break})^{-\alpha_x}$, f_{break} being the flux density at the break time t_{break}, κ is the break smoothness parameter, and the subscripts 1, 2 indicate pre- and post-break, respectively. We did not consider data before 0.06 days (~5 ks) because they are still dominated by the initial rapid decay. Even before any modelling was performed, it is clear that the optical light curve is initially flat at least until ~0.25 days (~20 ks; see Fig. 4.5), while at the same time the X-ray behaviour is difficult to discern, though the two groups of observations at 4 ks and 7 ks show possible fading, in contrast to the optical. Not knowing the precise evolution of the early X-ray data, we allowed the initial X-ray decay to be different from the optical. Note that a different decay implies a colour evolution between X-rays and the optical. We find a shallow break with $t_{break,\,opt} = 0.326 \pm 0.011$ d (27.7 ± 1.2 ks), a flat optical decay with $\alpha_{1,opt} = 0.00 \pm 0.01$, and an optical to X-ray decay index $\alpha_{2,} = 1.85 \pm 0.04$, with a break smoothness $\kappa = 1.4 \pm 0.1$, with χ^2/d.o.f.=2.6.

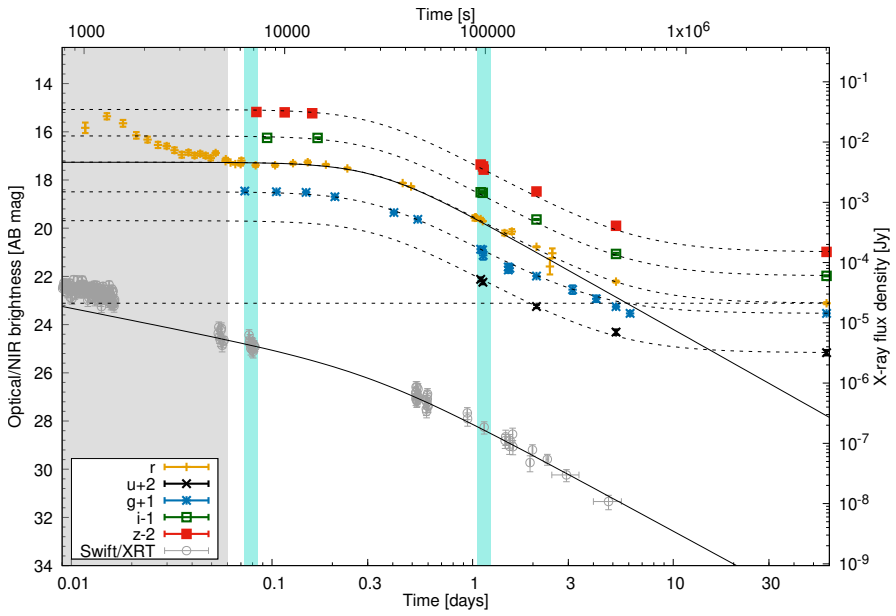

Figure 4.5: GRB optical to X-ray light curve fit to available photometry (see Tab. B.1) and *Swift* X-ray data. The grey shaded region is not taken into account for the fit as it may be contaminated by the prompt emission. The clear cyan regions mark the times we chose to derive the SED of the light curve. The data are shown with an offset in flux for better visibility.

After the break, we analysed the full optical to X-ray SED when we the coverage in both frequency regimes was best. To build this SED, we first created the XRT spectra using the time-slice tool in the XRT repository (Evans et al. 2007, 2009) in the range 30ks-50ks at a mid-time of 1.2 days. We then shifted the optical GTC/HIPERCAM ugriz data at 1.097 days closer to these times using the decay indices found above.

We modelled the afterglow SED from optical to X-ray frequencies using `Xspec v12.13.0` (Arnaud 1996). The redshift was fixed to $z = 1.1341$, and we fixed the Galactic hydrogen

column density to $N_H = 3.94 \times 10^{20}\,\mathrm{cm}^{-2}$ (Willingale et al. 2013). The data are best modelled by a single power-law (χ^2/d.o.f. = 264.5/298) with $\beta = 0.869^{+0.003}_{-0.007}$, intrinsic absorption $N_H = 18.3^{+6.5}_{-5.9} \times 10^{20}\,\mathrm{cm}^{-2}$ (using the Tübingen-Boulder ISM absorption model; Wilms et al. 2000) and E(B-V) < 0.01 mag, using the Small Magellanic Cloud (SMC) extinction law (Pei 1992).

We also obtained an optical to X-ray SED at 0.079 days (6871 s) taking the X-ray data between 6000 and 8000 s and using the optical light curve above to shift the corresponding griz photometry. After fixing the redshift, extinction, and absorption as for the late epoch and following the same fitting procedure, we find that the data are best modelled by a broken power law (χ^2/d.o.f. = 143.3/197) with $\beta_{opt} = 0.43^{+0.046}_{-0.046}$, and $\beta_X = \beta_{opt} + 0.5$, which indicates the presence of a spectral break, like the cooling break for synchrotron emission. We note that the spectral index of the high-frequency branch is consistent with the value found at late time, suggesting that the break shifted to lower frequencies with time, which is expected for an ISM environment within the fireball model and before the jet-break occurs (Sari et al. 1998). However, the shallow decay of the early light curve cannot be explained within the standard fireball model, unless we consider a more complex scenario such as an energy injection (e.g., Zhang et al. 2006).

4.4.3 Optical Spectrum analysis

The afterglow spectrum observed by OSIRIS ~0.25 days after the burst shows several transitions of FeII, MgII, and MgI (see Tab. 4.2), all of them at a common redshift of $z = 1.1341 \pm 0.0004$ (see Fig. 4.6 and Table 4.2). This value is a lower limit for the burst redshift due to the non-detection of fine-structure lines excited by the GRB itself. The detection of the afterglow in the bluest band from *Swift*/UVOT sets an upper limit of $z = 1.7$, using the so-called Lyman drop-out technique, following (Jakobsson et al. 2012). Considering this limit and the lack of absorption lines common to GRBs (Christensen et al. 2011) at higher redshift, we hence adopted $z = 1.1341$ as the redshift of GRB 210610B. We also detected two absorption features that correspond to the Mgii doublet in an intervening system at $z = 0.5572 \pm 0.0002$.

The equivalent widths (EWs) of the detected absorption lines were measured using the GRB-spec database tools (de Ugarte Postigo et al. 2014a; Blažek et al. 2020) (see Tab. 4.2). We followed de Ugarte Postigo et al. (2012) to compare these values with the common trend for long GRB sight-line environments. The line strength parameter (LSP) measured for GRB 210610B is extremely low, LSP = -2.17±1.13, implying that this line of sight has weaker features than 99.85 % of the GRBs in the aforementioned sample. The line-strength diagram in Fig. 4.6 shows that the Fe II lines are particularly weak and are only detected through the very high signal-to-noise ratio of the spectrum. The magnesium features are stronger, but still among the weakest in the sample. The low EW values imply a low column density and hence a low amount of gas and possibly dust in the line of sight consistent with a negligible dust-induced polarisation.

Table 4.2: Equivalent widths in observer frame measured in the afterglow spectrum.

Observed λ (Å)	Feature	z'	EW (Å)
5001.69	FeII 2344.21	1.1336	0.49 ± 0.07
5066.45	FeII 2374.46	1.1337	0.23 ± 0.06
5084.79	FeII 2382.77	1.1340	0.61 ± 0.07
5520.91	FeII 2586.65	1.1344	0.25 ± 0.07
5549.64	FeII 2600.17	1.1343	0.53 ± 0.07
5976.16	MgII 2796.35	1.1341	3.29 ± 0.10
	MgII 2803.53	1.1345	
6090.41	MgII 2852.96	1.1348	0.64 ± 0.07
4353.92	MgII 2796.35	0.5570	0.39 ± 0.10
4366.46	MgII 2803.53	0.5575	0.23 ± 0.08

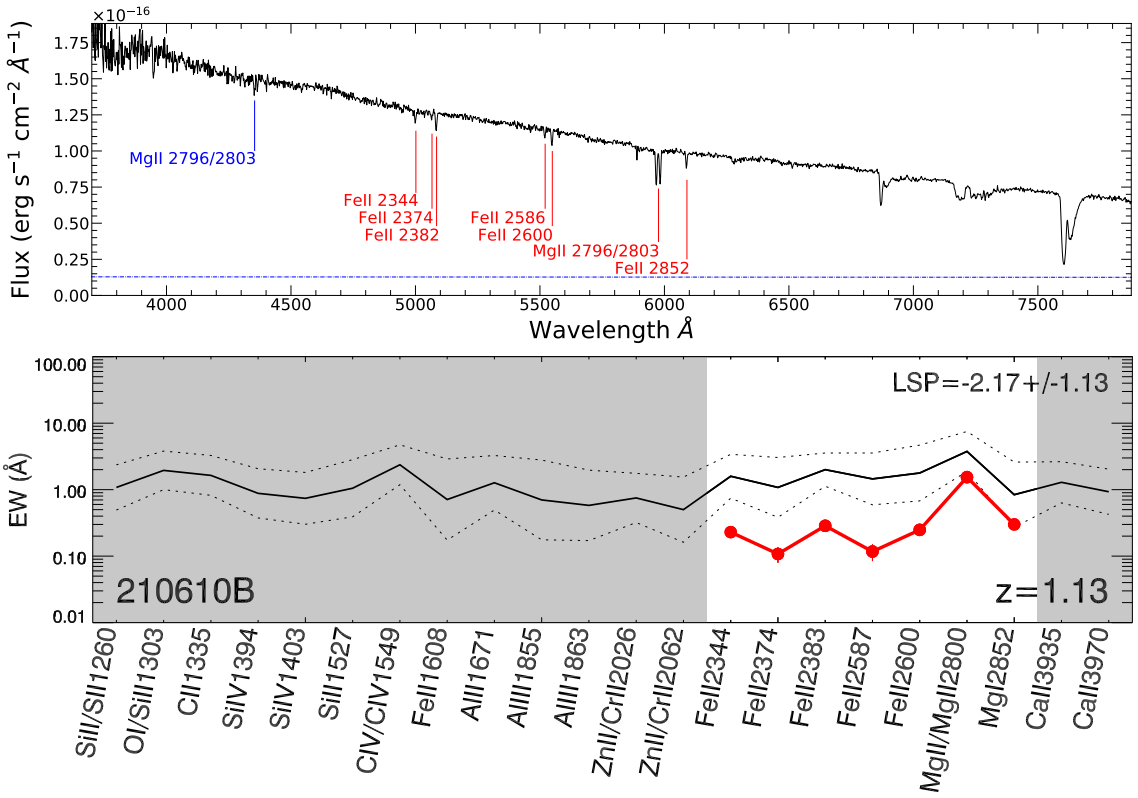

Figure 4.6: Absorption spectroscopy and line properties for GRB 210610B. *Top:* Spectral features detected at the redshift of the GRB, plotted in red, and the features from the intervening system are shown in blue. The dashed blue line shows the error spectrum. *Bottom:* Line-strength diagram for the spectral features in the host galaxy. The diagram compares the features measured in our spectrum (red) with the average values of a larger sample (black) (see Sect. 4.4.3).

4.4.4 Host galaxy

We observed the location of GRB 210610B ~ 58 days after the burst using GTC/HiPERCAM and ~ 253 days after with GTC/EMIR. In the HiPERCAM images, we detect an underlying object at the GRB position and we consider this object to be the host. We also find a putative companion galaxy towards north-west of the host candidate (see Fig. 4.1) at a distance of ~ 2.7", which would correspond to a distance of 22 kpc at the redshift of the system. The photometry of the host galaxy is shown in Tab. B.1, together with the values for the companion.

We performed a SED analysis for the two galaxies assuming that both of them are at the GRB redshift. For this analysis, we used the SED fitting code `CIGALE`[7] (Burgarella et al. 2005; Noll et al. 2009; Boquien et al. 2019) in its latest version. To fit the star formation history (SFH), we chose a delayed star formation history with an age for the main stellar population ranging from 0.1 to 13 Gyr and a late burst with an age varying from 20 – 500 Myr. We allowed the code to vary the corresponding mass fraction from the total galaxy mass for the late burst from 0, which implies a single decaying exponential for the SFH modelling, up to 0.6, that is, 60% of the total galaxy mass. We use the initial mass function (IMF) as described in Chabrier (2003) with a Bruzual & Charlot (2003) stellar population model, assuming a stellar sub-solar metallicity (Z_*) for the galaxy (see Sect. 4.4.3 and 4.5) that was set to vary from 0.004 to 0.008, according to the scheme used in Bruzual & Charlot (2003). The nebular emission was modelled considering the same metallicity values for the gas.

For the attenuation law, we considered the modified Calzetti et al. (2000) law implemented in `CIGALE`, assuming a Small Magellanic Cloud (SMC) extinction law for the attenuation of the emission lines. We did not observe a colour evolution for the Galactic-dust-corrected (Schlafly & Finkbeiner 2011) magnitudes, and we do not detect the host galaxy in the H band down to 22.9 magnitudes. This might indicate a low level of dust emission due to low dust heating from UV massive star photons, indicating a low number of massive stars or an intrinsic lack of dust in this system. Since the amount of detected Mg, typically formed in the explosion of massive stars, is large compared to the amount of Fe in the traced system, although still low for common lGRBs sight-lines (see Fig.4.6), this favours the scenario of low intrinsic extinction rather than the absence of massive stars (see Sect. 4.5 for an extended explanation). Therefore, we chose the colour excess of the nebular lines to be lower than 0.1. The slope of the attenuation curve (Boquien et al. 2019) was allowed to vary between -0.6 and 0.6. For the dust emission, we selected the Dale et al. (2014) models and allowed the exponent that controls the radiation field distribution of the re-emitted energy by dust heating to vary between 1.0 and 3.0.

We applied the same SED fit to both galaxies. However, the companion galaxy shows colour excess in the HiPERCAM observations, and we therefore allowed the colour excess for the nebular lines to range up to 0.4. The results for the computed physical properties from the SED fit can be found in Tab. 4.3 and the best fit is shown in Fig. 4.7. The SED of the companion galaxy allowed us to determine a photometric redshift that is consistent with the redshift for GRB 210610B. The companion is at a distance of 2.67 arcsec, corresponding to a physical distance of 22.6 kpc at a

[7] https://cigale.lam.fr/

redshift of $z = 1.1341$. We therefore assumed that these two galaxies are part of a group.

Table 4.3: Fitted physical properties of the putative host galaxy of GRB 210610B and its putative companion.

	Host galaxy	Host companion
$\log_{10}(M_*)(M_\odot)$	$9.10^{+0.40}_{-0.20}$	$9.60^{+0.55}_{-0.24}$
$\log_{10}(SFR)\ (M_\odot/yr)$	$1.06^{+0.12}_{-0.10}$	$0.47^{+0.32}_{-0.10}$
$sSFR\ (Gyr^{-1})$	9.26 ± 6.02	0.76 ± 0.68
A_V (mag)	0.19 ± 0.10	0.51 ± 0.33
Z_*	0.006 ± 0.002	0.006 ± 0.002
Reduced χ^2	0.49	0.50

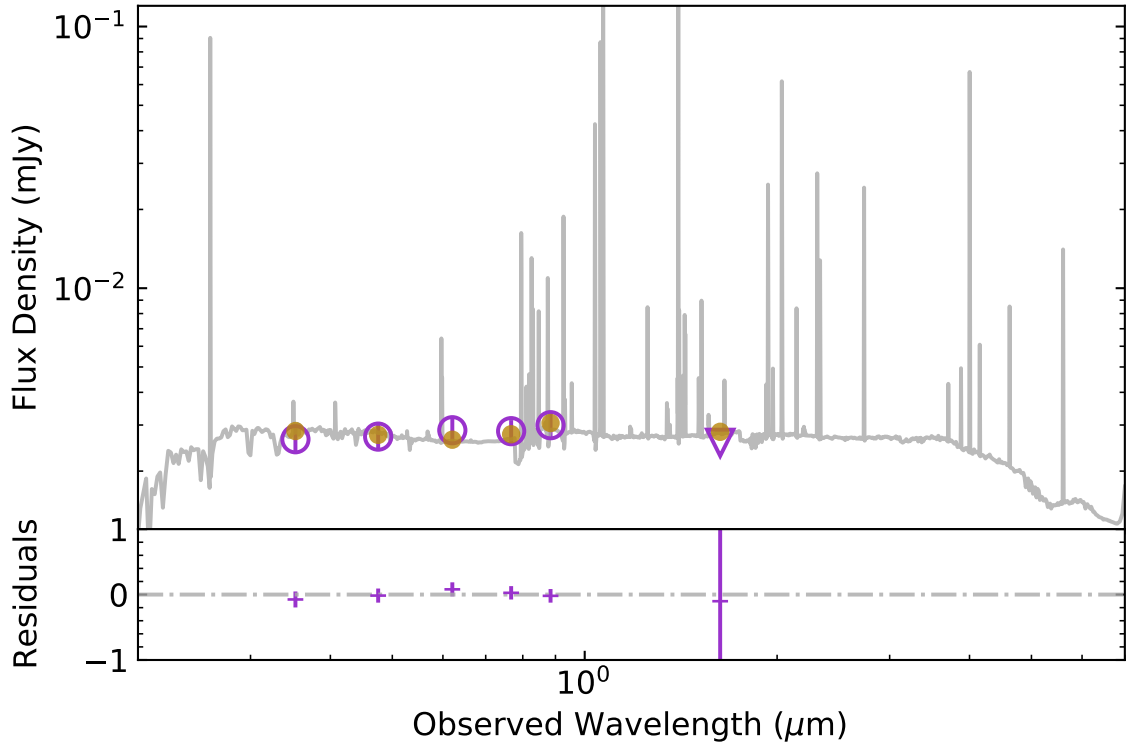

Figure 4.7: GRB host SED with the corresponding residuals modelled using the CIGALE fitting code (Burgarella et al. 2005; Noll et al. 2009; Boquien et al. 2019) for the putative host galaxy of GRB 210610B. The vertical blue arrow indicates the *H* band upper limit.

4.5 Discussion

A broad study of the GRB prompt and afterglow emission together with its host galaxy is crucial for better constraints of the characteristics of GRB 210610B. The burst prompt emission presents the GRB as a hard burst, as observed by *Swift*, positioning it in the top part of the long GRB region

of the hardness ratio versus T_{90} relation (see e.g. Lien et al. 2016). The isotropic equivalent energy, together with the observed peak energy, shows that GRB 210610B is fully consistent with the Amati relation (Amati et al. 2002; Amati 2006) for long GRBs. The prompt, high-energy emission of GRB 210610B has been analysed with Fermi data by (Chen et al. 2022). They reported that the prompt emission is best fit by a hybrid jet model (Gao & Zhang 2015) in which a hot fireball component dominates the emission in the beginning, while a Poynting flux component supersedes at later times. Chen et al. (2022) described these results as consistent with the magnetar model as a plausible central engine (Metzger et al. 2011).

4.5.1 Host galaxy

The SED analysis of the GRB 210610B host reveals a galaxy with a low stellar mass, consistent with a dwarf galaxy that is actively forming stars and has low extinction. At the same redshift, the companion is more massive than the GRB host, with a higher stellar mass but lower SFR. The extinction for this galaxy is also higher than that of the GRB host assuming the same extinction law.

From the afterglow spectrum, we find that GRB 210610B is embedded in an environment with low amounts of FeII and somewhat higher values for MgII and MgI. The low amount of Fe could be indicative of a low number of SN Ia in the host, since these explosions are the main sources of Fe (Pagel 2009). This could mean that either there is an intrinsic lack of this type of stellar explosions near the absorber site or that the system itself is too young to have been Fe-enriched via SN Ia. However, the absence of fine-structure lines in the spectrum does not allow us to determine the distance of the absorbing clouds to the explosion site and, therefore, the afterglow spectrum could be tracing gas in the external parts of the host galaxy, where we would expect it to be less enriched. Nevertheless, we find a higher relative value for the EWs of Mg, although it is still low compared to the mean value found for GRB sites (de Ugarte Postigo et al. 2012). Mg is released into the ISM through the explosion of massive stars (Pagel 2009). Together with the low amount of Fe, this might suggest that the host galaxy is a very young system. This is also supported by the extinction we measure from the SED fit. The A_V value may indicate that the host galaxy has a low amount of dust, which is expected for a low metallicity and, therefore, for a young system.

4.5.2 Afterglow

The GRB afterglow follows a decay-plateau-decay behaviour with an initial decay that is well fitted by a broken power law with an optical spectral slope at ~0.08 days of $\beta_{opt} = 0.43^{+0.05}_{-0.05}$ and a $\beta_{XR} \sim 0.83$. Afterwards, the light curve enters a plateau phase that lasts ~0.247 days to finally change to the final decay at ~0.326 days after burst. This final decay is better fitted by a power law with $\beta = 0.869^{+0.003}_{-0.007}$, consistent within errors with β_{XR} at ~0.08 days after GRB. The change in the spectral slope at ~0.08 days might be indicating a spectral break at the beginning of the plateau phase. The SED fit shows negligible extinction on the line of sight towards the GRB and a low X-ray Hydrogen column density, as compared to N_H values for relatively low redshift GRBs (Campana et al. 2010). This low N_H together with the low E(B-V), contradicts what would be

expected for low-redshift bursts, where a higher dust-to-gas ratio is expected for lowly N_H X-ray absorbed bursts (Campana et al. 2010).

4.5.3 Polarisation

Our polarisation observations match three very important stages of the GRB 210610B afterglow light-curve. The first polarimetry measurements were performed 0.1205 days after burst, right after the light curve entered the plateau. The second epoch at ~0.26 days is close to the end of this plateau phase, almost consistent with the break of the optical light curve at 0.326 days after the GRB. After this, the light curve undergoes its final decay, where a final polarimetry epoch was observed. The afterglow is polarised at the beginning and towards the end of the light-curve evolution, but not around the optical break at 0.326 days after burst, where the polarisation drops to zero with a small rise to 0.61% in the next observation, which is slightly above the $P_{\text{Host ISP}}$ limit, but only at a 2.5-σ level. In the final decay, the polarisation increases to 2.27% and then decreases to 1.69% as the afterglow fades away. We find that *b* and *z* bands show polarisation values consistent with zero at a close epoch to the 2.5-σ *R*-band measurement. Therefore, the multi-band observations do not allow us to asses chromaticity/achromaticity in the afterglow polarisation. The PA varies by ~54° between the 3σ detections. The measured polarisation is well consistent with prior measurements for linear polarimetry of GRB afterglows, as shown in Fig. 4.4.

One important aspect when determining the intrinsic polarisation is to constrain any contribution from the dust in the host galaxy. A possible polarisation from the MW was removed during the analysis (see Sect. 4.4.1). The SED fit to the GRB light curve results in a negligible value for the afterglow extinction on the line of sight and the inferred upper limit for the GRB host ISP is rather small compared to errors of the measured 3-σ polarisation detections (see Sect. 4.4.1). This means that either the polarisation contribution of the host galaxy along the line of sight is well below the $P_{\text{Host ISP}}$ limit or that this contribution would cancel the afterglow polarisation out. The relatively high values we measured for the 3σ detections and the very low limit for the host galaxy polarisation led us to assume that the host contribution is negligible. This low extinction also supports the scenario in which the polarisation is interpreted as intrinsic to the GRB afterglow. This is further confirmed by the polarisation non-detection in the second epoch, which is an indirect measurement of the host ISP.

4.5.4 Theoretical Interpretations of the polarisation signals

The first polarimetry observations show a rather high linear polarisation degree of $\sim$ 4% at $t \sim$ 0.1205 day. Considering that the observations were carried out during a shallow decay/plateau phase, a non-negligible fraction of optical photons might originate from refreshed shocks in the original ejecta from the central engine. As previous polarimetry studies of the early afterglow indicate that ejecta from the central engine contain large-scale ordered magnetic fields, at least for a subgroup of GRBs if not for all (e. g. Mundell et al. 2013), the refreshed shock emission can be polarised due to the ordered magnetic fields in the ejecta. The combination of the polarised refreshed shock emission and unpolarised forward shock emission is likely to give low-

/intermediate-polarisation signals. For GRB 191016A, Shrestha et al. (2022) reported the detection of polarisation signals with $P \sim 5-15\%$ which are coincident with the start of the plateau phase. An energy injection model was discussed to explain the coincidence.

The optical light curve starts to decline at $t \sim 0.2$ days (see the top panel of Fig.4.3). This indicates that the energy injection stops around that time and that the optical band is dominated by the forward-shock emission well before the second polarisation epoch is conducted at $t \sim 0.24$ day. The magnetic fields in the forward-shock region (the shocked ambient medium) are conventionally assumed to be generated locally by microscopic instabilities in shocks (see e.g. Medvedev & Loeb 1999), and they are expected to be highly tangled. The PD of the forward-shock emission is expected to be zero when the line of sight does not run along the jet edge. The low polarisation at $t \sim 0.24-0.28$ days can be explained naturally when the optical emission is dominated by the forward-shock emission.

Due to the relativistic beaming effect, the observer can see only a small visible region (a small patch with an angular size of $1/\Gamma$, located around the point at which the line of sight intersects the jet) instead of the entire surface of a shock front. The visible region appears as a ring due to a relativistic limb-brightening effect (Granot et al. 1999). Synchrotron emission from each small segment of the ring can be polarised when the random magnetic fields parallel and perpendicular to the shock normal have different averaged strengths. However, the net PD is zero because of the symmetry of the visible region.

As the forward shock slows down, the angular size of the visible region grows as $1/\Gamma \propto t^{3/8}$ (ISM) or $t^{1/4}$ (wind medium). Eventually, a part of the ring is located outside the jet edge and the emission region becomes asymmetric. This might have occurred by the third polarisation epoch at $t \sim 1.27$ day. Between the second and third epochs, the angular size of the visible region can grow by a factor of ~ 1.7 (ISM) or 1.4 (wind medium). Optical linear polarisation measurements have been carried out for many late GRB afterglows typically several hours to a few days after the prompt gamma-ray emission (e. g. Covino & Gotz 2016). In this period, a jet break is expected to occur. The detection or upper limits of the linear PD are generally low (less than a few percent), which might indicate that the shock-generated random magnetic fields parallel and perpendicular to the shock normal have similar averaged strengths. The polarisation signals $P \sim 2\%$ at $t \sim 1.27$ days might be explained in this geometrical model. If the large-scale magnetic fields in the ejecta are toroidal, the PA change between $t \sim 0.24$ days and $t \sim 1.27$ days is expected to be 0 or 90 degree. However, the large-scale magnetic fields in the ejecta can be largely distorted before they inject energy into the forward shock (or the original magnetic structure can be very different from the toroidal configuration). The position angle change can be any value. However, this model predicts a steeper decline at late times. Even in the non-spreading jet model, the expected decay index is $\alpha = 3(p-1)/4+3/4 \sim 2.05$ (ISM) or $(3p-1)/4+1/2 \sim 2.30$ (wind medium) for $p = 2.74$, which is steeper than the observed value $\alpha = 1.85 \pm 0.04$. If we rely on the rather high value of p obtained from the SED modelling, we can rule this geometrical model out.

The nature of magnetic fields that are generated in shock instabilities is not yet fully understood. The microscopic-scale tangled magnetic fields may decay so rapidly in the downstream of the shock that they could not account for the observed synchrotron flux (e. g. Sironi et al. 2015).

Alternatively, the forward-shock region could have magnetic field turbulence on large scales, comparable to the width of shocked region $\sim R/16\Gamma$ (e. g. Sironi & Goodman 2007). In this case, the PD and PA temporally change in a random manner, and PD $\sim 70\%/\sqrt{N}$, where N is the number of patches with a coherent magnetic field within the angular scale $1/\Gamma$ Gruzinov & Waxman (1999). Kuwata et al. (2023) constructed a semi-analytic model with a varying large-scale turbulent field in the forward-shock region, for which they performed numerical calculations in the case of isotropic turbulence and zero viewing angle. They obtained a randomly varying PD on a timescale of hours at a level of $\sim 1-3\%$ and PA with changes that were not limited to 90°. These properties appear to be consistent with our data of GRB 210610B. When hydrodynamic-scale turbulent magnetic fields are assumed, we have two possible scenarios: 1) the $\sim 4\%$, $\sim 0.2\%$, and $\sim 2\%$ polarisation signals are all due to turbulent magnetic fields, or 2) the $\sim 4\%$ polarisation signal is due to polarised refreshed shock emission, and the other two signals are due to turbulent magnetic fields.

For non-spreading top-hat jets with microscopic-scale tangled fields, the PD light curve would have two maxima around a jet break, with the polarisation PA changing by 90 degrees between the first and second maximum (Ghisellini & Lazzati 1999; Sari 1999). A possible jet break associated with the PA change of 90 degrees has been detected for GRB 121024A (Wiersema et al. 2014). We studied a non-axisymmetric top-hat jet model (homogeneous jets with elliptic jet edge) to determine whether the main features can be explained in this model. Jets like this might be produced due to the interaction between jets and stellar envelope/neutron star wind ejecta (see Fig. 1 in Lamb et al. (2022)) or jet precession (Huang et al. 2019). For non-axisymmetric jets, the PA change can be different from 90 degrees. Following Sari (1999), we estimated the polarisation light curve and the PA change around a jet break. However, we find that this model does not work for this event. The main reasons are that a) this model also predicts the steep decay at late times, as discussed in the geometrical model. b) We needed to fine-tune the timing of the second polarisation measurement (we need to place the observation precisely in the "valley" of the polarisation curve), or equivalently, we needed to fine-tune a combination of parameters that provide the jet break time. c) In the "valley", the polarisation needs to be very low (0.18-0.6%), compared to the earlier observation of $\sim 4\%$. To achieve this, Stokes u also needs to be almost zero when q flips sign. According to our rough parameter search (the geometrical parameters were ellipse eccentricity, ellipse orientation, and viewing angle), the eccentricity of the jet edge needs to be lower than roughly about 0.3. The low eccentricity does not allow the PA change to be significantly different from 90 degrees (in our example case to fit the polarisation light curve, the PA change is about 80 degrees).

4.6 Conclusions

GRB 210610B presents an exceptional scenario for performing polarimetry on the optical afterglow of a GRB. The light curve follows a decay-plateau-decay trend with a break after the plateau phase to a steep decay of the light curve. The SED modelling of the afterglow from X-rays to the optical indicates a dust free line of sight towards the GRB as well as a low N_H. This negligible amount of dust is confirmed by the low A_V value we derive for the host galaxy and is further

confirmed for the polarisation non-detection on the second polarimetry epoch. We also find that the GRB is embedded in a low-mass galaxy that seems to have a low amount of metals, which is indicative of a very young system.

The low amount of dust we find for GRB 210610B allowed us to study the intrinsic polarisation of the GRB afterglow. The optical afterglow is polarised at the beginning of the plateau phase of the light curve, disappears around the break achromatically, and reappears in the final decay of the light curve. In this complex behaviour, the first epoch seems to be dominated by the refreshed shock, which could explain the high polarisation value, while in the following epoch, the polarisation degree drops to zero as the forward shock would be dominating the optical emission. In the final decay of the light curve, the polarisation increases to $\sim 2\%$ which could be explained assuming a geometrical model or hydrodinamics-scale turbulent magnetic fields.

Some models predict that GRB afterglow polarisation evolves from high polarisation at early stages, while the prompt emission or the refreshed shocks dominate, followed by a fast decay of the polarisation often reaching a zero polarisation. Afterwards, the polarisation again increases to moderate/low values, including changes in the polarisation position angle (see Covino & Gotz (2016) for a review). To better understand the polarisation evolution of GRBs, we should pursue two approaches: On one hand, we need to study polarisation throughout different GRB light curve phases, and on the other hand we need to obtain larger samples of GRBs.

Chapter 5

The SHOALS Sample. Integrated properties of long GRB host galaxies.

Contents

5.1 Introduction

Over the last years, the GRB progenitor problem has become in a true problem. The commonly accepted division between long and short GRBs is not always clear from the duration of the prompt emission and its hardness (see Rastinejad et al. 2022 for an example of a long GRB that originated from a compact object binary merger). The host galaxy properties might help to find a solution for these cases. Long GRB host galaxies are actively star forming galaxies while for short GRBs the galaxy type seems to be more heterogeneous with lower star formation rates than for long GRB hosts (see e.g. Nugent et al. 2022; Fong et al. 2022; O'Connor et al. 2022).

Long GRBs are expected to originate from low metallicity massive stars at the end of their lives. They have been found to coincide temporally and spatially with observed type Ic-BL supernovae. Since the progenitor star is very massive, it is expected to have a short evolution time, which implies recent star formation activity at the GRB position in the host galaxy (see Sect. 1.3.1 for an extensive explanation and references). Observations of the underlying host galaxy have revealed that long GRBs are found in the brightest regions of their host galaxies (Lyman et al. 2017) and that they are actively star forming galaxies (Palmerio et al. 2019). Long GRB host galaxies studies are an unique tool to investigate the star formation rate (SFR) accross cosmic time since GRBs can be detected at many redshifts (see e.g. GRB 210905A at $z > 6$ Saccardi et al. 2023) and in many different galaxy, from small dwarfs (Thöne et al. 2021) to massive galaxies (see e.g. Thöne et al. 2024).

It is still not possible to detect directly these long GRB progenitors due to these large distances. Therefore, we can use host galaxies studies as an indirect tool to infer properties of the stellar population and star forming activity at the GRB site. Previous works on this topic have shown that long GRBs usually happen in metal poor galaxies (see e.g. Perley et al. 2016b; Palmerio et al. 2019) although some have been found in solar-metallicity host galaxies (see e.g. Heintz et al. 2018a). When resolved observations are possible, long GRBs are shown to happen in star forming and metal poor regions of their host galaxies, which do not necessarily have to be low mass and

metal poor overall. (Thöne et al. 2021, 2024). This suggest that long GRBs might happens only if metallicity is below a certain threshold (Schulze et al. 2015; Perley et al. 2016b).

Compared to field galaxies, long GRB hosts have a higher star formation rate and especially, a higher specific star formation rate i.e., the SFR per stellar mass unit (Schulze et al. 2018). It has been suggested that long GRBs occur primarly in starburst galaxies (Perley et al. 2015) but this is not the only place where long GRBs can happen. The star formation rate can also be enhanced via neutral gas infall onto GRB host galaxies (Michałowski et al. 2016; Thöne et al. 2024; de Ugarte Postigo et al. 2024) and through galaxy encounters (see e.g. Thöne et al. 2009). In both cases, the SFR increases leading to the formation of GRB progenitors.

In this Chapter we will explore different physical properties of the *Swift* GRB host-galaxy legacy survey (SHOALS) sample (see Sect. 1.4.1 using Spectral Energy Distribution (SED) techniques fitting the available photometry from the SHOALS sample to a galaxy SED template and compute different parameters and characterize long GRB hosts over a large and unbiased sample.

5.2 Sample and analysis

The SHOALS project includes deep observations of GRB host galaxies of bursts detected in the *Swift* era down to 2012 and covering the mid-IR spectral range with observations at 3.6 and 4.5 μm obtained under a large program with *Spitzer*, with additional observations in the optical and NIR from different facilities, including the Hubble Space Telescope (HST). The sample is selected from GRBs detected with the *Swift* satellite from 2005 to 2013 using different criteria and focusing on collapsar-origin long GRBs. To assess compliance of this condition, the sample is constructed by imposing, among other properties, a cut on the GRB fluence of $S_{15-150keV} < 10^{-6}\, erg\, cm^{-2}$. This criterion removes almost all short GRBs from the sample, except for GRB 060614 and GRB 080503 that are not included in the sample as they present properties that resemble those of merger-driven GRBs. Most of the host galaxies have a confirmed redshift from either afterglow spectroscopy or from host galaxy spectroscopy. From the initial sample of the SHOALS cataloge with a total of 119 objects (Perley et al. 2016a,b), we selected a sample for those objects with at least 5 detections in different photometric bands and a secure redshift determined via absorption line spectroscopy in the GRB afterglow or through absorption or emission line spectroscopy of the host galaxy. This sample is includes a total of 61 long GRB host galaxies. This ensures a wide spectral coverage which is crucial when performing SED fitting analysis (Pforr et al. 2012).

SED fitting codes usually have different models for each component that contribute for the final fitted SED, as indicated in Sect. 2.3. Following Pacifici et al. 2023 we select those modules that better match the characteristic of the sample and the available data and we also selected the SED fitting code that is more consistent with the sample characteristics. The `CIGALE` SED fitting code is a useful tool to derive physical integrated properties when infrared data is available (Boquien et al. 2019). and chose the models that fits better to the data and galaxy characteristics. The computed output values have been obtained using a probability density function (PDF), taking the mean and standard deviation for each computed parameter.

To model the star formation rate, we chose the implemented delayed star formation rate func-

tion as indicated in Sect. 2.3. The star formation history (SFH) is modeled following an exponential SFR and allowing for a late burst of constant SFR and an age for the main population that will be smoothed by an e-folding time. This is motivated by the results found in Pforr et al. (2012) in which more simple SFH functions might understimate the star formation rate. To avoid fitting biased in a best-effort basis, we let the age of the main stellar population to vary from 1 to 13 Gyr with a recent burst of 20 to 100 Myr. We assume that part of the total stellar mass of the galaxy is generated in this late burst that we estimate to contribute 10 to 30 % of the total stellar mass. Since we assume the GRB not to happen in a late burst, we let the e-folding time τ of the main stellar population to change from 0.1 to 13 Gyr. This way, we model the SFH to vary from a quasi-constant star formation to a increasing or decreasing SFR.

The stellar synthesis models of Bruzual & Charlot (2003) are used to fit the stellar population, the initial mass function is taken from Chabrier (2003) using low metallicity to solar and super-solar metallicity values, which allows for the possibility of long GRBs happening in more evolved host galaxies. We assume a minimum separation age of 10 Myr between the young and old stellar populations, without imposing a strict boundary beyond this threshold. The nebular emission is modeled assuming that its metallicity is lower than for the stellar population, therefore, as the maximum value for the metallicity is a super-solar value, we bias the nebular metallicity to vary from the lowest value of the stellar component up to the solar value i.e., $Z = 0.02$.

The dust attenuation is modelled using a Calzetti et al. (2000) modified law in which the nebular lines attenuation is modelled separately from the stellar component. The nebular lines are attenuated with values for the $E(B-V)_{lines}$ that range from nearly negligible extinction up to 2 magnitudes. We assume that the color excess of the nebular lines is related to the stellar component color excess with a factor of 0.44 as found for local starburst galaxies (Calzetti et al. 2000). We adopt a Large Magellanic Cloud extinction law for the line emission attenuation (Pei 1992) for which the ratio between the extinction in the V-band and the color excess, $R_V = 3.16$. The spectral slope of the attenuation curve is free to change between -1.0 and 1.0, accordingly to Corre et al. (2018).

As dust absorbs the UV photons emitted by massive stars heating it and then being re-emitted in the IR, specially at larger wavelengths, we use the Dale et al. (2014) models for dust emission which depends only in the AGN emission fraction (assumed to be zero) and α, which correspond to the exponent of the radiation field intensity. As the galaxies are detected at larger wavelengths than NIR values, it is fixed to $\alpha = 2.0$ accordingly to the results from Dale & Helou (2002).

5.3 Results

From the SED fit to the SHOALS photometry we compute different integrated properties, total stellar mass, the SFR and the visual extincition. We compute the stellar age for the main stellar population and the metallicity of the stellar component. We include the rest-frame module available in CIGALE, to retrieve the rest-frame luminosity of the fitted SED for each host and in different bands. Our results for the stellar mass, the SFR, A_V and the main stellar population age are presented in Tab. 5.1.

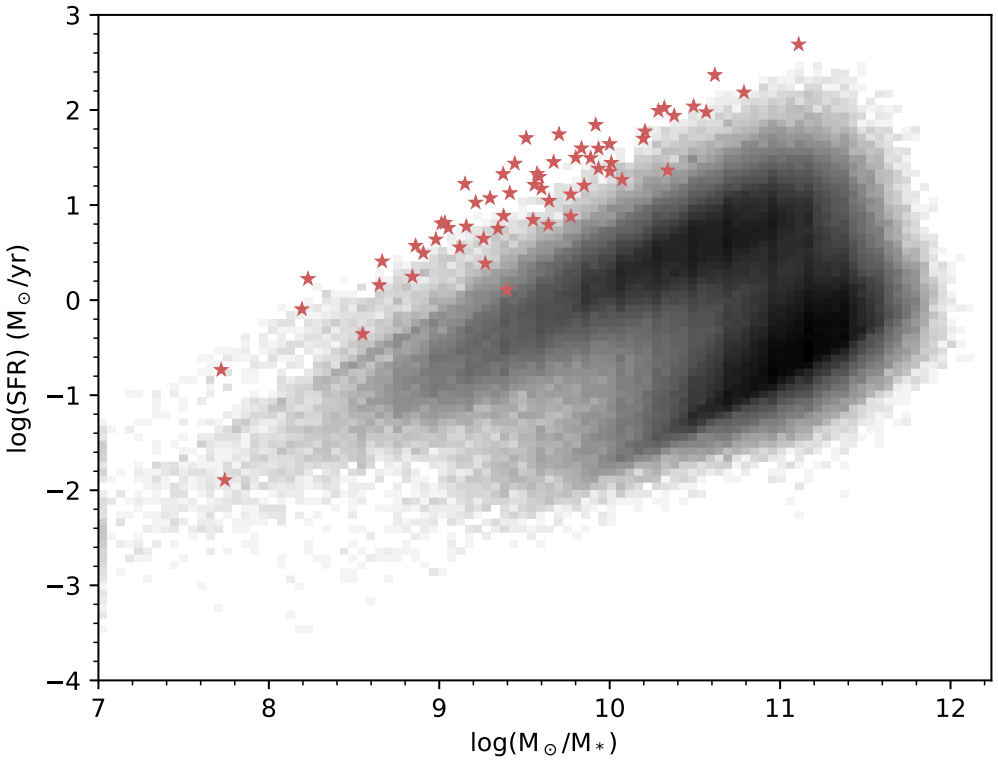

Figure 5.1: Star formation rate for long GRB hosts increasing with the stellar mass. In gray scale we show the derived values for field galaxies as obtained from optical and IR photometry in Chang et al. (2015). We do not show error-bars for clarity.

When using SED fitting techniques, we typically fit the continuum emission. Hence we take into account the stellar continuum contribution to the galaxy light and not only the hot gas emission. This approach makes SED fitting a good proxy to derive the total stellar mass as we are not biasing this measurement to galaxy regions with warm gas from massive and young stars.

The stellar mass of the SHOALS sample follows the general trend for field galaxies, with an increasing SFR towards more massive host galaxies (see in Fig. 5.1). We compare our results with those presented in Chang et al. (2015). Who apply SED fitting methods to optical and IR photometry for 858,365 field galaxies detected in the SDSS and *WISE* surveys. Their sample covers the redshift range $0.0 < z < 0.6$ with the majority of them at $z < 0.2$. Although the comparison is not fully consistent (since the redshift ranges are different), we conclude that long GRB host galaxies have a higher SFR than for the bulk of field galaxies, falling at the upper part of the Chang et al. 2015 sample. This further confirms that long burst are far more common in galaxies with high SFR, with values varying in the range $-1.0 < \log(SFR) < 3.0\,M_\odot$/yr but with most of them at SFR $> 0.5\,M_\odot$/yr, than those with less activity. This is indeed consistent with previous results on SFR at higher redshift (Madau & Dickinson 2014). It is also interesting that most host galaxies are low mass galaxies although they are not in the lowest end for the mass distribution compared to field galaxies.

An indicative measure of the star formation activity in host galaxies is the specific star for-

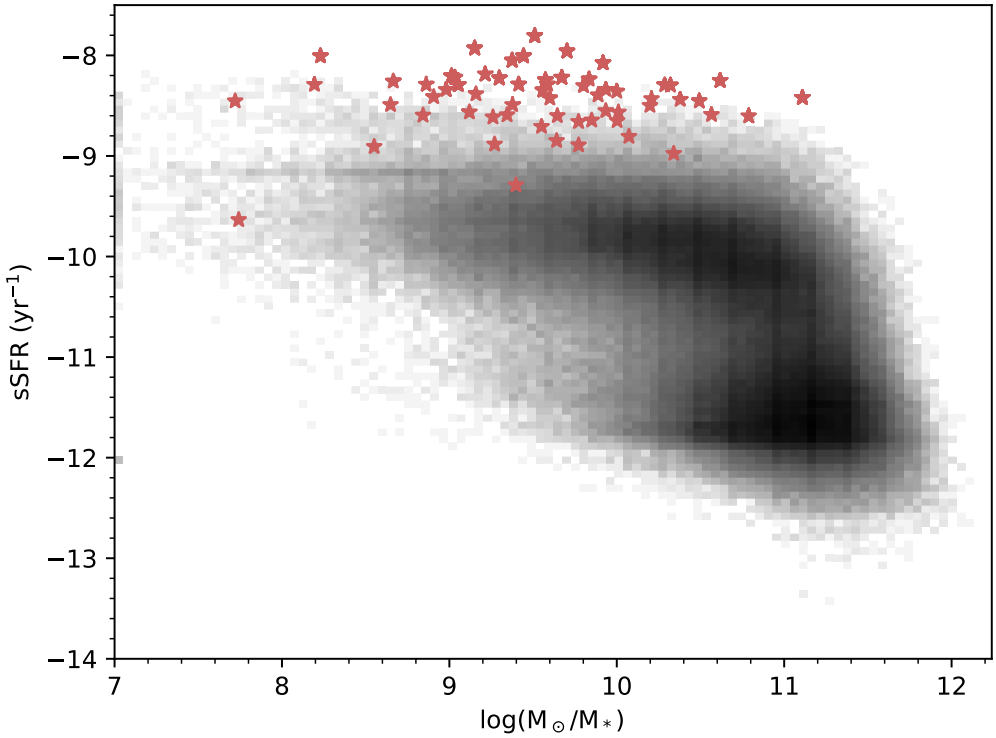

Figure 5.2: Long GRB hosts specific SFR evolution with the stellar mass on top of the values from Chang et al. (2015). We do not show error-bars for clarity.

mation rate (sSFR), the SFR relative to the total stellar mass. High values of sSFR imply high efficiency creating new stars in the host galaxy as the measured SFR is strongly contributing to the total stelar mass. I Fig. 5.2 we see that long GRB hosts show the highest values for the sSFR compared to field galaxies. These host galaxies are actively forming stars at a high rate despite the host are relatively massive.

Comparing computed stellar mass to the stellar age for the main stellar population, we see in Fig. 5.3 that the majority of the host galaxies have low values for the stellar age with most of the host being younger than 2.5 Gyrs. We also see that lower ages are more common in more massive host galaxies while less massive galaxies present a higher fraction of older populations. A similar trend is found for the SFR, those galaxies with older stellar populations have lower SFRs while the opposite happens for hosts with younger ages for the main stellar population

The evolution of the stellar mass as well as the SFR with redshift is shown in Fig. 5.4. We clearly see that both properties increases with redshift. This could simply be an observational bias since at larger distances only brighter objects can be detected. However it is surprising that at redshifts lower than ∼1, long GRB hosts generally shows lower masses than hosts beyond this cut. This is consistent with Perley et al. 2016b where they find this evolution of the stellar mass with redshift. This evolution is also present for the SFR although the difference is not so significant as for the mass. The evolution of the SFR as well as the weak increase of the stellar mass at $z > 1.0$ is consistent with findings in Palmerio et al. 2019.

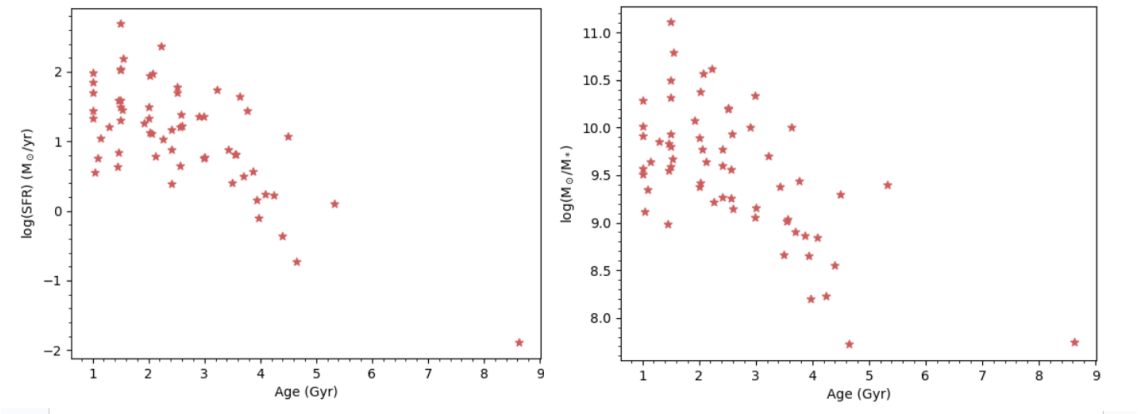

Figure 5.3: Comparison of the computed star formation rate and total stellar mass of long GRB hosts with the age of the main stellar population of the host galaxy. We do not show error-bars for clarity.

The SFR is strongly affected by the extinction when modeling the galaxy SFR. This is due to dust absorbing the UV photons heating it and afterwards re-emitted in the IR (Walcher et al. 2011). The SFR estimated from UV-SED fitting is typically found to be underpredicted (Conroy 2013). This issue can be handled if IR photometry is available which recovers dust obscuration of the UV light (Boquien et al. 2019). With the `CIGALE` fitting code this degeneration would be accounted as for the SFR and the A_V are fitted taking into account the attenuation curve. This permit us to obtain a robust measurement of the SFR (Buat et al. 2014). We thus also check whether there is an evolution of the SFR with the extinction in the V-band. In Fig. 5.5 we see that despite the computed A_V for long GRB hosts is high, the overal SFR does not seems to change significantly. The majority of the objects in the sample seems to have a high extincion of $A_V \sim 1$ while the SFR seems to be around the same range without presenting a trend with A_V.

The rest-frame luminosity has been computed in different bands using *SDSS* optical filter re-

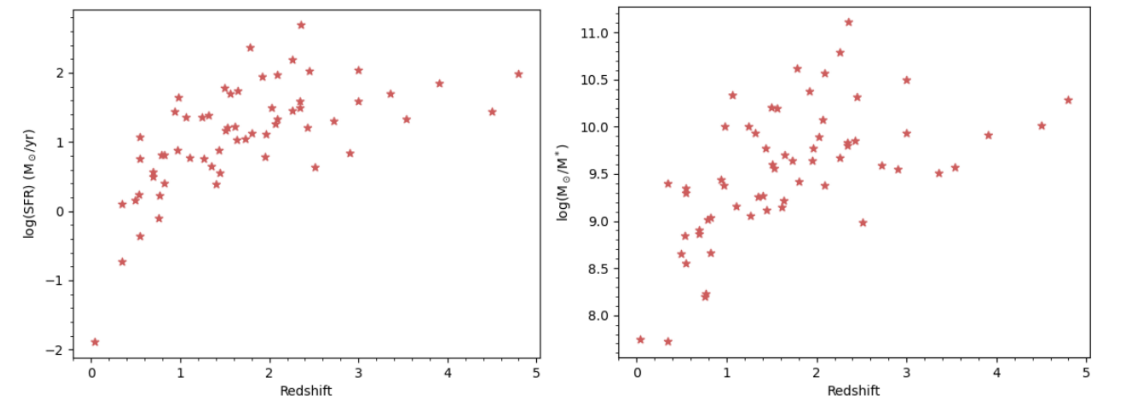

Figure 5.4: Star formation rate *(left)* and stellar mass *(right)* evolution with redshift. We do not show error-bars for clarity.

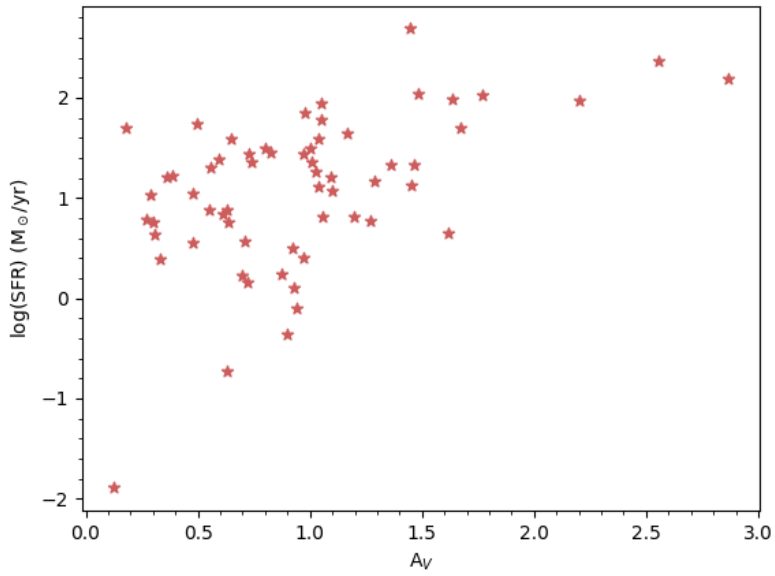

Figure 5.5: Dependence of the extincition in the V-band (A_V) with the star formation rate of the host galaxy. We do not show error-bars for clarity.

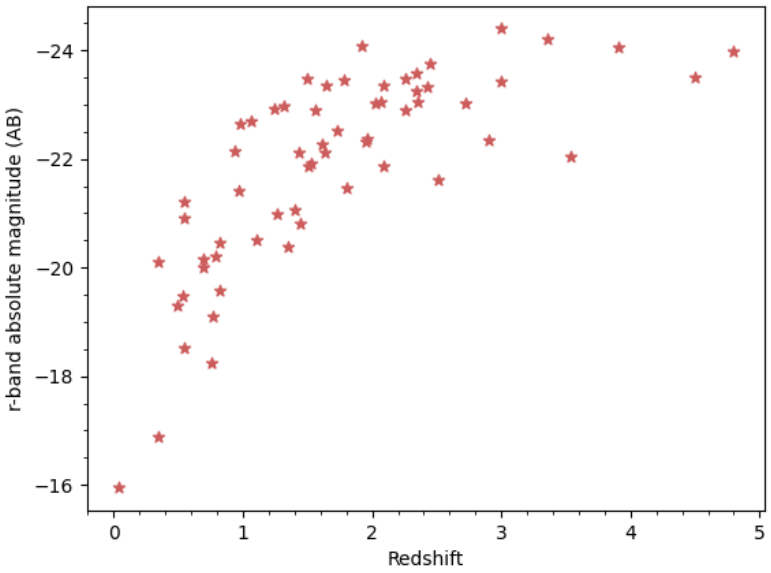

Figure 5.6: Apparent magnitud of rest-frame computed r-band luminosity *(left)* and r-band Absolute magnitude *(right)* evolution with redshift. We do not show error-bars for clarity.

sponse curve and we have calculated the r-band magnitude for all the SHOALS sample selected targets. We see in Fig. 5.6 that the sample is generally tracing low luminosity galaxies with an evolution in redshift towards brighter targets. This result is consistent with the evolution of the stellar mass and the SFR with redshift (see Fig. 5.4) as there is a contribution of the SFR to the

total galaxy light that is typically higher at higher redshift (Madau & Dickinson 2014).

Table 5.1: Computed integrated properties using the CIGALE code as indicated in Sect. 5.2

Host	Redshift	$\chi^2_{\rm red}$	$\log(M_*/M_\odot)$	log(SFR)	sSFR ($\rm yr^{-1}$)	A_V	Age (Gyr)	Z/Z_*
GRB050315	1.9500	0.07	$9.64^{+0.12}_{-0.09}$	$0.79^{+0.20}_{-0.13}$	1.42 ± 0.61	0.27 ± 0.23	2.12 ± 0.78	0.0144
GRB050401	2.8983	0.88	$9.55^{+0.18}_{-0.13}$	$0.84^{+0.20}_{-0.14}$	1.96 ± 0.97	0.61 ± 0.29	1.46 ± 0.50	0.0116
GRB050822	1.4340	0.31	$9.77^{+0.14}_{-0.10}$	$0.88^{+0.25}_{-0.16}$	1.28 ± 0.65	0.55 ± 0.30	2.40 ± 1.10	0.0146
GRB050922B	4.5000	1.80	$10.01^{+1.66}_{-0.30}$	$1.44^{+1.88}_{-0.30}$	2.72 ± 3.78	0.97 ± 0.75	1.00 ± 0.00	0.0127
GRB051001	2.4296	0.99	$9.85^{+0.07}_{-0.06}$	$1.21^{+0.09}_{-0.07}$	2.27 ± 0.54	0.36 ± 0.10	1.29 ± 0.45	0.0091
GRB051006	1.0590	1.04	$10.34^{+0.14}_{-0.11}$	$1.36^{+0.32}_{-0.18}$	1.06 ± 0.63	1.01 ± 0.42	2.99 ± 1.36	0.0244
GRB060115	3.5328	0.69	$9.57^{+0.30}_{-0.40}$	$1.33^{+0.30}_{-0.40}$	5.70 ± 12.10	1.47 ± 0.98	1.00 ± 0.00	0.0107
GRB060202	0.7850	2.46	$9.01^{+0.32}_{-0.18}$	$0.81^{+0.31}_{-0.18}$	6.23 ± 4.56	1.20 ± 0.28	3.55 ± 1.72	0.0142
GRB060204B	2.3393	1.26	$9.83^{+0.13}_{-0.10}$	$1.60^{+0.36}_{-0.19}$	5.79 ± 3.58	0.65 ± 0.26	1.46 ± 0.50	0.0099
GRB060210	3.9122	2.47	$9.92^{+0.52}_{-0.23}$	$1.84^{+1.26}_{-0.29}$	8.42 ± 9.88	0.97 ± 0.74	1.00 ± 0.00	0.0071
GRB060218	0.0331	0.74	$7.74^{+0.13}_{-0.10}$	$-1.89^{+0.21}_{-0.14}$	0.23 ± 0.11	0.12 ± 0.05	8.63 ± 2.94	0.0061
GRB060306	1.5590	0.78	$10.20^{+0.15}_{-0.11}$	$1.70^{+0.33}_{-0.19}$	3.17 ± 1.92	1.67 ± 0.30	2.52 ± 1.11	0.0099
GRB060719	1.5320	0.02	$9.56^{+0.20}_{-0.14}$	$1.21^{+0.41}_{-0.21}$	4.51 ± 3.23	1.09 ± 0.34	2.57 ± 1.11	0.0145
GRB060729	0.5428	2.45	$8.55^{+0.17}_{-0.12}$	$-0.36^{+1.04}_{-0.28}$	1.24 ± 1.20	0.90 ± 0.21	4.39 ± 2.35	0.0061
GRB060814	1.9229	0.06	$10.38^{+0.23}_{-0.15}$	$1.94^{+0.41}_{-0.21}$	3.64 ± 2.66	1.05 ± 0.35	2.02 ± 0.81	0.0134
GRB060912A	0.9370	0.99	$9.44^{+0.19}_{-0.13}$	$1.44^{+0.19}_{-0.13}$	9.85 ± 4.91	0.73 ± 0.20	3.77 ± 1.68	0.0146
GRB061007	1.2622	0.34	$9.05^{+0.19}_{-0.13}$	$0.76^{+0.53}_{-0.23}$	5.09 ± 4.00	0.64 ± 0.40	2.98 ± 1.41	0.0088
GRB061021	0.3463	0.54	$7.72^{+0.23}_{-0.15}$	$-0.73^{+0.90}_{-0.27}$	3.52 ± 3.39	0.63 ± 0.39	4.65 ± 2.60	0.0073
GRB061110A	0.7578	0.53	$8.19^{+0.32}_{-0.18}$	$-0.10^{+0.58}_{-0.24}$	5.13 ± 4.61	0.94 ± 0.49	3.98 ± 2.01	0.0113
GRB061121	1.3145	1.01	$9.93^{+0.17}_{-0.12}$	$1.38^{+0.53}_{-0.23}$	2.81 ± 2.18	0.59 ± 0.30	2.58 ± 1.11	0.0137
GRB061202	2.2530	0.48	$9.67^{+0.17}_{-0.12}$	$1.45^{+0.35}_{-0.19}$	6.03 ± 3.86	0.83 ± 0.31	1.54 ± 0.50	0.0176
GRB061222A	2.0880	2.24	$9.37^{+0.23}_{-0.15}$	$1.33^{+0.85}_{-0.27}$	8.93 ± 8.49	1.36 ± 0.74	2.00 ± 0.82	0.0060
GRB070110	2.3521	0.89	$11.11^{+-1.04}_{-1.11}$	$2.69^{+-0.65}_{-0.81}$	3.81 ± 49.95	1.45 ± 1.32	1.50 ± 0.50	0.0110
GRB070129	2.3384	1.87	$9.80^{+0.13}_{-0.10}$	$1.50^{+0.46}_{-0.22}$	4.99 ± 3.52	0.80 ± 0.35	1.50 ± 0.50	0.0094
GRB070223	1.6295	0.39	$9.21^{+0.15}_{-0.11}$	$1.03^{+0.29}_{-0.17}$	6.51 ± 3.71	0.29 ± 0.21	2.26 ± 1.14	0.0101
GRB070306	1.4959	0.19	$10.21^{+0.18}_{-0.12}$	$1.78^{+0.53}_{-0.23}$	3.70 ± 2.87	1.05 ± 0.38	2.51 ± 1.11	0.0096
GRB070419B	1.9588	0.98	$9.77^{+0.16}_{-0.11}$	$1.11^{+0.53}_{-0.23}$	2.19 ± 1.68	1.04 ± 0.37	2.06 ± 0.80	0.0098
GRB070508	0.8200	0.65	$9.03^{+0.26}_{-0.16}$	$0.81^{+0.32}_{-0.18}$	6.04 ± 4.12	1.06 ± 0.28	3.57 ± 1.71	0.0143
GRB070521	2.0865	1.00	$10.57^{+0.33}_{-0.18}$	$1.98^{+2.21}_{-0.30}$	2.57 ± 2.90	2.20 ± 0.64	2.08 ± 0.80	0.0122
GRB070808	1.3500	0.70	$9.26^{+0.20}_{-0.14}$	$0.65^{+0.57}_{-0.24}$	2.43 ± 1.99	1.62 ± 0.51	2.57 ± 1.10	0.0103
GRB071021	2.4520	0.99	$10.32^{+0.14}_{-0.10}$	$2.02^{+0.30}_{-0.17}$	5.04 ± 2.84	1.77 ± 0.27	1.50 ± 0.50	0.0118
GRB071025	4.8000	1.16	$10.29^{+0.28}_{-0.40}$	$1.99^{+0.98}_{-0.32}$	5.08 ± 9.55	1.63 ± 1.04	1.00 ± 0.00	0.0107
GRB071112C	0.8227	0.41	$8.66^{+0.24}_{-0.16}$	$0.41^{+0.39}_{-0.20}$	5.54 ± 4.06	0.97 ± 0.33	3.50 ± 1.72	0.0113
GRB080205	2.7200	0.06	$9.59^{+0.19}_{-0.13}$	$1.30^{+0.41}_{-0.21}$	5.15 ± 3.62	0.56 ± 0.34	1.50 ± 0.50	0.0125
GRB080319A	2.0265	0.35	$9.89^{+0.14}_{-0.11}$	$1.49^{+0.56}_{-0.24}$	4.03 ± 3.14	1.00 ± 0.37	2.01 ± 0.81	0.0093
GRB080325	1.7800	0.52	$10.62^{+0.23}_{-0.15}$	$2.37^{+0.91}_{-0.27}$	5.63 ± 5.46	2.56 ± 0.66	2.23 ± 0.80	0.0089
GRB080413B	1.1014	0.50	$9.16^{+0.23}_{-0.15}$	$0.78^{+0.65}_{-0.25}$	4.14 ± 3.64	1.27 ± 0.44	3.00 ± 1.41	0.0107
GRB080430	0.7670	0.54	$8.23^{+0.23}_{-0.15}$	$0.22^{+0.22}_{-0.14}$	9.85 ± 5.63	0.70 ± 0.29	4.24 ± 1.95	0.0071
GRB080605	1.6403	2.83	$9.70^{+0.22}_{-0.14}$	$1.74^{+0.14}_{-0.11}$	11.01 ± 5.31	0.49 ± 0.19	3.23 ± 0.86	0.0200
GRB080805	1.5042	0.47	$9.60^{+0.16}_{-0.11}$	$1.17^{+0.42}_{-0.21}$	3.75 ± 2.60	1.29 ± 0.34	2.41 ± 1.12	0.0080
GRB080810	3.3604	1.73	$9.51^{+0.09}_{-0.07}$	$1.70^{+0.07}_{-0.06}$	15.66 ± 3.79	0.18 ± 0.07	1.00 ± 0.00	0.0074
GRB080916A	0.6887	0.65	$8.86^{+0.22}_{-0.15}$	$0.57^{+0.42}_{-0.21}$	5.15 ± 3.79	0.71 ± 0.30	3.87 ± 2.01	0.0091
GRB081109A	0.9787	1.08	$10.00^{+0.21}_{-0.14}$	$1.64^{+0.44}_{-0.21}$	4.38 ± 3.24	1.16 ± 0.30	3.63 ± 1.69	0.0113
GRB081121	2.5120	0.38	$8.98^{+0.22}_{-0.15}$	$0.64^{+0.41}_{-0.21}$	4.56 ± 3.35	0.31 ± 0.26	1.44 ± 0.50	0.0090
GRB081210	2.0631	1.52	$10.07^{+0.12}_{-0.09}$	$1.27^{+1.61}_{-0.30}$	1.56 ± 1.57	1.03 ± 0.39	1.92 ± 0.83	0.0068
GRB081221	2.2600	0.29	$10.79^{+0.16}_{-0.12}$	$2.19^{+0.19}_{-0.13}$	2.50 ± 1.18	2.87 ± 0.32	1.55 ± 0.50	0.0127

Table 5.1: Continued.

Host	Redshift	$\chi^2_{\rm red}$	$\log(M_*/M_\odot)$	log(SFR) (M_*/yr^{-1})	sSFR (yr^{-1})	A_V	Age (Gyr)	Z/Z_*
GRB090404	3.0000	1.40	$10.49^{+0.14}_{-0.11}$	$2.04^{+0.29}_{-0.17}$	3.51 ± 1.97	1.48 ± 0.29	1.51 ± 0.50	0.0129
GRB090417B	0.3450	0.62	$9.40^{+0.13}_{-0.10}$	$0.11^{+0.32}_{-0.18}$	0.51 ± 0.30	0.93 ± 0.13	5.32 ± 2.33	0.0078
GRB090418A	1.6080	0.96	$9.15^{+0.16}_{-0.12}$	$1.22^{+0.16}_{-0.12}$	11.79 ± 5.18	0.38 ± 0.19	2.60 ± 1.12	0.0094
GRB090424	0.5440	0.31	$9.30^{+0.23}_{-0.15}$	$1.07^{+0.35}_{-0.19}$	5.94 ± 4.13	1.10 ± 0.28	4.50 ± 2.33	0.0105
GRB090618	0.5400	2.42	$8.84^{+0.22}_{-0.15}$	$0.25^{+0.60}_{-0.24}$	2.54 ± 2.15	0.88 ± 0.35	4.10 ± 2.29	0.0088
GRB090709A	1.8000	0.77	$9.41^{+0.21}_{-0.14}$	$1.13^{+0.69}_{-0.25}$	5.15 ± 4.56	1.45 ± 0.47	2.02 ± 0.81	0.0104
GRB090715B	3.0000	0.07	$9.93^{+0.45}_{-0.22}$	$1.59^{+0.72}_{-0.26}$	4.57 ± 4.73	1.04 ± 0.57	1.51 ± 0.50	0.0111
GRB090814A	0.6960	0.57	$8.91^{+0.23}_{-0.15}$	$0.49^{+0.59}_{-0.24}$	3.87 ± 3.27	0.92 ± 0.29	3.69 ± 2.06	0.0066
GRB090926B	1.2400	0.48	$10.00^{+0.15}_{-0.11}$	$1.35^{+0.53}_{-0.23}$	2.24 ± 1.71	0.74 ± 0.28	2.91 ± 1.40	0.0080
GRB091018	0.9710	0.56	$9.38^{+0.20}_{-0.14}$	$0.89^{+0.56}_{-0.24}$	3.22 ± 2.63	0.63 ± 0.34	3.42 ± 1.71	0.0118
GRB091127	0.4900	0.69	$8.65^{+0.22}_{-0.14}$	$0.16^{+0.59}_{-0.24}$	3.23 ± 2.71	0.72 ± 0.30	3.93 ± 2.31	0.0056
GRB100615A	1.3980	0.25	$9.27^{+0.12}_{-0.09}$	$0.39^{+0.22}_{-0.14}$	1.31 ± 0.60	0.33 ± 0.25	2.41 ± 1.11	0.0141
GRB100621A	0.5420	1.76	$9.34^{+0.10}_{-0.08}$	$0.75^{+0.10}_{-0.08}$	2.56 ± 0.73	0.30 ± 0.24	1.09 ± 0.28	0.0236
GRB100814A	1.4400	4.33	$9.12^{+0.16}_{-0.12}$	$0.56^{+0.17}_{-0.12}$	2.73 ± 1.23	0.48 ± 0.32	1.04 ± 0.21	0.0500
GRB120119A	1.7280	1.32	$9.64^{+0.06}_{-0.05}$	$1.04^{+0.06}_{-0.05}$	2.51 ± 0.46	0.48 ± 0.07	1.15 ± 0.37	0.0084

5.4 Discussion

The environment in which GRBs occur may play a critical role in facilitating these explosions. The collapsar model suggests that long GRB progenitors require massive stars with low metallicity to produce GRBs (Yoon et al. 2006). Such stars are typically formed in star-forming galaxies. Consequently, long GRB host galaxies are expected to be low-metallicity, star-forming galaxies. Hereafter, we refer to collapsar-origin GRBs as long GRBs, as all the host galaxies in the sample are associated with long GRBs resulting from the collapse of massive stars.

In this chapter, we derived integrated properties such as the star formation rate (SFR) and stellar mass for a sample of 61 long GRB host galaxies using SED fitting techniques. Our results indicate that long GRBs occur in galaxies with high SFRs, which are among the highest values observed compared to field galaxies (see Fig. 5.1). However, we note that the Chang et al. 2015 sample is limited to $z < 0.6$ galaxies, while the SHOALS survey spans a broader redshift distribution.

We also find that SFR increases with redshifts (see Fig. 5.4), consistent with previous findings for long GRB hosts. Specifically, the computed SFR values are higher than those of typical star-forming galaxies and increase with redshift (Krühler et al. 2015; Palmerio et al. 2019). Additionally, we observe that SFR decreases as the stellar age of the dominant population increases (see Fig. 5.3), while A_V increases with SFR (see Fig. 5.5). This evolution with A_V can be explained by the general tendency of star-forming galaxies to become dustier. At higher SFRs, A_V increases, and the dominant stellar population is younger. This is further supported by the specific star formation rate (sSFR), which we find to be at the upper end of the distribution compared to the Chang et al. 2015 sample of field galaxies (see Fig. 5.2). The sSFR, which measures how much

stellar mass in a galaxy is due to ongoing star formation, is notably high for our sample.

The overall stellar mass distribution for the GRB host sample is lower than that for field galaxies (see Fig. 5.1). However, the distribution does not appear to be entirely biased toward low-mass galaxies, some hosts are consistent with being massive galaxies, in agreement with previous studies (Perley et al. 2016b; Palmerio et al. 2019). Examining the evolution of stellar mass with redshift (Fig. 5.4), we observe an increase in stellar mass, particularly at $z > 1$. In Palmerio et al. 2019, a weak correlation between stellar mass and redshift is reported for the range $1 < z < 2$, which only partially aligns with our findings. While their result suggests that stellar mass evolves from $\log(M_*/M_\odot) \sim 9.0$ to ~ 9.4 at $1 < z < 2$, we find that stellar masses can exceed their upper limit within the same redshift range (see Fig. 5.4). This discrepancy may arise from differences in methodology, as our analysis includes MIR observations, which they do not. Incorporating MIR data is crucial for accurately estimating the total stellar mass because dust-absorbed UV radiation from massive stars is re-emitted in these wavelengths.

We also observe that at higher redshifts, GRBs tend to trace more massive galaxies. This trend could reflect an observational bias, as only the brightest galaxies are detected (see 5.4 and 5.6). At lower stellar masses, the dominant stellar population tends to be older (see Fig. 5.3) , which, combined with a lower SFR, suggests a reduced efficiency in star formation and, consequently, in producing GRBs.

A key parameter for GRB production is the host galaxy metallicity. In our sample, we fit long GRBs by allowing metallicity to vary from metal-poor stellar populations to solar and super-solar metallicities. In most cases, the dominant stellar population is fitted to sub-solar metallicity (see Tab. 5.1). However, there are exceptions, such as the hosts of GRB 080605 and GRB 100814A, for which we derive solar and super-solar metallicities, respectively (although we note that the reduced-χ^2 values for these fits are very high). Our findings are consistent with previous studies, which also report sub-solar metallicities for the hosts of long GRBs (Krühler et al. 2015; Perley et al. 2016b; Palmerio et al. 2019).

The high SFR, low metallicity, and relatively low stellar masses we derive are generally consistent with previous studies (Krühler et al. 2015; Perley et al. 2016b; Palmerio et al. 2019). However, it is important to note that, while these properties align with the characteristics of low-metallicity, highly star-forming galaxies, there are some exceptions. For example, Heintz et al. 2018a found that the host galaxy of GRB 160804A is massive and metal-rich, indicating that long GRBs can also occur in more evolved galaxies.

To date, only a few long GRB host galaxies have been studied in detail using resolved observations. Such studies have revealed that GRB sites within their host galaxies are typically regions of high SFR, low metallicity, and high specific SFR (Christensen et al. 2008; Thöne et al. 2014; Izzo et al. 2017). A notable example is GRB,171205A, whose host is a massive spiral galaxy. Despite the galaxy's overall characteristics, the GRB site itself is a metal-poor, star-forming region with a young stellar population (Thöne et al. 2024). This finding aligns with results based on integrated properties and reinforces the evidence from resolved and spectroscopic studies that long GRBs occur in metal-poor, star-forming environments.

It is interesting to compare the differences between collapsar-origin GRBs and merger-origin

GRBs, which are traditionally associated with short GRBs. To do this, we compare our results with those obtained by Nugent et al. 2022 for a sample of 69 short GRB host galaxies using photometric data from Fong et al. (2022). We show how these results compare to the Chang et al. 2015 sample of field galaxies in Fig. 5.7. The Nugent et al. 2022; Fong et al. 2022 sample is more consistent with field galaxies and quite different from long GRB host galaxies. While long GRB hosts have higher SFRs compared to the bulk of field galaxies, Nugent et al. 2022 finds that a majority of short GRB hosts ($\sim$ 84%) are star-forming galaxies with SFR values comparable to those of field galaxies. Short GRB host galaxies are not biased towards massive, metal-rich galaxies; instead, their metallicity fits show a broad spread across a wide range for short GRB hosts. This is in clear contrast to long GRB hosts, which are more commonly associated with sub-solar metallicities. However, we find that the stellar masses of long GRB hosts are not significantly different from the distribution of short GRB hosts.

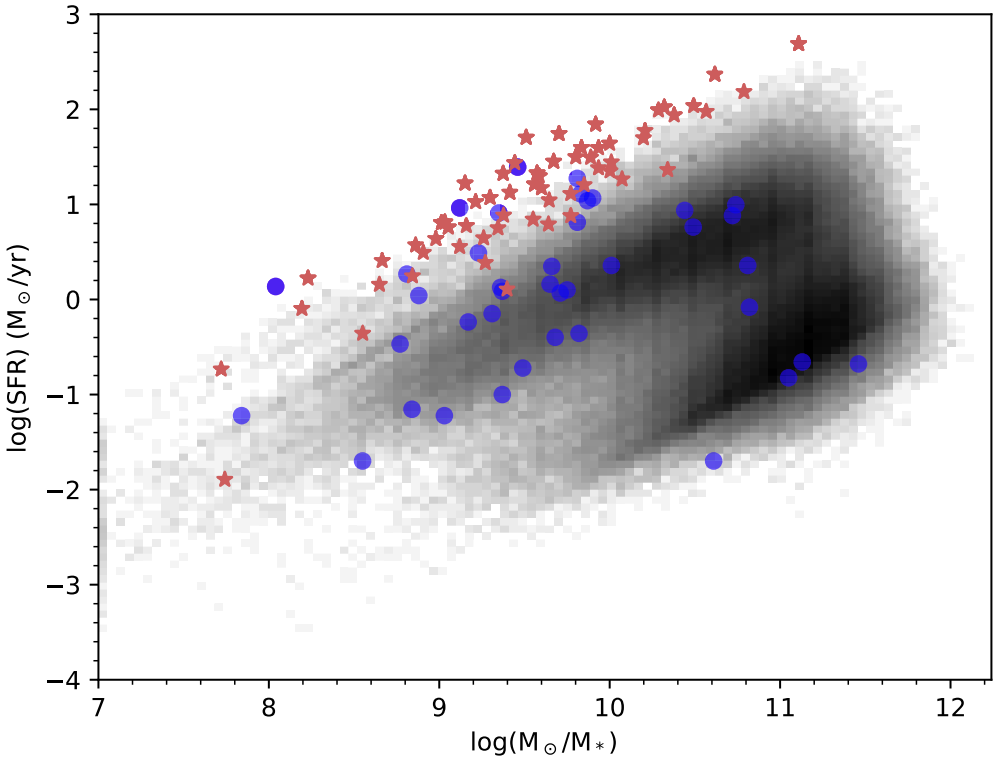

Figure 5.7: Comparison of the SFR-Stellar Mass relation for long GRB hosts with the same relation (blue dots) for short GRB host and data from (Nugent et al. 2022). We also compare to field galaxies. We do not show error-bars for clarity.

To summarize, we find significant differences from our results for collapsar-origin GRB hosts and other transients. Long GRB hosts galaxies have larger SFR when comparing to merger-origin GRBs (Nugent et al. 2022). Some difference also exist to short GRB host galaxies, that are slightly more massive although from Fig. 5.7, the distinction is not completely clear. Long GRBs seems to occur more in sub-solar metallicity environment while short bursts does not show a metallicity preference (Nugent et al. 2022). However, we note that the computed uncertainties for most

properties remain high, except for the stellar mass. This may indicate that while the stellar mass is well constrained, the star formation history (SFH) might be degenerate due to the limitations of the assumed SFH model or the incomplete UV-to-NIR coverage, despite the broad spectral range of the SHOALS sample. This could also explain the large uncertainties in properties such as age and extinction (see Tab. 5.1).

Overall, we find that the high SFR, A_V, specific star formation rates, the relatively low masses, metallicity and the dominant intermediate-age stellar populations together with dust content are positioning these host galaxies as outliers when comparing them with field galaxy. These results are consistent with previous works where it was already suggested that long GRB hosts have these characteristics (Krühler et al. 2015; Perley et al. 2016b; Palmerio et al. 2019). Our results support the idea of collapsar-origin GRBs trace the most active star-forming galaxies and that they are far more common in low metallicity environments. We then conclude that integrated properties studies of GRB host galaxies are an important tool to distinguish between merger and collapsar GRBs as well as to understand the mechanisms that trigger these explosions.

Chapter 6

Conclusions

In this thesis, we have presented several studies to constrain the various properties of Gamma-ray Bursts (GRBs) related to the environments in which they occur and their progenitors. The analysis makes use of a wealth of data, combining spectroscopy, photometry, and photopolarimetry of the afterglow emission, as well as spectral energy distribution (SED) techniques applied to data for the host galaxy. The main conclusions of this thesis are outlined below.

In Chapter 3, we presented the analysis of two short GRBs originating from the merger of two neutron stars (NS) (Agüí Fernández et al. 2023). We conducted a study of the afterglow emission of both short GRBs using spectroscopic data obtained with ground-based facilities. GRB 160410A was observed using the X-shooter spectrograph at the VLT, and GRB 201221D was observed with OSIRIS/GTC, with the aim of determining their redshifts and uncovering the chemical composition and ionization of their environments. We also utilized photometric data obtained with different instruments to study the light curve evolution of GRB,160410A and performed photometric observations of the host galaxies of both GRB 160410A and GRB 201221D, which led to a non-detection for the former.

GRB 160410A represents the first study in depth of the ISM of a short GRB host conducted through absorption line spectroscopy of its afterglow emission and the first metallicity determination for a short GRB environment. The GRB was located at a redshift of 1.7177, the highest ever detected for a merger GRB from its afterglow spectrum. The GRB spectrum shows broad neutral hydrogen absorption, consistent with a Damped Lyman-α (DLA) system. We measured a metallicity of [Fe/ H] = -2.5, the lowest ever recorded for a GRB-DLA. We also find an environment with very low ionization compared to the long GRB sample of de Ugarte Postigo et al. 2012. Dust-depletion analysis revealed no depletion of elements, which is consistent with the non-detection of dust along the line of sight from the SED analysis of the GRB light curve.

Deep observations in the *r*-band with OSIRIS/GTC and in the 3.6μm channel with *Spitzer*

did not detect the GRB host galaxy. From the *Spitzer* observations, we derive an upper limit for the stellar mass of the host galaxy, $M_* \lesssim 1.14 \times 10^9, M_\odot$, indicating that the underlying host galaxy must be a low-mass galaxy. We did not detect a galaxy in the GRB field close enough to be identified as its host. Together with the detection of a metal-poor DLA system and the non-detection of an underlying host galaxy down to deep limits, this suggests that the host at the GRB location is more similar to a faint dwarf galaxy than to a massive galaxy. For GRB 201221D , we find an underlying massive, star-forming host galaxy, which is more consistent with previous results for short GRB hosts but very different from the host of GRB 160410A.

This study has revealed that rapid follow-up of merger GRBs is crucial for observing these transients with deep observations to uncover their ISM characteristics. We show that the immediate environment of short GRBs has diverse characteristics, supporting the idea that merger bursts do not appear to be biased toward evolved galaxies.

In Chapter 4, we investigate the GRB afterglow of the collapsar-origin long GRB 210610B and its host galaxy (Agüí Fernández et al. 2024). We performed imaging polarimetry observations of the GRB afterglow emission using CAFOS/CAHA and FORS2/VLT. We also observed the GRB spectroscopically with OSIRIS/GTC and obtained photometric data of both the afterglow and the GRB host galaxy using different facilities. The GRB light curve follows a decay-plateau-decay trend, with a steep decay in the final stage. The polarimetry measurements show that the GRB was polarized at the beginning of the plateau phase, with a polarization degree of ∼4.2%, before evolving to unpolarized light at the end of the plateau. We observe the polarization disappearing at the end of the plateau in different bands. Finally, the polarization increased again to ∼2% during the final steep decay of the GRB light curve.

The light curve SED modeling from X-rays to the optical shows no dust along the line of sight and a low column density of neutral hydrogen. This is further confirmed by the low A_V we obtain from the SED fitting of the GRB host galaxy. We also find that the host galaxy is a low-mass, star-forming, and metal-poor galaxy based on the SED fit. This is supported by the spectroscopic observations of the GRB afterglow, from which we infer a low amount of metals and low ionization values, indicative of very young stellar populations when compared to the de Ugarte Postigo et al. 2012 sample.

The lack of dust along the line of sight allows us to observe the intrinsic GRB polarization. The GRB polarization seems to be dominated by the refreshed shock in the first epoch. The polarization disappears afterward, when the forward shock dominates the emission, and then increases again to relatively low values, which could be explained by assuming magnetic fields at a hydrodynamical scale or a geometric model.

GRB 210610B occurred in a dust-free, low-mass, metal-poor, young environment with a high star formation rate. Its afterglow polarization appears to be dominated by different shocks at early stages, while various models could explain the later observations. We conclude that further polarimetry observations, along with photometric observations of the GRB, may help to better understand afterglow polarization.

Polarimetric analysis of GRB afterglows is highly relevant for understanding the physics that dominates this emission. However, the available observations using this technique are still limited,

and the analyses are too varied to be fully comparable. In the near future, we will systematically study all available GRB observations using imaging polarimetry and expand the sample as optically bright GRBs are detected.

In Chapter 5, we study the integrated properties of collapsar long GRB host galaxies using the CIGALE SED fitting code. We used observations based on The Swift GRB Host-Galaxy Legacy Survey (SHOALS) (Perley et al. 2016a,b) complemented by observations at VIS and NIR wavelenths, from which we selected a sample of 61 objects with secure redshift measurements and photometric observations in various bands covering a wide spectral range. We fitted the stellar mass, the SFR, the age of the main stellar population, its metallicity, and the dust attenuation. This is the largest sample of long GRB host properties to date.

In general, long GRB hosts show very high values for the SFR across a wide range of stellar masses. While at $z < 1$ the SFR has relatively low values (although still significantly high) compared to higher redshifts, at $z \geq 1$ the evolution steepens, with a broader spread of SFR values beyond $z \geq 2$. We do not find a correlation between the SFR and A_V, but we observe that higher A_V is more common in highly star-forming galaxies, while the SFR distribution at values of $A_V < 1.5$ mag is more dispersed.

The stellar mass distribution of the analyzed sample covers a wide range of values, with only one-third of the objects being consistent with dwarf galaxies ($\log(M_*/M_\odot) \lesssim 9.3$). However, we do not find that long GRB hosts are concentrated at the lower end of the stellar mass distribution; in fact, some of them are consistent with massive galaxies. At lower redshifts, long GRBs tend to occur in less massive galaxies, in a similar manner to their relation with the SFR.

Our results show a very high specific SFR for the entire sample. This is indicative of a strong contribution from star formation activity to the total stellar mass of the host galaxies. We also find an overall low metallicity, with only two cases showing solar or super-solar metallicities, and no evidence of metallicity evolution with redshift.

Overall, collapsar long GRB hosts are galaxies with a high SFR, with a strong contribution from ongoing star formation to the total stellar mass. Long GRBs occur in low-metallicity environments across a wide range of stellar masses, although generally on the lower end. Compared to merger GRBs, collapsar GRBs occur in galaxies with significantly higher SFR and within a lower metallicity range. However, we do not find that collapsar GRBs preferentially occur in galaxies with lower stellar masses than merger GRBs.

The star formation rate of collapsar GRBs is among the highest when compared to star-forming field galaxies, although the distribution shows some dispersion, particularly at lower masses. This highlights the importance of characterizing a larger sample of collapsar GRBs, especially fainter objects at higher redshifts, where the distribution appears to be dominated by more massive galaxies. Since the SHOALS sample was obtained for GRBs discovered between 2005 and 2012, many new collapsar GRBs have been identified, and we plan to extend the analysis to include host galaxies of more recent GRBs. Resolved studies have shown that collapsar GRBs occur in regions with lower metallicity and higher SFR compared to the broader host distribution, suggesting that the environment plays a crucial role in their production. We also aim to conduct a similar analysis for merger GRBs to better understand the differences between them and collapsar GRBs.

Appendix A

Extended analysis on the short/long nature of GRB 160410A

Contents

A.1 Additional Type I GRBs and Analysis

Further to several Type I GRBs taken from the sample of Kann et al. (2011), we include the following events for our comparison with GRB 160410A light curve:

A.1.1 GRB 130603B

Data are taken from de Ugarte Postigo et al. (2014b); Pandey et al. (2019); Cucchiara et al. (2013); Berger et al. (2013). This bright Type I GRB is famous for showing the first clear evidence of a kilonova signature (Tanvir et al. 2013; Berger et al. 2013), having the first high S/N afterglow spectrum of a short GRB (de Ugarte Postigo et al. 2014b) and also showing clear evidence for a jet break (de Ugarte Postigo et al. 2014b; Fong et al. 2014). We fit the joint light curve with a smoothly broken power-law, finding $\alpha_1 = -0.24 \pm 0.20$, $\alpha_2 = 2.55 \pm 0.15$, $t_b = 0.281 \pm 0.028$ days. $n = 1$ has been fixed, and with the exception of UVOT *uvm*2 and *u* data, the host galaxy has been subtracted by the authors of the data sources. We fit the SED (*uvm*2, *u*, g', *V*, r', i', z', *J*, *K*) with an intrinsic spectral slope of $\beta = 0.65$, following de Ugarte Postigo et al. (2014b), and find a large extinction $A_V = 0.84 \pm 0.11$ mag, in full agreement with de Ugarte Postigo et al. (2014b). Note that this is lower than the result found by Japelj et al. (2015), who find $A_V = 1.19^{+0.23}_{-0.12}$ mag, and SMC dust, albeit for a bluer spectral slope $\beta = 0.42^{+0.12}_{-0.22}$.

A.1.2 GRB 150424A

Data are taken from Knust et al. (2017); Jin et al. (2018) as well as GCNs (Malesani et al. 2015; Butler et al. 2015). The redshift for this GRB is likely unknown, Klose et al. (2019) report spectroscopy of a nearby galaxy yields $z = 0.2981$, however, deep HST imaging reveals a faint extended red object under the afterglow, likely the host galaxy (Knust et al. 2017; Jin et al. 2018). Knust et al. (2017) estimate $z \approx 1$ from the afterglow SED, a value we adopt here.

We initially fit the afterglow with a broken power-law, and find $\alpha_1 = -0.01 \pm 0.03$, $\alpha_2 = 1.60 \pm 0.03$, $t_b = 0.396 \pm 0.017$ days, $n = 10$ has been fixed, and no host is included (the late HST data from Jin et al. 2018 are host-subtracted, and the host is very faint compared to the early data). However, this fit is statistically bad (χ^2/d.o.f. = 3.38), and we find that especially the late-time HST data decay steeper than the extrapolation of the GROND data, which already indicates a steep decay, as initially reported by Kann et al. (2015). Using data only after the break ($t > 0.5$ days), and setting $J_G = F125W$, we find a best fit with another broken power-law $\alpha_{2,1} = 1.48 \pm 0.04$, $\alpha_{2,2} = 2.54 \pm 0.21$, $t_b = 4.139 \pm 0.739$ days, $n = 10$ fixed, no host. This is fully in agreement with the results of Jin et al. (2018). For this fit, the SED (g'_G, $F606W$, r'_G, i'_G, z'_G, J_G, $F160W$) is well-fit by a straight power-law with $\beta = 0.60 \pm 0.36$, in accordance with the value Jin et al. (2018) assumed. We note that the SED derived from our initial fit shows more scatter and a shallower slope, $\beta = 0.31 \pm 0.07$. Neither show evidence for extinction. As we assume $z = 1$, $dRc = 0$. Finally, we create a further SED by carefully aligning early UVOT data to the *white* "backbone", and connecting that to late data by the early Keck observation (Knust et al. 2017). This SED yields $\beta = 0.50 \pm 0.09$, in good agreement with our late-time SED. This likely indicates some intrinsic

afterglow variability during the early plateau phase which is not captured by our broken power-law fit.

A.1.3 GRB 160821B

Data have been taken from Lamb et al. (2019); Troja et al. (2019); Kasliwal et al. (2017); Jin et al. (2018) and the GCN Circulars (Breeveld & Siegel 2016). This short GRB at $z = 0.16$ (Lamb et al. 2019) is known for its secure detection of a kilonova (Lamb et al. 2019; Troja et al. 2019). It is also the only short GRB so far with an (albeit tentative) detection of VHE emission (Acciari et al. 2021). As much of the light curve is dominated by kilonova light, we use the X-ray observations of the afterglow (G. P. Lamb, priv. comm.) as a stand-in, similar to the analysis of Lamb et al. (2019). We convert the flux densities to pseudo-magnitudes and shift the earliest (post-extended emission) point to the contemporaneous early optical observations, which are unlikely to be influenced by kilonova emission ($t < 0.1$ days). We find that at later times ($t \approx 5 - 10$ days) the optical emission in the bluest available bands (g' and $F606W$) is in agreement with the shifted X-ray emission, indicating the kilonova emission has become very red and faded under the afterglow level in these bands. Spectral information is sparse, but a $r'i'z'$ SED from early-time data is fit well by a simple power-law with slope $\beta = 0.62 \pm 0.13$, therefore we assume no dust, in agreement with the localisation offset from its host galaxy.

A.1.4 GRB 180418A

Data are taken from Becerra et al. (2019); Rouco Escorial et al. (2021) as well as GCN Circulars (Guidorzi et al. 2018; Choi et al. 2018; Horiuchi et al. 2018; Misra et al. 2018; Malesani et al. 2018; Schady 2018; Schady & Chen 2018; Troja et al. 2018). This is an event with a very bright early afterglow (Becerra et al. 2019) whose classification is unclear, however, the arguments presented in Rouco Escorial et al. (2021) indicate it is likely a short GRB, therefore we include it in this sample. The redshift is also unknown, but the host galaxy underlying the afterglow is very faint, and Rouco Escorial et al. (2021) estimate $z \approx 1.0 - 1.5$; similar to GRB 150424A, we adopt $z = 1$ here. Using data starting 0.00417 days after the trigger (the early emission is dominated by what is likely a reverse-shock flash, Becerra et al. 2019), and host-subtracting the data from sources other than Rouco Escorial et al. (2021), we find that using a single-power law decay yields a decay slope of $\alpha = 0.926 \pm 0.003$, in general agreement with the decay slopes found in Becerra et al. (2019); Rouco Escorial et al. (2021). Scatter combined with small error bars leads to a statistically bad fit (χ^2/d.o.f. = 5.41). We find this fit can be improved significantly (χ^2/d.o.f. = 3.32) by a broken power-law with $\alpha_1 = 0.837 \pm 0.009$, $\alpha_2 = 1.121 \pm 0.014$, $t_b = 0.033 \pm 0.004$ days, $n = 10$ fixed, and no host. The $\Delta\alpha$ is likely too small, and the post-break decay too shallow, for this to be a jet break. The broad SED ($uvw2$, $uvm2$, $uvw1$, u, b, g', v, r', i', z') shows some scatter, and is blue ($\beta = 0.43 \pm 0.17$) with no evidence for dust. The UVOT lenticular filters are somewhat depressed compared to the rest of the data, especially $uvw2$, which is what one would expect for $z \approx 1$.

A.1.5 GRB 181123B

GRB 181123B was a high-redshift short GRB at $z = 1.754$ with a bright host galaxy and a faint afterglow detection (Paterson et al. 2020). It shows extended emission (Dichiara et al. 2021) and was rapidly observed in the radio bands (Rowlinson et al. 2021; Anderson et al. 2021). As there is only a single i' detection, we have no information on colour or potential line-of-sight extinction. However, as the redshift is nearly identical to that of GRB 160410A, we assume the same dRc to plot it in the $z = 1$ frame. Generally, the afterglow is significantly fainter and the host significantly brighter than in the case of GRB 160410A.

A.1.6 Observed GRB Afterglows

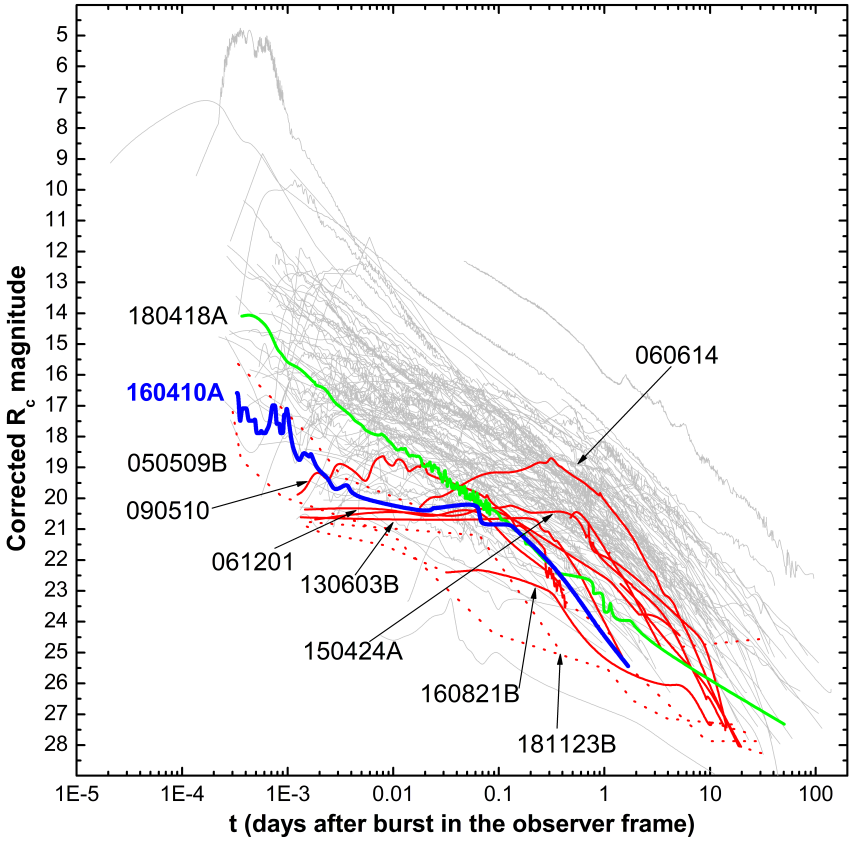

Figure A.1: The afterglow of GRB 160410A (thick blue line) in the context of a large sample of GRB afterglows. Light curves are corrected for Galactic extinction but otherwise as observed. Thin grey lines are afterglows of Type II GRBs. Thicker red lines are a selection of afterglows of other Type I GRB. We have highlighted several. The optical afterglow of GRB 050509B was undetected, the "light curve" consists of deep upper limits only. GRB 060614 is a peculiar temporally long-lasting likely Type I GRB, the afterglow shows a very late peak. The other highlighted afterglows all show early plateau phases. The afterglow of GRB 160410A, seen to be one of the brightest ever detected (among afterglows of type I GRBs) at very early times, also evinces a plateau phase, but after an early steep decay.

Observationally, the afterglow of GRB 180418A, where the classification is unclear (but with more evidence pointing toward it being a Type I GRB) is the brightest at early times, followed by that of GRB 160410A. The afterglow of GRB 180418A lacks a plateau phase and at 0.1 days, the two afterglows are of the same magnitude; however, later on, GRB 180418A decays less rapidly. Several other afterglows of Type I GRBs, such as the late-rising GRB 060614 and the long-plateau GRB 150424A, are also brighter at late times.

A.2 Photometric data on GRB 160410A

Table A.1: Photometry of the afterglow of GRB 160410A. Data are given in AB magnitudes and are not corrected for Galactic foreground extinction. Note that for UVOT data, the given exposure time is the total time coverage of each observation, for late-time data these values exceed the actual exposure time.

Time after burst (days)	Magnitude (AB)	Bin Width/ Exposure Time	Filter	Telescope/Instrument
0.062233	$21.884^{+0.670}_{-0.411}$	200	*uvw*1	*Swift*/UVOT
0.131352	$22.564^{+0.479}_{-0.331}$	900	*uvw*1	*Swift*/UVOT
0.641592	> 23.195	3001	*uvw*1	*Swift*/UVOT
0.003639	$20.349^{+1.399}_{-0.592}$	60	*u*	*Swift*/UVOT
0.003870	$19.848^{+0.713}_{-0.427}$	20	*u*	*Swift*/UVOT
0.004102	$20.280^{+1.200}_{-0.556}$	20	*u*	*Swift*/UVOT
0.004333	> 19.357	20	*u*	*Swift*/UVOT
0.064602	$21.289^{+0.468}_{-0.326}$	200	*u*	*Swift*/UVOT
0.140726	$21.893^{+0.394}_{-0.288}$	705	*u*	*Swift*/UVOT
0.532774	> 22.269	907	*u*	*Swift*/UVOT
0.716085	> 21.919	454	*u*	*Swift*/UVOT
0.050357	> 19.841	200	*b*	*Swift*/UVOT
0.066983	$20.842^{+0.680}_{-0.415}$	200	*b*	*Swift*/UVOT
0.540848	$22.142^{+2.779}_{-0.710}$	477	*b*	*Swift*/UVOT
0.023807	20.610 ± 0.057	198	g'_{GROND}	2.2m MPG/GROND
0.846850	24.440 ± 0.207	9715	g'_{GROND}	2.2m MPG/GROND
0.057488	> 19.510	200	*v*	*Swift*/UVOT
0.074104	$20.371^{+1.125}_{-0.541}$	200	*v*	*Swift*/UVOT
0.001169	$19.823^{+0.294}_{-0.231}$	20	*white*	*Swift*/UVOT
0.001400	$19.676^{+0.257}_{-0.207}$	20	*white*	*Swift*/UVOT
0.001632	$20.034^{+0.351}_{-0.265}$	20	*white*	*Swift*/UVOT

Table A.1: continued.

Time after burst (days)	Magnitude (AB)	Bin Width/ Exposure Time	Filter	Telescope/Instrument
0.001864	$20.362^{+0.514}_{-0.348}$	20	*white*	*Swift*/UVOT
0.002095	> 20.081	20	*white*	*Swift*/UVOT
0.002440	$20.572^{+0.391}_{-0.287}$	40	*white*	*Swift*/UVOT
0.002731	$21.130^{+3.621}_{-0.733}$	10	*white*	*Swift*/UVOT
0.052726	$21.122^{+0.330}_{-0.253}$	200	*white*	*Swift*/UVOT
0.069352	$22.172^{+0.508}_{-0.345}$	200	*white*	*Swift*/UVOT
0.0003298	$16.8^{+0.5}_{-0.5}$	1	r'	0.25m TAROT
0.0003414	$16.8^{+0.5}_{-0.5}$	1	r'	0.25m TAROT
0.0003530	$18.0^{+0.5}_{-0.5}$	1	r'	0.25m TAROT
0.0003645	$17.3^{+0.7}_{-0.5}$	1	r'	0.25m TAROT
0.0003761	$17.3^{+0.7}_{-0.5}$	1	r'	0.25m TAROT
0.0003877	$17.3^{+0.7}_{-0.5}$	1	r'	0.25m TAROT
0.0003993	$17.3^{+0.7}_{-0.5}$	1	r'	0.25m TAROT
0.0004108	$17.3^{+0.7}_{-0.5}$	1	r'	0.25m TAROT
0.0004224	$17.7^{+0.7}_{-0.5}$	1	r'	0.25m TAROT
0.0004340	$17.7^{+0.7}_{-0.4}$	1	r'	0.25m TAROT
0.0004456	$17.7^{+0.7}_{-0.4}$	1	r'	0.25m TAROT
0.0004571	$17.7^{+0.7}_{-0.4}$	1	r'	0.25m TAROT
0.0004687	$17.7^{+0.7}_{-0.4}$	1	r'	0.25m TAROT
0.0004803	$17.7^{+0.7}_{-0.4}$	1	r'	0.25m TAROT
0.0004919	$17.6^{+0.7}_{-0.4}$	1	r'	0.25m TAROT
0.0005034	$18.1^{+0.2}_{-0.6}$	1	r'	0.25m TAROT
0.0005150	$18.1^{+0.2}_{-0.6}$	1	r'	0.25m TAROT
0.0005266	$18.1^{+0.2}_{-0.6}$	1	r'	0.25m TAROT
0.0005382	$18.1^{+0.2}_{-0.6}$	1	r'	0.25m TAROT
0.0005497	$18.1^{+0.2}_{-0.6}$	1	r'	0.25m TAROT
0.0005613	$18.0^{+0.2}_{-0.6}$	1	r'	0.25m TAROT
0.0005729	$18.1^{+0.1}_{-0.7}$	1	r'	0.25m TAROT
0.0005845	$18.1^{+0.1}_{-0.7}$	1	r'	0.25m TAROT
0.0005960	$18.1^{+0.1}_{-0.7}$	1	r'	0.25m TAROT
0.0006076	$18.1^{+0.1}_{-0.7}$	1	r'	0.25m TAROT
0.0006192	$18.1^{+0.1}_{-0.7}$	1	r'	0.25m TAROT

Table A.1: continued.

Time after burst (days)	Magnitude (AB)	Bin Width/ Exposure Time	Filter	Telescope/Instrument
0.0006308	$18.0^{+0.1}_{-0.7}$	1	r'	0.25m TAROT
0.0006423	> 18.1	1	r'	0.25m TAROT
0.0006539	> 18.1	1	r'	0.25m TAROT
0.0006655	> 18.1	1	r'	0.25m TAROT
0.0006771	> 18.1	1	r'	0.25m TAROT
0.0006886	> 18.1	1	r'	0.25m TAROT
0.0007002	> 18.1	1	r'	0.25m TAROT
0.0007118	$17.2^{+0.5}_{-0.4}$	1	r'	0.25m TAROT
0.0007234	$17.2^{+0.5}_{-0.4}$	1	r'	0.25m TAROT
0.0007349	$17.2^{+0.5}_{-0.4}$	1	r'	0.25m TAROT
0.0007465	$17.2^{+0.5}_{-0.4}$	1	r'	0.25m TAROT
0.0007581	$17.2^{+0.5}_{-0.4}$	1	r'	0.25m TAROT
0.0007697	$17.4^{+0.6}_{-0.3}$	1	r'	0.25m TAROT
0.0007812	$17.8^{+0.6}_{-0.5}$	1	r'	0.25m TAROT
0.0007928	$17.8^{+0.6}_{-0.5}$	1	r'	0.25m TAROT
0.0008044	$17.8^{+0.6}_{-0.5}$	1	r'	0.25m TAROT
0.0008160	$17.8^{+0.6}_{-0.5}$	1	r'	0.25m TAROT
0.0008275	$17.8^{+0.6}_{-0.5}$	1	r'	0.25m TAROT
0.0008391	$17.8^{+0.6}_{-0.5}$	1	r'	0.25m TAROT
0.0008507	$18.1^{+0.3}_{-0.6}$	1	r'	0.25m TAROT
0.0008622	$18.1^{+0.3}_{-0.6}$	1	r'	0.25m TAROT
0.0008738	$18.1^{+0.3}_{-0.6}$	1	r'	0.25m TAROT
0.0008854	$18.1^{+0.3}_{-0.6}$	1	r'	0.25m TAROT
0.0008970	$18.1^{+0.3}_{-0.6}$	1	r'	0.25m TAROT
0.0009085	$18.1^{+0.3}_{-0.6}$	1	r'	0.25m TAROT
0.0009201	$17.5^{+0.7}_{-0.4}$	1	r'	0.25m TAROT
0.0009317	$17.5^{+0.7}_{-0.4}$	1	r'	0.25m TAROT
0.0009433	$17.5^{+0.7}_{-0.4}$	1	r'	0.25m TAROT
0.0009548	$17.5^{+0.7}_{-0.4}$	1	r'	0.25m TAROT
0.0009664	$17.5^{+0.7}_{-0.4}$	1	r'	0.25m TAROT
0.0009780	$17.1^{+0.6}_{-0.4}$	1	r'	0.25m TAROT
0.0009896	> 17.9	1	r'	0.25m TAROT

Table A.1: continued.

Time after burst (days)	Magnitude (AB)	Bin Width/ Exposure Time	Filter	Telescope/Instrument
0.0010011	> 17.9	1	r'	0.25m TAROT
0.0010127	> 17.9	1	r'	0.25m TAROT
0.005347	20.249 ± 0.037	5	r'	8.2m VLT/X-shooter
0.713489	23.944 ± 0.042	2700	r'	2.5m NOT/ALFOSC
1.677059	25.649 ± 0.291	3600	r'	2.5m NOT/ALFOSC
44.683899	> 27.450	1800	r'	10.4m GTC/OSIRIS
0.023807	20.533 ± 0.065	198	r'_{GROND}	2.2m MPG/GROND
0.849788	24.573 ± 0.312	10440	r'_{GROND}	2.2m MPG/GROND
0.023807	20.726 ± 0.089	198	i'_{GROND}	2.2m MPG/GROND
0.849788	23.702 ± 0.294	10875	i'_{GROND}	2.2m MPG/GROND
0.023807	20.194 ± 0.108	198	z'_{GROND}	2.2m MPG/GROND
0.853656	> 23.395	10440	z'_{GROND}	2.2m MPG/GROND
0.023906	> 20.383	180	J'_{GROND}	2.2m MPG/GROND
0.849844	> 21.510	9600	J'_{GROND}	2.2m MPG/GROND
0.023906	> 19.905	180	H'_{GROND}	2.2m MPG/GROND
0.865926	> 20.976	9720	H'_{GROND}	2.2m MPG/GROND
0.023906	> 19.116	180	K'_{GROND}	2.2m MPG/GROND
0.849844	> 19.066	9360	K'_{GROND}	2.2m MPG/GROND
499.651238	> 24.740	3600	3.6 μm	*Spitzer*/IRAC

Our photometry for GRB 160410A is given in Tab. A.1 as used for the light-curve and subsequent SED fitting.

A.3 SED fit for the GRB 201221D host

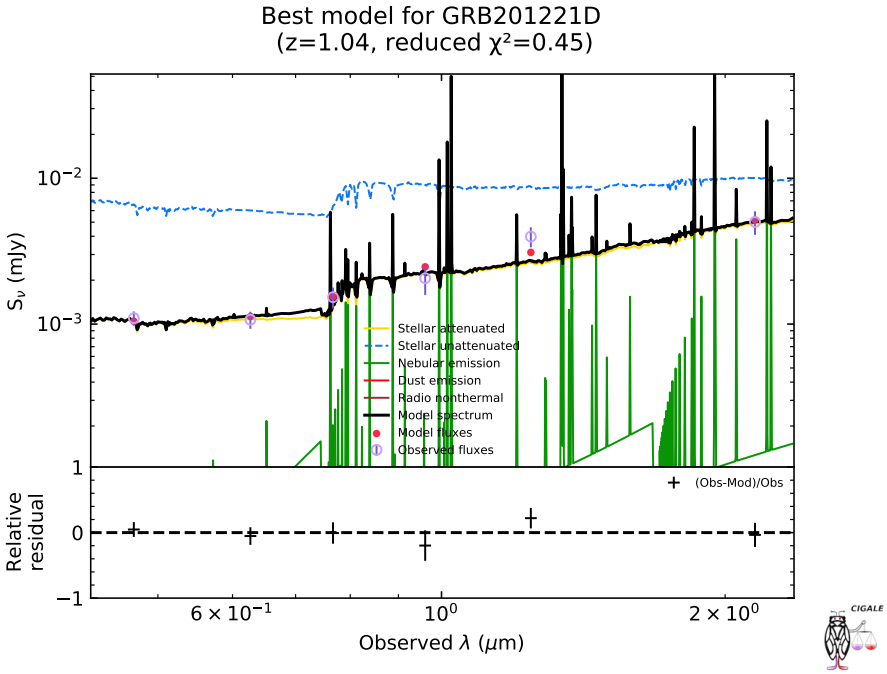

Figure A.2: Best-fit SED modelling of the host of GRB 201221D. The upper panel shows the flux density distribution for the performed SED fitting with the photometry presented in Tab.3.3 and the lower panel the corresponding residuals.

Appendix B

GRB 210610B Afterglow and host galaxy photometry

B.1 Afterglow and host galaxy photometry

Table B.1: Photometry of the afterglow of GRB 210610B. (t_0 = 19:51:05.05 UT). Magnitudes are given in the AB system and are not corrected for Galactic extinction. We give three magnitudes at 58 days, for the host galaxy measured in an aperture identical to that used in afterglow photometry, for the full host galaxy, and for the companion galaxy, respectively.

Epoch t-t_0 (day)	Band	Telescope/Instrument	Exposure (s)	Magnitudes	ref
1.09710	u'	GTC/HiPERCAM	10×60	20.311 ± 0.082	This Work
1.12521	u'	LT/IO:O	1×120	20.430 ± 0.082	(Perley 2021)
2.08091	u'	GTC/HiPERCAM	10×60	21.438 ± 0.067	This Work
5.18532	u'	GTC/HiPERCAM	10×60	22.498 ± 0.112	This Work
58.1043	u'	GTC/HiPERCAM	30×60	23.353 ± 0.076	This Work
58.1043	u'	GTC/HiPERCAM	30×60	23.034 ± 0.076	This Work
58.1043	u'	GTC/HiPERCAM	30×60	24.901 ± 0.096	This Work
0.07316	g'	Ondrejov D50	3×300	17.597 ± 0.018	This work
0.10523	g'	Ondrejov D50	3×300	17.627 ± 0.019	This work
0.14793	g'	Ondrejov D50	3×300	17.652 ± 0.023	This work
0.20578	g'	Ondrejov D50	10×180	17.833 ± 0.083	This work
0.40536	g'	1.22m Palomar P48 Schmidt/ZTF	1×30	18.490 ± 0.020	Ho et al. (2022)
0.53296	g'	1.22m Palomar P48 Schmidt/ZTF	1×30	18.770 ± 0.030	Ho et al. (2022)
1.09710	g'	GTC/HiPERCAM	10×60	20.010 ± 0.040	This work
1.12103	g'	LT/IO:O	1×90	20.040 ± 0.050	(Perley 2021)
1.12951	g'	Ondrejov D50	86×180	20.263 ± 0.181	This work
1.50546	g'	1.22m Palomar P48 Schmidt/ZTF	1×30	20.750 ± 0.140	Ho et al. (2022)
1.50646	g'	1.22m Palomar P48 Schmidt/ZTF	1×30	20.870 ± 0.120	Ho et al. (2022)
1.53416	g'	1.22m Palomar P48 Schmidt/ZTF	1×30	20.800 ± 0.140	Ho et al. (2022)
2.08091	g'	GTC/HiPERCAM	10×60	21.124 ± 0.031	This work
3.15081	g'	Ondrejov D50	97×180	21.689 ± 0.177	This work
4.13012	g'	Ondrejov D50	78×180	22.067 ± 0.098	This work
5.18532	g'	GTC/HiPERCAM	10×60	22.394 ± 0.058	This work
6.09497	g'	Perek 2.0m	9×300	22.672 ± 0.098	This work
58.1043	g'	GTC/HiPERCAM	30×60	23.307 ± 0.043	This work
58.1043	g'	GTC/HiPERCAM	30×60	22.960 ± 0.044	This work
58.1043	g'	GTC/HiPERCAM	30×60	24.866 ± 0.053	This work
0.04880	R	FRAM-ORM	23×60	17.211 ± 0.065	This work
0.05869	r'	Ondrejov D50	1×300	17.322 ± 0.017	This work
0.06069	R	FRAM-ORM	8×60	17.314 ± 0.080	This work
0.06219	r'	Ondrejov D50	1×300	17.377 ± 0.014	This work
0.06568	r'	Ondrejov D50	1×300	17.441 ± 0.019	This work

Table B.1 – Continued

Epoch t-t_0 (day)	Band	Telescope/ Instrument	Exposure (s)	Mag	ref
0.06642	R	FRAM-ORM	7×60	17.487 ± 0.087	This work
0.06981	r'	Ondrejov SBT	17×120	17.442 ± 0.063	This work
0.07042	r'	NOT	1×10	17.299 ± 0.100	(Fynbo et al. 2021)
0.07176	R	FRAM-ORM	7×60	17.569 ± 0.087	This work
0.07673	R	FRAM-ORM	6×60	17.416 ± 0.079	This work
0.08170	R	FRAM-ORM	7×60	17.489 ± 0.078	This work
0.08290	r'	Ondrejov SBT	18×120	17.489 ± 0.066	This work
0.08667	R	FRAM-ORM	6×60	17.572 ± 0.096	This work
0.09125	R	FRAM-ORM	6×60	17.664 ± 0.097	This work
0.09621	R	FRAM-ORM	7×60	17.534 ± 0.084	This work
0.10119	R	FRAM-ORM	6×60	17.533 ± 0.095	This work
0.10362	r'	Ondrejov SBT	23×120	17.491 ± 0.063	This work
0.12734	r'	Ondrejov SBT	25×120	17.402 ± 0.058	This work
0.15077	r'	Ondrejov SBT	34×120	17.363 ± 0.071	This work
0.18566	r'	Ondrejov D50	10×180	17.462 ± 0.031	This work
0.23746	r'	GTC/OSIRIS	1×30	17.621 ± 0.040	This work
0.44806	r'	Palomar P48 Schmidt/ZTF	1×30	18.229 ± 0.020	(Ho et al. 2022)
0.49346	r'	Palomar P48 Schmidt/ZTF	1×30	18.369 ± 0.020	(Ho et al. 2022)
1.02539	r'	CAHA/CAFOS	1×60	19.672 ± 0.112	This work
1.03206	r'	CAHA/CAFOS	1×180	19.653 ± 0.035	This work
1.03495	r'	CAHA/CAFOS	1×180	19.647 ± 0.030	This work
1.03791	r'	CAHA/CAFOS	1×180	19.663 ± 0.027	This work
1.09710	r'	GTC/HiPERCAM	10×60	19.720 ± 0.050	This work
1.12244	r'	LT/IO:O	1×90	19.809 ± 0.020	(Perley 2021)
1.44226	r'	Palomar P48 Schmidt/ZTF	1×30	20.299 ± 0.100	(Ho et al. 2022)
1.56876	r'	Palomar P48 Schmidt/ZTF	1×30	20.239 ± 0.100	(Ho et al. 2022)
2.08091	r'	GTC/HiPERCAM	10×60	20.873 ± 0.018	This work
2.42766	r'	Palomar P48 Schmidt/ZTF	1×30	21.689 ± 0.330	(Ho et al. 2022)
2.49606	r'	Palomar P48 Schmidt/ZTF	1×30	21.139 ± 0.200	Ho et al. (2022)
5.18532	r'	GTC/HiPERCAM	10×60	22.315 ± 0.042	This work
58.1043	r'	GTC/HiPERCAM	30×60	23.212 ± 0.042	This work
58.1043	r'	GTC/HiPERCAM	30×60	22.861 ± 0.042	This work
58.1043	r'	GTC/HiPERCAM	30×60	24.486 ± 0.058	This work
0.09453	i'	Ondrejov D50	5×180	17.328 ± 0.016	This work
0.16882	i'	Ondrejov D50	5×180	17.330 ± 0.025	This work
1.09710	i'	GTC/HiPERCAM	10×60	19.585 ± 0.048	This work
1.12383	i'	LT/IO:O	1×90	19.609 ± 0.030	(Perley 2021)
2.08091	i'	GTC/HiPERCAM	10×60	20.715 ± 0.022	This work

Table B.1 – Continued

Epoch t-t_0 (day)	Band	Telescope/ Instrument	Exposure (s)	Mag	ref
5.18532	i'	GTC/HiPERCAM	10×60	22.145 ± 0.047	This work
6.13124	i'	Ondrejov D50	96×180	> 22.760	This work
58.1043	i'	GTC/HiPERCAM	30×60	23.052 ± 0.023	This work
58.1043	i'	GTC/HiPERCAM	30×60	22.843 ± 0.024	This work
58.1043	i'	GTC/HiPERCAM	30×60	24.142 ± 0.049	This work
0.08363	z'	Ondrejov D50	5×180	17.234 ± 0.029	This work
0.11569	z'	Ondrejov D50	5×180	17.246 ± 0.028	This work
0.15862	z'	Ondrejov D50	5×180	17.285 ± 0.034	This work
1.0971	z'	GTC/HiPERCAM	10×60	19.413 ± 0.040	This work
1.1269	z'	LT/IO:O	1×90	19.491 ± 0.060	(Perley 2021)
1.1354	z'	Ondrejov D50	9×300	19.624 ± 0.140	This work
2.0809	z'	GTC/HiPERCAM	10×60	20.530 ± 0.027	This work
5.1853	z'	GTC/HiPERCAM	10×60	21.953 ± 0.052	This work
58.1043	z'	GTC/HiPERCAM	30×60	23.037 ± 0.028	This work
58.1043	z'	GTC/HiPERCAM	30×60	22.769 ± 0.031	This work
58.1043	z'	GTC/HiPERCAM	30×60	23.620 ± 0.057	This work
0.01173	Clear	Ondrejov SBT	20×12	15.931 ± 0.218	This work
0.01504	Clear	Ondrejov SBT	20×12	15.451 ± 0.128	This work
0.01809	Clear	Ondrejov SBT	20×12	15.743 ± 0.141	This work
0.02108	Clear	Ondrejov SBT	20×12	16.243 ± 0.136	This work
0.02399	Clear	Ondrejov SBT	20×12	16.419 ± 0.120	This work
0.02705	Clear	Ondrejov SBT	20×12	16.640 ± 0.128	This work
0.02988	Clear	Ondrejov SBT	20×12	16.685 ± 0.099	This work
0.03266	Clear	Ondrejov SBT	20×12	16.860 ± 0.113	This work
0.03550	Clear	Ondrejov SBT	20×12	17.047 ± 0.119	This work
0.03835	Clear	Ondrejov SBT	20×12	16.954 ± 0.095	This work
0.04113	Clear	Ondrejov SBT	20×12	17.075 ± 0.099	This work
0.04391	Clear	Ondrejov SBT	20×12	17.002 ± 0.088	This work
0.04668	Clear	Ondrejov SBT	20×12	17.083 ± 0.096	This work
0.04953	Clear	Ondrejov SBT	20×12	17.187 ± 0.096	This work
0.05238	Clear	Ondrejov SBT	20×12	16.975 ± 0.075	This work
0.05886	Clear	Ondrejov SBT	43×12	17.233 ± 0.059	This work
252.3749	H	GTC/EMIR	349	> 22.9	This work

Appendix C

Polarisation detection on GRBs optical afterglow emission.

C.1 Lineal polarisation measurements on GRBs afterglow emission.

Table C.1: Measured values for the lineal polarisation and PA on GRB afterglow from literature.

GRB	Redshift	T_{mid} (days)	P_{Lin}	θ (%)	Ref. (º)
GRB 990510	1.62	0.7708	1.7 ± 0.2	101 ± 3	(Covino et al. 1999)
		0.8583	1.6 ± 0.2	96 ± 4	(Wijers et al. 1999)
		1.8083	$2.2^{+1.1}_{-0.9}$	112^{+15}_{-17}	
GRB 990712	0.43	0.44	2.9 ± 0.4	121.1 ± 3.5	(Rol et al. 2000)
		0.70	1.2 ± 0.4	116.2 ± 10.1	
		1.45	2.2 ± 0.7	139.1 ± 10.4	
GRB 020405	0.695	1.2292	1.50 ± 0.40	172 ± 8	(Masetti et al. 2003)
		1.3208	9.89 ± 1.30	180 ± 4	(Bersier et al. 2003)
		2.2682	1.96 ± 0.33	154 ± 5	(Covino et al. 2003)
		3.8792	1.47 ± 0.43	168 ± 9	
GRB 020813	1.35	0.21528	2.22 ± 0.07	157.6 ± 1.0	(Barth et al. 2003)
		0.26181	1.98 ± 0.04	153.4 ± 1.7	
		0.34167	1.96 ± 0.07	152.0 ± 1.2	
		0.89792	1.07 ± 0.22	154.3 ± 5.9	(Gorosabel et al. 2004)
		0.93750	1.42 ± 0.25	137.0 ± 4.4	
		0.97542	1.11 ± 0.22	150.5 ± 5.5	
		1.01625	1.05 ± 0.23	146.4 ± 6.2	
		1.11667	1.43 ± 0.44	155.8 ± 8.5	
		1.97958	1.26 ± 0.34	164.7 ± 7.4	
GRB 021004	2.33	0.37	1.72 ± 0.56	187.7 ± 8.3	(Rol et al. 2003)
		0.38	2.09 ± 0.60	173.0 ± 7.9	
GRB 030329	0.17	0.5321	0.92 ± 0.10	86.13 ± 2.43	(Covino & Gotz 2016)**
		0.5492	0.86 ± 0.09	86.74 ± 2.40	
		0.5671	0.87 ± 0.09	88.60 ± 2.64	
		0.5850	0.80 ± 0.09	91.12 ± 2.88	
		0.6921	0.66 ± 0.07	78.52 ± 2.94	
		0.7129	0.66 ± 0.07	76.69 ± 2.89	
		0.7342	0.56 ± 0.05	74.37 ± 3.11	
		1.5204	1.97 ± 0.48	83.20	
		1.5500	1.37 ± 0.11	61.65 ± 2.38	
		1.5800	1.50 ± 0.12	62.29 ± 2.44	
		1.6700	1.07 ± 0.09	59.41 ± 2.51	
		1.7000	1.09 ± 0.08	66.07 ± 2.45	
		1.7200	1.02 ± 0.08	67.05 ± 2.60	
		1.7400	1.13 ± 0.08	70.56 ± 2.51	

Table C.1: Continued.

		2.6800	0.52 ± 0.06	30.76 ± 5.04	
		2.7000	0.52 ± 0.12	12.55 ± 4.63	
		2.7200	0.31 ± 0.07	24.50 ± 6.94	
		3.5400	0.57 ± 0.09	53.85 ± 4.08	
		3.5600	0.53 ± 0.08	57.08 ± 4.06	
		3.5800	0.42 ± 0.10	62.21 ± 6.10	
		5.6600	1.68 ± 0.18	66.32 ± 3.38	
		7.6400	2.22 ± 0.28	75.16 ± 3.32	
		9.5900	1.33 ± 0.14	70.91 ± 3.31	
		13.6000	2.04 ± 0.57	1.16 ± 7.64	
		22.5000	0.58 ± 0.10	42.7 ± 9.26	
		37.5000	1.48 ± 0.48	25.42 ± 9.41	
XR 080109	0.007	3.6416	0.95 ± 0.20	114.9 ± 5.9	(Gorosabel et al. 2010)
		5.5552	0.85 ± 0.28	106.1 ± 9.4	
		20.6279	1.05 ± 0.06	135.3 ± 1.7	
		20.6443	1.28 ± 0.06	132.5 ± 1.4	
		52.5578	1.42 ± 0.46	139.0 ± 9.1	
GRB 080928	1.6919	1.7	$4.49^{+1.16}_{-0.96}$	41.3 ± 6.3	(Brivio et al. 2022)
GRB 090102	1.55	0.0025	10.1 ± 1.3	–	(Steele et al. 2009)
GRB 091208B	1.063	0.0042	10.4 ± 2.5	92 ± 6	(Uehara et al. 2012)
GRB 091018	0.971	0.2461	1.07 ± 0.30	179.2 ± 16.1	(Wiersema et al. 2012)
		0.4548	1.44 ± 0.32	2.2 ± 12.6	
		1.1394	1.73 ± 0.36	69.8 ± 11.7	
		1.1552	3.25 ± 0.35	57.6 ± 6.1	
		1.1735	1.99 ± 0.35	27.6 ± 10.0	
		1.1893	1.42 ± 0.36	114.6 ± 14.0	
		1.3918	0.97 ± 0.32	32.8 ± 17.8	
		1.4493	1.08 ± 0.35	88.7 ± 17.9	
		2.3902	1.45 ± 0.37	169.0 ± 14.3	
GRB 120308	2.22	0.0033	28^{+4}_{-4}	34 ± 4	(Mundell et al. 2013)
		0.0042	23^{+4}_{-4}	44 ± 6	
		0.0052	17^{+5}_{-4}	51 ± 9	
		0.0062	16^{+7}_{-4}	40 ± 10	
		0.0081	16^{+5}_{-4}	55 ± 9	
GRB 121024A	2.298	0.2194	4.09 ± 0.2	163.7 ± 2.8	(Wiersema et al. 2014)
		0.2302	4.83 ± 0.2	160.3 ± 2.3	
		0.2782	3.82 ± 0.2	182.7 ± 3.0	
		0.2928	3.12 ± 0.19	175.3 ± 3.5	
		0.3088	3.39 ± 0.18	178.0 ± 2.9	

Table C.1: Continued.

		0.3252	3.49 ± 0.18	180.3 ± 3.0	
		0.3412	3.2 ± 0.18	174.5 ± 3.3	
		1.2995	2.66 ± 0.6	83.0 ± 12.6	
GRB 191221B	1.148	0.121	1.4 ± 0.1	68 ± 5	(Urata et al. 2023)
		0.417	1.0 ± 0.1	57 ± 5	
		2.525	1.3 ± 0.1	62 ± 6	
GRB 210610B	1.1345	0.0973	4.27 ± 1.45	183 ± 9	This work
		0.2407	0.22 ± 0.20	267 ± 19	
		0.2688	0.03 ± 0.17	–	
		0.2793	0.15 ± 0.28	–	
		1.2655	2.27 ± 0.22	237 ± 3	
		1.2829	1.69 ± 0.27	238 ± 5	
GRB 210619B	1.937	0.1057	2.2 ± 0.7	22.0 ± 10.0	(Mandarakas et al. 2023)
		0.1070	2.6 ± 0.8	2.0 ± 8.0	

We include only the values from literature for which we calculate $P/\sigma_P > 3.0$ with T_{mid} in observer frame.

(*) From the spectropolarimetric measurements in (Barth et al. 2003), since we do not consider chromaticity in the polarization, we show the median value of the measured polarisation on the different wavelength bins, for the three epochs they presents.

(**) For GRB 030329 we made use of the data presented in Covino & Gotz (2016) and, specifically, the results presented in this review taken from Greiner et al. (2003) and Magalhaes et al. (2003).

List of publications

Main publications for this thesis

- GRB 160410A: The first chemical study of the interstellar medium of a short GRB

Agüí Fernández, J. F., Thöne, C. C., Kann, D. A., de Ugarte Postigo, A., Selsing, J., Schady, P., Yates, R. M., Greiner, J., Oates, S. R., Malesani, D. B., Xu, D., Klotz, A., Campana, S., Rossi, A., Perley, D. A., Blažek, M., D'Avanzo, P., Giunta, A., Hartmann, D., Heintz, K. E., Jakobsson, P., Kirkpatrick, C. C., Kouveliotou, C., Melandri, A., Pugliese, G., Salvaterra, R., Starling, R. L. C., Tanvir, N. R., Vergani, S. D., and Wiersema, K.
Monthly Notices of the Royal Astronomical Society, Volume 520, Issue 1, pp.613-636
10.1093/mnras/stad099

- Varying linear polarisation in the dust-free gamma-ray burst 210610B

Agüí Fernández, J. F., de Ugarte Postigo, A., Thöne, C. C., Kobayashi, S., Rossi, A., Toma, K., Jelínek, M., Kann, D. A., Covino, S., Wiersema, K., Hartmann, D., Jakobsson, P., Martin-Carrillo, A., Melandri, A., De Pasquale, M., Pugliese, G., Savaglio, S., Starling, R. L. C., Štrobl, J., Della Valle, M., de Wet, S., and Zafar, T.
Astronomy & Astrophysics, Volume 690, id.A216, 17 pp.
10.1051/0004-6361/202348572

- The SHOALS Sample. Integrated properties of long GRB host galaxies.

Agüí Fernández, J. F., de Ugarte Postigo, A., Thöne, C. C., in preparation

Other refereed publications

- Rocking the BOAT: the ups and downs of the long-term radio light curve for GRB 221009A

Rhodes, L., van der Horst, A. J., Bright, J. S., Leung, J. K., Anderson, G. E., Fender, R., **Agüí Fernández, J. F.**, Bremer, M., Chandra, P., Dobie, D., Farah, W., Giarratana, S., Gourdji, K., Green, D. A., Lenc, E., Michałowski, M. J., Murphy, T., Nayana, A. J., Pollak, A. W., Rowlinson, A., Schussler, F., Siemion, A., Starling, R. L. C., Scott, P., Thöne, C. C., Titterington, D., and de Ugarte Postigo, A.
Monthly Notices of the Royal Astronomical Society, Volume 533, Issue 4, pp.4435-4449
DOI:10.1093/mnras/stae2050

- Unveiling the Multifaceted GRB 200613A: Prompt Emission Dynamics, Afterglow Evolution, and the Host Galaxy's Properties

Fu, Shao-Yu, Xu, Dong, Lei, Wei-Hua, de Ugarte Postigo, Antonio, Kann, D. Alexander,

Thöne, Christina C., **Agüí Fernández, José Feliciano**, Shuang-Xi, Yi, Xie, Wei, Zou, Yuan-Chuan, Liu, Xing, Jiang, Shuai-Qing, Lu, Tian-Hua, An, Jie, Zhu, Zi-Pei, Zheng, Jie, Tang, Qing-Wen, Zhao, Peng-Wei, Xin, Li-Ping, and Wei, Jian-Yan
The Astrophysical Journal, Volume 974, Issue 2, id.221, 21 pp.
DOI:10.3847/1538-4357/ad6306

- The host of GRB 171205A in 3D: A resolved multiwavelength study of a rare grand-design spiral GRB host

Thöne, C. C., de Ugarte Postigo, A., Izzo, L., Michalowski, M. J., Levan, A. J., Leung, J. K., **Agüí Fernández, J. F.**, Géron, T., Friesen, R., Christensen, L., Covino, S., D'Elia, V., Hartmann, D. H., Jakobsson, P., De Pasquale, M., Pugliese, G., Rossi, A., Schady, P., Wiersema, K., and Zafar, T.
Astronomy & Astrophysics, Volume 690, id.A66, 28 pp.
DOI:10.1051/0004-6361/202348141

- Fires in the deep: The luminosity distribution of early-time gamma-ray-burst afterglows in light of the Gamow Explorer sensitivity requirements

Kann, D. A., White, N. E., Ghirlanda, G., Oates, S. R., Melandri, A., Jelínek, M., de Ugarte Postigo, A., Levan, A. J., Martin-Carrillo, A., Paek, G. S. -H., Izzo, L., Blazek, M., Thöne, C. C., **Agüí Fernández, J. F.**, Salvaterra, R., Tanvir, N. R., Chang, T. -C., O'Brien, P., Rossi, A., Perley, D. A., Im, M., Malesani, D. B., Antonelli, A., Covino, S., Choi, C., D'Avanzo, P., D'Elia, V., Dichiara, S., Fausey, H. M., Fugazza, D., Gomboc, A., Gorski, K. M., Granot, J., Guidorzi, C., Hanlon, L., Hartmann, D. H., Hudec, R., Jun, H. D., Kim, J., Kim, Y., Klose, S., Kluźniak, W., Kobayashi, S., Kouveliotou, C., Lidz, A., Marongiu, M., Martone, R., Meintjes, P., Mundell, C. G., Murphy, D., Nalewajko, K., Park, W. -K., Szécsi, D., Smith, R. J., Stecklum, B., Steele, I. A., Štrobl, J., Sung, H. -I. -, Updike, A., Urata, Y., and van der Horst, A. J.
Astronomy & Astrophysics, Volume 686, id.A56, 43 pp.
DOI:10.1051/0004-6361/202348159

- Multiband analyses of the bright GRB 230812B and the associated SN2023pel

Hussenot-Desenonges, T., Wouters, T., Guessoum, N., Abdi, I., Abulwfa, A., Adami, C., **Agüí Fernández, J. F.**, Ahumada, T., Aivazyan, V., Akl, D., Anand, S., Andrade, C. M., Antier, S., Ata, S. A., D'Avanzo, P., Azzam, Y. A., Baransky, A., Basa, S., Blazek, M., Bendjoya, P., Beradze, S., Boumis, P., Bremer, M., Brivio, R., Buat, V., Bulla, M., Burkhonov, O., Burns, E., Cenko, S. B., Coughlin, M. W., Corradi, W., Daigne, F., Dietrich, T., Dornic, D., Ducoin, J. -G., Duverne, P. -A., Elhosseiny, E. G., Elnagahy, F. I., El-Sadek, M. A., Ferro, M., Le Floc'h, E., Freeberg, M., Fynbo, J. P. U., Götz, D., Gurbanov, E., Hamed, G. M., Hasanov, E., Healy, B. F., Heintz, K. E., Hello, P., Inasaridze, R., Iskandar, A., Ismailov, N., Izzo, L., Jhawar, S., Jegou du Laz, T., Kamel, T. M., Karpov, S., Klotz, A., Koulouridis, E., Kuin, N. P., Kochiashvili, N., Leonini, S., Lu, K. -X., Malesani, D. B., Mašek, M., Mao, J., Melandri, A., Mihov, B. M., Natsvlishvili, R., Navarete,

F., Nedora, V., Nicolas, J., Odeh, M., Palmerio, J., Pang, P. T. H., De Pasquale, M., Peng, H. W., Pormente, S., Peloton, J., Pradier, T., Pyshna, O., Rajabov, Y., Rakotondrainibe, N. A., Rivet, J. -P., Rousselot, L., Saccardi, A., Sasaki, N., Schneider, B., Serrau, M., Shokry, A., Slavcheva-Mihova, L., Simon, A., Sokoliuk, O., Srinivasaragavan, G., Strausbaugh, R., Takey, A., Tanvir, N. R., Thöne, C. C., Tillayev, Y., Tosta e Melo, I., Turpin, D., de Ugarte Postigo, A., Vasylenko, V., Vergani, S. D., Vidadi, Z., Xu, D., Wang, L. T., Wang, X. F., Winters, J. M., Zhang, X. -L., and Zhu, Z.
Monthly Notices of the Royal Astronomical Society, Volume 530, Issue 1, pp.1-19
DOI:10.1093/mnras/stae503

- Highly luminous supernovae associated with gamma-ray bursts. II. The luminous blue bump in the afterglow of GRB 140506A

Kann, D. A., Rossi, A., Oates, S. R., Klose, S., Blazek, M., **Agüí Fernández, J. F.**, de Ugarte Postigo, A., Thöne, C. C., and Schulze, S.
Astronomy & Astrophysics, Volume 684, id.A164, 10 pp.
DOI:10.1051/0004-6361/202142344

- Optical and Near-infrared Observations of the Distant but Bright "New Year's Burst" GRB 220101A

Zhu, Zi-Pei, Lei, Wei-Hua, Malesani, Daniele B., Fu, Shao-Yu, Liu, Dong-Jie, Xu, Dong, D'Avanzo, Paolo, **Agüí Fernández, José Feliciano**, Fynbo, Johan P. U., Gao, Xing, Nicuesa Guelbenzu, Ana, Jiang, Shuai-Qing, Kann, David Alexander, Klose, Sylvio, Liu, Jin-Zhong, Liu, Xing, De Pasquale, Massimiliano, de Ugarte Postigo, Antonio, Stecklum, Bringfried, Thöne, Christina, Markku Viuho, Joonas Kari, Zhu, Yi-Nan, Li, Jin-Da, Gao, He, Lu, Tian-Hua, Xiao, Shuo, Zou, Yuan-Chuan, Xin, Li-Ping, and Wei, Jian-Yan
The Astrophysical Journal, Volume 959, Issue 2, id.118, 12 pp.
DOI:10.3847/1538-4357/ad05c8

- A long-duration gamma-ray burst of dynamical origin from the nucleus of an ancient galaxy

Levan, Andrew J., Malesani, Daniele B., Gompertz, Benjamin P., Nugent, Anya E., Nicholl, Matt, Oates, Samantha R., Perley, Daniel A., Rastinejad, Jillian, Metzger, Brian D., Schulze, Steve, Stanway, Elizabeth R., Inkenhaag, Anne, Zafar, Tayyaba, **Agüí Fernández, J. Feliciano**, Chrimes, Ashley A., Bhirombhakdi, Kornpob, de Ugarte Postigo, Antonio, Fong, Wen-fai, Fruchter, Andrew S., Fragione, Giacomo, Fynbo, Johan P. U., Gaspari, Nicola, Heintz, Kasper E., Hjorth, Jens, Jakobsson, Pall, Jonker, Peter G., Lamb, Gavin P., Mandel, Ilya, Mandhai, Soheb, Ravasio, Maria E., Sollerman, Jesper, and Tanvir, Nial R.
Nature Astronomy, Volume 7, p. 976-985
DOI:10.1038/s41550-023-01998-8

- GRB 221009A: The Boat

Burns, Eric, Svinkin, Dmitry, Fenimore, Edward, Kann, D. Alexander, **Agüí Fernández, José Feliciano**, Frederiks, Dmitry, Hamburg, Rachel, Lesage, Stephen, Temiraev, Yuri, Tsvetkova, Anastasia, Bissaldi, Elisabetta, Briggs, Michael S., Dalessi, Sarah, Dunwoody, Rachel, Fletcher, Cori, Goldstein, Adam, Hui, C. Michelle, Hristov, Boyan A., Kocevski, Daniel, Lysenko, Alexandra L., Mailyan, Bagrat, Mangan, Joseph, McBreen, Sheila, Racusin, Judith, Ridnaia, Anna, Roberts, Oliver J., Ulanov, Mikhail, Veres, Peter, Wilson-Hodge, Colleen A., and Wood, Joshua
The Astrophysical Journal Letters, Volume 946, Issue 1, id.L31, 14 pp.
DOI:10.3847/2041-8213/acc39c

- The First JWST Spectrum of a GRB Afterglow: No Bright Supernova in Observations of the Brightest GRB of all Time, GRB 221009A

Levan, A. J., Lamb, G. P., Schneider, B., Hjorth, J., Zafar, T., de Ugarte Postigo, A., Sargent, B., Mullally, S. E., Izzo, L., D'Avanzo, P., Burns, E., **Agüí Fernández, J. F.**, Barclay, T., Bernardini, M. G., Bhirombhakdi, K., Bremer, M., Brivio, R., Campana, S., Chrimes, A. A., D'Elia, V., Della Valle, M., De Pasquale, M., Ferro, M., Fong, W., Fruchter, A. S., Fynbo, J. P. U., Gaspari, N., Gompertz, B. P., Hartmann, D. H., Hedges, C. L., Heintz, K. E., Hotokezaka, K., Jakobsson, P., Kann, D. A., Kennea, J. A., Laskar, T., Le Floc'h, E., Malesani, D. B., Melandri, A., Metzger, B. D., Oates, S. R., Pian, E., Piranomonte, S., Pugliese, G., Racusin, J. L., Rastinejad, J. C., Ravasio, M. E., Rossi, A., Saccardi, A., Salvaterra, R., Sbarufatti, B., Starling, R. L. C., Tanvir, N. R., Thöne, C. C., van der Horst, A. J., Vergani, S. D., Watson, D., Wiersema, K., Wijers, R. A. M. J., and Xu, Dong
The Astrophysical Journal Letters, Volume 946, Issue 1, id.L28, 14 pp.
DOI:10.3847/2041-8213/acc2c1

- Publisher Correction: A very luminous jet from the disruption of a star by a massive black hole

Andreoni, Igor, Coughlin, Michael W., Perley, Daniel A., Yao, Yuhan, Lu, Wenbin, Cenko, S. Bradley, Kumar, Harsh, Anand, Shreya, Ho, Anna Y. Q., Kasliwal, Mansi M., de Ugarte Postigo, Antonio, Sagués-Carracedo, Ana, Schulze, Steve, Kann, D. Alexander, Kulkarni, S. R., Sollerman, Jesper, Tanvir, Nial, Rest, Armin, Izzo, Luca, Somalwar, Jean J., Kaplan, David L., Ahumada, Tomás, Anupama, G. C., Auchettl, Katie, Barway, Sudhanshu, Bellm, Eric C., Bhalerao, Varun, Bloom, Joshua S., Bremer, Michael, Bulla, Mattia, Burns, Eric, Campana, Sergio, Chandra, Poonam, Charalampopoulos, Panos, Cooke, Jeff, D'Elia, Valerio, Das, Kaustav Kashyap, Dobie, Dougal, **Agüí Fernández, José Feliciano**, Freeburn, James, Fremling, Cristoffer, Gezari, Suvi, Goode, Simon, Graham, Matthew J., Hammerstein, Erica, Karambelkar, Viraj R., Kilpatrick, Charles D., Kool, Erik C., Krips, Melanie, Laher, Russ R., Leloudas, Giorgos, Levan, Andrew,

Lundquist, Michael J., Mahabal, Ashish A., Medford, Michael S., Miller, M. Coleman, Möller, Anais, Mooley, Kunal P., Nayana, A. J., Nir, Guy, Pang, Peter T. H., Paraskeva, Emmy, Perley, Richard A., Petitpas, Glen, Pursiainen, Miika, Ravi, Vikram, Ridden-Harper, Ryan, Riddle, Reed, Rigault, Mickael, Rodriguez, Antonio C., Rusholme, Ben, Sharma, Yashvi, Smith, I. A., Stein, Robert D., Thöne, Christina, Tohuvavohu, Aaron, Valdes, Frank, van Roestel, Jan, Vergani, Susanna D., Wang, Qinan, and Zhang, Jielai
Nature, Volume 613, Issue 7945, p.E6-E6
DOI:10.1038/s41586-023-05699-0

- A very luminous jet from the disruption of a star by a massive black hole

Andreoni, Igor, Coughlin, Michael W., Perley, Daniel A., Yao, Yuhan, Lu, Wenbin, Cenko, S. Bradley, Kumar, Harsh, Anand, Shreya, Ho, Anna Y. Q., Kasliwal, Mansi M., de Ugarte Postigo, Antonio, Sagués-Carracedo, Ana, Schulze, Steve, Kann, D. Alexander, Kulkarni, S. R., Sollerman, Jesper, Tanvir, Nial, Rest, Armin, Izzo, Luca, Somalwar, Jean J., Kaplan, David L., Ahumada, Tomás, Anupama, G. C., Auchettl, Katie, Barway, Sudhanshu, Bellm, Eric C., Bhalerao, Varun, Bloom, Joshua S., Bremer, Michael, Bulla, Mattia, Burns, Eric, Campana, Sergio, Chandra, Poonam, Charalampopoulos, Panos, Cooke, Jeff, D'Elia, Valerio, Das, Kaustav Kashyap, Dobie, Dougal, **Agüí Fernández, José Feliciano**, Freeburn, James, Fremling, Cristoffer, Gezari, Suvi, Goode, Simon, Graham, Matthew J., Hammerstein, Erica, Karambelkar, Viraj R., Kilpatrick, Charles D., Kool, Erik C., Krips, Melanie, Laher, Russ R., Leloudas, Giorgos, Levan, Andrew, Lundquist, Michael J., Mahabal, Ashish A., Medford, Michael S., Miller, M. Coleman, Möller, Anais, Mooley, Kunal P., Nayana, A. J., Nir, Guy, Pang, Peter T. H., Paraskeva, Emmy, Perley, Richard A., Petitpas, Glen, Pursiainen, Miika, Ravi, Vikram, Ridden-Harper, Ryan, Riddle, Reed, Rigault, Mickael, Rodriguez, Antonio C., Rusholme, Ben, Sharma, Yashvi, Smith, I. A., Stein, Robert D., Thöne, Christina, Tohuvavohu, Aaron, Valdes, Frank, van Roestel, Jan, Vergani, Susanna D., Wang, Qinan, and Zhang, Jielai
Nature, Volume 612, Issue 7940, p.430-434
DOI:10.1038/s41586-022-05465-8

- A kilonova following a long-duration gamma-ray burst at 350 Mpc

Rastinejad, Jillian C., Gompertz, Benjamin P., Levan, Andrew J., Fong, Wen-fai, Nicholl, Matt, Lamb, Gavin P., Malesani, Daniele B., Nugent, Anya E., Oates, Samantha R., Tanvir, Nial R., de Ugarte Postigo, Antonio, Kilpatrick, Charles D., Moore, Christopher J., Metzger, Brian D., Ravasio, Maria Edvige, Rossi, Andrea, Schroeder, Genevieve, Jencson, Jacob, Sand, David J., Smith, Nathan, **Agüí Fernández, José Feliciano**, Berger, Edo, Blanchard, Peter K., Chornock, Ryan, Cobb, Bethany E., De Pasquale, Massimiliano, Fynbo, Johan P. U., Izzo, Luca, Kann, D. Alexander, Laskar, Tanmoy, Marini, Ester, Paterson, Kerry, Escorial, Alicia Rouco, Sears, Huei M., and Thöne, Christina C.
Nature, Volume 612, Issue 7939, p.223-227

DOI:10.1038/s41586-022-05390-w

- Multiwavelength analysis of short GRB 201221D and its comparison with other high low redshift short GRBs

Dimple, Misra, K., Kann, D. A., Arun, K. G., Ghosh, A., Gupta, R., Resmi, L., **Agüí Fernández, J. F.**, Thöne, C. C., de Ugarte Postigo, A., Pandey, S. B., and Yadav, L.
Monthly Notices of the Royal Astronomical Society, Volume 516, Issue 1, pp.1-12
DOI:10.1093/mnras/stac2162

- Cosmological Fast Optical Transients with the Zwicky Transient Facility: A Search for Dirty Fireballs

Ho, Anna Y. Q., Perley, Daniel A., Yao, Yuhan, Svinkin, Dmitry, de Ugarte Postigo, A., Perley, R. A., Kann, D. Alexander, Burns, Eric, Andreoni, Igor, Bellm, Eric C., Bissaldi, Elisabetta, Bloom, Joshua S., Brink, Thomas G., Dekany, Richard, Drake, Andrew J., **Agüí Fernández, José Feliciano**, Filippenko, Alexei V., Frederiks, Dmitry, Graham, Matthew J., Hristov, Boyan A., Kasliwal, Mansi M., Kulkarni, S. R., Kumar, Harsh, Laher, Russ R., Lysenko, Alexandra L., Mailyan, Bagrat, Malacaria, Christian, Miller, A. A., Poolakkil, S., Riddle, Reed, Ridnaia, Anna, Rusholme, Ben, Savchenko, Volodymyr, Sollerman, Jesper, Thöne, Christina, Tsvetkova, Anastasia, Ulanov, Mikhail, and von Kienlin, Andreas
The Astrophysical Journal, Volume 938, Issue 1, id.85, 27 pp.
DOI:10.3847/1538-4357/ac8bd0

- Outflows from GRB hosts are ubiquitous: Kinematics of z ¡ 0.3 GRB-SN hosts resolved with FLAMES

Thöne, C. C., Izzo, L., Flores, H., de Ugarte Postigo, A., Vergani, S. D., **Agüí Fernández, J. F.**, Kann, D. A., Christensen, L., Covino, S., Della Valle, M., Hammer, F., Melandri, A., Puech, M., Rodrigues, M. A., and Gorosabel, J.
Astronomy & Astrophysics, Volume 656, id.A136, 22 pp.
DOI:10.1051/0004-6361/201935652

Non-refereed publications

GRB 241030B: GTC/OSIRIS+ tentative spectroscopic redshift z = 2.82
Tanvir, N. R., Thoene, C. C., Fynbo, J. P. U., de Ugarte Postigo, A., Izzo, L., Malesani, D. B., Martin-Carrillo, A., **Agui Fernandez, J. F.**, Lombardi, G., Geier, S., and Gómez Velarde, G.
GRB Coordinates Network, Circular Service, No. 38004

GRB 241029A: GTC/OSIRIS+ spectroscopic redshift z=1.072

Agui Fernandez, J. F., de Ugarte Postigo, A., Malesani, D. B., Martin-Carrillo, A., Lombardi, G., Thoene, C. C., Tanvir, N. R., Izzo, L., Geier, S., and Perez Valladares, D.
GRB Coordinates Network, Circular Service, No. 37950

GRB 240912A: Redshift from OSIRIS+/GTC
de Ugarte Postigo, A., **Agui Fernandez, J. F.**, Thoene, C. C., Rakotondrainibe, N. A., Tanvir, N. R., Izzo, L., Geier, S., Lombardi, G., Fynbo, J. P. U., Martin-Carrillo, A., Garcia Rodriguez, A., and Perez Romero, A.
GRB Coordinates Network, Circular Service, No. 37469

GRB 240910A: Redshift from OSIRIS+/GTC
de Ugarte Postigo, A., **Agui Fernandez, J. F.**, Thoene, C. C., Rakotondrainibe, N. A., Tanvir, N. R., Izzo, L., Geier, S., Lombardi, G., Fynbo, J. P. U., Martin-Carrillo, A., Garcia Rodriguez, A., and Perez Romero, A.
GRB Coordinates Network, Circular Service, No. 37467

GRB 240825A: VLT/X-shooter redshift
Martin-Carrillo, A., Schneider, B., Pugliese, G., Izzo, L., Malesani, D. B., Saccardi, A., Laskar, T., **Agui Fernandez, J. F.**, Vergani, S. D., and Stargate Collaboration
GRB Coordinates Network, Circular Service, No. 37293

HI and CO spectroscopy of the unusual host of GRB 171205A: A grand design spiral galaxy with a distorted HI field
de Ugarte Postigo, A., Michalowski, M., Thoene, C. C., Martin, S., Ashok, A.,**Agui Fernandez, J. F.**, Bremer, M., Misra, K., Perley, D. A., Heintz, K. E., Cherukuri, S. V., Dimitrov, W., Geron, T., Ghosh, A., Izzo, L., Kann, D. A., Koprowski, M. P., Lesniewska, A., Leung, J. K., Levan, A., Omar, A., Oszkiewicz, D., Polinska, M., Resmi, L., and Schulze, S.
eprint arXiv:2406.16726

GRB 240529A: NOEMA detection
de Ugarte Postigo, A., Winters, J. M., Bremer, M., Thoene, C. C., **Agui Fernandez, J. F.**, Antier, S., Basa, S., Michalowski, M., Perley, D. A., and Ducoin, J. -G.
GRB Coordinates Network, Circular Service, No. 36642

GRB 240529A: Redshift from GTC/OSIRIS+
de Ugarte Postigo, A., Thoene, C. C., **Agui Fernandez, J. F.**, Malesani, D. B., Rakotondrainibe, Tanvir, N. R., Fynbo, J. P. U., Izzo, L., Lombardi, G., Geier, S., Cabrera Lavers, A., Perez-Toledo, F., and Tejero, A.
GRB Coordinates Network, Circular Service, No. 36574

GRB 240511A: Observations from GTC/OSIRIS+

de Ugarte Postigo, A., **Agui Fernandez, J. F.**, Rakotondrainibe, N. A., Thoene, C. C., Malesani, D. B., Tanvir, N. R., Fynbo, J. P. U., Izzo, L., Geier, S., and Scarpa, R.
GRB Coordinates Network, Circular Service, No. 36498

The fast X-ray transient EP240315a: a z 5 gamma-ray burst in a Lyman continuum leaking galaxy
Levan, Andrew J., Jonker, Peter G., Saccardi, Andrea, Bjørn Malesani, Daniele, Tanvir, Nial R., Izzo, Luca, Heintz, Kasper E., Mata Sánchez, Daniel, Quirola-Vásquez, Jonathan, Torres, Manuel A. P., Vergani, Susanna D., Schulze, Steve, Rossi, Andrea, D'Avanzo, Paolo, Gompertz, Benjamin, Martin-Carrillo, Antonio, de Ugarte Postigo, Antonio, Schneider, Benjamin, Yuan, Weimin, Ling, Zhixing, Zhang, Wenjie, Mao, Xuan, Liu, Yuan, Sun, Hui, Xu, Dong, Zhu, Zipei, **Agüí Fernández, José Feliciano**, Amati, Lorenzo, Bauer, Franz E., Campana, Sergio, Carotenuto, Francesco, Chrimes, Ashley, van Dalen, Joyce N. D., D'Elia, Valerio, Della Valle, Massimo, De Pasquale, Massimiliano, Dhillon, Vikram S., Galbany, Lluís, Gaspari, Nicola, Gianfagna, Giulia, Gomboc, Andreja, Habeeb, Nusrin, van Hoof, Agnes P. C., Hu, Youdong, Jakobsson, Pall, Julakanti, Yashaswi, Korth, Judith, Kouveliotou, Chryssa, Laskar, Tanmoy, Littlefair, Stuart P., Maiorano, Elisabetta, Mao, Jirong, Melandri, Andrea, Miller, M. Coleman, Mukherjee, Tamal, Oates, Samantha R., O'Brien, Paul, Palmerio, Jesse T., Parviainen, Hannu, Pieterse, Daniëlle L. A., Piranomonte, Silvia, Piro, Luigi, Pugliese, Giovanna, Ravasio, Maria E., Rayson, Ben, Salvaterra, Ruben, Sánchez-Ramírez, Rubén, Sarin, Nikhil, Shilling, Samuel P. R., Starling, Rhaana L. C., Tagliaferri, Gianpiero, Linesh Thakur, Aishwarya, Thöne, Christina C., Wiersema, Klaas, Worssam, Isabelle, and Zafar, Tayyaba
eprint arXiv:2404.16350

GRB 240414A: NOEMA detection
de Ugarte Postigo, A., Bremer, M., Thoene, C. C., **Agui Fernandez, J. F.**, Antier, S., Basa, S., Michalowski, M., Perley, D. A., and Ducoin, J. -G.
GRB Coordinates Network, Circular Service, No. 36318

GRB 240414A: Photometric observation from 2.2m CAHA
de Ugarte Postigo, A., **Agui Fernandez, J. F.**, Thoene, C. C., Calatayud-Borras, Y., and Gongora, S.
GRB Coordinates Network, Circular Service, No. 36117

GRB 240414A: Redshift confirmation from GTC/OSIRIS+
de Ugarte Postigo, A., Lombardi, G., **Agui Fernandez, J. F.**, Thoene, C. C., Fynbo, J. P. U., Izzo, L., Tanvir, N. R., Martin-Carrillo, A., and Geier, S.
GRB Coordinates Network, Circular Service, No. 36087

GRB 240411B: HiPERCAM/GTC observation
de Ugarte Postigo, A., Tanvir, N. R., **Agui Fernandez, J. F.**, Martin-Carrillo, A., Thoene, C. C.,

Izzo, L., Fynbo, J. P. U., Lombardi, G., and Geier, S.
GRB Coordinates Network, Circular Service, No. 36074

GRB 240209A: NOEMA non-detection of AT2024cew / GOTO24pw counterpart candidate
de Ugarte Postigo, A., Bremer, M., Thoene, C. C., **Agui Fernandez, J. F.**, Antier, S., Basa, S., Michalowski, M., Perley, D. A., and Martin, S.
GRB Coordinates Network, Circular Service, No. 35717

GRB 240122A: Redshift from OSIRIS+/GTC
Thoene, C. C., de Ugarte Postigo, A., **Agui Fernandez, J. F.**, Izzo, L., Fynbo, J. P. U., Tanvir, N. R., Blazek, M., Geier, S., Garcia-Rodriguez, A., and Rivero Mendez, Miguel
GRB Coordinates Network, Circular Service, No. 35598

GRB 231215A: Redshift from OSIRIS+ / GTC
Thoene, C. C., de Ugarte Postigo, A., **Agui Fernandez, J. F.**, Izzo, L., Fynbo, J. P. U., Tanvir, N. R., Blazek, M., Geier, S., Cabrera-Lavers, A., Perez Toledo, Fabricio, and Rivero, Miguel
GRB Coordinates Network, Circular Service, No. 35373

AT2023sva: redshift from OSIRIS+/GTC of the ZTF afterglow
de Ugarte Postigo, A., Malesani, D. B., **Agui Fernandez, J. F.**, Thoene, C. C., and Geier, S.
GRB Coordinates Network, Circular Service, No. 34740

Transient Classification Report for 2023-08-29
Agui Fernandez, J. F., de Ugarte Postigo, A., Thoene, C. C., Malesani, D. B., Izzo, L., and Cabrera Lavers, A. L.
Transient Name Server Classification Report, No. 2023-2115

STARGATE Transient Classification Report for 2023-08-14
Martin-Carrillo, A., Levan, A. J., de Ugarte Postigo, A., Izzo, L., Schneider, B., Laskar, T., Gompertz, B. P., Malesani, D. B., Finneran, G., **Agui Fernandez, J. F.** ., Thoene, C. C., D'Elia, V., Tanvir, N. R., Jakobsson, P., and Pugliese, G.
Transient Name Server Classification Report, No. 2023-1961

GRB 230812B: Spectroscopic detection of the associated SN 2023pel.
Agui Fernandez, J. F., de Ugarte Postigo, A., Thoene, C. C., Malesani, D. B., Izzo, L., and Cabrera Lavers, A. L.
GRB Coordinates Network, Circular Service, No. 34597

GRB 230812B: NOEMA detection
de Ugarte Postigo, A., Winters, J. M., Thoene, C. C., Antier, S., **Agui-Fernandez, J. F.**, Bremer, M., Perley, D. A., and Martin, S.

GRB Coordinates Network, Circular Service, No. 34468

GRB 230812B: Redshift from OSIRIS+/GTC
de Ugarte Postigo, A., **Agui Fernandez, J. F.**, Thoene, C. C., and Izzo, L.
GRB Coordinates Network, Circular Service, No. 34409

ZTF23aaoohpy/AT2023lcr: JWST spectroscopy confirmation of an associated type Ic-BL supernova
Martin-Carrillo, A., Levan, A. J., de Ugarte Postigo, A., Izzo, L., Schneider, B., Laskar, T., Gompertz, B. P., Malesani, D. B., Finneran, G., **Agui Fernandez, J. F.**, Thoene, C. C., D'Elia, V., Tanvir, N. R., Jakobsson, P., and Pugliese, G.
GRB Coordinates Network, Circular Service, No. 34385

ZTF23aaoohpy/AT2023lcr: JWST observations consistent with the presence of a supernova
Martin-Carrillo, A., Schneider, B., Laskar, T., Gompertz, B. P., Malesani, D. B., de Ugarte Postigo, A., Levan, A. J., Finneran, G., **Agui Fernandez, J. F.**, Thoene, C. C., D'Elia, V., and Izzo, L.
GRB Coordinates Network, Circular Service, No. 34370

GRB 230723B: Further CAHA observations and host galaxy detection
Agui Fernandez, J. F., de Ugarte Postigo, A., Thoene, C. C., Flores, J., and Guijarro Roman, Ana
GRB Coordinates Network, Circular Service, No. 34271

GRB 230723B: Optical afterglow candidate from CAHA
Agui Fernandez, J. F., de Ugarte Postigo, A., Thoene, C. C., Blazek, M., and Guijarro Roman, Ana
GRB Coordinates Network, Circular Service, No. 34251

GRB 230723B: Optical limit from CAHA
Agui Fernandez, J. F., de Ugarte Postigo, A., Thoene, C. C., and Blazek, M.
GRB Coordinates Network, Circular Service, No. 34241

GRB 230427A: OSIRIS+/GTC observations
Agui Fernandez, J. F., de Ugarte Postigo, A., Thoene, C. C., Perez, Fabricio, Tejero, Alvaro, and Cabrera Lavers, A. L.
GRB Coordinates Network, Circular Service, No. 33704

GRB 230414B: Redshift from OSIRIS/GTC
Agui Fernandez, J. F., Thoene, C. C., de Ugarte Postigo, A., Scarpa, R., Marante, A., and Cabrera Lavers, A. L.
GRB Coordinates Network, Circular Service, No. 33629

GRB 230328B: CAHA 2.2m/CAFOS detection

Agui Fernandez, J. F., de Ugarte Postigo, A., Thoene, C. C., Blazek, M., Guijarro, Ana, and Cikota, S.

GRB Coordinates Network, Circular Service, No. 33549

The brightest GRB ever detected: GRB 221009A as a highly luminous event at z = 0.151

Malesani, D. B., Levan, A. J., Izzo, L., de Ugarte Postigo, A., Ghirlanda, G., Heintz, K. E., Kann, D. A., Lamb, G. P., Palmerio, J., Salafia, O. S., Salvaterra, R., Tanvir, N. R., **Agüí Fernández, J. F.**, Campana, S., Chrimes, A. A., D'Avanzo, P., D'Elia, V., Della Valle, M., De Pasquale, M., Fynbo, J. P. U., Gaspari, N., Gompertz, B. P., Hartmann, D. H., Hjorth, J., Jakobsson, P., Palazzi, E., Pian, E., Pugliese, G., Ravasio, M. E., Rossi, A., Saccardi, A., Schady, P., Schneider, B., Sollerman, J., Starling, R. L. C., Thöne, C. C., van der Horst, A. J., Vergani, S. D., Watson, D., Wiersema, K., Xu, D., and Zafar, T.

eprint arXiv:2302.07891

Transient Classification Report for 2022-11-28

de Ugarte Postigo, A., Kann, D. A., Thoene, C. C., Izzo, L., **Agui Fernandez, J. F.** ., Antier, S., Beradze, S., Blazek, M., Masek, M., Fouad, A. M., Freeberg, M., Gurbanov, E., Hello, P., Hussenot, T., Janati, A., Midavaine, T., Noysena, K., Pyshna, O., Simon, A., Turpin, D., and Vannoye, G.

Transient Name Server Classification Report, No. 2022-3475

GRB 221009A: Spectroscopic detection of emerging SN features

de Ugarte Postigo, A., Izzo, L., Thoene, C. C., Fynbo, J. P. U., Kann, D. A., **Agui Fernandez, J. F.**, and Tanvir, N. R.

GRB Coordinates Network, Circular Service, No. 32800

GRB 221009A: VLT spectroscopic detection of the host galaxy

Izzo, L., Saccardi, A., Fynbo, J. P. U., Palmerio, J., Malesani, D. B.,**Agui Fernandez, J. F.**, Kann, D. A., Melandri, A., Vergani, S. D., Wiersema, K., and Stargate Consortium

GRB Coordinates Network, Circular Service, No. 32765

GRB 221009A: Armchair Energetics

Kann, D. A. and **Agui Fernandez, J. F.**

GRB Coordinates Network, Circular Service, No. 32762

MAXI GRB 221006A: Redshifts of the possible host galaxies

Cunha, P. A. C., Ma, G., O'Rourke Brogan, R., Thoene, C. C., de Ugarte Postigo, A., Kann, D. A., **Agui Fernandez, J. F.**, Izzo, L., Fynbo, J. P. U., Tanvir, N. R., Blazek, M., and Garcia Alvarez, D.

GRB Coordinates Network, Circular Service, No. 32742

GRB 221009A: NOEMA mm detection
de Ugarte Postigo, A., Bremer, Michael, Thoene, C. C., Michalowski, M., Misra, K., Antier, S., Kann, D. A., **Agui Fernandez, J. F.**, Resmi, L., Martin, S., Perley, D. A., and Schulze, S.
GRB Coordinates Network, Circular Service, No. 32676

EIFIS: a modular extreme integral field spectrograph for the 10.4m GTC
Thöne, Christina C., de Ugarte Postigo, Antonio, García Vargas, Marisa, **Agüí Fernández, José Feliciano**, Pérez Calpena, Ana, Sánchez Blanco, Ernesto, and Maldonado, Manuel
Proceedings of the SPIE, Volume 12184, id. 121840H 9 pp. (2022).

GRB 220627A: VLT MUSE redshift
Izzo, L., D'Elia, V., de Ugarte Postigo, A., Fynbo, J. P. U., Kann, D. A., Levan, A. J., Malesani, D. B., Saccardi, A., Thoene, C. C., **Agui Fernandez, J. F.**, de Wet, S., Groot, P. J., and Stargate Consortium
GRB Coordinates Network, Circular Service, No. 32291

ZTF22aaajecb/AT 2022cmc: CAHA 2.2m/CAFOS detection, luminous transient
Kann, D. A., de Ugarte Postigo, A., Thoene, C. C., Blazek, M., **Agui Fernandez, J. F.**, Vico, I., and Guijarro, A.
GRB Coordinates Network, Circular Service, No. 31626

GRB 220118A: 2.2m CAHA/CAFOS detections
Kann, D. A., Malesani, D. B., de Ugarte Postigo, A., Thoene, C. C., Blazek, M., **Agui Fernandez, J. F.**, Guijarro, A., and Fernandez, A.
GRB Coordinates Network, Circular Service, No. 31507

GRB 220101A: CAHA 2.2m/CAFOS detection
de Ugarte Postigo, A., Kann, D. A., Thoene, C. C., Blazek, M., **Agui Fernandez, J. F.**, Martin, P., and Hermelo, I.
GRB Coordinates Network, Circular Service, No. 31358

GRB 211227A: Deep early CAHA 2.2m/CAFOS observation
Kann, D. A., de Ugarte Postigo, A., Thoene, C. C., Blazek, M., **Agui Fernandez, J. F.**, and Gongora, S.
GRB Coordinates Network, Circular Service, No. 31341

GRB 211211A: Very fast decay observed from CAFOS/2.2mCAHA
de Ugarte Postigo, A., Kann, D. A., Thoene, C., **Agui Fernandez, J. F.**, Blazek, M., Vico, I., and Guijarro, A.
GRB Coordinates Network, Circular Service, No. 31229

GRB 211211A: Further observations from CAFOS/2.2m CAHA
de Ugarte Postigo, A., Kann, D. A., Thoene, C., **Agui Fernandez, J. F.**, Blazek, M., Vico, I., and Guijarro, A.
GRB Coordinates Network, Circular Service, No. 31228

GRB 211211A: Afterglow detection from CAFOS/2.2m CAHA
de Ugarte Postigo, A., Kann, D. A., Thoene, C., **Agui Fernandez, J. F.**, Blazek, M., and Guijarro, A.
GRB Coordinates Network, Circular Service, No. 31218

GRB 211024B: CAHA 2.2m Detection; ultra-long GRB?
Kann, D. A., de Ugarte Postigo, A., Thoene, C. C., Blazek, M., **Agui Fernandez, J. F.**, Guijarro, A., and Martin-Fernandez, P.
GRB Coordinates Network, Circular Service, No. 30995

Possible Short GRB 211023B: CAHA 2.2m Detection
Kann, D. A., de Ugarte Postigo, A., Thoene, C. C., Blazek, M., **Agui Fernandez, J. F.**, Guijarro, A., and Martin-Fernandez, P.
GRB Coordinates Network, Circular Service, No. 30992

GRB 211023A: OAJ Bright Afterglow Confirmation
Kann, D. A., de Ugarte Postigo, A., Thoene, C. C., Blazek, M., **Agui Fernandez, J. F.**, Iglesias-Marzoa, and Lacruz
GRB Coordinates Network, Circular Service, No. 30982

GRB 210919A OSN 1.5m Source Confirmation
Kann, D. A., Rossi, A., de Ugarte Postigo, A., Thoene, C., Blazek, M., **Agui Fernandez, J. F.**, and Aceituno, F.
GRB Coordinates Network, Circular Service, No. 30884

GRB 210919A CAHA 2.2m Observations: Afterglow/Host Galaxy Candidate
Kann, D. A., Rossi, A., de Ugarte Postigo, A., Thoene, C., Blazek, M., **Agui Fernandez, J. F.**, and Minguez, P.
GRB Coordinates Network, Circular Service, No. 30883

GRB 210912A: CAHA 2.2m Detection
Kann, D. A., de Ugarte Postigo, A., Thoene, C., Blazek, M., **Agui Fernandez, J. F.**, and Gongora, S.
GRB Coordinates Network, Circular Service, No. 30834

GRB 210820A: CAHA 2.2m Optical Detection

Kann, D. A., de Ugarte Postigo, A., Thoene, C., Blazek, M., **Agui Fernandez, J. F.**, Fernandez, A., and Hermelo, I.
GRB Coordinates Network, Circular Service, No. 30731

GRB 210822A: CAHA 2.2m observations
Kann, D. A., de Ugarte Postigo, A., Thoene, C., Blazek, M., **Agui Fernandez, J. F.**, Fernandez, A., Hermelo, I., and Martin, P.
GRB Coordinates Network, Circular Service, No. 30723

GRB 210820A: LT optical upper limit
Blazek, M., Kann, D. A., de Ugarte Postigo, A., Thoene, C. C., and **Agui Fernandez, J. F.**
GRB Coordinates Network, Circular Service, No. 30674

GRB 210724A: Early CAHA 2.2m limit
Kann, D. A., de Ugarte Postigo, A., Thoene, C., Blazek, M., **Agui Fernandez, J. F.**, Gardini, A., and Hermelo, I.
GRB Coordinates Network, Circular Service, No. 30551

GRB 210726A: OSIRIS/GTC observations
Kann, D. A., de Ugarte Postigo, A., Thoene, C., Blazek, M., **Agui Fernandez, J. F.**, Fynbo, J. P. U., Izzo, L., Tanvir, N. R., and Gomez Velarde, G.
GRB Coordinates Network, Circular Service, No. 30545

GRB 210726A: Deep CAHA 2.2m limit
Kann, D. A., de Ugarte Postigo, A., Thoene, C., Blazek, M., **Agui Fernandez, J. F.**, Gardini, A., and Hermelo, I.
GRB Coordinates Network, Circular Service, No. 30543

GRB 210724A: Afterglow candidate from OSIRIS/GTC
de Ugarte Postigo, A., Thoene, C. C., Kann, D. A., Blazek, M., **Agui Fernandez, J. F.**, Fynbo, J. P. U., Izzo, L., Tanvir, N. R., Castro-Rodriguez, N., and Marante, A.
GRB Coordinates Network, Circular Service, No. 30511

GRB 210722A: Redshift from OSIRIS/GTC
Thoene, C. C., de Ugarte Postigo, A., Kann, D. A., Blazek, M., **Agui Fernandez, J. F.**, Fynbo, J. P. U., Izzo, L., Tanvir, N. R., and Castro, N.
GRB Coordinates Network, Circular Service, No. 30487

GRB 210704A: OAJ T80 multi-color detections
Kann, D. A., de Ugarte Postigo, A., Thoene, C., Blazek, M., **Agui Fernandez, J. F.**, Maicas, N., and Lamadrid (COAJ, J. L.

GRB Coordinates Network, Circular Service, No. 30401

GRB 210704A: OSIRIS/GTC spectroscopy
de Ugarte Postigo, A., Kann, D. A., Thoene, C., Blazek, M., **Agui Fernandez, J. F.**, Fynbo, J. P. U., Izzo, L., Tanvir, N. R., Lombardi, G., and Marante, A.
GRB Coordinates Network, Circular Service, No. 30392

GRB 210704A: CAHA 2.2m Afterglow Detection
Kann, D. A., de Ugarte Postigo, A., Thoene, C., Blazek, M., **Agui Fernandez, J. F.**, and Martin-Fernandez, P.
GRB Coordinates Network, Circular Service, No. 30391

GRB 210619B: Deep CAHA 2.2m detection and late-time light curve behavior
Kann, D. A., de Ugarte Postigo, A., Jelinek, M., Blazek, M., Thoene, C., **Agui Fernandez, J. F.**, and Minguez, P.
GRB Coordinates Network, Circular Service, No. 30338

GRB 210619B: CAHA 2.2m photometric monitoring
Kann, D. A., de Ugarte Postigo, A., Blazek, M., Thoene, C., **Agui Fernandez, J. F.**, Ginger, and Vico Linares, J. I.
GRB Coordinates Network, Circular Service, No. 30275

GRB 210619B: Liverpool Telescope r'-band observations
Blazek, M., Kann, D. A., de Ugarte-Postigo, A., Thoene, C., and **Agui Fernandez, J. F.**
GRB Coordinates Network, Circular Service, No. 30274

GRB 210619B: Redshift from OSIRIS/GTC
de Ugarte Postigo, A., Kann, D. A., Thoene, C., Blazek, M., **Agui Fernandez, J. F.**, Izzo, L., Tanvir, N. R., Fynbo, J. P. U., Garcia Rodriguez, A. M., and Gomez, G.
GRB Coordinates Network, Circular Service, No. 30272

GRB 210610A: CAHA 2.2m Second Epoch
Kann, D. A., de Ugarte Postigo, A., **Agui Fernandez, J. F.**, Thoene, C. C., Blazek, M., Fernandez-Martin, A., and Azzaro, M.
GRB Coordinates Network, Circular Service, No. 30232

GRB 210610A: CAHA 2.2m observations and light-curve behavior
Kann, D. A., de Ugarte Postigo, A., **Agui Fernandez, J. F.**, Thoene, C. C., Blazek, M., Fernandez, A., Hermelo, I., and Pedraz, S.
GRB Coordinates Network, Circular Service, No. 30211

GRB 210610B: Redshift confirmation from GTC
de Ugarte Postigo, A., Thoene, C., **Agui Fernandez, J. F.**, Blazek, M., Kann, D. A., Fynbo, J. P. U., Izzo, L., and Garcia Alvarez, D.
GRB Coordinates Network, Circular Service, No. 30194

GRB 210420B: Redshift from GTC
de Ugarte Postigo, A., Blazek, M., Thoene, C., Kann, D. A., **Agui Fernandez, J. F.**, and Geier, S.
GRB Coordinates Network, Circular Service, No. 29853

GRB 210321A: OSN Upper Limit
Kann, D. A., de Ugarte Postigo, A., Thoene, C. C., Blazek, M., **Agui Fernandez, J. F.**, and Aceituno, F.
GRB Coordinates Network, Circular Service, No. 29725

Short GRB 210323A: GTC Observations
de Ugarte Postigo, A., Kann, D. A., Malesani, D. B., Tanvir, N. R., Thoene, C., Blazek, M., **Agui Fernandez, J. F.**, and Geier, S.
GRB Coordinates Network, Circular Service, No. 29717

GRB 210312B: OSN Afterglow Observations
Kann, D. A., Jelinek, M., de Ugarte Postigo, A., Thoene, C. C., Blazek, M., **Agui Fernandez, J. F.**, Sota, A., and Eloy, R. M.
GRB Coordinates Network, Circular Service, No. 29716

GRB 210321A: Redshift from OSIRIS/GTC
de Ugarte Postigo, A., Kann, D. A., Thoene, C., Blazek, M., **Agui Fernandez, J. F.**, Geier, S., and Tejero, A.
GRB Coordinates Network, Circular Service, No. 29685

GRB 210312B: Redshift from OSIRIS/GTC
Kann, D. A., de Ugarte Postigo, A., Thoene, C. C., Blazek, M., **Agui Fernandez, J. F.**, and Scarpa, R.
GRB Coordinates Network, Circular Service, No. 29655

GRB 210312B: GTC photometry
Kann, D. A., de Ugarte Postigo, A., Thoene, C. C., Blazek, M., **Agui Fernandez, J. F.**, and Scarpa, R.
GRB Coordinates Network, Circular Service, No. 29653

GRB 210222B: Redshift from FORS2/VLT
Agui Fernandez, J. F., de Ugarte Postigo, A., Izzo, L., Xu, D., Kann, D. A., Malesani, D. B.,

Fynbo, J. P. U., and Wiersema, K.
GRB Coordinates Network, Circular Service, No. 29552

GRB 210210A: CAHA 2nd epoch and jet break confirmation
Kann, D. A., de Ugarte Postigo, A., Thoene, C. C., Blazek, M., **Agui Fernandez, J. F.**, Minguez, P., and Pedraz, S.
GRB Coordinates Network, Circular Service, No. 29502

GRB 210210A: CAHA detection and likely jet break
Kann, D. A., de Ugarte Postigo, A., Thoene, C. C., Blazek, M., **Agui Fernandez, J. F.**, Mínguez, P., and Pedraz, S.
GRB Coordinates Network, Circular Service, No. 29476

GRB 210210A: Redshift from OSIRIS/GTC
de Ugarte Postigo, A., Kann, D. A., Thoene, C. C., Blazek, M., **Agui Fernandez, J. F.**, and Garcia, D.
GRB Coordinates Network, Circular Service, No. 29450

ZTF21aaeyldq: GROND and CAHA jet break confirmation
Kann, D. A., Nicuesa Guelbenzu, A., de Ugarte Postigo, A., Thoene, C. C., Blazek, M., **Agui Fernandez, J. F.**, Rau, A., Klose, S., and Vico Linares, J. I.
GRB Coordinates Network, Circular Service, No. 29344

ZTF21aaeyldq CAHA 2.2m detection and power-law decay
Kann, D. A., de Ugarte Postigo, A., Thoene, C. C., Blazek, M., **Agui Fernandez, J. F.**, and Vico Linares, J. I.
GRB Coordinates Network, Circular Service, No. 29321

GRB 200613A: Host galaxy redshift from OSIRIS/GTC
de Ugarte Postigo, A., Kann, D. A., Thoene, C. C., Blazek, M., and **Agui Fernandez, J. F.**
GRB Coordinates Network, Circular Service, No. 29320

GRB 210112A: Deep CAHA 2.2m detection
Kann, D. A., de Ugarte Postigo, A., Thoene, C. C., Blazek, M., **Agui Fernandez, J. F.**, and Vico Linares, J. I.
GRB Coordinates Network, Circular Service, No. 29319

GRB 210104A: Late-time CAHA 2.2m detection
Kann, D. A., Rossi, A., de Ugarte Postigo, A., Thoene, C. C., Blazek, M., **Agui Fernandez, J. F.**, and Vico Linares, J. I.
GRB Coordinates Network, Circular Service, No. 29318

ZTF21aaeyldq: GTC Redshift and GRB afterglow nature confirmation
de Ugarte Postigo, A., Kann, D. A., Perley, D. A., Thoene, C. C., Blazek, M., **Agui Fernandez, J. F.**, and Scarpa, R.
GRB Coordinates Network, Circular Service, No. 29307

GRB 210112A: OSN second epoch, decay
Kann, D. A., de Ugarte Postigo, A., Thoene, C. C., Blazek, M., **Agui Fernandez, J. F.**, and Sota, A.
GRB Coordinates Network, Circular Service, No. 29300

GRB 210112A: OSN Reddened Afterglow Detection
Kann, D. A., de Ugarte Postigo, A., Thoene, C. C., Blazek, M., **Agui Fernandez, J. F.**, and Sota, A.
GRB Coordinates Network, Circular Service, No. 29296

GRBSpec and GRBPhot: social networks to share gamma ray burst data
Blažek, Martin, de Ugarte Postigo, A., Kann, D. A., Thöne, C. C., **Agüí Fernández, J. F.**, and Izzo, L.
Proceedings of the SPIE, Volume 11452, id. 1145218 8 pp. (2020).

GATOS: A fast multi-channel imager and spectrograph for the Gran Telescopio Canarias
de Ugarte Postigo, A., Thöne, C. C., Muñoz-Darias, T., Labiano, A., Gil de Paz, A., García Vargas, M. L., Dhillon, V., Izzo, L., Kann, D. A., Pérez, A., Piqueras López, J., **Agüí Fernández, J. F.**, Alonso Herrero, A., Barrado, D., Blazek, M., Casares, J., Fernández, M., García Rojas, J., Gardini, A., Garrido, R., González Delgado, R., Huélamo, N., Lodieu, N., Maldonado, M., Ortiz, J. L., Ramos Almeida, C., Sánchez Blanco, E., Simón-Díaz, Sergio, and Watson, A. M.
Proceedings of the SPIE, Volume 11447, id. 114476Z 7 pp. (2020).

Short GRB201221D: High Redshift from OSIRIS/GTC
de Ugarte Postigo, A., Kann, D. A., Izzo, L., Thoene, C. C., Blazek, M., **Agui Fernandez, J. F.**, and Lombardi, G.
GRB Coordinates Network, Circular Service, No. 29132

GRB 201116A: OSN Afterglow Candidate
de Ugarte Postigo, A., Kann, D. A., Blazek, M., Thoene, C. C., **Agui Fernandez, J. F.**, and Sota, A.
GRB Coordinates Network, Circular Service, No. 28915

GRB 201020B: Redshift from GTC/OSIRIS
Kann, D. A., de Ugarte Postigo, A., Blazek, M., **Agui Fernandez, J. F.**, Thoene, C. C., Geier, S.,

and Rivero, M.
GRB Coordinates Network, Circular Service, No. 28765

GRB 201024A: Redshift from GTC/OSIRIS
de Ugarte Postigo, A., Kann, D. A., Blazek, M., **Agui Fernandez, J. F.**, Thoene, C. C., Geier, S., and Rivero, M.
GRB Coordinates Network, Circular Service, No. 28764

GRB 201020A: Redshift from GTC/OSIRIS
Kann, D. A., de Ugarte Postigo, A., Blazek, M., **Agui Fernandez, J. F.**, Thoene, C. C., Lombardi, G., and Tejero, A.
GRB Coordinates Network, Circular Service, No. 28717

GRB 201014A: Redshift from GTC/OSIRIS
de Ugarte Postigo, A., Kann, D. A., Blazek, M., **Agui Fernandez, J. F.**, Thoene, C., Gomez Velarde, G., and Perez Romero, A.
GRB Coordinates Network, Circular Service, No. 28650

GRB 201015A: Redshift from GTC/OSIRIS
de Ugarte Postigo, A., Kann, D. A., Blazek, M.,**Agui Fernandez, J. F.**, Thoene, C., and Gomez Velarde, G.
GRB Coordinates Network, Circular Service, No. 28649

GRB 200925B: OSN Afterglow Candidate Discovery
de Ugarte Postigo, A., Kann, D. A., Thoene, C. C., Blazek, M., **Agui Fernandez, J. F.**, and Aceituno, F.
GRB Coordinates Network, Circular Service, No. 28501

GRB 200906A: EMIR/GTC NIR upper limit
de Ugarte Postigo, A., Kann, D. A., Thoene, C. C., Blazek, M., **Agui Fernandez, J. F.**, and Reverte Paya, D.
GRB Coordinates Network, Circular Service, No. 28382

GRB 200906A: OSN 1.5m Upper Limit
Kann, D. A., de Ugarte Postigo, A., Thoene, C. C., Blazek, M., **Agui Fernandez, J. F.**, and Casanova, V.
GRB Coordinates Network, Circular Service, No. 28376

GRB 200806A: CAHA optical afterglow confirmation
Kann, D. A., de Ugarte Postigo, A., Thoene, C. C., Blazek, M., **Agui Fernandez, J. F.**, and Montoya, L.

GRB Coordinates Network, Circular Service, No. 28227

GRB 200716C: CAHA optical observation // Anomalous light curve behavior?
Kann, D. A., Jelinek, M., Izzo, L., de Ugarte Postigo, A., Thoene, C. C., Blazek, M., **Agui Fernandez, J. F.**, Arroyo, B., Bergond, G., and Pedraz, S.
GRB Coordinates Network, Circular Service, No. 28152

GRB 200623A: OAJ deep multi-color imaging, XRT 2 is pre-detected
Kann, D. A., de Ugarte Postigo, A., Blazek, M., Thoene, C. C., **Agui Fernandez, J. F.**, Tilve, V., Moreno Signes, A., and Vasquez Ramio, H.
GRB Coordinates Network, Circular Service, No. 28022

GRB 200613A: Candidate afterglow from OAJ
Kann, D. A., de Ugarte Postigo, A., Blazek, M., Thoene, C., **Agui Fernandez, J. F.**, Moreno, A., and Vasquez Ramio, H.
GRB Coordinates Network, Circular Service, No. 27935

GRB 200528A: CAHA Upper Limit
Kann, D. A., de Ugarte Postigo, A., Blazek, M., Thoene, C. C., **Agui Fernandez, J. F.**, and Hermelo, I.
GRB Coordinates Network, Circular Service, No. 27860

GRB 200524A: OAJ multicolor afterglow detection
Blazek, M., Kann, D. A., de Ugarte Postigo, A., Thoene, C., **Agui Fernandez, J. F.**, and Maicas, N.
GRB Coordinates Network, Circular Service, No. 27810

GRB 200524A: CAHA multicolor afterglow detection
de Ugarte Postigo, A., Kann, D. A., Blazek, M., Thoene, C., **Agui Fernandez, J. F.**, Hedrosa, R. Pedro, and Guijarro, A.
GRB Coordinates Network, Circular Service, No. 27807

GRB 200306C: Calar Alto 2.2m upper limit
Kann, D. A., de Ugarte Postigo, A., Blazek, M., Thoene, C. C., **Agui Fernandez, J. F.**, Hedrosa, R. Pedro, and Gallego, E.
GRB Coordinates Network, Circular Service, No. 27348

GRB 200306C: OSN 1.5m afterglow detection
Kann, D. A., Blazek, M., de Ugarte Postigo, A., Thoene, C. C.,**Agui Fernandez, J. F.**, and Casanova, V.
GRB Coordinates Network, Circular Service, No. 27335

GRB 200303A: Optical limit from CAHA

De Ugarte Postigo, A., Kann, D. A., Thoene, C., **Agui Fernandez, J. F.**, Blazek, M., and Hedrosa, R. Pedro

GRB Coordinates Network, Circular Service, No. 27303

GRB 200224A: Calar Alto 2.2m optical afterglow detection

Agui Fernandez, J. F., Blazek, M., Kann, D. A., de Ugarte Postigo, A., Thoene, C. C., Gallego-Cano, E., and Guijarro, A.

GRB Coordinates Network, Circular Service, No. 27222

GRB 200219C: OAJ afterglow confirmation

Blazek, M., Kann, D. A., de Ugarte Postigo, A., Thoene, C. C., **Agui Fernandez, J. F.**, Maicas, N., and Lamadrid, J. L.

GRB Coordinates Network, Circular Service, No. 27166

LIGO/Virgo S200213t : No significant candidates in FRAM - OAJ - TAROT - GRANDMA observations

Blazek, M., Agayeva, S., Baransky, A., Hello, P., Howell, E., Bensch, K., Boer, M., Christensen, N., Eymar, L., **Agüí-Fernández, J. Feliciano**, Izzo, L., Kann, D. A., Karpov, S., Prouza, M., Klotz, A., Masek, M., Noysena, K., Thoene, C., Ugarte Postigo, A., Antier, S., Coleiro, A., Corre, D., Coughlin, M., Coward, D., Ducoin, J. G., Gendre, B., Kochiashvili, N., Lachaud, C., Leroy, N., Turpin, D., Wang, X., Fram Collaboration, Tarot Collaboration, Heth Collaboration, and Grandma Collaboration

GRB Coordinates Network, Circular Service, No. 27116

Additional Research Contributions Not Included in the Thesis

This thesis does not cover several additional research efforts carried out during the PhD, which have resulted in multiple scientific publications. These include the analysis of the spectral energy distributions (SEDs) of host galaxies of low-luminosity GRBs, short GRBs, superluminous supernovae, as well as of metal-poor dwarf galaxies. High-energy analyses of the prompt emission from a large sample of long and short GRBs have also been conducted, contributing to significant publications in the GRB field. Although these works were carried out during the PhD and have been included in peer-reviewed articles, they are not part of this manuscript.

In addition, data analysis from observations performed during the PhD has been published in several high-impact (Q1) journals, with the PhD candidate listed as a co-author. These analyses are not detailed in this thesis.

Throughout the PhD, the candidate has actively participated in the discovery and follow-up of GRBs using various observatories, including the Very Large Telescope (VLT), the Gran Telescopio Canarias (GTC), and the Calar Alto Observatory (CAHA). These observations have contributed to further publications in which the candidate is involved. A significant number of these observations were conducted under observing proposals led by the student, which were successfully accepted at VLT, GTC, and CAHA. Notably, data obtained from these facilities formed the basis of the candidate's second first-author publication.

The candidate has also played an active role in the STARGATE collaboration and was awarded the Alex Kann Prize for outstanding contributions to GRB science within this project. Furthermore, the candidate has been involved in several other collaborative efforts in the GRB research community.

List of Figures

List of Tables

Bibliography

Abbott, B. P., Abbott, R., Abbott, T. D., et al. 2017a, ApJ, 848, L13

Abbott, B. P., Abbott, R., Abbott, T. D., et al. 2017b, Multi-messenger Observations of a Binary Neutron Star Merger

Acciari, V. A., Ansoldi, S., Antonelli, L. A., et al. 2021, ApJ, 908, 90

Ackermann, M., Asano, K., Atwood, W. B., et al. 2010, ApJ, 716, 1178

Agüí Fernández, J. F., de Ugarte Postigo, A., Thöne, C. C., et al. 2024, A&A, 690, A216

Agüí Fernández, J. F., Thöne, C. C., Kann, D. A., et al. 2023, mnras, 520, 613

Ahumada, T., Singer, L. P., Anand, S., et al. 2021, Nature Astronomy, 5, 917

Alam, S., Albareti, F. D., Allende Prieto, C., et al. 2015, ApJS, 219, 12

Amati, L. 2006, mnras, 372, 233

Amati, L., Frontera, F., Tavani, M., et al. 2002, A&A, 390, 81

Anderson, G. E., Bell, M. E., Stevens, J., et al. 2021, mnras, 503, 4372

Anderson, J. 2015, FORS2 User Manual, Vol. 96.0 (European Southern Observatory)

Andreoni, I., Coughlin, M. W., Kool, E. C., et al. 2021, ApJ, 918, 63

Antier, S., Agayeva, S., Almualla, M., et al. 2020, mnras, 497, 5518

Aptekar, R. L., Frederiks, D. D., Golenetskii, S. V., et al. 1995, Space Sci. Rev., 71, 265

Arnaud, K. A. 1996, in Astronomical Society of the Pacific Conference Series, Vol. 101, Astronomical Data Analysis Software and Systems V, ed. G. H. Jacoby & J. Barnes, 17

Asplund, M., Grevesse, N., Sauval, A. J., & Scott, P. 2009, ARA&A, 47, 481

Atteia, J. L., Cordier, B., & Wei, J. 2022, International Journal of Modern Physics D, 31, 2230008

Atwood, W. B., Abdo, A. A., Ackermann, M., et al. 2009, ApJ, 697, 1071

Bagnulo, S., Landolfi, M., Landstreet, J. D., et al. 2009, PASP, 121, 993

Band, D., Matteson, J., Ford, L., et al. 1993, ApJ, 413, 281

Barth, A. J., Sari, R., Cohen, M. H., et al. 2003, ApJ, 584, L47

Barthelmy, S. D., Barbier, L. M., Cummings, J. R., et al. 2005, Space Sci. Rev., 120, 143

Becerra, R. L., Dichiara, S., Watson, A. M., et al. 2019, ApJ, 881, 12

Belczynski, K., Kalogera, V., & Bulik, T. 2002, ApJ, 572, 407

Belczynski, K., Perna, R., Bulik, T., et al. 2006, ApJ, 648, 1110

Bellm, E. C., Kulkarni, S. R., Graham, M. J., et al. 2019, PASP, 131, 018002

Beniamini, P., Hotokezaka, K., & Piran, T. 2016a, ApJ, 829, L13

Beniamini, P., Hotokezaka, K., & Piran, T. 2016b, ApJ, 832, 149

Beniamini, P., Nava, L., Duran, R. B., & Piran, T. 2015, mnras, 454, 1073

Beniamini, P. & Piran, T. 2019, mnras, 487, 4847

Berger, E. 2009, ApJ, 690, 231

Berger, E. 2010, ApJ, 722, 1946

Berger, E. 2014, ARA&A, 52, 43

Berger, E., Fong, W., & Chornock, R. 2013, ApJ, 774, L23

Bersier, D., McLeod, B., Garnavich, P. M., et al. 2003, ApJ, 583, L63

Bertin, E. 2010, SWarp: Resampling and Co-adding FITS Images Together, Astrophysics Source Code Library, record ascl:1010.068

Beuermann, K., Hessman, F. V., Reinsch, K., et al. 1999, A&A, 352, L26

Blanchard, P. K., Villar, V. A., Chornock, R., et al. 2024, Nature Astronomy, 8, 774

Blandford, R. D. & Znajek, R. L. 1977, mnras, 179, 433

Blažek, M., de Ugarte Postigo, A., Kann, D. A., et al. 2020, in Society of Photo-Optical Instrumentation Engineers (SPIE) Conference Series, Vol. 11452, Society of Photo-Optical Instrumentation Engineers (SPIE) Conference Series, 1145218

Bloom, J. S., Kulkarni, S. R., & Djorgovski, S. G. 2002, AJ, 123, 1111

Bloom, J. S., Sigurdsson, S., & Pols, O. R. 1999, mnras, 305, 763

Bolmer, J., Ledoux, C., Wiseman, P., et al. 2019, A&A, 623, A43

Boquien, M., Burgarella, D., Roehlly, Y., et al. 2019, A&A, 622, A103

Breeveld, A. A., Landsman, W., Holland, S. T., et al. 2011, in American Institute of Physics Conference Series, Vol. 1358, American Institute of Physics Conference Series, ed. J. E. McEnery, J. L. Racusin, & N. Gehrels, 373–376

Breeveld, A. A. & Siegel, M. H. 2016, GRB Coordinates Network, 19839

Briggs, M. S., Paciesas, W. S., Pendleton, G. N., et al. 1996, ApJ, 459, 40

Brivio, R., Covino, S., D'Avanzo, P., et al. 2022, A&A, 666, A179

Bruzual, G. & Charlot, S. 2003, mnras, 344, 1000

Buat, V., Heinis, S., Boquien, M., et al. 2014, A&A, 561, A39

Burgarella, D., Buat, V., & Iglesias-Páramo, J. 2005, mnras, 360, 1413

Burns, E., Svinkin, D., Fenimore, E., et al. 2023, ApJ, 946, L31

Burrows, D. N., Hill, J. E., Nousek, J. A., et al. 2005a, Space Sci. Rev., 120, 165

Burrows, D. N., Hill, J. E., Nousek, J. A., et al. 2005b, Space Sci. Rev., 120, 165

Butler, N., Watson, A. M., Kutyrev, A., et al. 2015, GRB Coordinates Network, 17762

Calzetti, D., Armus, L., Bohlin, R. C., et al. 2000, ApJ, 533, 682

Campana, S., Thöne, C. C., de Ugarte Postigo, A., et al. 2010, mnras, 402, 2429

Cano, Z., Wang, S.-Q., Dai, Z.-G., & Wu, X.-F. 2017, Advances in Astronomy, 2017, 8929054

Cao, Y., Kulkarni, S. R., Yan, L., et al. 2016, GRB Coordinates Network, 19278

Cardelli, J. A., Clayton, G. C., & Mathis, J. S. 1989, ApJ, 345, 245

Cepa, J., Aguiar, M., Escalera, V. G., et al. 2000, in Society of Photo-Optical Instrumentation Engineers (SPIE) Conference Series, Vol. 4008, Optical and IR Telescope Instrumentation and Detectors, ed. M. Iye & A. F. Moorwood, 623–631

Chabrier, G. 2003, PASP, 115, 763

Chang, Y.-Y., van der Wel, A., da Cunha, E., & Rix, H.-W. 2015, ApJS, 219, 8

Chen, J.-M., Peng, Z.-Y., Du, T.-T., & Yin, Y. 2022, ApJ, 932, 25

Choi, C., Kim, Y., Park, W., Shin, S., & Im, M. 2018, GRB Coordinates Network, 22668

Chris, S. 2023, NASA Goddard Space Flight Center (USRA/GESTAR)

Christensen, L., Fynbo, J. P. U., Prochaska, J. X., et al. 2011, ApJ, 727, 73

Christensen, L., Møller, P., Fynbo, J. P. U., & Zafar, T. 2014, mnras, 445, 225

Christensen, L., Vreeswijk, P. M., Sollerman, J., et al. 2008, A&A, 490, 45

Chruslinska, M., Belczynski, K., Klencki, J., & Benacquista, M. 2018, mnras, 474, 2937

Cikota, A., Patat, F., Cikota, S., & Faran, T. 2017, mnras, 464, 4146

Cobb, B. E. 2016, GRB Coordinates Network, 19311

Collett, E. & Schaefer, B. 2008, Appl. Opt., 47, 4009

Conroy, C. 2013, ARA&A, 51, 393

Corre, D., Buat, V., Basa, S., et al. 2018, A&A, 617, A141

Costa, E., Frontera, F., Heise, J., et al. 1997, Nature, 387, 783

Covino, S. & Gotz, D. 2016, Astronomical and Astrophysical Transactions, 29, 205

Covino, S., Lazzati, D., Ghisellini, G., et al. 1999, A&A, 348, L1

Covino, S., Malesani, D., Ghisellini, G., et al. 2003, A&A, 400, L9

Csizi, B., Tortorelli, L., Siudek, M., et al. 2024, A&A, 689, A37

Cucchiara, A., Levan, A. J., Fox, D. B., et al. 2011, ApJ, 736, 7

Cucchiara, A., Prochaska, J. X., Perley, D., et al. 2013, ApJ, 777, 94

Curran, P. A., van der Horst, A. J., Beardmore, A. P., et al. 2007, A&A, 467, 1049

Dale, D. A. & Helou, G. 2002, ApJ, 576, 159

Dale, D. A., Helou, G., Magdis, G. E., et al. 2014, ApJ, 784, 83

De Cia, A., Ledoux, C., Mattsson, L., et al. 2016, A&A, 596, A97

De Cia, A., Ledoux, C., Petitjean, P., & Savaglio, S. 2018, A&A, 611, A76

De Cia, A., Ledoux, C., Savaglio, S., Schady, P., & Vreeswijk, P. M. 2013, A&A, 560, A88

de Ugarte Postigo, A., Blazek, M., Janout, P., et al. 2014a, in Society of Photo-Optical Instrumentation Engineers (SPIE) Conference Series, Vol. 9152, Software and Cyberinfrastructure for Astronomy III, 91520B

de Ugarte Postigo, A., Castro-Tirado, A. J., Gorosabel, J., et al. 2005, A&A, 443, 841

de Ugarte Postigo, A., Fynbo, J. P. U., Thöne, C. C., et al. 2012, A&A, 548, A11

de Ugarte Postigo, A., Izzo, L., Pugliese, G., et al. 2022a, GRB Coordinates Network, 32648, 1

de Ugarte Postigo, A., Izzo, L., Thoene, C. C., et al. 2022b, GRB Coordinates Network, 32800, 1

de Ugarte Postigo, A., Kann, D. A., Izzo, L., et al. 2020, GRB Coordinates Network, 29132

de Ugarte Postigo, A., Michalowski, M., Thoene, C. C., et al. 2024, arXiv e-prints, arXiv:2406.16726

de Ugarte Postigo, A., Thöne, C. C., Bolmer, J., et al. 2018, A&A, 620, A119

de Ugarte Postigo, A., Thöne, C. C., Rowlinson, A., et al. 2014b, A&A, 563, A62

D'Elia, V., Fiore, F., Perna, R., et al. 2009a, ApJ, 694, 332

D'Elia, V., Fiore, F., Perna, R., et al. 2009b, A&A, 503, 437

Della Valle, M., Chincarini, G., Panagia, N., et al. 2006, Nature, 444, 1050

Dhillon, V. S., Bezawada, N., Black, M., et al. 2021, mnras, 507, 350

Dichiara, S., Troja, E., Beniamini, P., et al. 2021, ApJ, 911, L28

Dichiara, S., Troja, E., Cenko, S. B., et al. 2020, GRB Coordinates Network, 29128

Dimple, A., Panchal, A., Gangopadhyay, A., et al. 2020, GRB Coordinates Network, 29148

Evans, P. A., Beardmore, A. P., Page, K. L., et al. 2009, mnras, 397, 1177

Evans, P. A., Beardmore, A. P., Page, K. L., et al. 2007, A&A, 469, 379

Fong, W. & Berger, E. 2013, ApJ, 776, 18

Fong, W., Berger, E., Metzger, B. D., et al. 2014, ApJ, 780, 118

Fong, W.-f., Nugent, A. E., Dong, Y., et al. 2022, ApJ, 940, 56

Fontana, A., Dunlop, J. S., Paris, D., et al. 2014, A&A, 570, A11

Fox, A. J., Ledoux, C., Vreeswijk, P. M., Smette, A., & Jaunsen, A. O. 2008, A&A, 491, 189

Frederiks, D., Golenetskii, S., Aptekar, R., et al. 2020, GRB Coordinates Network, 29130

Frederiks, D., Golenetskii, S., Aptekar, R., et al. 2016, GRB Coordinates Network, 19288

Frederiks, D., Golenetskii, S., Lysenko, A., et al. 2021, GRB Coordinates Network, 30196, 1

Freudling, W., Romaniello, M., Bramich, D. M., et al. 2013, A&A, 559, A96

Friis, M., De Cia, A., Krühler, T., et al. 2015, mnras, 451, 167

Fruchter, A. S., Levan, A. J., Strolger, L., et al. 2006, Nature, 441, 463

Fynbo, J. P. U., Izzo, L., de Ugarte Postigo, A., Malesani, D. B., & Pursimo, T. 2021, GRB Coordinates Network, 30182, 1

Fynbo, J. P. U., Prochaska, J. X., Sommer-Larsen, J., Dessauges-Zavadsky, M., & Møller, P. 2008, ApJ, 683, 321

Fynbo, J. P. U., Watson, D., Thöne, C. C., et al. 2006, Nature, 444, 1047

Gaia Collaboration, Brown, A. G. A., Vallenari, A., et al. 2018, A&A, 616, A1

Galama, T. J., Vreeswijk, P. M., van Paradijs, J., et al. 1998, Nature, 395, 670

Gao, H. & Zhang, B. 2015, ApJ, 801, 103

Garzón, F., Balcells, M., Gallego, J., et al. 2022, A&A, 667, A107

Gatkine, P., Veilleux, S., & Cucchiara, A. 2019, ApJ, 884, 66

Gehrels, N., Chincarini, G., Giommi, P., et al. 2004, ApJ, 611, 1005

Gehrels, N., Norris, J. P., Barthelmy, S. D., et al. 2006, Nature, 444, 1044

Ghisellini, G. & Lazzati, D. 1999, mnras, 309, L7

Giallongo, E., Ragazzoni, R., Grazian, A., et al. 2008, A&A, 482, 349

Gibson, S. L., Malesani, D., Page, K. L., Palmer, D. M., & Siegel, M. H. 2016, GRB Coordinates Network, 19271

Gill, R., Granot, J., & Kumar, P. 2020, mnras, 491, 3343

Gill, R., Kole, M., & Granot, J. 2021, Galaxies, 9, 82

Goldstein, A., Veres, P., Burns, E., et al. 2017, ApJ, 848, L14

Gompertz, B. P., Ravasio, M. E., Nicholl, M., et al. 2022, Nature Astronomy

Gonneau, A., Lyubenova, M., Lançon, A., et al. 2020, A&A, 634, A133

González-Gaitán, S., Mourão, A. M., Patat, F., et al. 2020, A&A, 634, A70

Gorosabel, J., de Ugarte Postigo, A., Castro-Tirado, A. J., et al. 2010, A&A, 522, A14

Gorosabel, J., Rol, E., Covino, S., et al. 2004, A&A, 422, 113

Graham, M. J., Kulkarni, S. R., Bellm, E. C., et al. 2019, PASP, 131, 078001

Granot, J. & Königl, A. 2003, ApJ, 594, L83

Granot, J., Piran, T., & Sari, R. 1999, ApJ, 513, 679

Greiner, J. 2019, PASP, 131, 015002

Greiner, J., Bornemann, W., Clemens, C., et al. 2008, PASP, 120, 405

Greiner, J., Klose, S., Reinsch, K., et al. 2003, Nature, 426, 157

Gruzinov, A. & Waxman, E. 1999, ApJ, 511, 852

Guidorzi, C., Gomboc, A., Kobayashi, S., et al. 2007, A&A, 463, 539

Guidorzi, C., Martone, R., Kobayashi, S., et al. 2018, GRB Coordinates Network, 22648

Hamburg, R., Malacaria, C., Meegan, C., & Fermi GBM Team. 2020, GRB Coordinates Network, 29140

Hamuy, M., Suntzeff, N. B., Heathcote, S. R., et al. 1994, PASP, 106, 566

Heintz, K. E., De Cia, A., Thöne, C. C., et al. 2023, A&A, 679, A91

Heintz, K. E., Malesani, D., Wiersema, K., et al. 2018a, mnras, 474, 2738

Heintz, K. E., Watson, D., Jakobsson, P., et al. 2018b, mnras, 479, 3456

Hjorth, J. & Bloom, J. S. 2012, The Gamma-Ray Burst - Supernova Connection, 169–190

Hjorth, J., Malesani, D., Jakobsson, P., et al. 2012, ApJ, 756, 187

Hjorth, J., Sollerman, J., Møller, P., et al. 2003, Nature, 423, 847

Ho, A. Y. Q., Perley, D. A., Yao, Y., et al. 2022, ApJ, 938, 85

Horiuchi, T., Hanayama, H., Honma, M., et al. 2018, GRB Coordinates Network, 22670

Horne, K. 1986, PASP, 98, 609

Huang, B.-Q., Lin, D.-B., Liu, T., et al. 2019, mnras, 487, 3214

Hurley, K., Mitrofanov, I., Kozyrev, A., et al. 2006, ApJS, 164, 124

Izzo, L., Thöne, C. C., Schulze, S., et al. 2017, mnras, 472, 4480

Jakobsson, P., Fynbo, J. P. U., Ledoux, C., et al. 2006, A&A, 460, L13

Jakobsson, P., Hjorth, J., Malesani, D., et al. 2012, ApJ, 752, 62

Japelj, J., Covino, S., Gomboc, A., et al. 2015, A&A, 579, A74

Jespersen, C. K., Severin, J. B., Steinhardt, C. L., et al. 2020, ApJ, 896, L20

Ji, A. P., Frebel, A., Chiti, A., & Simon, J. D. 2016a, Nature, 531, 610

Ji, A. P., Frebel, A., Ezzeddine, R., & Casey, A. R. 2016b, ApJ, 832, L3

Jin, Z.-P., Li, X., Wang, H., et al. 2018, ApJ, 857, 128

Johnson, B. D., Leja, J., Conroy, C., & Speagle, J. S. 2021, ApJS, 254, 22

Jordana-Mitjans, N., Mundell, C. G., Kobayashi, S., et al. 2020, ApJ, 892, 97

Juvan, I., Bluemcke, M., Baak, D., et al. 2016, GRB Coordinates Network, 19309

Kann, D. A. & Agui Fernandez, J. F. 2022, GRB Coordinates Network, 32762, 1

Kann, D. A., Klose, S., & Zeh, A. 2006, ApJ, 641, 993

Kann, D. A., Klose, S., Zhang, B., et al. 2011, ApJ, 734, 96

Kann, D. A., Klose, S., Zhang, B., et al. 2010, ApJ, 720, 1513

Kann, D. A., Tanga, M., & Greiner, J. 2015, GRB Coordinates Network, 17757

Kann, D. A., White, N. E., Ghirlanda, G., et al. 2024, A&A, 686, A56

Kasliwal, M. M., Korobkin, O., Lau, R. M., Wollaeger, R., & Fryer, C. L. 2017, ApJ, 843, L34

Kilpatrick, C. D., Malesani, D. B., & Fong, W. 2020, GRB Coordinates Network, 29133

Klebesadel, R. W., Strong, I. B., & Olson, R. A. 1973, ApJ, 182, L85

Klose, S., Nicuesa Guelbenzu, A. M., Michałowski, M. J., et al. 2019, ApJ, 887, 206

Klotz, A., Gendre, B., Stratta, G., et al. 2006, A&A, 451, L39

Klotz, A., Turpin, D., Atteia, J. L., et al. 2016, GRB Coordinates Network, 19287

Knust, F., Greiner, J., van Eerten, H. J., et al. 2017, A&A, 607, A84

Kobayashi, S., Piran, T., & Sari, R. 1997, ApJ, 490, 92

Kouveliotou, C., Meegan, C. A., Fishman, G. J., et al. 1993, ApJ, 413, L101

Krimm, H. A., Barthelmy, S. D., Cummings, J. R., et al. 2021, GRB Coordinates Network, 30207, 1

Krimm, H. A., Barthelmy, S. D., Laha, S., et al. 2020, GRB Coordinates Network, 29139

Krogager, J.-K. 2018, VoigtFit: A Python package for Voigt profile fitting

Krühler, T., Küpcü Yoldaș, A., Greiner, J., et al. 2008, ApJ, 685, 376

Krühler, T., Ledoux, C., Fynbo, J. P. U., et al. 2013, A&A, 557, A18

Krühler, T., Malesani, D., Fynbo, J. P. U., et al. 2015, A&A, 581, A125

Kuin, N. P. M. & Swift/UVOT Team. 2019, GRB Coordinates Network, 26538

Kuwata, A., Toma, K., Kimura, S. S., Tomita, S., & Shimoda, J. 2023, ApJ, 943, 118

Laing, R. A. 1980, mnras, 193, 439

Lamb, G. P., Kann, D. A., Fernández, J. J., et al. 2021, mnras, 506, 4163

Lamb, G. P., Nativi, L., Rosswog, S., et al. 2022, Universe, 8, 612

Lamb, G. P., Tanvir, N. R., Levan, A. J., et al. 2019, ApJ, 883, 48

Landi Degl'Innocenti, E., Bagnulo, S., & Fossati, L. 2007, in Astronomical Society of the Pacific Conference Series, Vol. 364, The Future of Photometric, Spectrophotometric and Polarimetric Standardization, ed. C. Sterken, 495

Langer, N. & Norman, C. A. 2006, ApJ, 638, L63

Laskar, T., Alexander, K. D., Gill, R., et al. 2019, ApJ, 878, L26

Lazzati, D., Covino, S., di Serego Alighieri, S., et al. 2003, A&A, 410, 823

Ledoux, C., Petitjean, P., Bergeron, J., Wampler, E. J., & Srianand, R. 1998, A&A, 337, 51

Lee, W. H. & Ramirez-Ruiz, E. 2007, New Journal of Physics, 9, 17

Leibler, C. N. & Berger, E. 2010, ApJ, 725, 1202

Levan, A. J., Gompertz, B. P., Salafia, O. S., et al. 2024a, Nature, 626, 737

Levan, A. J., Jonker, P. G., Saccardi, A., et al. 2024b, arXiv e-prints, arXiv:2404.16350

Levan, A. J., Lamb, G. P., Schneider, B., et al. 2023a, ApJ, 946, L28

Levan, A. J., Lyman, J. D., Tanvir, N. R., et al. 2017, ApJ, 848, L28

Levan, A. J., Malesani, D. B., Gompertz, B. P., et al. 2023b, Nature Astronomy, 7, 976

Li, Y., Zhang, B., & Lü, H.-J. 2016, ApJS, 227, 7

Li, Y., Zhang, B., & Yuan, Q. 2020, ApJ, 897, 154

Lien, A., Sakamoto, T., Barthelmy, S. D., et al. 2016, ApJ, 829, 7

Lipkin, Y. M., Ofek, E. O., Gal-Yam, A., et al. 2004, ApJ, 606, 381

Lodders, K., Palme, H., & Gail, H. P. 2009, Landolt Börnstein, 4B, 712

Loeb, A. & Perna, R. 1998, ApJ, 495, 597

Lü, H.-J., Liang, E.-W., Zhang, B.-B., & Zhang, B. 2010, ApJ, 725, 1965

Lü, H.-J., Zhang, B., Liang, E.-W., Zhang, B.-B., & Sakamoto, T. 2014, mnras, 442, 1922

Lyman, J. D., Levan, A. J., Tanvir, N. R., et al. 2017, mnras, 467, 1795

Lyutikov, M. & Blandford, R. 2003, arXiv e-prints, astro

Ma, X., Hopkins, P. F., Faucher-Giguère, C.-A., et al. 2016, mnras, 456, 2140

MacFadyen, A. I. & Woosley, S. E. 1999, ApJ, 524, 262

Madau, P. & Dickinson, M. 2014, ARA&A, 52, 415

Magalhaes, A. M., Pereyra, A., Dominici, T., & Abraham, Z. 2003, GRB Coordinates Network, 2163, 1

MAGIC Collaboration, Acciari, V. A., Ansoldi, S., et al. 2019, Nature, 575, 455

Malacaria, C., Hristov, B., & Fermi GBM Team. 2021, GRB Coordinates Network, 30199, 1

Malesani, D., Heintz, K. E., Stone, M., & Stone, J. 2018, GRB Coordinates Network, 22660

Malesani, D. & Kirkpatrick, C. 2016, GRB Coordinates Network, 19295

Malesani, D., Xu, D., & Kuutma, T. 2016, GRB Coordinates Network, 19300

Malesani, D., Xu, D., Watson, D. J., & Blay, P. 2015, GRB Coordinates Network, 17756

Malesani, D. B., Levan, A. J., Izzo, L., et al. 2023, arXiv e-prints, arXiv:2302.07891

Maller, A. H., Prochaska, J. X., Somerville, R. S., & Primack, J. R. 2003, mnras, 343, 268

Mandarakas, N., Blinov, D., Aguilera-Dena, D. R., et al. 2023, A&A, 670, A144

Mandhai, S., Lamb, G. P., Tanvir, N. R., et al. 2022, mnras, 514, 2716

Maraston, C. 2005, mnras, 362, 799

Marshall, F. E. & Gibson, S. L. 2016, GRB Coordinates Network, 19275

Masetti, N., Palazzi, E., Pian, E., et al. 2003, A&A, 404, 465

Mazets, E. P., Golenetskii, S. V., Ilinskii, V. N., et al. 1981, Ap&SS, 80, 3

Medvedev, M. V. & Loeb, A. 1999, ApJ, 526, 697

Meegan, C., Lichti, G., Bhat, P. N., et al. 2009, ApJ, 702, 791

Mészáros, P. & Rees, M. J. 1997, ApJ, 476, 232

Metzger, B. D. 2019, Living Reviews in Relativity, 23, 1

Metzger, B. D. 2020, Living Reviews in Relativity, 23, 1

Metzger, B. D., Giannios, D., Thompson, T. A., Bucciantini, N., & Quataert, E. 2011, mnras, 413, 2031

Metzger, B. D., Martínez-Pinedo, G., Darbha, S., et al. 2010, mnras, 406, 2650

Metzger, M. R., Djorgovski, S. G., Kulkarni, S. R., et al. 1997, Nature, 387, 878

Michałowski, M. J., Castro Cerón, J. M., Wardlow, J. L., et al. 2016, A&A, 595, A72

Michałowski, M. J., Kamble, A., Hjorth, J., et al. 2012, ApJ, 755, 85

Minaev, P. Y. & Pozanenko, A. S. 2020, mnras, 492, 1919

Minaev, P. Y. & Pozanenko, A. S. 2021, mnras, 504, 926

Misra, K., Paswan, A., Singh, M., et al. 2018, GRB Coordinates Network, 22663

Modigliani, A., Goldoni, P., Royer, F., et al. 2010, in Society of Photo-Optical Instrumentation Engineers (SPIE) Conference Series, Vol. 7737, Observatory Operations: Strategies, Processes, and Systems III, 773728

Modjaz, M., Kewley, L., Kirshner, R. P., et al. 2008, AJ, 135, 1136

Morgan, A. N., Vanden Berk, D. E., Roming, P. W. A., et al. 2008, ApJ, 683, 913

Mundell, C. G., Kopač, D., Arnold, D. M., et al. 2013, Nature, 504, 119

Muraki, Y., Ono, Y., Fujiwara, T., et al. 2016, GRB Coordinates Network, 19285

Nagao, T., Patat, F., Maeda, K., et al. 2022, ApJ, 941, L4

Nakar, E. 2007, Phys. Rep., 442, 166

Negro, M., Di Lalla, N., Omodei, N., et al. 2023, ApJ, 946, L21

Nicuesa Guelbenzu, A. M., Klose, S., Schady, P., et al. 2021, A&A, 650, A117

Noll, S., Burgarella, D., Giovannoli, E., et al. 2009, A&A, 507, 1793

Norris, J. P. & Bonnell, J. T. 2006, ApJ, 643, 266

Nugent, A. E., Fong, W., Dong, Y., et al. 2020, ApJ, 904, 52

Nugent, A. E., Fong, W.-f., Castrejon, C., et al. 2024, ApJ, 962, 5

Nugent, A. E., Fong, W.-F., Dong, Y., et al. 2022, ApJ, 940, 57

Oates, S. R., Page, M. J., Schady, P., et al. 2009, mnras, 395, 490

O'Connor, B., Troja, E., Dichiara, S., et al. 2022, mnras, 515, 4890

Ofek, E. O., Cenko, S. B., Gal-Yam, A., et al. 2007, ApJ, 662, 1129

Oke, J. B. 1974, ApJS, 27, 21

Oke, J. B. 1990, AJ, 99, 1621

Pacifici, C., Iyer, K. G., Mobasher, B., et al. 2023, ApJ, 944, 141

Page, K. L., Barthelmy, S. D., Gropp, J. D., et al. 2020, GRB Coordinates Network, 29112

Page, K. L., Gropp, J. D., Kennea, J. A., et al. 2021, GRB Coordinates Network, 30170, 1

Pagel, B. E. J. 2009, Nucleosynthesis and Chemical Evolution of Galaxies

Palmerio, J. T., Vergani, S. D., Salvaterra, R., et al. 2019, A&A, 623, A26

Pandey, S. B., Hu, Y., Castro-Tirado, A. J., et al. 2019, mnras, 485, 5294

Patat, F. & Romaniello, M. 2006, PASP, 118, 146

Patat, F. & Taubenberger, S. 2011, A&A, 529, A57

Paterson, K., Fong, W., Nugent, A., et al. 2020, ApJ, 898, L32

Pei, Y. C. 1992, ApJ, 395, 130

Perley, D. A. 2021, GRB Coordinates Network, 30216, 1

Perley, D. A., Krühler, T., Schulze, S., et al. 2016a, ApJ, 817, 7

Perley, D. A., Levan, A. J., Tanvir, N. R., et al. 2013, ApJ, 778, 128

Perley, D. A., Perley, R. A., Hjorth, J., et al. 2015, ApJ, 801, 102

Perley, D. A., Tanvir, N. R., Hjorth, J., et al. 2016b, ApJ, 817, 8

Pforr, J., Maraston, C., & Tonini, C. 2012, mnras, 422, 3285

Piran, T. 1999, Phys. Rep., 314, 575

Planck Collaboration, Ade, P. A. R., Aghanim, N., et al. 2014a, A&A, 571, A16

Planck Collaboration, Ade, P. A. R., Aghanim, N., et al. 2014b, A&A, 571, A16

Plaszczynski, S., Montier, L., Levrier, F., & Tristram, M. 2014, mnras, 439, 4048

Poole, T. S., Breeveld, A. A., Page, M. J., et al. 2008, 383, 627

Prochaska, J. X., Chen, H.-W., Dessauges-Zavadsky, M., & Bloom, J. S. 2007, ApJ, 666, 267

Rahaman, S. k. M., Granot, J., & Beniamini, P. 2024, mnras, 528, L45

Rastinejad, J., Paterson, K., Kilpatrick, C. D., & Fong, W. 2020, GRB Coordinates Network, 29142

Rastinejad, J. C., Fong, W., Kilpatrick, C. D., et al. 2021, ApJ, 916, 89

Rastinejad, J. C., Gompertz, B. P., Levan, A. J., et al. 2022, Nature, 612, 223

Rees, M. J. & Meszaros, P. 1994, ApJ, 430, L93

Roederer, I. U., Mateo, M., Bailey, John I., I., et al. 2016, AJ, 151, 82

Rol, E., Wijers, R. A. M. J., Fynbo, J. P. U., et al. 2003, A&A, 405, L23

Rol, E., Wijers, R. A. M. J., Vreeswijk, P. M., et al. 2000, ApJ, 544, 707

Roming, P. W. A., Kennedy, T. E., Mason, K. O., et al. 2005, Space Sci. Rev., 120, 95

Rossi, A. & CIBO Collaboration. 2021, GRB Coordinates Network, 29311

Rossi, A., Rothberg, B., Palazzi, E., et al. 2022, ApJ, 932, 1

Rossi, E. M., Lazzati, D., Salmonson, J. D., & Ghisellini, G. 2004, mnras, 354, 86

Rouco Escorial, A., Fong, W., Veres, P., et al. 2021, ApJ, 912, 95

Rowlinson, A., Starling, R. L. C., Gourdji, K., et al. 2021, mnras, 506, 5268

Saccardi, A., Vergani, S. D., De Cia, A., et al. 2023, A&A, 671, A84

Sahu, S., Medina-Carrillo, B., Páez-Sánchez, D. I., Sánchez-Colón, G., & Rajpoot, S. 2024, mnras, 533, L64

Sahu, S., Medina-Carrillo, B., Sánchez-Colón, G., & Rajpoot, S. 2023, ApJ, 942, L30

Sakamoto, T., Barthelmy, S. D., Cummings, J. R., et al. 2016, GRB Coordinates Network, 19276

Salpeter, E. E. 1955, ApJ, 121, 161

Sari, R. 1999, ApJ, 524, L43

Sari, R. & Piran, T. 1997, mnras, 287, 110

Sari, R., Piran, T., & Narayan, R. 1998, ApJ, 497, L17

Savaglio, S., Glazebrook, K., & Le Borgne, D. 2009, ApJ, 691, 182

Savchenko, V., Ferrigno, C., Kuulkers, E., et al. 2017, ApJ, 848, L15

Schady, P. 2018, GRB Coordinates Network, 22662

Schady, P. & Chen, T. W. 2018, GRB Coordinates Network, 22666

Schlafly, E. F. & Finkbeiner, D. P. 2011, ApJ, 737, 103

Schmidt, G. D., Elston, R., & Lupie, O. L. 1992, AJ, 104, 1563

Schulze, S., Chapman, R., Hjorth, J., et al. 2015, ApJ, 808, 73

Schulze, S., Krühler, T., Leloudas, G., et al. 2018, mnras, 473, 1258

Science Software Branch at STScI. 2012, PyRAF: Python alternative for IRAF, Astrophysics Source Code Library, record ascl:1207.011

Seifert, W., Appenzeller, I., Baumeister, H., et al. 2003, in Society of Photo-Optical Instrumentation Engineers (SPIE) Conference Series, Vol. 4841, Instrument Design and Performance for Optical/Infrared Ground-based Telescopes, ed. M. Iye & A. F. M. Moorwood, 962–973

Selsing, J., Malesani, D., Goldoni, P., et al. 2019, A&A, 623, A92

Selsing, J., Vreeswijk, P. M., Japelj, J., et al. 2016, GRB Coordinates Network, 19274

Serkowski, K., Mathewson, D. S., & Ford, V. L. 1975, ApJ, 196, 261

Shahmoradi, A. & Nemiroff, R. J. 2015, mnras, 451, 126

Shrestha, M., Steele, I. A., Kobayashi, S., et al. 2022, mnras, 509, 5964

Siegel, M. H., Baer, M., Page, K. L., & Swift/UVOT Team. 2021, GRB Coordinates Network, 30247, 1

Sironi, L. & Goodman, J. 2007, ApJ, 671, 1858

Sironi, L., Keshet, U., & Lemoine, M. 2015, Space Sci. Rev., 191, 519

Skrutskie, M. F., Cutri, R. M., Stiening, R., et al. 2006, AJ, 131, 1163

Stanek, K. Z., Matheson, T., Garnavich, P. M., et al. 2003, ApJ, 591, L17

Starling, R. L. C., Willingale, R., Tanvir, N. R., et al. 2013, mnras, 431, 3159

Steele, I. A., Mundell, C. G., Smith, R. J., Kobayashi, S., & Guidorzi, C. 2009, Nature, 462, 767

Strong, I. B. & Klebesadel, R. W. 1976, Scientific American, 235, 66

Svensson, K. M., Levan, A. J., Tanvir, N. R., Fruchter, A. S., & Strolger, L. G. 2010, mnras, 405, 57

Tanga, M., Krühler, T., Schady, P., et al. 2018, A&A, 615, A136

Tanvir, N. R., Fox, D. B., Levan, A. J., et al. 2009, Nature, 461, 1254

Tanvir, N. R., Fynbo, J. P. U., de Ugarte Postigo, A., et al. 2019, mnras, 483, 5380

Tanvir, N. R., Levan, A. J., Fruchter, A. S., et al. 2013, Nature, 500, 547

Tanvir, N. R., Levan, A. J., González-Fernández, C., et al. 2017, ApJ, 848, L27

Teboul, O. & Shaviv, N. J. 2021, mnras, 507, 5340

Thöne, C. C., Christensen, L., Prochaska, J. X., et al. 2014, mnras, 441, 2034

Thöne, C. C., de Ugarte Postigo, A., Izzo, L., et al. 2024, A&A, 690, A66

Thöne, C. C., Fynbo, J. P. U., Goldoni, P., et al. 2013, mnras, 428, 3590

Thöne, C. C., Fynbo, J. P. U., Östlin, G., et al. 2008, ApJ, 676, 1151

Thöne, C. C., Izzo, L., Flores, H., et al. 2021, A&A, 656, A136

Thöne, C. C., Michałowski, M. J., Leloudas, G., et al. 2009, ApJ, 698, 1307

Tody, D. 1993, in Astronomical Society of the Pacific Conference Series, Vol. 52, Astronomical Data Analysis Software and Systems II, ed. R. J. Hanisch, R. J. V. Brissenden, & J. Barnes, 173

Troja, E., Butler, N., Watson, A. M., et al. 2018, GRB Coordinates Network, 22664

Troja, E., Castro-Tirado, A. J., Becerra González, J., et al. 2019, mnras, 489, 2104

Troja, E., Fryer, C. L., O'Connor, B., et al. 2022, Nature, 612, 228

Trotter, A., Reichart, D., Haislip, J., et al. 2016, GRB Coordinates Network, 19277

Tsutsui, R., Yonetoku, D., Nakamura, T., Takahashi, K., & Morihara, Y. 2013, mnras, 431, 1398

Tsvetkova, A., Frederiks, D., Golenetskii, S., et al. 2017, ApJ, 850, 161

Tsvetkova, A., Frederiks, D., Svinkin, D., et al. 2021, ApJ, 908, 83

Turnshek, D. A., Bohlin, R. C., Williamson, R. L., I., et al. 1990, AJ, 99, 1243

Uehara, T., Toma, K., Kawabata, K. S., et al. 2012, ApJ, 752, L6

Updike, A. C., Haislip, J. B., Nysewander, M. C., et al. 2008, ApJ, 685, 361

Urata, Y., Toma, K., Covino, S., et al. 2023, Nature Astronomy, 7, 80

van Dokkum, P. G. 2001, PASP, 113, 1420

van Paradijs, J., Groot, P. J., Galama, T., et al. 1997, Nature, 386, 686

Vargas, L. C., Geha, M., Kirby, E. N., & Simon, J. D. 2013, ApJ, 767, 134

Vernet, J., Dekker, H., D'Odorico, S., et al. 2011, A&A, 536, A105

Vernet, J., Dekker, H., D'Odorico, S., et al. 2010, in Society of Photo-Optical Instrumentation Engineers (SPIE) Conference Series, Vol. 7735, Ground-based and Airborne Instrumentation for Astronomy III, 77351I

von Kienlin, A., Meegan, C. A., Paciesas, W. S., et al. 2020, ApJ, 893, 46

Vreeswijk, P. M., Ellison, S. L., Ledoux, C., et al. 2004, A&A, 419, 927

Vreeswijk, P. M., Ledoux, C., Smette, A., et al. 2007, A&A, 468, 83

Vreeswijk, P. M., Ledoux, C., Smette, A., et al. 2011, A&A, 532, C3

Walcher, J., Groves, B., Budavári, T., & Dale, D. 2011, Ap&SS, 331, 1

Wang, C. J., Mao, J., & Bai, J. M. 2016, GRB Coordinates Network, 19280

Watson, D., Hansen, C. J., Selsing, J., et al. 2019, Nature, 574, 497

Wei, J., Cordier, B., Antier, S., et al. 2016, arXiv e-prints, arXiv:1610.06892

Weibel, E. S. 1959, Phys. Rev. Lett., 2, 83

Wiersema, K., Covino, S., Toma, K., et al. 2014, Nature, 509, 201

Wiersema, K., Curran, P. A., Krühler, T., et al. 2012, mnras, 426, 2

Wiersma, R. P. C., Schaye, J., Theuns, T., Dalla Vecchia, C., & Tornatore, L. 2009, mnras, 399, 574

Wijers, R. A. M. J., Vreeswijk, P. M., Galama, T. J., et al. 1999, ApJ, 523, L33

Willingale, R., Starling, R. L. C., Beardmore, A. P., Tanvir, N. R., & O'Brien, P. T. 2013, mnras, 431, 394

Wilms, J., Allen, A., & McCray, R. 2000, ApJ, 542, 914

Wolfe, A. M., Gawiser, E., & Prochaska, J. X. 2005, ARA&A, 43, 861

Wolfe, A. M. & Prochaska, J. X. 2000, ApJ, 545, 591

Woosley, S. & Janka, T. 2005, Nature Physics, 1, 147

Woosley, S. E. 1993, ApJ, 405, 273

Woosley, S. E. & Bloom, J. S. 2006, ARA&A, 44, 507

Woosley, S. E. & Heger, A. 2006, ApJ, 637, 914

Yang, J., Ai, S., Zhang, B.-B., et al. 2022, Nature, 612, 232

Yates, R., Kruehler, T., & Greiner, J. 2016, GRB Coordinates Network, 19272

Yoldaș, A. K., Krühler, T., Greiner, J., et al. 2008, in American Institute of Physics Conference Series, Vol. 1000, Gamma-ray Bursts 2007, ed. M. Galassi, D. Palmer, & E. Fenimore, 227–231

Yoon, S. C., Langer, N., & Norman, C. 2006, A&A, 460, 199

Yuan, W., Zhang, C., Chen, Y., & Ling, Z. 2022, in Handbook of X-ray and Gamma-ray Astrophysics, ed. C. Bambi & A. Sangangelo, 86

Yuan, W., Zhang, C., Feng, H., et al. 2015, arXiv e-prints, arXiv:1506.07735

Zafar, T., Watson, D., Fynbo, J. P. U., et al. 2011, A&A, 532, A143

Zhang, B. 2006, Nature, 444, 1010

Zhang, B., Fan, Y. Z., Dyks, J., et al. 2006, ApJ, 642, 354

Zhang, B. & Yan, H. 2011, ApJ, 726, 90

Zhang, B., Zhang, B.-B., Virgili, F. J., et al. 2009, ApJ, 703, 1696

Zhang, B. B., Liu, Z. K., Peng, Z. K., et al. 2021, Nature Astronomy, 5, 911

Zhang, Z.-B., Yang, E.-B., Choi, C.-S., & Chang, H.-Y. 2016, mnras, 462, 3243

Zhang, Z. B., Zhang, C. T., Zhao, Y. X., et al. 2018, PASP, 130, 054202